MICROWAVE ENABLED FABRICATION OF HIGHLY CONDUCTIVE

GRAPHENE AND POROUS CARBON/METAL HYBRIDS FOR SUSTAINABLE

CATALYSIS AND ENERGY STORAGE

by

Keerthi Savaram

A Dissertation submitted to the

Graduate School-Newark

Rutgers, The State University of New Jersey

in partial fulfillment of the requirements

for the degree of

Doctor of Philosophy

Graduate Program in Chemistry

written under the direction of

Professor Huixin He

and approved by

_____

_____

_____

_____

Newark, New Jersey

October, 2017

Copyright Page

Abstract of the dissertation

MICROWAVE ENABLED FABRICATION OF HIGHLY CONDUCTIVE GRAPHENE AND POROUS CARBON/METAL HYBRIDS FOR SUSTAINABLE CATALYSIS AND ENERGY STORAGE

By Keerthi Savaram

Dissertation Director: Prof. Huixin He

Carbon is the most abundant material next to oxygen in terms of sustainability. The potential of carbon based materials has been recognized in recent decades by the discovery of fullerene (1996 Nobel prize in chemistry), carbon nanotubes (2008 Kavli prize in nanoscience) and graphene (2010 Nobel prize in physics). The synthesis of carbon materials with well controlled morphologies lead to their exploration in both fundamental research and industrial applications. Graphene also commonly referred to as a wonder material has been under extensive research for more than a decade, due to its excellent electronic, optical, thermal and mechanical properties. However, the realization of these applications for practical purposes require its large scale synthesis. The common method of graphene synthesis involves reduction of graphene oxide. Nevertheless, complete restoration of intact graphene basal plane destroyed by oxidation cannot be achieved, limiting the application of as synthesized graphene in flexible macro electronics, mechanically and electronically reinforced composites etc. Hence, research was pursued in regards to achieve controlled oxidation, sufficient enough to overcome the Vander-Waals forces and preserving the graphene domains.

One such approach reported by our group is the solution processable graphene achieved *via* controlled oxidation, by the use of nitronium oxidation approach. However, toxic NO_x gases and byproducts generated during the synthesis, limits the scalability of this approach. In this thesis, for the first time, we reported the synergy of piranha etching solution with intercalated graphite for the controlled oxidation of graphite particles *via* microwave heating in **chapter 2**. The controlled oxidation leads to rapid (60 seconds) and direct generation of highly conductive, clean low oxygen containing graphene sheets without releasing any detectable toxic gases or aromatic by-products as demonstrated by gas chromatography-mass spectrometry. These highly conductive graphene sheets have unique molecular structures, different from both graphene oxide and pristine graphene sheets. They can be dispersed in both aqueous and common organic solvents without surfactants/stabilizers producing "clean" graphene sheets in solution phase. "Paper-like" graphene films are generated *via* simple filtration resulting in films with a conductivity of 2.26×10^4 S m^{-1}, the highest conductivity observed for graphene films assembled *via* vacuum filtration from solution processable graphene sheets to date. After 2-hour low temperature annealing at 300 °C, the conductivity further increased to 7.44×10^4 S m^{-1}. This eco-friendly and rapid approach for scalable production of highly conductive and "clean" solution-phase graphene sheets would enable a broad spectrum of applications at low cost.

Irrespective of the vast applications of highly conductive graphene, it exhibits limited catalytic centers, is impervious, and limits the diffusion of ions. This inadequacy can be overcome by the hole generation on highly conductive graphene. Current approaches for large scale production of holey graphene require graphene oxide

(GO) or reduced GO (rGO) as starting materials. Thus generated holey graphene derivatives still contain a large number of defects on their basal planes, which not only complicates fundamental studies, but also influences certain practical applications due to their largely decreased conductivity, thermal and chemical stability. This work reports a novel scalable approach exploiting the wireless joule heating mechanism provided by microwave irradiation of partially oxidized graphite intercalation compounds in **chapter 3**. The wireless joule heating mechanism affords region-selective heating, which not only enable fabrication of holey graphene materials with their basal plane nearly intact, but also engineers the edges associated with holes to be rich in zigzag geometry. The term pristine holey graphene was given, to differentiate from the holey graphene derivatives with basal plane defects, as reported in the literature. The pristine holey graphene with zigzag edges were studied and explored as a metal free catalyst for reduction reactions via hydrogen atom transfer mechanism. The pristine holey graphene nanoplatelets not only exhibited high catalytic activity and desired selectivity, but also provided excellent chemical stability for recyclability, which is very different from its counterpart holey graphene derivatives with basal plane defects. It was also reported that the reduction of nitrobenzene occurs *via* condensation pathway with this catalyst.

To further provide insight into combustion of graphite in air with microwave irradiation, the stabilized intercalated graphene without point defects was used to generate holes in **chapter 4**. The co-intercalated O_2 into graphite intercalated compound act as the internal oxidant, to oxidize the carbon, along with the surrounding air. High local temperatures were achieved via joule heating mechanism, hence promoting combustion of graphene to generate holes and edges. We observed that in combination to hole generation, higher

conductivity was also observed in comparison to the holey graphene synthesized in **chapter 3**. The highly conductive holey graphene was tested for their electro-catalytic activity in the reduction of oxygen. The reduction of oxygen occurs *via* $2e^-$ pathway, where peroxide with 90% yield was recorded. This opens path for onsite peroxide production in alkaline media, and therefore allowing its use in bleaching industries.

In concern of carbon based materials being explored for catalysis, their high amount to facilitate the reaction, limits practicality of the catalyst for industrial applications. However, the immobilization of metal nanoparticles onto porous carbon supports, synthesized from sustainable and cheap biomass was widely pursued. It was widely reported that the doping of carbon support with N further improved their interaction with the metal and promoted higher catalytic activity. In **chapter 5**, for the first time, the influence of P doped carbon support on catalytic activity of Pd was reported. A single step microwave assisted fabrication of Pd embedded into porous phosphorous doped graphene like carbon was demonstrated. Structural characterization revealed that, the metal nanoparticles are in the range of 10nm with a surface area of $1133m^2/g$. The developed method is not only sustainable as it is synthesized from biomass and anti-nutrient molecule (phytic acid), but also energy efficient as microwave irradiation (50sec) is used for the catalyst synthesis. The as synthesized catalyst recorded 90% conversion with a TOF of $23000h^{-1}$ for benzyl alcohol oxidation, which remained constant even after 8 recycles indicating the stability of catalyst. Different wt% of Pd onto PGC was tested for their alcohol oxidation capacity and found that the 3% Pd-PGc which activates O_2 more towards $4e^-$ in ORR has the best conversion and selectivity.

The biomass molecule phytic acid used for the synthesis of phosphorous doped carbon support was also used as a phosphorous source in the synthesis of tin phosphides in **chapter 6**. Current studies have shown that sodium, a low cost and naturally abundant metal, can act as a substituent for lithium in lithium ion batteries (LIB), hence, allowing their applications in real world. This transition towards the use of sodium ion batteries (SIB) has entailed research to improve the cycle stability and energy density of battery by introducing tin phosphides as anodes for batteries. Tin phosphides exhibit a self-healing mechanism, hence decreases the capacity decay as observed in the case of Sn metal. However, it was reported that the self-healing mechanism is not completely reversible with partial pulverization observed. Therefore, we pursued a time efficient method to synthesize tin phosphide in a phosphorous doped carbon matrix (SnP@PGc) *via* microwave irradiation. The SnP@PGc formed when tested as anode for SIBs, demonstrated superior capacity of 515 mAh/g after 750 cycles at a charge and discharge current of 0.2 C. The superior cycle stability can be attributed to the protection against volume expansion by phosphorous doped porous carbon shell during battery charge and discharge process and hence mitigating the pulverization of tin phosphides.

Preface

Chapter 1, **Figures 1.1.** is reprinted with permission from "Royal Society of Chemistry", enclosed with the title "Graphdiyne and graphyne: from theoretical predictions to practical construction, Chem. Soc. Rev., 2014, **43**, 2572-2586". **Figure 1.2.1** is reprinted with permission from "Materials today", enclosed with the title "Production and processing of graphene and 2d crystals, Volume 15, Issue 12, December 2012, Pages 564-589".**Figure 1.2.2** is reprinted with permission from "Journal of Controlled Release", enclosed with the title "Production and processing of graphene and 2d crystals, Volume 226, 28 March 2016, Pages 217-228".**Figure 1.5.2** is reprinted with permission from "Springer Link", enclosed with the title "**Microwave synthesis solutions from personal chemistry**, Molecular Diversity, June 2003, Volume 7, Issue 2–4, pp 291–298".

Chapter 2, A large portion of this material has been published as a full journal article in "*Green Chemistry*". All the figures and text of this published article are reprinted in this chapter with permission from "Keerthi Savaram , Malathi Kalyanikar , Mehulkumar Patel, Roman Brukh, Carol R. Flach, Ruiming Huang, M. Reza Khoshi,Richard Mendelsohn, Andrew Wang, Eric Garfunkel and Huixin He, *Green Chem.*, 2015, **17**, 869-881, Royal Society Chemistry".

Dedication

This dissertation is dedicated to my Father

Nagachandra Rao Savaram and to my Family

Acknowledgement

It is with utmost respect I acknowledge my deepest gratitude to my Advisor Dr. Huixin He, for letting me able to fulfil my dream. I appreciate her advice and guidance throughout my Master's and her encouragement to let me further pursue Ph.D., without whom this task is highly impossible. I sincerely appreciate her patience in molding me into an independent researcher. I would also acknowledge my sincerest thanks to my committee members, Dr. Phillip Huskey, Dr. Jenny Lockard, and Dr. Chunsheng Wang, who have readily agreed on such short notice in spite of their busy schedules. I really appreciate their time and efforts in correcting my thesis.

I would also like to thank my collaborators for their efforts in characterizing my graphene/ metal carbon hybrids and their valuable inputs: (1) Dr. Chunseng Wang and his students (Xiulin Fan, Tao Gao) form University of Maryland, for their help to characterize the crystal lattice of Sn_4P_3 via TEM and testing the material for sodium ion batteries. (2) Prof. Eric Garfunkel and his students (Malathi Kalyanikar, Hongbin Yang, Mengjun Li) from Rutgers University New Brunswick, for XPS (X-ray photoelectron spectroscopy) and RBS (Rutherford Backscattering Spectroscopy) characterization and analysis. (3) Prof. Richard Mendelsohn, Dr. Carol R Flach and his post doc (Dr. Qihong Zhang) for their help in FT-IR and Raman measurement. (4) Prof. Kristina Keating and her student (Gordon Osterman) from Dept of Environmental Science from Rutgers University, Newark, for surface area measurement of carbon metal hybrids samples by Brunauer–Emmett–Teller (BET) method. (5) Vladimir Ossipov (Ioffe Physical-Technical Institute, Russia) for his EPR and Raman measurements of holey graphene mentioned in chapter 3, (6) Kazuyuki Takai and his students (Kentaro Tajima, Takuya Hayashi, Department of Chemistry, Tokyo Institute

Last but not the least, I would like to thank my Rutgers family cum friends (Dr. Ruiming Huang, Dr. Mehul Patel, Amir Khoshi) who helped me to learn the ropes in research and supporting me in conducting research here at Rutgers, other lab members (Qingdong Li, Bowei Li) and my students (Zille Huma, Faujiya Lima, Mehul Modi, Nicole Taylor). My sincere thanks to the department of chemistry for bearing with me and making my Ph.D. journey memorable.

Lastly I would thank my father (Nagachandra Rao Savaram), my mother (Jhansi Lakshmi Savaram), my sister (Madhuri Pagadala), my brother in law (Naresh Pagadala) and my cutie nephew (Sathvik Pagadala) for giving me the opportunity and encouragement to pursue my higher study here in U.S.A. I would also like to thank my grandparents (Subba Rao Kolli and Swarajya Lakshmi Kolli), who always encouraged me to pursue my dreams. Without all their support this dream of mine to pursue Ph.D. would be hardly achievable.

Table of Contents

List of Figures

List of Schematic drawings

List of Tables

Chapter 1: Introduction

1.1 Carbon and its allotropes

Carbon is the fourth most abundant element on earth and its various physical states as allotropes can be attributed to its disparate hybridized electron configurations (sp, sp^2, sp^3). These result in the formation of varying types of carbon-carbon bonds (single, double, triple, aromatic), which differ in strengths and spatial arrangements of electron orbitals, allowing their occurrence as allotropes. Based on their physical form, carbon is differentiated as either amorphous or crystalline carbon. The former carbon form consists of activated carbons whereas the latter exhibits a wide variety of allotropes. Fullerenes (0D with 3 carbons connected), carbon nanotubes (1D with 3 carbons connected), carbynes (1D with 2 carbons connected), graphite and graphene (2D with 3 carbons connected), diamond, londsdaleite, cold compressed graphite (3D with 4 carbons connected) are the different allotropes of crystalline carbon that exist in nature or can be synthesized (**Figure 1.1**).
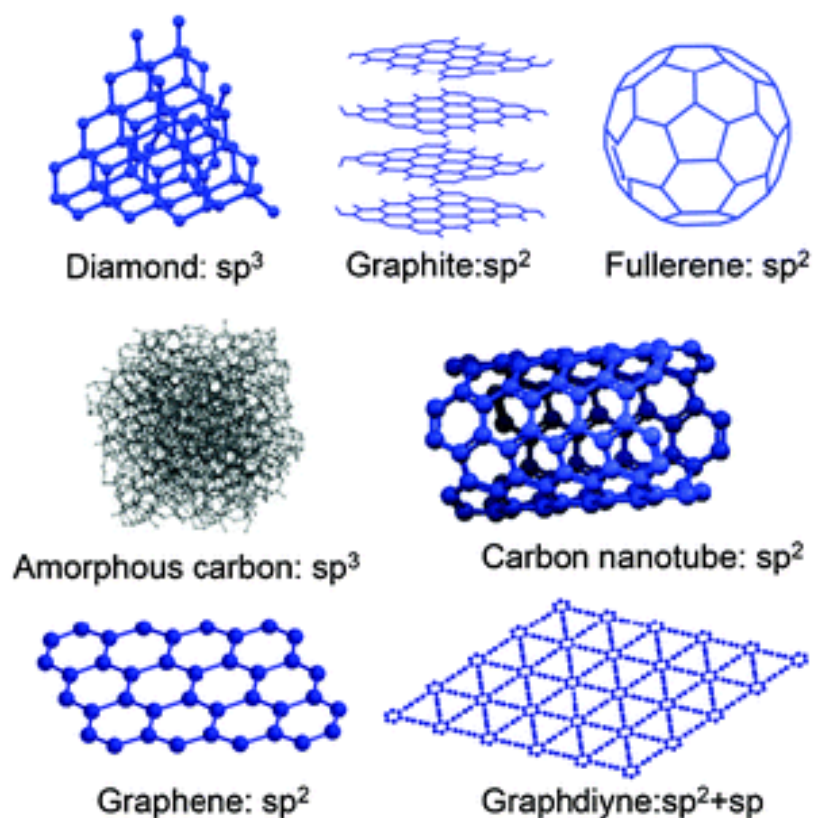
Figure 1.1. Natural and synthesized carbon allotropes [1].

1.1.1. Amorphous carbon

Amorphous carbon lacks crystallinity and its low density makes it more susceptible to harsh oxidizing reagents. Most amorphous carbons contain microscopic crystals of either graphite-like[2] or diamond-like[3] carbon. Commonly found amorphous carbon, such as carbon black, activated carbon and coal, are synthesized by pyrolysis. The presence of graphite-like domains in carbon black allows its use as a conductive filler in energy storage devices and fuel cells, whereas the high surface area of activated carbon promotes its use as a carbon support for metal nanoparticles which are used in catalysis. **Figure 1.1.1** depicts the SEM images of various types of amorphous carbon.
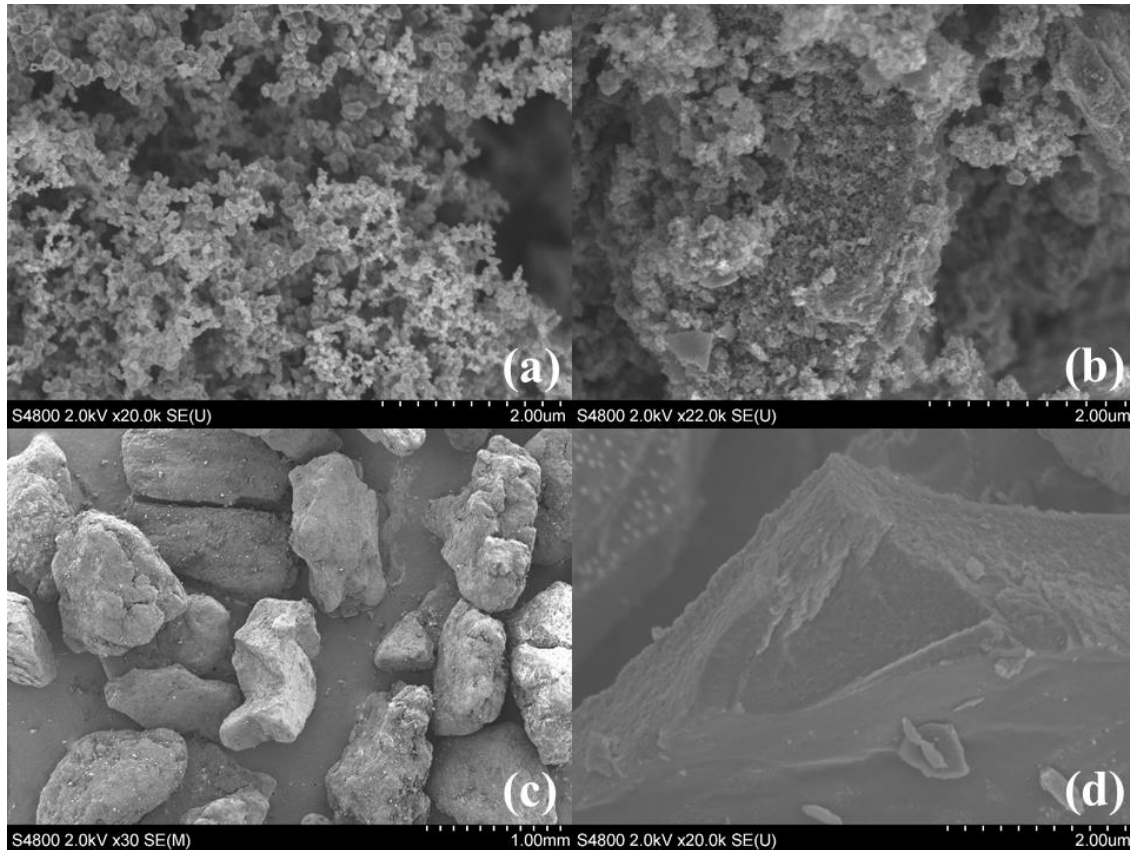
Figure 1.1.1. The SEM image of carbon black (a), activated carbon (b), coal (c) with its cross sectional view (d).

1.1.2. Crystalline carbon

As the name implies, carbon atoms are arranged in a crystal lattice. The most abundant naturally available crystalline carbon includes diamond and graphite. Diamond is known for its strong rigidness and is mostly used in cutting and grinding tools, whereas graphite is most commonly used as a lubricant due to the weak bonds between carbon layers, owing to its soft and slippery properties. The synthesized crystalline carbon allotropes include fullerenes, carbon fibers, carbon nanotubes and graphene (**Figure 1.1.2**).
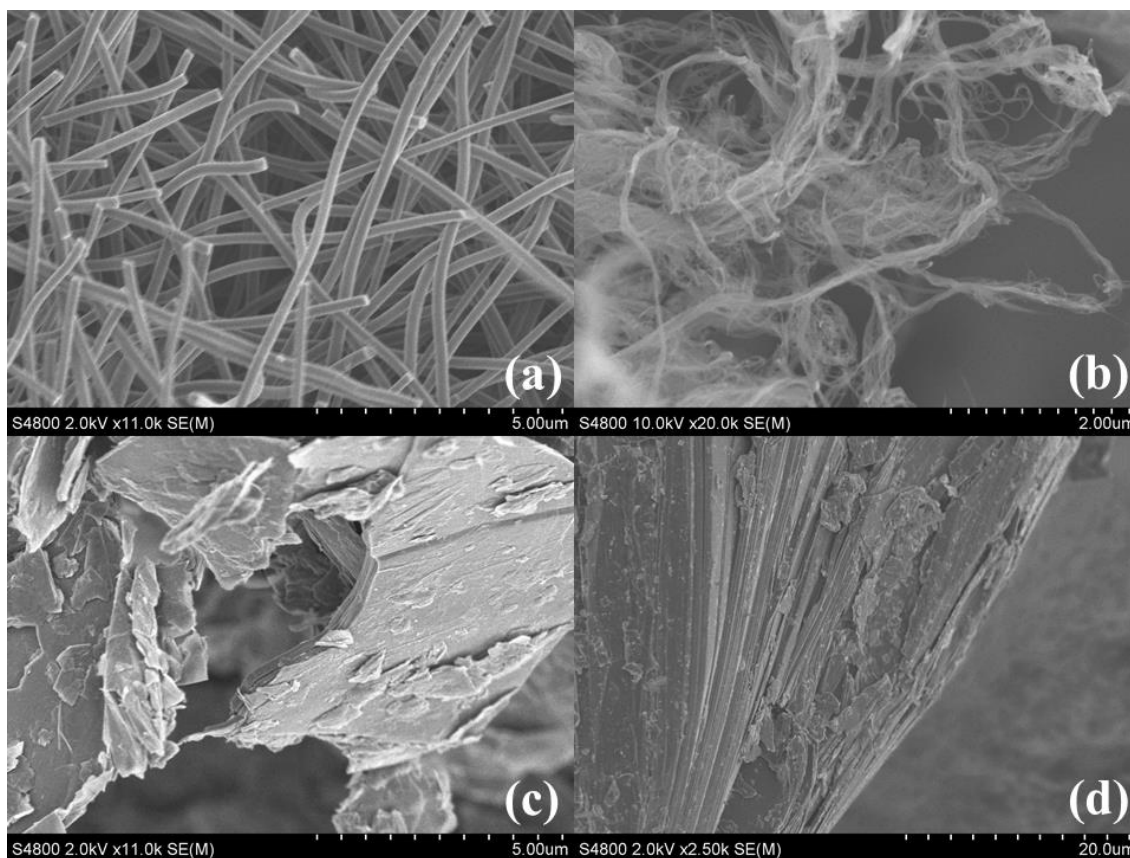
Figure 1.1.2. SEM images of some of the crystalline allotropes such as, carbon fibers (a), single walled carbon nanotubes (b), graphite (c), with its cross sectional view (d).

1.2. Graphene

(a) Graphene   (b) Few-layer graphene   (c) Graphite

(d) Reduced graphene oxide (rGO)   (e) Graphene oxide (GO)
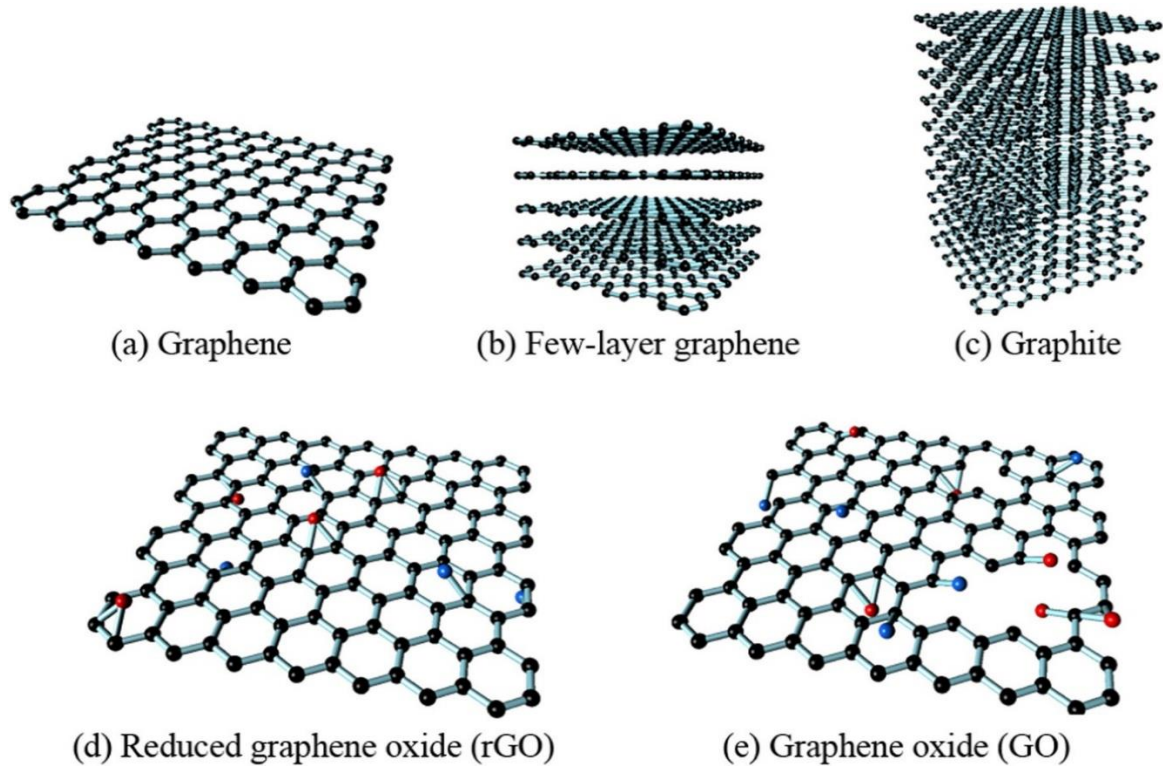
Figure 1. 2. 1. Naturally occurring or synthesized 2D carbon allotropes [57].

A single layer of sp^2 hybridized carbon arranged in a honeycomb network is referred to as graphene. The stacks of graphene are held together by Vander Waals forces and is referred to as graphite which can occur either naturally or be synthesized (**Figure 1.2.1.**). Graphite has been known as mineral for more than 500 years. Synthesis of single-layer graphene can be achieved by overcoming Vander Waals attraction between the first and second carbon layers in graphite, without disrupting adjacent sheets. In 2004, Geim and coworkers at Manchester University exfoliated a single graphene layer using a scotch tape method, which bestowed them the Nobel Prize in 2010[4]. It is the strongest material by weight, and exhibits superior properties such as (1) impermeability to ions and gases[5], (2) mechanical stiffness (young's modulus of 1TPa)[6], (3) strength (130 GPa)[6], (4) elasticity, (5) thermal conductivity ($>3000 WmK^{-1}$)[7], (6) electron mobility ($2.5 \times 10^5 cm^2 v^{-1} s^{-1}$)[8], (7) optical

transparency (~97.7%), (8) having large spring constant (1-5 Nm^{-1})[9], (9) sustaining high densities of electric current[10], (10) being chemically inert to various gases and (11) having high surface area (2630m^{2}g^{-1})[11]. Graphene is a semi-metal with degenerate valence and conduction band at K point in the Brillouin zone (occurring only for special unit cell geometry and orientation relative to graphene's high axis symmetry)[12]. The unique properties of graphene allow its application in various fields such as electronics, photonics, energy storage and generator, super capacitors, catalysts etc. The properties of graphene with some of their applications are listed in **Table 1.2.1**.

Table 1.2.1. The property of graphene and its respective applications.

Graphene Property	Application
Transparency with electrical conductivity	Flexible and optical electronics
Electrical and thermal conductivity	Graphene-based paints for conductive ink, in Li ion batteries as conductive filler to improve electrical conductivity and to help dissipate the generated heat *via* thermal conductivity.
Large surface area	Support for loading metal nanoparticles
Large surface area + chemical purity + ease of functionalization	Sensors for the detection of glucose, cholesterol, hemoglobin, drug delivery, etc.
Large surface area + conductivity	Super-capacitors
Mechanical strength	Tissue engineering and regenerative medicine

The mentioned applications depend on reliability of producing high quality single-layer graphene in a scalable approach. The top-down or bottom-up approaches are two different strategies involved in graphene synthesis as shown in **Figure 1.2.2.**
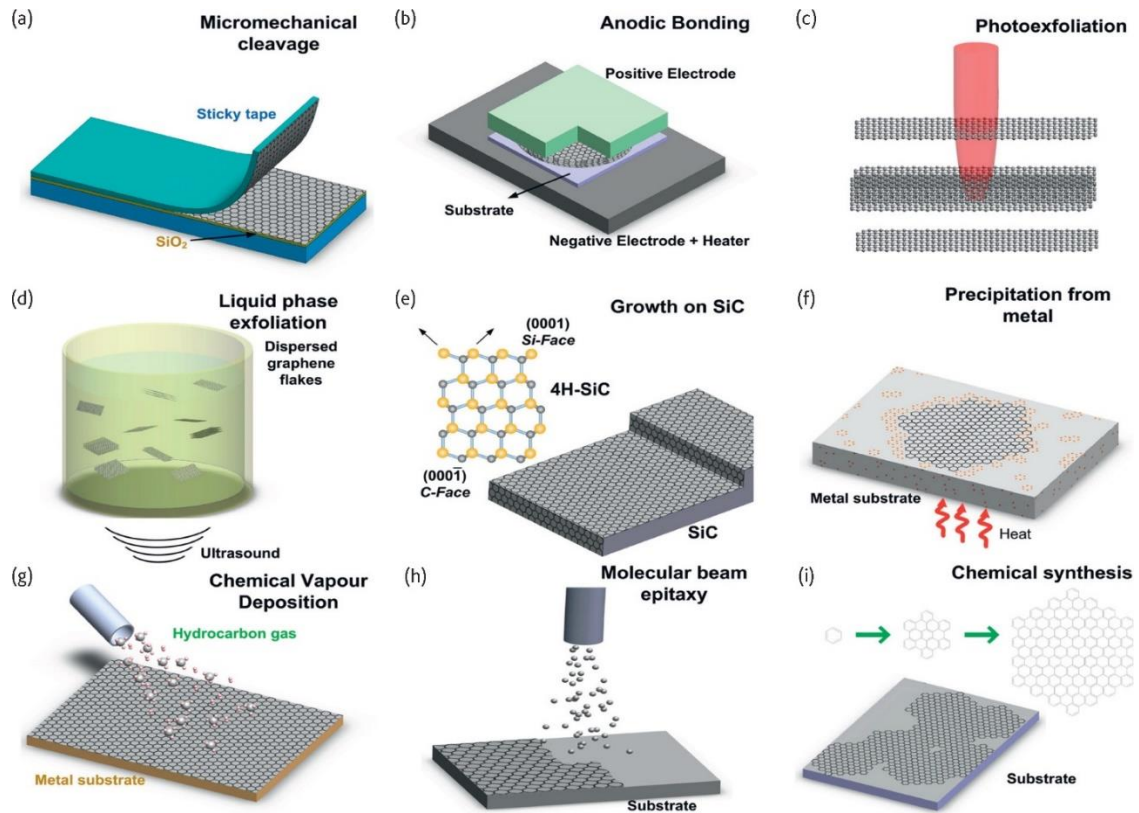
Figure 1. 2. 2. Different production and processing techniques of Graphene[13].

1.2.1. Bottom-up approach

The bottom-up approach is achieved through organic synthesis of small molecule precursors such as hexa-peri-hexabenzocoronene[14], N,N´-bis(2,6-diisopropyphneyl)-3,4,9,10-perylenetetracarboxylic diimide[15] and polycyclic aromatic hydrocarbons (PAHs)[16]. Uniform single-layered graphene can be produced by this technique, however limited size range of starting molecule hinders the application of this technique for

synthesis of large graphene sheets. The use of large macromolecules can solve this problem, nonetheless they become insoluble in reaction media and also lead to unwanted side reactions, thereby degrading the quality of graphene sheets. Substrate-assisted growth can be used as an alternative to generate single-layer graphene sheets up to several μm in lateral size. The substrate acts as a catalytically active solid support and aids in synthesis of single- layer graphene. This technique, Chemical Vapor Deposition (CVD), is used to synthesize high quality graphene for its use in various electronic and photonic applications. The cheap transition metals, such as Cu[17] and Ni[18], are most commonly used substrates (Ru[19], Pt[20], Pd[21], etc., were also used). In this technique, hydrocarbon source decomposes and after nucleation, the conditions need to be carefully controlled to promote crystal growth and prevent growth of additional layers. Another technique involves the production of graphene from silicon carbide (SiC). It was reported as early as 1896 by Acheson[22] for lubrication purposes, and this technique is referred to as epitaxial growth. Graphene forms much faster on carbon surface rather than on silica surface, due to large mismatch between SiC and graphene [4b, 23].

The bottom-up approach facilitates the synthesis of graphene with controlled morphology [18c]. Besides high temperature demand, the use of substrates and lengthy synthesis procedures often limit the scalability of these approaches.

1.2.2. Top-down approach

The top-down approach of graphene synthesis involves the use of graphite as a precursor and its exfoliation. The mechanical exfoliation of graphite delivers high quality graphene, however, suffers from the drawback of high throughput and yield. Laser ablation[24] and photo exfoliation[25] techniques can also be pursued to achieve high quality graphene.

8

These techniques utilize laser pulses to exfoliate or ablate graphite flakes. The process is best implemented under inert and vacuum conditions. However, this technique is still in its infancy with further development needed. Hence, exploration to synthesize graphene in a scalable approach has been pursued. The most common way to synthesize graphene is through the reduction of graphene oxide. In 1859, Brodie[26] demonstrated that adding potassium chlorate ($KClO_3$) in fuming nitric acid (HNO_3) to graphite reaction mixture results in oxidation of graphite. Later in 1898, Staudenmaier[27] improved this protocol by adding sulfuric acid (H_2SO_4) in HNO_3 and gradually incorporating $KClO_3$ into graphite mixture to achieve oxidation of graphite. In 1958, Hummers [28] reported the addition of potassium permanganate ($KMnO_4$) and sodium nitrate ($NaNO_3$) in a mixture of H_2SO_4 and HNO_3 to oxidize graphite. This method was further modified by decreasing $NaNO_3$ and increasing $KMnO_4$ amount. The principle involves disruption of Vander Waals forces in graphite layers by their oxidation. The graphite oxide upon mild sonication or dispersion leads to their exfoliation to graphene oxide (GO), **Figure 1.2.1**. GO, nonetheless compromises the unique properties of graphene due to heavily oxidized groups at edges and on their surface. Hence, high temperature annealing[29] or reduction *via* chemical reagents, such as hydrazine[30], or both[31] are required. Other reducing agents such as $NaBH_4$[32], ascorbic acid[33], hydroiodic acid[34], etc., or microwave treatment of graphite oxide is necessary to restore the compromised properties in GO[35] and is referred to as reduced graphene oxide (rGO), **Figure 1.2.1**. Recently, Manish et al. developed a high quality graphene from microwave-assisted reduction of partially reduced GO[36]. The scalability of these approaches is not plausible, due to their low quality graphene in some

scenarios, lengthy reaction times, post treatment of product, extensive cleaning procedures, metal impurities trapped within the product during their synthesis, cost etc.

Liquid phase exfoliation of graphite through sonication in either organic solvents or aqueous surfactant solutions was developed to yield single to few-layer graphene free from oxides and structural defects. Thin graphene films were fabricated by vacuum filtration of as prepared graphene dispersions, which exhibited superior conductivity. Graphene/polymer composites, which have application in microelectronic devices, can be synthesized by direct addition of polymer into graphene dispersion. Liquid phase exfoliation provides a simple and cost-effective way to fabricate moderate to high quality graphene sheets, without requirement of expensive substrates. The mechanism underlying liquid phase exfoliation can be elaborated from a thermodynamic point of view, as the enthalpy of mixing, combined with charge transfer between the carbon layers of graphite and solvent molecules [37]. Organic solvents with surface tensions and energies similar to that of graphene were found to be effective dissolution media using the expression[37a]

$$\frac{\Delta H_{mix}}{V_{mix}} = \frac{2}{T_{NS}} (\sqrt{E_{S,S}} - \sqrt{E_{S,G}})^2 \emptyset_G$$

Where ΔH_{mix} is enthalpy of mixing, V_{mix} is the volume of mixture, T_{NS} is the thickness of graphene sheet, $E_{S,S}$ and $E_{S,G}$ are the surface energies of solvent and graphene, and $\emptyset_G$ is the volume of graphene dispersed. Good exfoliating solvents based on the above equation include 1-methyl-2-pyrrolidinone (NMP)[37a, 38], ortho-dichlorobenzene (o-DCB)[39] and N,N-dimethylformamide (DMF)[40].

The zeta potential and electrophoresis measurements of liquid exfoliated graphene indicates that the dispersed graphene is either positively or negatively charged. The actual

charge is dependent on solvent used, and hence preventing the exfoliated graphene aggregation in solvents. The charge transfer mechanism allows for exfoliation of graphite in solvents such as ionic liquids[41] and chlorosulphonic acid[42], due to their strong interactions with π electrons of graphite/graphene owing to their ionicities. These liquids are costly and hence cannot be scaled up.

Water is an ideal solvent for numerous biological applications, due to its biocompatibility and non-toxicity. The highly hydrophobic nature of graphite/graphene prevents its exfoliation and dispersion in water and other hydrophilic solvents. Hence, surfactants such as sodium cholate[43], sodium dodecyl benzenesulfonate[44], pluronic[45] or polymers such as polyvinyl pyrrolidone[46], pyrene derivatives[47], etc., were used for the exfoliation and stabilization of dispersed graphene.

Nevertheless, water is not an ideal choice for graphene-based electronic devices because of the dielectrics at interface which enhances charge trapping phenomenon[48]. The use of surfactants to stabilize water-dispersed graphene reduces the electrical conductivity of as fabricated devices. NMP and DMF, commonly used solvents which aids in graphene exfoliation are toxic and irritants [49] [50]. Apart from toxicity, complete removal of these solvents is necessary for graphene to be used in electrical measurements. Residual solvents have a strong impact on the performance of these devices and thus dispersion of graphene in low boiling point solvents such as ethanol is preferred. Low boiling point solvents exhibit lower surface energies than that of graphite hence pose difficulties in regard to their exfoliation. Hence, a simple solvent exchange technique was reported to disperse the exfoliated graphene in NMP to ethanol, with a conductivity as high as 1130cm^{-1}. A

summary with different approaches to synthesize graphene and its applications is listed in

Table 1.2.2.

Table 1.2.2. The property of graphene and its respective applications.

Method	Crystalline size (µm)	Sample size (mm)	Charge carrier mobility	Application	Quality of the graphene	Disadvantage of this method
Mechanical exfoliation[4a]	>1000	>1	>2× 10^5	Research	High	Scalability
Chemical exfoliation[51]	≤0.1	Infinite as a layer of overlapping flakes	100	Coatings, paints, ink, composites, transparent, conductive layers, energy storage, bio applications	Low-moderate	Toxic chemicals, need of large solvents to clean the synthesized product, unnecessary functionalization of graphene.
Reduced GO[30a, c, 52]	~100	Infinite as a layer of overlapping flakes	1	Coatings, paints, ink, composites, transparent, conductive layers, energy storage, bio applications	Low-moderate	Strong oxidizing agents, need of large solvents to clean the synthesized product, need an additional heating step (high temperature) to restore the properties of graphene, lengthy reaction times
CVD[17a, 18a-d]	1000	1000	10000	Photonics, nanoelectronics,	Moderate-high	High temperature, transfer

				transparent, conductive layers, sensors, bio applications		process necessary, expensive owing to large energy consumption, removal of metal catalyst.
SiC[53]	50	100	10000	High frequency transistors and other electronic devices	Moderate-high	High cost of SiC, high temperature ($>1000^0C$) not compatible with the Si electronics technology, small diameter wafers, elimination of terraces
Liquid phase exfoliation				Electronics, Catalytic applications etc	Moderate to high	Large quantity of solvents

After sonication of graphite flakes with respective solvents, the dispersion contains a mixture of graphite flakes with exfoliated graphene, which is separated by centrifugation. The yield of graphene is as low as 0.025mg/ml[54], indicating the inaccessibility of inner graphene layers by the solvent. The distance between graphene layers in pristine graphite is 0.34nm, which is too small to be accessed by most solvents. Hence, the interlayer distance can be increased by introduction of intercalants. The exfoliation of Graphite Intercalation Compound (GIC) can be achieved either by solvent-assisted exfoliation[55] or by thermal exfoliation[56]. In former case, the GIC's are sonicated with solvents, while in latter case, acid intercalated graphite is treated thermally or *via* microwave irradiation. In

either case, the graphene sheets need to be dispersed by either mild sonication or stirring. The thickness of as synthesized graphene sheets depends on intercalation stage and stability of GIC under atmospheric conditions. The use of stage 1 GIC (where every alternating layer is intercalated) leads to synthesis of single to few-layer graphene sheets.

The GIC's can be synthesized by either solid, liquid or gaseous intercalants and can be achieved either *via* single or multiple steps (when direct intercalation is not possible). Donor intercalants such as alkali earth metals, metal alloys or acceptor intercalants such as metal chlorides, halogens, acidic oxides, etc., are commonly used to achieve intercalation of graphite. The enlarged interlayer distance allows for the accessibility of inner graphitic layers and hence enhances the exfoliation process. The intercalation of graphite can be obtained by using a mixture of H_2SO_4 and HNO_3 (1:1 ratio)[58], H_2SO_4 and H_2O_2 (20:1 ratio)[56, 59], $FeCl_3$ *via* vapor transport technique[60], ammonium bicarbonate[61], using potassium or sodium potassium (NaK_2) metal[62], etc. The as obtained intercalated product is sonicated *via* probe or ultra-sonication or stirring for a wide range of time intervals to attain single to few-layers of graphene in solution phase. These techniques make use of NMP or polar solvents to achieve their dispersion, with yields as high as 12wt%. The use of acids such as HNO_3 leads to generation of toxic NO_2 gas whereas the use of $FeCl_3$ requires extensive cleaning to remove unreacted $FeCl_3$ from reaction mixture. The alkali earth metals such as Na and K require careful handling in glove box, limiting their scalability. A list of some of the intercalating agents, along with their uses is listed in **Table 1.2.3.**

Table 1.2.3. The summary of GIC's synthesized with intercalating agents and the use of exfoliated graphene.

Graphite type	Intercalating agents	Use
[63]Commercial expanded graphite (160-50N of Grafguard)	Oleum, TBA In DMF	To synthesize graphene in large scale in various solvents and to study various properties of graphene via Langmuir Blodgett films.
[64]Mildly oxidized graphite with unreacted graphite	TBA in DMF	Study of the ionic screening effect in graphene transistors
[65]Natural flake graphite 400µm (grade 3061) and 45 µm (grade 230) from Asbury carbons	HNO_3 + H_2SO_4+ $KClO_3$ (Staudenmaier method)	The study of mechanism involved in thermal expansion and exfoliation of oxidized graphite
[66]Graphite GTOSCh (Taiginka occurrence	H_2SO_4, H_3PO_4, CH_3COOH	The study of various co-intercalants in the graphite nitrate intercalated compound is pursued.
[67]Graphite	Carboxylic acid, H_2O_2	Synthesis of graphite platelets, nanoplatelets and flexible sheets was studied with the intercalated graphite.
[56]Natural graphite 80mesh 99wt%	H_2SO_4 (98 wt%) and H_2O_2 (30wt%)	High quality graphene sheet synthesis by liquid face exfoliation is studied.
[68]Natural graphite flakes (ABCR Karlsruhe, Germany)	$FeCl_3$	The characteristic features of few-layer graphene with a large lateral size is studied along with its application in lithium-ion batteries.
[69]Expandable graphite from Carbone Lorraine	Ammonia	The characteristics of few-layer graphene synthesized from expanded graphite is studied.
[62]Graphite from Cornerstone Inc.	Potassium, Cesium	The intercalation and exfoliation of graphite nanoplatelets was studied.
[70]HOPG	Ammonium bicarbonate	Simple and fast method for the synthesis of graphene that is used in field-effect transistors
[71]HOPG SPI-3 10×10×1 from SPI. Graphite powder from Asbury Graphite Mills	$LiClO_4$ + Propylene carbonate	High yield synthesis of few-layer graphene through electrochemical expansion, conductive sheets developed by sonicating the expanded graphite in various solvents

[72]Graphite powder from Bay Carbon Inc (SP-1 graphite powder)	KCl:NaCl:ZnCl$_2$ (eutectic mixture) 0.2:0.2:0.6	Study of simple and cost-effective intercalation-based exfoliation for the synthesis of high quality graphene flakes
[73]Graphite Source not mentioned	FeCl$_3$ + Nitromethane	The study of a scalable method for high quality graphene synthesis via low temperature exfoliation of graphite under mild chemical conditions
[74]Graphite foil (99.8% metal basis) thickness 0.5mm Source not mentioned	Bromine	The suspension of high quality graphene via solution-based Br intercalation and mild sono chemical exfoliation is studied.
[75]HOPG SPI, Grade SPI-2 #466HP	IBr, ICl are the ionic intercalants used	The study of solution phase technique for production of large area, bilayer and trilayer graphene with controlled stacking was pursued.
[76]Natural graphite from Aldrich, Expandable graphite (Nacional de Grafite, Brazil)	K metal	It was studied that the thermodynamics drive spontaneous dissolution of graphite compound in NMP to form stable solutions.
[77]Graphite powder from fluka. Particle size <100μm	1,1'-Didodecyl-4,4'-bipyridinium bis(triflimide) (ILC)	Easy and cost-effective route for the mass production of graphene nanosheets was designed for real world applications
[78]Natural graphite powder (SP-1 Graphite, Bay carbon)	KI + anhydrous dichlorobenzene	High quality graphite flake synthesis without oxidation is pursued.

We recently developed a fast, scalable, and oxidative approach without involving metallic compounds to directly and controllably produce highly conductive graphene sheets that can be dispersed in both aqueous and organic solvents without the aid of surfactants.[79] In the recent work reported by our group, KMnO$_4$ (as is used in Hummers and Tour's methods) was intentionally excluded while nitronium aromatic oxidation combined with microwave heating (fast and local heating) was exploited. The unique process leads to a controllable oxidation of randomly positioned carbon atoms across entire

graphene sheets, so that a low density of oxygen containing groups was observed and is shown to be sufficient enough for exfoliation and dispersion of graphene into aqueous solutions. The dispersed graphene sheets are highly conductive and do not require further reduction [80]. By adjusting the concentration of nitronium ions, size of graphene sheets can be controlled from a µm to nm range [81]. Unfortunately, the use of nitronium ions results in release of NO_2, a potentially toxic gas, and generates toxic polycyclic aromatic hydrocarbons as a byproduct.

In **chapter 2**, an eco-friendlier approach, which retains the merits of nitronium oxidation, and without releasing toxic gases or generating potentially toxic polycyclic aromatic hydrocarbons as a byproduct, was realized. This new approach replaces the mixture of H_2SO_4 and HNO_3 and exploits carbon oxidation chemistry by utilizing piranha solution, a mixture of H_2SO_4 and H_2O_2. To gain access to the inner graphite layers, intercalation was pursued by ammonium persulfate and sulfuric acid. The obtained graphene can be exfoliated into water and other organic solvents with yields as high as 0.4mg/ml and conductivity as high as 2.3×10^4 S m^{-1}, which further increased to 7.4×10^4 S m^{-1} upon thermal annealing at 300°C.

1.3. Edge Graphene

The disruption in aromaticity of π-π conjugation in graphene network alters the properties of graphene[82], creating edges. Edges generated at the disrupted sites, can be differentiated as zigzag edges or armchair edges based on their crystallographic orientation, **Figure 1.3.1**. The atoms come from same sub lattice in zigzag edges, whereas in the case of armchair edges, carbon atoms are from two sub lattice forming different boundaries. The atomic structure at the edges determines different chemical reactivity and electronic properties [83],

which differ from chemical reactivity of the basal plane[84]. Under an ideal vacuum condition, edges are di-radicals with unsaturated sp^2 and p_z orbitals [85]. A radical singlet is observed in the case of zigzag edges [86] (p_z electrons on each outer carbon atom) and is commonly referred to as an edge state, whereas the electrons of an armchair edge form a triple bond between outer carbon atoms to reduce their energy[87]. The reconstruction of edge states in zigzag edges to either pentagonal or heptagonal structures is necessary to lower their energy.
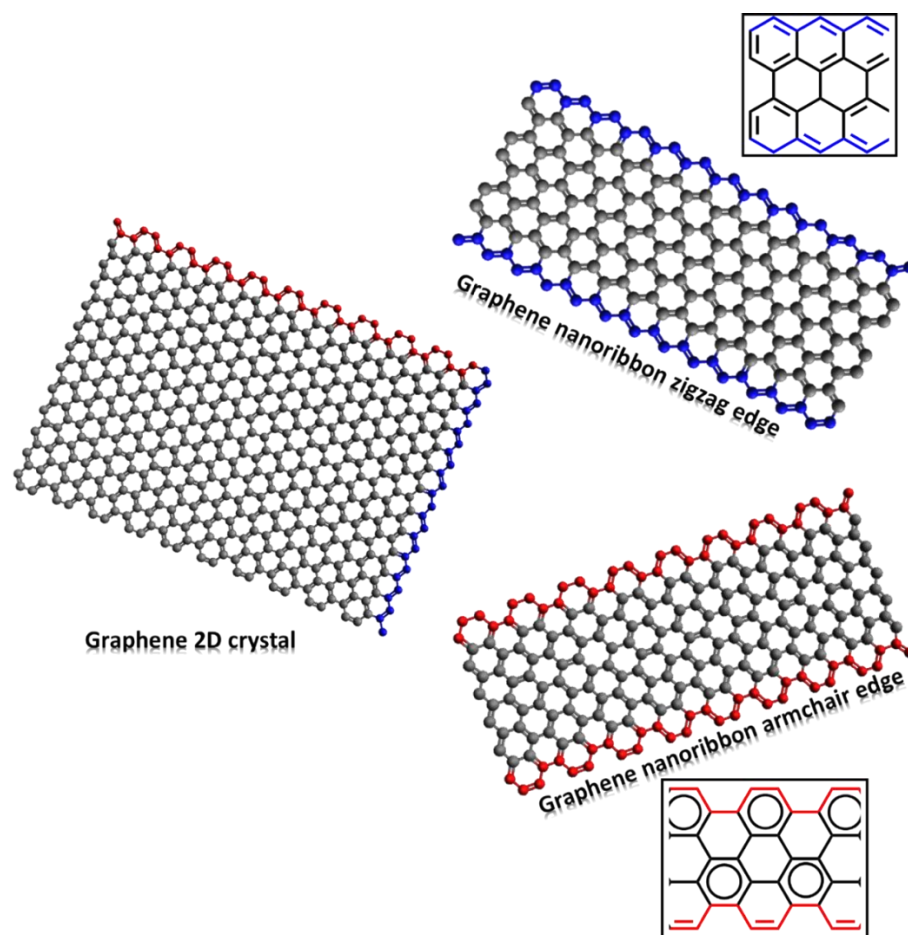
Figure 1.3.1. The schematic of edges in graphene, with macroscopic view of zigzag and armchair edge in graphene nanoribbons, as shown here. The resonance observed via Clar's structures of respective edges are shown in the insets.

Similar to PAH, the aromaticity of graphene and its reactive edges can be defined as overlap of different isomeric Clar's structures (Clar's rule, the Kekulé's resonance structures in largest number of disjoint aromatic π sextet)[88]. The edge studies were conducted in quasi one-dimensional nanostructure obtained by finite termination of graphene structures, referred to as graphene nanoribbons. The theoretical[89] and experimental[90] works show that the quantum confinement and edge effects result in a bandgap in the as synthesized graphene ribbons. In a semi-infinite ribbon, zigzag edges exhibit infinite Clar's structures, whereas limited structures were exhibited by armchair edges, indicating high reactivity in former case. The overall aromaticity and chemical reactivity depends on width of the nanoribbon. The major difference between zigzag and armchair can be inferred to, as the presence of localized double bonds in former case and presence of either an aromatic ring or localized double bond in the latter case, **Figure 1.3.1**.

The edge in graphene of nanometer size can be developed by controlled chemistry of small molecules on a substrate. One such technique allows the dehalogenation and radical formation in first step, which is followed by cyclo dehydrogenation[91]. The molecule's chemistry can be tuned to control parameters such as the type of edge and size of nanoribbon. Other approaches include etching the surface of graphene with a scanning tunneling microscope (STM)[92], etching facilitated by thermally-activated nanoparticles[93], sonication and exfoliation of graphite[90b], lithography[53a, 94], chemical vapor deposition[95], and unzipping of carbon nanotubes either by physical means (plasma etching[96] or laser irradiation[97]) or by chemical methods (strong oxidizing agents[98]).

1.4. Holey Graphene

Highly conductive graphene sheets offer zero bandgap and the tortuosity of ion transport across basal plane is deemed infinite, hindering the accessibility of ions. The intact graphene sheets are also expected to have limited catalytic centers. This limits the application of graphene in fields such as transistors and catalytic reactions. The synthesis of nanoribbons, which alters bandgap by generation of edges, is one approach for the use of graphene in transistors[89, 99]. For practical applications, a dense ordered nanoribbon array is required to increase driving current. This implies the necessity to scale up production of nanoribbons, which is not realistic. Apart from the edges, generation of holes on graphene basal plane also opens the band gap, leading to a change in its electronic properties[100].

Hence, in order to overcome the inadequacy in relation to ion transport, holes are drilled onto graphene sheets. These holey structures not provide a "short cut" for efficient mass transport, but also possess significantly more catalytic centers due to increased edges, which alters the band gap. It was reported that, the holes increase overall volumetric performance in super-capacitors [101]. The unique properties of holes in basal plane leads to a wide range of applications, which cannot be achieved by its non-porous counterpart, such as electro catalytic applications [102], catalytic reactions[103] etc. Holey graphene (hG), also referred to as graphene nanomesh, differs from porous graphene, which is widely explored. The main differences between these two graphene structures are listed in the **Table 1.4.1**.

Table 1.4.1. The comparison between porous and holey graphene.

Porous graphene	Holey graphene
Physical space between graphene layers	Vacancies created by the conversion of in-plane atoms to edge atoms
3D network	2D structures
Graphene assembly	Graphene structural derivative
Low performance per volume	High volumetric performance
No such additional active sites are generated	Atoms at the edge are more active and similar to defect sites
No such additional faradaic storage pathways are observed	Abundant functional groups arise in some cases, which lead to additional faradaic storage pathways

In hG, the holes can be drilled by knocking out in-plane carbon atoms, which provide channels for efficient cross-plane ion diffusivity and tolerance to structural deformation. The advantages of hG over porous structures include:

1. Facile ion transport through in-plane vacancies, which offers less resistance and new diffusion channels for Li ion transport [104].

2. High packing density by interconnecting graphitic domains

3. Sustained structural integrity due to high flexibility of graphene sheets, which can accommodate large volume variations[105]

1.4.1. Applications of holey graphene

1. Electrodes for super capacitors and batteries: The high surface area in combination with either hole formation or pore formation promotes ionic transport and high volumetric performance. The oxygen functional groups at edges impart additional faradaic storage and better electrode wettability [106].

2. Membrane applications: High precision holes on an ultrathin graphene membrane was used for the separation of gas molecules[107], whereas thinner membranes are sufficient enough for water purification[108]. The main challenge in using graphene membrane for water purification includes its ability to withstand a high flow of water and pressure, ion blockage, membrane fouling, etc[109]. The ultra-thin graphene membranes are also used to detect the translocation event of biomolecules such as DNA, where blockage/turbulence created during the ion conduction can be detected and analyzed[110].

1.4.2. Synthesis of holey graphene

In order to realize the applications of hG, large scale synthesis of hG is necessary. Various approaches were discovered for hG fabrication which includes: electron beam drilling, nanolithography or template growth, are the common techniques applicable for hG synthesis *via* substrate supported graphene. In these high throughput methods, holes with controlled shapes could be formed on graphene. This hG can be used for morphological and electronic measurement kind of applications. High energy bombardment with ions or electrons could also lead to holes on graphene surface with techniques such as transmission electron microscope[111]. Pores of different shapes and arrays can be generated by controlling the position and/or movement of electron beam. High precision and highly localized holes can be obtained *via* this technique, but exhibits the limitation of scalability.

Nanolithography: This technique involves high throughput when compared to electron beam drilling, and is comprised of multiple steps: (1) substrate-assisted growth or deposition of graphene, (2) a porous template to cover the surface of graphene, (3)

etching process, (4) removal of template or mask. In this technique, an inert template is required to generate holes and prevent any morphological changes on the graphene. The template can be either block copolymer[112] or nano-imprint templates [113].

Template growth: Entails bottom-up growth of hG using CVD with gaseous carbons such as methane. This technique differs from nanolithography (graphene is first grown or deposited onto a substrate covered with nano-templates and then selectively etched), where the carbon source is first deposited on an active substrate, which is followed by CVD growth of graphene[114].

The above-mentioned approaches suffer from a serious limitation of scalability due to their long and complicated reaction procedures and the cost involved in their fabrication. The scalable method for holey graphene synthesis involves the use of either GO or rGO. The defect sites in GO or rGO serve as seeding sites for hole growth. The common techniques include:

Liquid phase oxidation: Several approaches were explored through the use of oxidizing agents to selectively etch graphene/graphene oxide sheets. The holey graphene can be synthesized by use of $KMnO_4$ with HNO_3 and H_2SO_4 with graphite *via* microwave irradiation[115]. In this approach, nitronium ion attacks the existing defects and graphitic carbons, whereas $KMnO_4$ preferentially reacts with the existing defects, generating holes. When GO was used as the starting material, $KMnO_4$ alone is sufficient enough to create holes [116]. However, the liquid exfoliated graphene upon treatment with $KMnO_4$ and hot HCl generates only few holes due to the presence of fewer defects[117]. The above results indicate that the hole generation depends on type

of graphene used. Below is a summary of starting graphene and the nature of oxidizing

agents used to generate hG, **Table 1.4.2.**

Table 1.4.2. The Summary of synthetic approaches of hG synthesized via liquid oxidation approach.

Starting product used	Oxidizing agents	Treatment technique	Product	Ref
Graphite	HNO_3, H_2SO_4, $KMnO_4$	Microwave irradiation for 40sec	hGO	[115]
GO	$KMnO_4$	Microwave irradiation	hGO	[116]
Exfoliated graphene	$KMnO_4$ + hot HCl	Room temperature	hG	[117]
GO	Conc. HNO_3	Bath sonication	hGO	[118]
Chemically reduced GO	Conc. HNO_3	Reflux for 4-11hrs	hG	[119]
GO	H_2O_2	Hydrothermal treatment	hG	[101a, 120]
rGO	Au / H_2O_2	UV photolysis	hG	[121]
GO	Horse radish peroxidase (HRP)	Incubation	hG	[122]
rGO	$ZnCl_2$ /CO_2	$650^{\circ}C$ for 2hrs	Porous GO	[123]
GO	CO_2	$800^{\circ}C$ for 25,60,75mins in CO_2	Porous GO	[124]

GO	ZnCl$_2$ and H$_3$PO$_4$	Freeze drying + 300°C for 1hr	Porous GO	[125]

Gaseous phase etching: The thermally reduced GO exhibits intrinsic point defects, formed from parent GO. Holey graphene can be synthesized by its oxidation or due to quick release of gaseous byproducts such as CO$_2$. The scalable production of hG can also be obtained by controlled air oxidation of GO or rGO, where hG was formed at temperatures as low as 390°C, when heated for a duration of 1hr. An increased duration or increased temperature did not lead to increased hole size, but did increase hG's electrochemical capacitance. The increased capacitance was accounted to, based on the following hypothesis. In initial phase, gasification of defective carbon is observed, followed by oxidation of graphitic carbon (functionalization of edges in the holes, which enhances faradaic storage capacity in supercapacitors)[106a]. Flynn et al. demonstrated that, hG can be synthesized by puncturing of holes through thick graphene sheets *via* air oxidation[126], where hole density was high in single-layer graphene. The gaseous etching technique was also applied for substrate supported graphene nanosheets, one such example includes air oxidation of substrate-supported GO under room temperature with UV light radiation [127].

Chemical activation: Ruoff and coworkers applied the phenomenon of active carbon activation with KOH, to generate holes in GO. In this scenario, microwave-exfoliated GO was treated with KOH at 800°C for 1hr to generate high porosity activated graphene with in-plane holes[128]. The generation of holes with KOH was applied to

GO films[129], t-rGO (thermally reduced GO)[128] and crumpled GO[130]. Another approach includes, planetary ball milling of GO for 30hrs with KOH, which resulted in 3D porous structures with in-plane holes. Precautions must be taken due to high KOH usage.

Guided etching with catalytic reactive nanoparticles: Chemical etching of graphene is promoted with the aid of nanoparticles deposited on graphene surface. The nanoparticles in this technique serve as a catalyst or active reactants, whereas in nanolithography, the nanospheres functions as mask. The shape control of holes and regularity of hole arrays are not of very high quality and precision as observed in nanolithography. Examples include, Ag nanoparticle decorated graphene hybrid, where the exposure of reaction mixture to air at $300\,^{\circ}C$ yields hG[131]. Weiss et al used Au and Pt nanoparticles by thermal oxidation in air[132] to generate hG, where Au nanoparticles catalyzed the oxidation of H_2O_2 to yield hydroxyl radicals, which react with rGO to form hG [121]. Other approaches include photochemical etching of GO by the use of ZnO nanorods[133] and TiO_2 nanoparticles[134]. In another approach, Cu nanoparticles[135], in a reductive atmosphere such as H_2 can cause the catalytic etching of graphene. However, additional treatment to remove the nanoparticles is necessary in this approach.

All the above techniques exhibit limitations in terms of cost, scalability, synthesis procedures. In **chapter 3**, a novel technique to synthesize holey edge graphene was pursued combining the advantages of holey and edge graphene *via* microwave approach. By controlling microwave irradiation, knocking of in-plane carbon atoms to generate holes in graphene basal planes can be controlled. The intercalation was achieved similar to the

process as described in **chapter 2**. In **chapter 3**, the intercalated graphite stabilized with O_2 is heated thermally to partially oxidize the graphitic domains. This creates point defects and is referred to as partially oxidized graphite (POG). POG upon microwave irradiation generates holey graphene with edges (POG-HE). The HRTEM suggests absence of defects on basal graphene plane with limited oxidation as recorded *via* XPS (96.37% C and 3.63% O). Hence, it was referred to as pristine holey graphene to differentiate from holey graphene reported so far using GO, rGO, **Figure 1.4.1.**
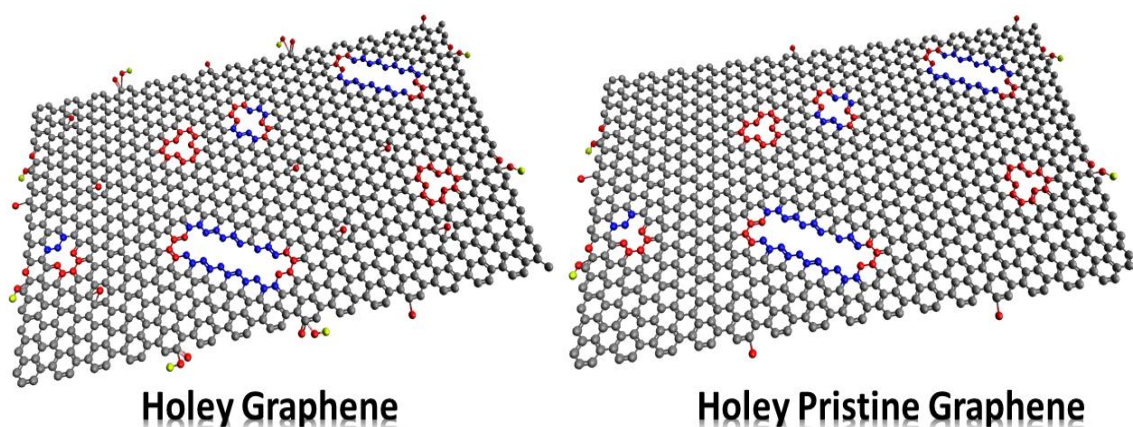
Figure 1.4.1. The schematic of holey graphene reported in literature with its comparison with pristine holey graphene reported in our work.

Following this approach, microwave irradiation chemistry is pursued on intercalated graphene without point defects in **chapter 4**. Here, intercalated graphite with O_2 (IGO) was used, where it was hypothesized that, the trapped O_2 in between layers of graphite and surrounding air, serves as oxidant to knock out in-plane carbon atoms with the high local temperatures achieved by microwave chemistry. Similar to POG-HE, the holey edge graphene obtained by this approach (IGO-HE) exhibits a defect-free basal plane with less oxidation (97.02% C and 2.98% O). The IGO-HE reports a higher conductivity (35,195 S/m) when compared to that of POG-HE (17,514 S/m), indicating higher crystalline graphitic domains in the former case.

1.5. Microwave chemistry

Exploration of environmentally benign methods for fabrication of various carbon based materials and metal nanoparticles was being pursued in both academia and industry. Microwave chemistry has gained immense attraction due to its selective heating of materials, shorter reaction times, low energy consumption and higher product yields. The mentioned advantages render microwave chemistry processes to be green [136]. To best describe the importance of microwave in chemistry, Hayes used following figurative expression: "Microwave synthesis: Chemistry at the speed of light, it is a breakthrough technology for chemistry: an idea whose time has come. The technology tends to rapidly evolve and exhibits a dramatic impact in the world of chemistry" [137]. Microwaves are electromagnetic waves with frequencies ranging from 0.3 to 300GHz and with wavelengths ranging in between 1mm to 1m. They lie in between infrared and radiofrequency waves in the electromagnetic spectrum, **Figure 1.5.1**.
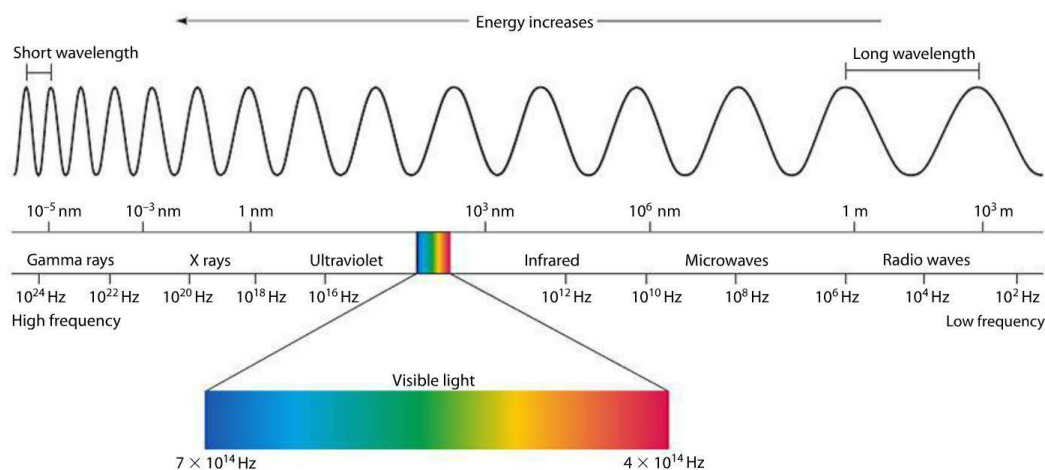
Figure 1.5.1. The Electromagnetic spectrum and their wide range of wavelength [138]. Microwave heating of the material depends on its absorption of electromagnetic energy and its conversion to heat. It is independent of thermal conductivity of the surrounding

28

materials, thereby providing an instant on and off heating mechanism. The microwaves used in laboratory research and in common households contain a frequency of 2.45GHz with a wavelength of 12.24cm. The energy of a photon of this frequency is too low to break chemical bonds in the molecule[139], but sufficient enough to initiate rotation of dipoles. The dipole rotation induces translation motion of free or bound charges in the reaction medium, i.e. rotation of dielectric or magnetic dipoles, leading to heating. An additional heating mechanism of microwaves is *via* induction of ohmic currents or ionic conduction or *via* Joule heating in case of conductive materials.

The microwave heating mechanism is different from traditional conventional heating methods and is explained with regard to the type of material used in microwave synthesis. In case of water, a polar molecule, microwave heating leads to a change in orientation of water molecules, within the rapidly changing alternating electric field. This generates heat by rotation, friction and collision of molecules[140]. In case of ionic compounds, the alternating electric field causes movement of ions in changing directions. This leads to friction and collision of ions, causing local temperature in the reaction media to rise [141]. In case of semiconducting and conducting samples, ions or electrons generate electric currents upon microwave adsorption, where the electric field tries to realign. Hence, the kinetic energy of ions or electrons generates heat due to molecular friction and random collisions [139]. In case of magnetic and high electrically conductive materials, magnetic loss provides additional strong heating [142]. The following **Table 1.5.1.** differentiates microwave heating *vs* traditional conventional heating, with depiction of high local temperature in **Figure 1.5.2**.

Table 1.5.1. The comparison of microwave *vs* conventional heating.

Microwave heating	Conventional heating
Efficient and uniform heating	Inefficient and non-uniform heating
Instant on and off	Instant on and off is not possible
Selective heating of materials	Initial heating of the reactor followed by simultaneous heat transfer to reactants either by conduction or convection
Contactless heating	Reactor acts as an intermediate media for heat transfer
Short reaction time to achieve target temperature	Long reaction time to achieve target temperature
Surrounding environment temperature is low	Surrounding environment temperature is high
Inverted thermal gradient is observed	Thermal gradient observed
Eg: Microwaves	Eg: Electric furnaces, oil bath, etc.
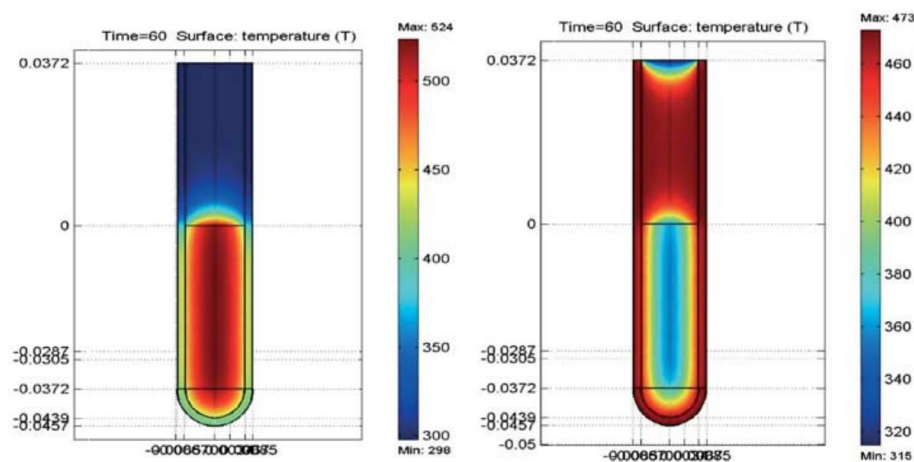
Figure 1.5.2. The picture depicting uniform heating of reaction volume *via* microwave towards left and its comparison with heating of reaction tube first followed by reaction volume in the conventional method [143].

The synthesis of carbon nanomaterials, which are emerging as important components in various electronic and catalytic applications, tend to be immensely important. Initially, microwave heating was pursued in the purification, functionalization or in annealing of carbon structures. Several parameters need to be considered to achieve high absorption of microwave irradiation by these materials. The two important parameters that determine microwave absorption by the material are penetration depth and loss factor. Quartz glass and Teflon exhibit a low loss factor and a high penetration depth, hence making them quasi transparent to microwave irradiation [144]. In case of conductive materials, the penetration depth is skin-deep and is dependent on conductivity and permeability of the material[145], whereas surface heating is observed with materials exhibiting a high loss factor and low penetration depth.

CNTs/graphite/metal carbon nanoparticles exhibit small skin depth, but microwave heating is not limited due to their nano-sized particles and are therefore heated in their entirety[142b]. The parameters to be considered for effective microwave heating in case of carbon materials is electrical conductivity imparted by the π-π conjugation and imperfections leading to electrical resistance, where microwave heating occurs by joule heating mechanism. The presence of oxygen functional groups on carbon having smaller π-π conjugation lowers electron mobility and thereby decreases the efficiency of microwave heating. Hence, oxidized carbons like graphene oxide are not microwave absorbers[146]. The microwave irradiation of amorphous carbons can achieve temperatures as high as 1283°C in 1min[147]. Unpurified CNTs (HiPCo) can reach temperature as high as 1850°C, which upon removal of metal impurities recorded a temperature of 500 to 650°C[148],

indicating microwave absorption efficiency due to the presence of metal. Additional heating in carbon materials was observed in some scenarios such as: (1) material-specific absorption of microwave irradiation, which leads to generation of strong local heating with localized hot spots. This leads to additional heating in the case of conductive materials [147]. (2) The loss factor increases significantly with temperature, as a result, thermal runway, leading to super high heating, is observed throughout the course of microwave absorption[149]. (3) During microwave irradiation of carbon, light emission is observed, which is perceived as electric arc formation. This is a result of electron excitation leading to ionization of the surrounding atmosphere. This generated gas plasma adds on to localized super heating of the materials[150]. Selective and efficient microwave heating is dependent on the type of microwave instruments, which can be either single mode or multimode. **Table 1.5.2.** breaks down the differences between these two types of instruments.

Table 1.5.2. The comparison of single and multimode microwave instruments.

	Single mode	Multimode
Cavity size	Small	Large
Field distribution	Homogeneous	Non-homogeneous
Output power	400W	700-1000W
Power density	High	Low
Reaction conditions	Reaction control and safety can be achieved to some extent by external sensors	Lack of reaction control and safety

Examples	Scientific microwaves	Domestic/household microwaves

1.5.1. Microwave-assisted synthesis of carbon

The carbon materials can be synthesized by different approaches and are listed below:

1. Solid phase with support: This technique falls under the category of a bottom-up approach, where solid precursors, such as sucrose, inositol, glucose, etc., are used. However, carbon synthesis depends on microwave absorption capacity of the solid precursors. Hence, additional microwave absorbers such as powdered graphite, activated carbon fibers, or metal carbon sources like iron acetate and ferrocene were used [151], along with use of substrates similar to CVD. Here, the catalyst is deposited on substrate and is heated in presence of a carbon source. The drawbacks include the damage of catalyst loaded onto polymer substrate or cracks of SiO_2 substrate during CNT synthesis. To improve CNT synthesis, additional microwave absorbers such as silica, chromium layer and Si wafer were used. In case of graphene, hardly any microwave-assisted bottom-up approach was reported in the literature.

2. Solid phase: Graphene is a good absorber of MW irradiation when compared to GO, which has a partially disconnected π system. MW absorption can be enhanced by decreasing the oxygen content in GO through partial reduction[146] . Examples include: Microwave irradiation of partially reduced GO to synthesize high quality graphene [36]. The GO film turned from brown to black upon exposure to MW irradiation at 400W for 2sec[152], indicating their reduction. Thermal exfoliation of

33

graphite intercalated compounds can also be achieved by microwave irradiation [153], where expansion of graphite was observed, which upon sonication in a suitable solvent, yields single to few-layer graphene. Few-layer graphitic sheets were synthesized upon microwave irradiation at 40% of 700W for 10-40sec, whereas prolonged microwave irradiation leads to oxidation of the sheets.

3. Liquid phase: The growth of CNTs on the surface of graphene was reported by Oh et al. by utilizing graphene oxide and nickelocene mixture[154]. Ionic liquid was also used as carbon source, with palladium acetate as a catalyst on graphene, to grow CNTs[155]. However, graphene synthesis was not yet pursued from liquid phase synthesis via microwave approach.

4. Purification of carbon: The carbon materials synthesized is treated with microwave, to purify metal impurities lying within. Reagent free modification [156], where carbon material is heated in the microwave, and is followed by treatment with acid is one such approach. Alternatively microwave treatment with carbon dissolved in acid [157] was also pursued.

Microwave chemistry is applied for the synthesis of various graphene structures and porous metal hybrids in this current thesis. In **chapter 2**, highly conductive pristine graphene was accomplished by microwave liquid chemistry approach. Mild oxidants, such as H_2O_2 and H_2SO_4, were used to oxidize the intercalated graphite with microwave irradiation. High quality graphene dispersible in a wide range of solvents was obtained *via* this approach. The scalability of this approach was pursued up to 200mg, which exhibits results similar to those on a smaller scale (20mg).

In **chapter 3**, dry microwave irradiation of POG was pursued with the aim to oxidize the defective carbon to generate vacancies. The partial oxidation of graphite leads to point defects, which can oxidize in presence of air with the aid of high local temperatures provided by microwave irradiation. No post treatment of the product is required and the use of microwave, renders this approach energy, cost and time-efficient. High quality hG with less defects was observed in this scenario.

In **chapter 4**, microwave irradiation of IGO was pursued with the aim to oxidize carbon to generate vacancies. In this approach, the oxidation capacity of intercalated O_2 and surrounding air, in combination with high local temperature to knock out in-plane carbon atoms to generate vacancies was studied with microwave. This approach is similar to **chapter 3**, except for a different starting material, and hence exhibits similar advantages. The high quality of hG with higher conductivity than POG derived hG was observed.

Microwave irradiation was also applied for the synthesis of metal porous hybrids in **chapter 5**. The noble metal Pd was incorporated into phosphorus doped carbon matrix through microwave irradiation of the metal with phytic acid in a single step process. Phytic acid is a biomass which acts as both a carbon and phosphorous source. The as obtained product contains Pd nanoparticles that are 10nm in size and embedded in the phosphorous doped porous carbon. The X-ray diffraction peaks at 40° combined with XPS binding energies of 336 and 341ev, indicates the presence of Pd as Pd^0.

In **chapter 6,** the cheap transition metal phosphide, tin phosphide was synthesized via microwave irradiation, with phytic acid as a phosphorous source. Tin phosphide was encapsulated in phosphorous doped porous carbon matrix, and covered with wrinkled phosphorous doped carbon, in this scenario. The X-ray diffraction peaks at 28.8° and 31.5°,

in correlation with 0.31nm and 0.28nm of marked d spacing's from TEM suggest the presence of tin phosphides as Sn_4P_3.

1.6. Catalysis

A catalyst is a substance which enhances the rate of reaction without itself getting consumed during the reaction. A catalyst can be either homogeneous or heterogeneous depending on its existence with the reaction medium. In catalysis, more than 90% of chemical reactions were processed with the aid of a metal catalyst in industries (homogeneous), however their limitations, explored the scope of heterogeneous catalyst as discussed in **Table 1.6.1.**

Table 1.6.1. The comparison of homogeneous *vs.* heterogeneous catalysts.

Property	Homogeneous catalyst	Heterogeneous catalyst
Existence in the reaction medium	Same phase	Separate phase
Active sites	Well-defined	Poorly defined
Catalytic activity	Moderate	High
Selectivity	High	Low
Catalyst modification	Possible	Unlikely
Temperature	Low ($<250^0C$)	Moderate – high (250-500^{0}C)
Catalyst recovery	Expensive and difficult	Rather facile
Diffusion and heat transfer	Facile	Difficult
Reaction mechanism	Well understood	Poorly understood

Examples	Soluble metal complexes	Metal/metal oxides on support, carbon catalyst

The surge of metal free carbo-catalysts in various organic and electro-catalytic applications was demonstrated over time, but low efficiency of carbo-catalyst in comparison to metal-based catalysts limits its practical applications. Hence, research is being pursued to design effective catalysts to realize practical purposes. Many industrial catalysts consist of metal/metal oxides supported on an appropriate support. The support plays an important role in catalysis. A good heterogeneous metal-based catalyst depends on the uniform dispersion of active phase on support, combined with obtaining a large active surface per unit weight. The supports used in industries[158] are selected based on chemical composition, surface area, stability and mechanical properties, as well as consist of the following characteristics:

1. Retard the sintering of active phase
2. Increase their resistance towards poisoning of active phase
3. Stability and inertness under acidic and basic reaction conditions
4. Enhancing dissipation of heat in reaction conditions
5. Promoting diffusion of reactants through pores to reach the active phase.
6. High surface area with well-defined porosity

The most commonly used supports in practice include alumina, silica and carbon. The advantages of a carbon support over alumina and silica include: low cost, high surface area and porosity, chemically stable sp^2 carbon network, superior electrical, thermal and

corrosion resistance, recovery of metal by burning the carbon in air (generating less solid waste), etc.

Carbon nanofibers[159], activated carbon, CNTs[160], graphene oxide[161], reduced graphene oxide[162], porous carbon etc. were used as carbon supports, on which, the precious metal catalyst were loaded. The common reactions explored were, liquid phase hydrogenation [163], dehydrogenation [164], oxidation [165], carbon-carbon coupling [162c, e, 166] etc. Porous carbon supports can be synthesized from biomass molecules, making it cheap and sustainable, while the metal can be loaded onto this carbon support *via* various techniques such as impregnation, precipitation-deposition etc. However, poor particle dispersion is the major drawback in these techniques, owing to low particle interaction with carbon support [167]. Stabilizers, such as surfactants [168], polymers [169], ligands [170] etc., were used to prevent particle aggregation, but interference in catalytic activity was observed due to these foreign structures.

Hence, the overall reactivity of heterogeneous catalyst depends on selecting a suitable support [171], not interfering in the catalytic reaction and which aids in the alteration of acid base properties, redox properties and promote metal support interaction by supporting the synergy of metal and carbon support. It was reported that the tailoring of electronic and chemical properties of support with heteroatom doping, can promote better dispersion of the nanoparticles. Thus, the synergy of metal with heteroatom doped carbon matrix was pursued to realize maximum efficiency of the catalyst. It was proved that the electron rich N improves the interaction of reactant with active center [172]. Due to the wide application of Pd as catalyst, extensive research was pursued on Pd immobilized onto N doped carbon supports. The uniform dispersion of the metal into the N doped carbon matrix occurs due

to the σ type donation from N and π back donation from Pd. As reported previously by our group, the large atomic size of phosphorous distorts the carbon matrix, generating wrinkled morphology[173]. The same valence e⁻ of P as N renders the support electron rich, transforming it to an n-type conductor, whereas opposite polarity of C-P bond can be observed due to the low electronegative nature of P, in comparison to N. It was also reported by our group that the activation energy for alcohol oxidation decreases when P doped carbon is used, indicating better reaction kinetics of these supports.

In **chapter 5**, Pd nanoparticles were embedded into the phosphorous doped carbon support to realize its catalytic activity in alcohol oxidation. In this work, the influence of P doped carbon support on Pd nanoparticles was studied. The catalyst exhibited a superior TOF of $23000h^{-1}$ higher than that of Pd@NGc ($14600h^{-1}$)[172f] and Pd@Gc ($2940h^{-1}$) [174] indicating the enhanced performance due to doping of phosphorous into the carbon matrix, which might act as a bulky ligand similar to N as reported.

The nitro compounds serve as building blocks in organic synthesis and as a precursor for the synthesis of amines. Metal catalysts such as Au, Pd, Pt and Ru have been proved to be effective in the reduction of nitrobenzene. However, sensitivity of the metals in presence of air and moisture, high price and scarcity limits their use as catalyst in large scale production [175]. Cost-effective metals such as Fe, Ni, Cu serve as an alternative [176], but agglomeration of the metals and metal oxides was observed, leading to deactivation of catalyst and hence lower conversions. High temperatures and high catalyst loadings were required to achieve considerable conversions.

Recent reports indicate that carbon can serve as a metal-free catalyst for nitroarenes reduction [177]. The catalytic application can be accounted to the π conjugated structure,

which allows better interaction with the aromatic reactants and their modified electronic and thermal properties.

It is a well-known fact that, the defect-free pristine graphene cannot serve as a catalyst due to the absence of active sites. Hence, tailoring of graphene matrix with either heteroatom dopants or co-dopants, or generation of edges, can enhance the catalytic activity. Heteroatoms, such as O[178], N[178d, e, 179] and P[173] doped into carbon supports, were widely explored as catalyst themselves due to their altered electronic and chemical properties. The disruption of π-π conjugation during doping, leads to alteration of electro neutrality. Henceforth, it was recently demonstrated that the generated defects or edges for doping can also act as the catalytic active sites for the reduction of oxygen[180].

In **chapter 3**, the as synthesized high quality holey edge graphene was tested for its catalytic activity in reduction of nitrobenzene. Low catalyst loading with high conversion was observed, which maintained selectivity towards aniline up to 3 recycles. The POG-HE exhibited higher stability in comparison to the traditional GO and rGO based catalyst. A unique mechanism was noted, where the reduction of nitrobenzene occurred solely *via* a condensation pathway rather than a direct pathway or a combination of both as reported widely in the literature.

1.7. Oxygen reduction reaction (ORR pathway)

The oxygen reduction reaction is one of the most important processes for clean and renewable energy, such as that found within fuel cells. Metal-based catalysts such as metal oxides or noble metals are commonly used, among which Pt/C is considered to be the best catalyst so far for ORR, due to its exceptional performance. However, it imposes serious

limitations, such as time-dependent drift, methanol cross over effect and cost of the catalyst. Nonmetal-based carbon catalysts are current hot topic, as they can act as a substitute for the traditional Pt/C. In 2009, Dai et al. have demonstrated the ORR activity of vertically aligned carbon nanotubes (VA CNT) [181]. In this work, improved ORR performance by incorporation of nitrogen into the VA CNT was also demonstrated. The superior performance was analyzed *via* quantum mechanical calculations, where doping-induced charge redistribution, facilitated by O_2 adsorption and electron transfer, was reported. Several heteroatoms such as N [182], P [183], S [184], B[185] etc., can be doped or co-doped[186] into the carbon matrix, which improve the electro catalytic O_2 reduction. The reactivity can be attributed to the electron transfer induced by heteroatom doping between electron donating/accepting heteroatom and the adjacent carbon. In the case of N doping, carbon next to N acts as the active center, whereas in B doping, the dopant itself [187] can act as the active center. It was also proposed that the electro neutrality break induced by the heteroatom occurs due to disruption of π-π conjugation, indicating that the generated edges and defects might also be catalytically active. It was reported that the defects in highly ordered pyrolytic graphite (HOPG) exhibited an electron rate transfer constant 7 times higher than that of the defect-free HOPG, indicative of varying electron structure between the basal plane and the edge plane[188]. The ORR activity in a droplet of electrolyte on the graphite basal plane and the edge revealed the catalytic active nature of graphene edges [189] as reported by Wang et al. Nevertheless, further research is needed to determine the catalytic activity of edge graphene.

The reduction of O_2 can occur either *via* $2e^-$ to generate HOO^- (peroxide) or *via* $4e^-$ to generate H_2O (water). Reduction *via* $2e^-$ is detrimental in fuel cells, as the intermediate is

corrosive to fuel cell and decreases the fuel cell efficiency. However, it can be applied for onsite peroxide production, which is a green chemical used in various organic and inorganic reactions as an oxidant. Common peroxide applications include its uses as a bleaching agent[190], in electronic industry, as detergents, in refining and processing metals [191], in degrading toxic waste in effluent water[192], as an oxidizing and reducing agent in some chemical synthesis[193], etc.

These vast applications implored an enormous demand of H_2O_2 (increased at the rate of 4% per annum till date). Anthraquinone oxidation[194], is the most commonly used technique for H_2O_2 production, but it suffers from limitations such as cost of raw materials, time consumption (3 step process) and the need of a stabilizer while transporting concentrated H_2O_2, as it is explosive due to intense decomposition. Hence, alternatives such as onsite production and utilization of H_2O_2 are being pursued either by directly mixing H_2 and O_2 [195] or through fuel cells with Pt, Au-modified membrane [196]. Unwanted side reactions combined with safety issues related to direct mixing of H_2 and O_2 was observed in the former case, whereas the use of noble metal-coated membrane increases the cost of production in latter case.

In **chapter 4**, the synthesized high quality and highly conductive holey edge graphene was tested for ORR reaction. The oxygen reduction occurs *via* 2e$^-$, with an onset potential much lower than that of carbon black electrodes. The catalyst is susceptible to methanol poisoning and exhibits a stability of ≈70% after 8hrs, with a faradaic efficiency of 90% even after 5hrs. Bleaching of paper is a huge industry [190], where peroxide in an alkaline medium is required. H_2O_2, common bleaching agent in paper conservations and bleaching industries, is less stable and decomposes in alkaline media to generate O_2[197]. The gas

generated leads to the blistering of the paper, hence damaging its quality. The performance of IGO-HE in **chapter 4** to synthesize peroxide in alkaline media, opens path for onsite peroxide production for bleaching applications, eliminating the possible decomposition of its parent compound H_2O_2. The drawbacks associated with the safety and handling of H_2O_2 can also be eliminated.

1.8. Metal phosphide

Metal phosphides are deemed important due to their widely useful properties such as superconductivity[198], magneto-caloric behavior[199], catalytic activity, magneto resistance and lithium intercalation capacity. Hydro desulfurization (HDS) and hydro denitrogenation (HDN) and hydro deoxygenation (HDO), which are important processes, in removing sulfur, nitrogen and oxygen atoms from petroleum feedstock's were pursued with the use of transition metal phosphides as catalyst. These low cost and resourceful transition metal phosphides have also gained wide acceptance in energy industry by exhibiting similar catalytic activity and long-term stability, in comparison to traditional catalysts such as Pt/C, $LiCoO_2$, and LiFePO4. The energy crisis in the present generation led to exploration of new forms of energy conversion and carriers, where the energy density can be increased by exploring reactions such as hydrogen evolution reaction (HER) and oxygen evolution reaction (OER) from water splitting, oxygen reduction reaction (ORR), the compact and portable lithium ion batteries. Fuel cells, such as direct methanol fuel cells, microbial fuel cells and proton exchange membrane fuel cells, are few examples where the above mentioned reactions are put into application. However, expensive and rare metals such as platinum (Pt) and lithium (Li) greatly hinder their use as electrodes in sustainable energy conversion and storage. Hence, an ideal alternative which is economic and abundant, with

similar performance, was being explored. Transition metal catalysts such as iron (Fe), cobalt (Co), manganese (Mn) were investigated as electrode materials due to their cheap resources and their activity, whereas Na was explored to replace Li in batteries. The defects and distortions in the crystal configuration of the metal phosphides promote the insertion of Li and Na ions, hence promoting their application in batteries [200]. Several synthesis techniques for metal phosphides are listed in the **Table1.8.1** [201].

Table 1.8.1. The synthesis techniques of metal phosphide and their corresponding equation.

Synthesis method	Reaction
Combination of elements	$M^0 + xP^0 \text{ (red)} \rightarrow MP_x$
Solid state metathesis	$MCl_x + Na_3P \rightarrow MP + NaCl$
Reaction with phosphine	$MCl_x + PH_3 \text{ (red)} \rightarrow MP + HCl + H_2$
Decomposition of organometallics	$TiCl_4(PH_2C_6H_{11})_2 \rightarrow TiP + PH_3 + HCl + C_6H_{10}$
Electrolysis of fused salts	$MO_x + NaPO_y \rightarrow MP + Na_2O$
Reduction of phosphates	$MPO_x + H_2 \rightarrow MP + xH_2O$

Na resources, are abundant in nature and low in cost, which permit the use of Sodium Ion batteries (SIBs) as an alternative for Lithium Ion Batteries (LIBs). Extensive efforts have been pursued in developing high capacity SIB by alloying with metals such as Sn[202], Sb[203], Ge[204]etc. The high cost and low theoretical specific capacity of Sb and Ge limits their use as an anode component in SIBs. Sn, a cheap and good electrical conductor which exhibits a discharge capacity as high as 400-1100mAhg^{-1} is pursued. On the other hand, P

(poor electrical conductor), which exhibits a high theoretical capacity of 2596 mAhg^{-1} was also explored [205]. The enormous volume expansion of 525% from Sn to Na$_{15}$Sn$_4$ and 490% from P to Na$_3$P leads to pulverization of the composite, thereby degrading battery performance. The pulverization results in the aggregation of nanoparticles [206] and dendrite formation which is observed in case of LIBs, and is the main cause of capacity decay. Tin phosphide, which exhibits a self-healing mechanism [207] can be pursued as an alternative to the Sn metal. The reversible conversion of Sn$_4$P$_3$ + 9 Na $\leftrightarrow$ 3Na$_3$P + 4Sn prevents continuous pulverization and aggregation of Sn alloy upon sodiation/desodiation and is referred to as a self-healing mechanism[207].

The synthesis of metal phosphides was pursued at high temperatures [208], temperature-controlled hydrothermal treatment [209] and Mechanical alloying [210]. Particle aggregation, handling of liquid solvents, generation of toxic phosphine, complex reaction procedure, zirconium contamination, inert environment such as N$_2$[209c], limits their synthesis for large scale approach using the above mentioned techniques. In Sn$_4$P$_3$, the thickness of the electrode increased to $\approx$200% after sodiation, whereas upon desodiation, it returned to $\approx$60% of its initial thickness. This indicates that the self-healing mechanism is not completely reversible and hence the possibility of partial pulverization cannot be eliminated. Lee et al. demonstrated that the addition of carbon reduced the thickness to 11% after desodiation[211]. Hence extra protective barriers were explored in order to mitigate the behavior of pulverization, such as core shell structures with either carbon nanocomposites (500 mAhg^{-1} at 100 mAhg^{-1} over 150 cycles)[212] or amorphous Sn-P (465 mAhg^{-1} at 100 mAhg^{-1} over 100 cycles)[210a]. Yu and coworkers[213] reported a yolk shell

structure to further enhance the discharge capacity, to as high as 360 mAhg^{-1} at 1.5C after 400 cycles).

In **chapter 6**, a one step, one pot approach to synthesize Sn_4P_3 via microwave chemistry is realized. Phytic acid is used as both a carbon and phosphorous source, where the P is not only involved in the formation of Sn_4P_3, but also forms a phosphorous doped carbon layer around the nanoparticles. These are sandwiched in between the phosphorous doped graphene-like carbon. The wrinkled morphology observed provide additional space and protection to accommodate to the volume change. A capacity of ~390 mAh/g was maintained even after 1150 cycles at a charge/discharge current of 1 C, indicating the robustness of the electrode for long-term use.

1.9. References

[1] Y. Li, L. Xu, H. Liu and Y. Li, *Chemical Society Reviews* **2014**, *43*, 2572-2586.

[2] R. L. V. Wal, *NASA Contractor Report 198469* **1996**.

[3] **1997**.

[4] S. F. Kiew, L. V. Kiew, H. B. Lee, T. Imae and L. Y. Chung, *Journal of Controlled Release* **2016**, *226*, 217-228.

[5] a) K. S. Novoselov, A. K. Geim, S. V. Morozov, D. Jiang, Y. Zhang, S. V. Dubonos, I. V. Grigorieva and A. A. Firsov, *Science* **2004**, *306*, 666-669; b) K. S. Novoselov, A. K. Geim, S. V. Morozov, D. Jiang, M. I. Katsnelson, I. V. Grigorieva, S. V. Dubonos and A. A. Firsov, *Nature* **2005**, *438*, 197-200.

[6] J. S. Bunch, S. S. Verbridge, J. S. Alden, A. M. van der Zande, J. M. Parpia, H. G. Craighead and P. L. McEuen, *Nano Letters* **2008**, *8*, 2458-2462.

[7] C. Lee, X. Wei, J. W. Kysar and J. Hone, *Science* **2008**, *321*, 385-388.

[8] A. A. Balandin, *Nat Mater* **2011**, *10*, 569-581.

[9] A. S. Mayorov, R. V. Gorbachev, S. V. Morozov, L. Britnell, R. Jalil, L. A. Ponomarenko, P. Blake, K. S. Novoselov, K. Watanabe, T. Taniguchi and A. K. Geim, *Nano Letters* **2011**, *11*, 2396-2399.

[10] a) F. Ricardo, A. D. Pablo, P. Helena, G. Cecilia and W. M. Álvaro, *Journal of Physics: Condensed Matter* **2009**, *21*, 285304; b) I. W. Frank, D. M. Tanenbaum, A. M. van der Zande and P. L. McEuen, *Journal of Vacuum Science & Technology B: Microelectronics and Nanometer Structures Processing, Measurement, and Phenomena* **2007**, *25*, 2558-2561; c) F. Scarpa, S. Adhikari and A. S. Phani, *Nanotechnology* **2009**, *20*, 065709.

[11] J. Moser, A. Barreiro and A. Bachtold, *Applied Physics Letters* **2007**, *91*, 163513.

[12] a) M. D. Stoller, S. Park, Y. Zhu, J. An and R. S. Ruoff, *Nano Letters* **2008**, *8*, 3498-3502; b) X. Dong, Y. Shi, Y. Zhao, D. Chen, J. Ye, Y. Yao, F. Gao, Z. Ni, T. Yu, Z. Shen, Y. Huang, P. Chen and L.-J. Li, *Physical Review Letters* **2009**, *102*, 135501.

[13] A. K. Geim and K. S. Novoselov, *Nat Mater* **2007**, *6*, 183-191.

[14] F. Bonaccorso, A. Lombardo, T. Hasan, Z. Sun, L. Colombo and A. C. Ferrari, *Materials Today* **2012**, *15*, 564-589.

[15] R. Liu, D. Wu, X. Feng and K. Müllen, *Journal of the American Chemical Society* **2011**, *133*, 15221-15223.

[16] R. Liu, D. Wu, X. Feng and K. Müllen, *Angewandte Chemie International Edition* **2010**, *49*, 2565-2569.

[17] a) X. Wang, L. Zhi, N. Tsao, Ž. Tomović, J. Li and K. Müllen, *Angewandte Chemie International Edition* **2008**, *47*, 2990-2992; b) X. Wan, K. Chen, D. Liu, J. Chen, Q. Miao and J. Xu, *Chemistry of Materials* **2012**, *24*, 3906-3915.

[18] a) X. Li, W. Cai, J. An, S. Kim, J. Nah, D. Yang, R. Piner, A. Velamakanni, I. Jung, E. Tutuc, S. K. Banerjee, L. Colombo and R. S. Ruoff, *Science* **2009**, *324*, 1312-1314; b) W. Wu, L. A. Jauregui, Z. Su, Z. Liu, J. Bao, Y. P. Chen and Q. Yu, *Advanced Materials* **2011**, *23*, 4898-4903; c) Z. Luo, S. Kim, N. Kawamoto, A. M. Rappe and A. T. C. Johnson, *ACS Nano* **2011**, *5*, 9154-9160; d) H. Wang, G. Wang, P. Bao, S. Yang, W. Zhu, X. Xie and W.-J. Zhang, *Journal of the American Chemical Society* **2012**, *134*, 3627-3630; e) X. Li, C. W. Magnuson, A. Venugopal, R. M. Tromp, J. B. Hannon, E. M. Vogel, L. Colombo and R. S. Ruoff, *Journal of the American Chemical Society* **2011**, *133*, 2816-2819; f) Y. Zhang, L. Zhang, P. Kim, M. Ge, Z. Li and C. Zhou, *Nano Letters* **2012**, *12*, 2810-2816.

[19] a) A. Reina, X. Jia, J. Ho, D. Nezich, H. Son, V. Bulovic, M. S. Dresselhaus and J. Kong, *Nano Letters* **2009**, *9*, 30-35; b) K. S. Kim, Y. Zhao, H. Jang, S. Y. Lee, J. M. Kim, K. S. Kim, J.-H. Ahn, P. Kim, J.-Y. Choi and B. H. Hong, *Nature* **2009**, *457*, 706-710; c) Q. Yu, J. Lian, S. Siriponglert, H. Li, Y. P. Chen and S.-S. Pei, *Applied Physics Letters* **2008**, *93*, 113103; d) L. G. D. Arco, Y. Zhang, A. Kumar

and C. Zhou, *IEEE Transactions on Nanotechnology* **2009**, *8*, 135-138; e) N. Liu, L. Fu, B. Dai, K. Yan, X. Liu, R. Zhao, Y. Zhang and Z. Liu, *Nano Letters* **2011**, *11*, 297-303.

[20] P. W. Sutter, J.-I. Flege and E. A. Sutter, *Nat Mater* **2008**, *7*, 406-411.

[21] P. Sutter, J. T. Sadowski and E. Sutter, *Physical Review B* **2009**, *80*, 245411.

[22] S.-Y. Kwon, C. V. Ciobanu, V. Petrova, V. B. Shenoy, J. Bareño, V. Gambin, I. Petrov and S. Kodambaka, *Nano Letters* **2009**, *9*, 3985-3990.

[23] E. G. Acheson in *Article of Carborundum and Process of the Manufacture Thereof*, *Vol.* **1898**.

[24] X. Du, I. Skachko, F. Duerr, A. Luican and E. Y. Andrei, *Nature* **2009**, *462*, 192-195.

[25] a) S. Dhar, A. R. Barman, G. X. Ni, X. Wang, X. F. Xu, Y. Zheng, S. Tripathy, Ariando, A. Rusydi, K. P. Loh, M. Rubhausen, A. H. C. Neto, B. Őzyilmaz and T. Venkatesan, *AIP Advances* **2011**, *1*, 022109; b) S. Lee, M. F. Toney, W. Ko, J. C. Randel, H. J. Jung, K. Munakata, J. Lu, T. H. Geballe, M. R. Beasley, R. Sinclair, H. C. Manoharan and A. Salleo, *ACS Nano* **2010**, *4*, 7524-7530.

[26] B. Lauritzen, J. Minář, H. de Riedmatten, M. Afzelius, N. Sangouard, C. Simon and N. Gisin, *Physical Review Letters* **2010**, *104*, 080502.

[27] B. C. Brodie, *Philosophical Transactions of the Royal Society of London* **1859**, *149*, 249-259.

[28] L. Staudenmaier, *Berichte der deutschen chemischen Gesellschaft* **1898**, *31*, 1481-1487.

[29] W. S. Hummers and R. E. Offeman, *Journal of the American Chemical Society* **1958**, *80*, 1339-1339.

[30] a) X. Wang, L. Zhi and K. Müllen, *Nano Letters* **2008**, *8*, 323-327; b) H. A. Becerril, J. Mao, Z. Liu, R. M. Stoltenberg, Z. Bao and Y. Chen, *ACS Nano* **2008**, *2*, 463-470.

[31] a) S. Stankovich, D. A. Dikin, R. D. Piner, K. A. Kohlhaas, A. Kleinhammes, Y. Jia, Y. Wu, S. T. Nguyen and R. S. Ruoff, *Carbon* **2007**, *45*, 1558-1565; b) D. Li, M. B. Muller, S. Gilje, R. B. Kaner and G. G. Wallace, *Nat Nano* **2008**, *3*, 101-105; c) S. Park, J. An, I. Jung, R. D. Piner, S. J. An, X. Li, A. Velamakanni and R. S. Ruoff, *Nano Letters* **2009**, *9*, 1593-1597.

[32] D. Yang, A. Velamakanni, G. Bozoklu, S. Park, M. Stoller, R. D. Piner, S. Stankovich, I. Jung, D. A. Field, C. A. Ventrice and R. S. Ruoff, *Carbon* **2009**, *47*, 145-152.

[33] a) H.-J. Shin, K. K. Kim, A. Benayad, S.-M. Yoon, H. K. Park, I.-S. Jung, M. H. Jin, H.-K. Jeong, J. M. Kim, J.-Y. Choi and Y. H. Lee, *Advanced Functional Materials* **2009**, *19*, 1987-1992; b) W. Gao, L. B. Alemany, L. Ci and P. M. Ajayan, *Nat Chem* **2009**, *1*, 403-408.

[34] a) J. Zhang, H. Yang, G. Shen, P. Cheng, J. Zhang and S. Guo, *Chemical Communications* **2010**, *46*, 1112-1114; b) M. J. Fernández-Merino, L. Guardia, J. I. Paredes, S. Villar-Rodil, P. Solís-Fernández, A. Martínez-Alonso and J. M. D. Tascón, *The Journal of Physical Chemistry C* **2010**, *114*, 6426-6432.

[35] S. Pei, J. Zhao, J. Du, W. Ren and H.-M. Cheng, *Carbon* **2010**, *48*, 4466-4474.

[36] a) Y. Zhu, S. Murali, M. D. Stoller, A. Velamakanni, R. D. Piner and R. S. Ruoff, *Carbon* **2010**, *48*, 2118-2122; b) W. Chen, L. Yan and P. R. Bangal, *Carbon* **2010**, *48*, 1146-1152.

[37] D. Voiry, J. Yang, J. Kupferberg, R. Fullon, C. Lee, H. Y. Jeong, H. S. Shin and M. Chhowalla, *Science* **2016**.

[38] a) Y. Hernandez, V. Nicolosi, M. Lotya, F. M. Blighe, Z. Sun, S. De, I. T. McGovern, B. Holland, M. Byrne, Y. K. Gun'Ko, J. J. Boland, P. Niraj, G. Duesberg, S. Krishnamurthy, R. Goodhue, J. Hutchison, V. Scardaci, A. C. Ferrari and J. N. Coleman, *Nat Nano* **2008**, *3*, 563-568; b) J. N. Coleman, *Accounts of Chemical Research* **2013**, *46*, 14-22.

[39] a) U. Khan, A. O'Neill, M. Lotya, S. De and J. N. Coleman, *Small* **2010**, *6*, 864-871; b) S. Y. Oh, S. H. Kim, Y. S. Chi and T. J. Kang, *Applied Surface Science* **2012**, *258*, 8837-8844; c) K. R. Paton, E. Varrla, C. Backes, R. J. Smith, U. Khan, A. O'Neill, C. Boland, M. Lotya, O. M. Istrate, P. King, T. Higgins, S. Barwich, P. May, P. Puczkarski, I. Ahmed, M. Moebius, H. Pettersson, E. Long, J. Coelho, S. E. O'Brien, E. K. McGuire, B. M. Sanchez, G. S. Duesberg, N. McEvoy, T. J. Pennycook, C. Downing, A. Crossley, V. Nicolosi and J. N. Coleman, *Nat Mater* **2014**, *13*, 624-630.

[40] C. E. Hamilton, J. R. Lomeda, Z. Sun, J. M. Tour and A. R. Barron, *Nano Letters* **2009**, *9*, 3460-3462.

[41] P. Blake, P. D. Brimicombe, R. R. Nair, T. J. Booth, D. Jiang, F. Schedin, L. A. Ponomarenko, S. V. Morozov, H. F. Gleeson, E. W. Hill, A. K. Geim and K. S. Novoselov, *Nano Letters* **2008**, *8*, 1704-1708.

[42] a) X. Wang, P. F. Fulvio, G. A. Baker, G. M. Veith, R. R. Unocic, S. M. Mahurin, M. Chi and S. Dai, *Chemical Communications* **2010**, *46*, 4487-4489; b) D. Nuvoli, V. Alzari, R. Sanna, S. Scognamillo, M. Piccinini, L. Peponi, J. M. Kenny and A. Mariani, *Nanoscale Research Letters* **2012**, *7*, 674.

[43] N. Behabtu, J. R. Lomeda, M. J. Green, A. L. Higginbotham, A. Sinitskii, D. V. Kosynkin, D. Tsentalovich, A. N. G. Parra-Vasquez, J. Schmidt, E. Kesselman, Y. Cohen, Y. Talmon, J. M. Tour and M. Pasquali, *Nat Nano* **2010**, *5*, 406-411.

[44] M. Lotya, P. J. King, U. Khan, S. De and J. N. Coleman, *ACS Nano* **2010**, *4*, 3155-3162.

[45] M. Lotya, Y. Hernandez, P. J. King, R. J. Smith, V. Nicolosi, L. S. Karlsson, F. M. Blighe, S. De, Z. Wang, I. T. McGovern, G. S. Duesberg and J. N. Coleman, *Journal of the American Chemical Society* **2009**, *131*, 3611-3620.

[46] L. Guardia, M. J. Fernández-Merino, J. I. Paredes, P. Solís-Fernández, S. Villar-Rodil, A. Martínez-Alonso and J. M. D. Tascón, *Carbon* **2011**, *49*, 1653-1662.

[47] A. B. Bourlinos, V. Georgakilas, R. Zboril, T. A. Steriotis, A. K. Stubos and C. Trapalis, *Solid State Communications* **2009**, *149*, 2172-2176.

[48] M. Zhang, R. R. Parajuli, D. Mastrogiovanni, B. Dai, P. Lo, W. Cheung, R. Brukh, P. L. Chiu, T. Zhou, Z. Liu, E. Garfunkel and H. He, *Small* **2010**, *6*, 1100-1107.

[49] L.-L. Chua, J. Zaumseil, J.-F. Chang, E. C. W. Ou, P. K. H. Ho, H. Sirringhaus and R. H. Friend, *Nature* **2005**, *434*, 194-199.

[50] H. M. Solomon, B. A. Burgess, G. L. Kennedy and R. E. Staples, *Drug and Chemical Toxicology* **1995**, *18*, 271-293.

[51] G. L. Kennedy, *Drug and Chemical Toxicology* **1986**, *9*, 147-170.

[52] a) S. Stankovich, D. A. Dikin, G. H. B. Dommett, K. M. Kohlhaas, E. J. Zimney, E. A. Stach, R. D. Piner, S. T. Nguyen and R. S. Ruoff, *Nature* **2006**, *442*, 282-286; b) S. Park and R. S. Ruoff, *Nat Nano* **2009**, *4*, 217-224.

[53] a) I. Jung, D. A. Dikin, R. D. Piner and R. S. Ruoff, *Nano Letters* **2008**, *8*, 4283-4287; b) J. M. Mativetsky, A. Liscio, E. Treossi, E. Orgiu, A. Zanelli, P. Samorì and V. Palermo, *Journal of the American Chemical Society* **2011**, *133*, 14320-14326.

[54] a) C. Berger, Z. Song, X. Li, X. Wu, N. Brown, C. Naud, D. Mayou, T. Li, J. Hass, A. N. Marchenkov, E. H. Conrad, P. N. First and W. A. de Heer, *Science* **2006**, *312*, 1191-1196; b) C. Berger, Z. Song, T. Li, X. Li, A. Y. Ogbazghi, R. Feng, Z. Dai, A. N. Marchenkov, E. H. Conrad, P. N. First and W. A. de Heer, *The Journal of Physical Chemistry B* **2004**, *108*, 19912-19916.

[55] C. Eun-Young, C. Won San, L. Young Boo and N. Yong-Young, *Nanotechnology* **2011**, *22*, 365601.

[56] C. Vallés, C. Drummond, H. Saadaoui, C. A. Furtado, M. He, O. Roubeau, L. Ortolani, M. Monthioux and A. Pénicaud, *Journal of the American Chemical Society* **2008**, *130*, 15802-15804.

[57] W. Gu, W. Zhang, X. Li, H. Zhu, J. Wei, Z. Li, Q. Shu, C. Wang, K. Wang, W. Shen, F. Kang and D. Wu, *Journal of Materials Chemistry* **2009**, *19*, 3367-3369.

[58] X. Leng, X. Xiong and J.-p. Zou, *Transactions of Nonferrous Metals Society of China* **2014**, *24*, 177-183.

[59] G. Xin, W. Hwang, N. Kim, S. M. Cho and H. Chae, *Nanotechnology* **2010**, *21*, 405201.

[60] X. Geng, Y. Guo, D. Li, W. Li, C. Zhu, X. Wei, M. Chen, S. Gao, S. Qiu, Y. Gong, L. Wu, M. Long, M. Sun, G. Pan and L. Liu, *Sci. Rep.* **2013**, *3*.

[61] I. Janowska, K. Chizari, O. Ersen, S. Zafeiratos, D. Soubane, V. Costa, V. Speisser, C. Boeglin, M. Houllé, D. Bégin, D. Plee, M.-J. Ledoux and C. Pham-Huu, *Nano Research* **2010**, *3*, 126-137.

[62] L. M. Viculis, J. J. Mack, O. M. Mayer, H. T. Hahn and R. B. Kaner, *Journal of Materials Chemistry* **2005**, *15*, 974-978.

[63] X. Li, G. Zhang, X. Bai, X. Sun, X. Wang, E. Wang and H. Dai, *Nat Nano* **2008**, *3*, 538-542.

[64] P. K. Ang, S. Wang, Q. Bao, J. T. L. Thong and K. P. Loh, *ACS Nano* **2009**, *3*, 3587-3594.

[65] M. J. McAllister, J.-L. Li, D. H. Adamson, H. C. Schniepp, A. A. Abdala, J. Liu, M. Herrera-Alonso, D. L. Milius, R. Car, R. K. Prud'homme and I. A. Aksay, *Chemistry of Materials* **2007**, *19*, 4396-4404.

[66] V. Avdeev, N. Sorokina, N. Maksimova, I. Y. Martynov and A. Sezemin, *Synthesis of Ternary Intercalation Compounds in the Graphite–HNO3–R (R= H2SO4, H3PO4, CH3COOH) Systems*, Springer, **2001**, p. 366-371.

[67] A. Zhamu and B. Z. Jang in *Environmentally benign graphite intercalation compound composition for exfoliated graphite, flexible graphite, and nano-scaled graphene platelets*, *Vol.* Google Patents, **2014**.

[68] X. Geng, Y. Guo, D. Li, W. Li, C. Zhu, X. Wei, M. Chen, S. Gao, S. Qiu and Y. Gong, *Scientific reports* **2013**, *3*.

[69] I. Janowska, K. Chizari, O. Ersen, S. Zafeiratos, D. Soubane, V. Da Costa, V. Speisser, C. Boeglin, M. Houllé and D. Bégin, *Microwave synthesis of large few-layer graphene sheets in aqueous solution of ammonia*, Springer, **2010**, p. 126-137.

[70] Y. B. Tang, C. S. Lee, Z. H. Chen, G. D. Yuan, Z. H. Kang, L. B. Luo, H. S. Song, Y. Liu, Z. B. He, W. J. Zhang, I. Bello and S. T. Lee, *Nano Letters* **2009**, *9*, 1374-1377.

[71] J. Wang, K. K. Manga, Q. Bao and K. P. Loh, *Journal of the American Chemical Society* **2011**, *133*, 8888-8891.

[72] K. H. Park, B. H. Kim, S. H. Song, J. Kwon, B. S. Kong, K. Kang and S. Jeon, *Nano Letters* **2012**, *12*, 2871-2876.

[73] W. Fu, J. Kiggans, S. H. Overbury, V. Schwartz and C. Liang, *Chemical Communications* **2011**, *47*, 5265-5267.

[74] E. Widenkvist, D. W. Boukhvalov, S. Rubino, S. Akhtar, J. Lu, R. A. Quinlan, M. I. Katsnelson, K. Leifer, H. Grennberg and U. Jansson, *Journal of Physics D: Applied Physics* **2009**, *42*, 112003.

[75] C.-J. Shih, A. Vijayaraghavan, R. Krishnan, R. Sharma, J.-H. Han, M.-H. Ham, Z. Jin, S. Lin, G. L. C. Paulus, N. F. Reuel, Q. H. Wang, D. Blankschtein and M. S. Strano, *Nat Nano* **2011**, *6*, 439-445.

[76] A. Catheline, C. Valles, C. Drummond, L. Ortolani, V. Morandi, M. Marcaccio, M. Iurlo, F. Paolucci and A. Penicaud, *Chemical Communications* **2011**, *47*, 5470-5472.

[77] A. Safavi, M. Tohidi, F. A. Mahyari and H. Shahbaazi, *Journal of Materials Chemistry* **2012**, *22*, 3825-3831.

[78] J. Kwon, S. H. Lee, K.-H. Park, D.-H. Seo, J. Lee, B.-S. Kong, K. Kang and S. Jeon, *Small* **2011**, *7*, 864-868.

[79] a) P. L. Chiu, D. Mastrogiovanni, D. Wei, C. Louis, M. Jeong, G. Yu, P. Saad, C. R. Flach, R. Mendelsohn, E. Garfunkel and H. X. He, *J. Am. Chem. Soc.* **2012**, *134*, 5850-5856; b) M. A. Patel, H. Yang, P. L. Chiu, D. Mastrogiovanni, C. R. Flach, K. Savaram, L. Gomez, A. Hemnarine, R. Mendelsohn, E. Garfunkel, H. Jiang and H. X. He, *Acs Nano* **2013**, *7*, 8147-8157.

[80] P. L. Chiu, D. D. T. Mastrogiovanni, D. Wei, C. Louis, M. Jeong, G. Yu, P. Saad, C. R. Flach, R. Mendelsohn, E. Garfunkel and H. He, *Journal of the American Chemical Society* **2012**, *134*, 5850-5856.

[81] M. A. Patel, H. Yang, P. L. Chiu, D. D. T. Mastrogiovanni, C. R. Flach, K. Savaram, L. Gomez, A. Hemnarine, R. Mendelsohn, E. Garfunkel, H. Jiang and H. He, *ACS Nano* **2013**, *7*, 8147-8157.

[82] Y. Kobayashi, K.-i. Fukui, T. Enoki and K. Kusakabe, *Physical Review B* **2006**, *73*, 125415.

[83] T. Enoki, S. Fujii and K. Takai, *Carbon* **2012**, *50*, 3141-3145.

[84] Z. Sun, D. K. James and J. M. Tour, *The Journal of Physical Chemistry Letters* **2011**, *2*, 2425-2432.

[85] a) F. Cervantes-Sodi, G. Csányi, S. Piscanec and A. C. Ferrari, *Physical Review B* **2008**, *77*, 165427; b) E. F. Sheka and L. A. Chernozatonskii, *International Journal of Quantum Chemistry* **2010**, *110*, 1938-1946.

[86] a) D.-e. Jiang, B. G. Sumpter and S. Dai, *The Journal of Chemical Physics* **2007**, *126*, 134701; b) P. Koskinen, S. Malola and H. Häkkinen, *Physical Review B* **2009**, *80*, 073401.

[87] K. He, G.-D. Lee, A. W. Robertson, E. Yoon and J. H. Warner, **2014**, *5*, 3040.

[88] a) M. Solà, *Frontiers in Chemistry* **2013**, *1*, 22; b) S. Fujii and T. Enoki, *Angewandte Chemie International Edition* **2012**, *51*, 7236-7241.

[89] Y.-W. Son, M. L. Cohen and S. G. Louie, *Physical Review Letters* **2006**, *97*, 216803.

[90] a) M. Y. Han, B. Özyilmaz, Y. Zhang and P. Kim, *Physical Review Letters* **2007**, *98*, 206805; b) X. Li, X. Wang, L. Zhang, S. Lee and H. Dai, *Science* **2008**, *319*, 1229-1232.

[91] J. Cai, P. Ruffieux, R. Jaafar, M. Bieri, T. Braun, S. Blankenburg, M. Muoth, A. P. Seitsonen, M. Saleh, X. Feng, K. Mullen and R. Fasel, *Nature* **2010**, *466*, 470-473.

[92] L. Tapaszto, G. Dobrik, P. Lambin and L. P. Biro, *Nat Nano* **2008**, *3*, 397-401.

[93] S. S. Datta, D. R. Strachan, S. M. Khamis and A. T. C. Johnson, *Nano Letters* **2008**, *8*, 1912-1915.

[94] E. Bekyarova, M. E. Itkis, P. Ramesh, C. Berger, M. Sprinkle, W. A. de Heer and R. C. Haddon, *Journal of the American Chemical Society* **2009**, *131*, 1336-1337.

[95] H. Murayama and T. Maeda, *Nature* **1990**, *345*, 791-793.

[96] L. Jiao, L. Zhang, X. Wang, G. Diankov and H. Dai, *Nature* **2009**, *458*, 877-880.

[97] P. Kumar, L. S. Panchakarla and C. N. R. Rao, *Nanoscale* **2011**, *3*, 2127-2129.

[98] D. V. Kosynkin, A. L. Higginbotham, A. Sinitskii, J. R. Lomeda, A. Dimiev, B. K. Price and J. M. Tour, *Nature* **2009**, *458*, 872-876.

[99] T. C. Li and S.-P. Lu, *Physical Review B* **2008**, *77*, 085408.

[100] J. Bai, X. Zhong, S. Jiang, Y. Huang and X. Duan, *Nat Nano* **2010**, *5*, 190-194.

[101] a) Y. Xu, Z. Lin, X. Zhong, X. Huang, N. O. Weiss, Y. Huang and X. Duan, **2014**, *5*, 4554; b) X. Han, M. R. Funk, F. Shen, Y.-C. Chen, Y. Li, C. J. Campbell, J. Dai, X. Yang, J.-W. Kim, Y. Liao, J. W. Connell, V. Barone, Z. Chen, Y. Lin and L. Hu, *ACS Nano* **2014**, *8*, 8255-8265.

[102] a) R. Lv, H. Wang, H. Yu and F. Peng, *Electrochimica Acta* **2017**, *228*, 203-213; b) M. Patel, W. Feng, K. Savaram, M. R. Khoshi, R. Huang, J. Sun, E. Rabie, C. Flach, R. Mendelsohn, E. Garfunkel and H. He, *Small* **2015**, *11*, 3358-3368.

[103] M. A. Chenliang Su, Kazuyuki Takai, Jiong Lu, Si-jia Hao, Yi Zheng, Pingping Wu, Qiaoliang Bao, Toshiaki Enoki, Yves J. Chabal & Kian Ping Loh, *Nature Communications*

[104] a) J. R. Miller, R. A. Outlaw and B. C. Holloway, *Science* **2010**, *329*, 1637-1639; b) J. K. Lee, K. B. Smith, C. M. Hayner and H. H. Kung, *Chemical Communications* **2010**, *46*, 2025-2027; c) A. Abouimrane, O. C. Compton, K. Amine and S. T. Nguyen, *The Journal of Physical Chemistry C* **2010**, *114*, 12800-12804.

[105] a) S. Yang, X. Feng, S. Ivanovici and K. Müllen, *Angewandte Chemie International Edition* **2010**, *49*, 8408-8411; b) H. Wang, L.-F. Cui, Y. Yang, H. Sanchez Casalongue, J. T. Robinson, Y. Liang, Y. Cui and H. Dai, *Journal of the American Chemical Society* **2010**, *132*, 13978-13980; c) S.-M. Paek, E. Yoo and I. Honma, *Nano Letters* **2009**, *9*, 72-75.

[106] a) Y. Lin, X. Han, C. J. Campbell, J.-W. Kim, B. Zhao, W. Luo, J. Dai, L. Hu and J. W. Connell, *Advanced Functional Materials* **2015**, *25*, 2920-2927; b) Y.-Y. Peng, Y.-M. Liu, J.-K. Chang, C.-H.

Wu, M.-D. Ger, N.-W. Pu and C.-L. Chang, *Carbon* **2015**, *81*, 347-356; c) C.-H. Yang, P.-L. Huang, X.-F. Luo, C.-H. Wang, C. Li, Y.-H. Wu and J.-K. Chang, *ChemSusChem* **2015**, *8*, 1779-1786.

[107] S. P. Koenig, L. Wang, J. Pellegrino and J. S. Bunch, *Nat Nano* **2012**, *7*, 728-732.

[108] a) S. P. Surwade, S. N. Smirnov, I. V. Vlassiouk, R. R. Unocic, G. M. Veith, S. Dai and S. M. Mahurin, *Nat Nano* **2015**, *10*, 459-464; b) D. Cohen-Tanugi and J. C. Grossman, *Nano Letters* **2012**, *12*, 3602-3608.

[109] C. Sun, B. Wen and B. Bai, *Science Bulletin* **2015**, *60*, 1807-1823.

[110] S. J. Heerema and C. Dekker, *Nat Nano* **2016**, *11*, 127-136.

[111] M. D. Fischbein and M. Drndić, *Applied Physics Letters* **2008**, *93*, 113107.

[112] M. Kim, N. S. Safron, E. Han, M. S. Arnold and P. Gopalan, *Nano Letters* **2010**, *10*, 1125-1131.

[113] a) Z. Zeng, X. Huang, Z. Yin, H. Li, Y. Chen, H. Li, Q. Zhang, J. Ma, F. Boey and H. Zhang, *Advanced Materials* **2012**, *24*, 4138-4142; b) J. Ding, K. Du, I. Wathuthanthri, C.-H. Choi, F. T. Fisher and E.-H. Yang, *Journal of Vacuum Science & Technology B, Nanotechnology and Microelectronics: Materials, Processing, Measurement, and Phenomena* **2014**, *32*, 06FF01.

[114] a) A. Sinitskii and J. M. Tour, *Journal of the American Chemical Society* **2010**, *132*, 14730-14732; b) I. Jung, H. Y. Jang and S. Park, *Applied Physics Letters* **2013**, *103*, 023105.

[115] M. Patel, W. Feng, K. Savaram, M. R. Khoshi, R. Huang, J. Sun, E. Rabie, C. Flach, R. Mendelsohn and E. Garfunkel, *Small* **2015**, *11*, 3358-3368.

[116] Z. Fan, Q. Zhao, T. Li, J. Yan, Y. Ren, J. Feng and T. Wei, *Carbon* **2012**, *50*, 1699-1703.

[117] S. Chen, J. Duan, M. Jaroniec and S. Z. Qiao, *Journal of Materials Chemistry A* **2013**, *1*, 9409-9413.

[118] a) X. Zhao, C. M. Hayner, M. C. Kung and H. H. Kung, *Advanced Energy Materials* **2011**, *1*, 1079-1084; b) X. Zhao, C. M. Hayner, M. C. Kung and H. H. Kung, *ACS Nano* **2011**, *5*, 8739-8749.

[119] X. Wang, L. Jiao, K. Sheng, C. Li, L. Dai and G. Shi, **2013**, *3*, 1996.

[120] Y. Xu, C.-Y. Chen, Z. Zhao, Z. Lin, C. Lee, X. Xu, C. Wang, Y. Huang, M. I. Shakir and X. Duan, *Nano Letters* **2015**, *15*, 4605-4610.

[121] J. G. Radich and P. V. Kamat, *ACS Nano* **2013**, *7*, 5546-5557.

[122] G. P. Kotchey, B. L. Allen, H. Vedala, N. Yanamala, A. A. Kapralov, Y. Y. Tyurina, J. Klein-Seetharaman, V. E. Kagan and A. Star, *ACS Nano* **2011**, *5*, 2098-2108.

[123] S. Liu, W. Peng, H. Sun and S. Wang, *Nanoscale* **2014**, *6*, 766-771.

[124] W. Peng, S. Liu, H. Sun, Y. Yao, L. Zhi and S. Wang, *Journal of Materials Chemistry A* **2013**, *1*, 5854-5859.

[125] S. Wang, F. Tristan, D. Minami, T. Fujimori, R. Cruz-Silva, M. Terrones, K. Takeuchi, K. Teshima, F. Rodríguez-Reinoso, M. Endo and K. Kaneko, *Carbon* **2014**, *76*, 220-231.

[126] L. Liu, S. Ryu, M. R. Tomasik, E. Stolyarova, N. Jung, M. S. Hybertsen, M. L. Steigerwald, L. E. Brus and G. W. Flynn, *Nano Letters* **2008**, *8*, 1965-1970.

[127] M. Koinuma, C. Ogata, Y. Kamei, K. Hatakeyama, H. Tateishi, Y. Watanabe, T. Taniguchi, K. Gezuhara, S. Hayami, A. Funatsu, M. Sakata, Y. Kuwahara, S. Kurihara and Y. Matsumoto, *The Journal of Physical Chemistry C* **2012**, *116*, 19822-19827.

[128] Y. Zhu, S. Murali, M. D. Stoller, K. J. Ganesh, W. Cai, P. J. Ferreira, A. Pirkle, R. M. Wallace, K. A. Cychosz, M. Thommes, D. Su, E. A. Stach and R. S. Ruoff, *Science* **2011**, *332*, 1537-1541.

[129] L. L. Zhang, X. Zhao, M. D. Stoller, Y. Zhu, H. Ji, S. Murali, Y. Wu, S. Perales, B. Clevenger and R. S. Ruoff, *Nano Letters* **2012**, *12*, 1806-1812.

[130] T. Kim, G. Jung, S. Yoo, K. S. Suh and R. S. Ruoff, *ACS Nano* **2013**, *7*, 6899-6905.

[131] Y. Lin, K. A. Watson, J.-W. Kim, D. W. Baggett, D. C. Working and J. W. Connell, *Nanoscale* **2013**, *5*, 7814-7824.

[132] M. L. Gethers, J. C. Thomas, S. Jiang, N. O. Weiss, X. Duan, W. A. Goddard and P. S. Weiss, *ACS Nano* **2015**, *9*, 10909-10915.

[133] O. Akhavan, *ACS Nano* **2010**, *4*, 4174-4180.

[134] O. Akhavan and E. Ghaderi, *Small* **2013**, *9*, 3593-3601.

[135] J. Liu, H. Cai, X. Yu, K. Zhang, X. Li, J. Li, N. Pan, Q. Shi, Y. Luo and X. Wang, *The Journal of Physical Chemistry C* **2012**, *116*, 15741-15746.

[136] W. Conover, *Journal of Chemical Education* **2003**, *80*, 268.

[137] B. L. Hayes, *Microwave Synthesis: Chemistry at the Speed of Light*, CEM Publishing: Matthews, **2002**, p.

[138] M. V. Savoskin, A. P. Yaroshenko, G. E. Whyman and R. D. Mysyk, *Journal of Physics and Chemistry of Solids* **2006**, *67*, 1127-1131.

[139] C. O. Kappe, D. Dallinger and S. S. Murphree in *Microwave Theory*, Wiley-VCH Verlag GmbH & Co. KGaA, **2009**, pp. 11-44.

[140] C. Gabriel, S. Gabriel, E. H. Grant, E. H. Grant, B. S. J. Halstead and D. Michael P. Mingos, *Chemical Society Reviews* **1998**, *27*, 213-224.

[141] I. Bilecka and M. Niederberger, *Nanoscale* **2010**, *2*, 1358-1374.

[142] a) K. I. Rybakov, V. E. Semenov, S. V. Egorov, A. G. Eremeev, I. V. Plotnikov and Y. V. Bykov, *Journal of Applied Physics* **2006**, *99*, 023506; b) J. Cheng, R. Roy and D. Agrawal, *Material Research Innovations* **2002**, *5*, 170-177.

[143] J.-S. Schanche, *Molecular Diversity* **2003**, *7*, 291-298.

[144] a) C. O. Kappe, D. Dallinger and S. S. Murphree in *Microwave Synthesis - An Introduction*, Wiley-VCH Verlag GmbH & Co. KGaA, **2009**, pp. 1-9; b) M. Nuchter, B. Ondruschka, W. Bonrath and A. Gum, *Green Chemistry* **2004**, *6*, 128-141.

[145] K. J. Rao, B. Vaidhyanathan, M. Ganguli and P. A. Ramakrishnan, *Chemistry of Materials* **1999**, *11*, 882-895.

[146] H. Hu, Z. Zhao, Q. Zhou, Y. Gogotsi and J. Qiu, *Carbon* **2012**, *50*, 3267-3273.

[147] K. MacKenzie, O. Dunens and A. T. Harris, *Separation and Purification Technology* **2009**, *66*, 209-222.

[148] A. Wadhawan, D. Garrett and J. M. Perez, *Applied Physics Letters* **2003**, *83*, 2683-2685.

[149] J. E. Atwater and J. Wheeler, R.R., *Applied Physics A* **2004**, *79*, 125-129.

[150] J. A. Menéndez, A. Arenillas, B. Fidalgo, Y. Fernández, L. Zubizarreta, E. G. Calvo and J. M. Bermúdez, *Fuel Processing Technology* **2010**, *91*, 1-8.

[151] a) U. O. Méndez, O. V. Kharissova and M. Rodríguez, *Rev. Adv. Mater. Sci* **2003**, *5*, 398; b) D.-M. Yoon, B.-J. Yoon, K.-H. Lee, H. S. Kim and C. G. Park, *Carbon* **2006**, *44*, 1339-1343; c) E. O. Pentsak, E. G. Gordeev and V. P. Ananikov, *ACS Catalysis* **2014**, *4*, 3806-3814.

[152] Z. Li, Y. Yao, Z. Lin, K.-S. Moon, W. Lin and C. Wong, *Journal of Materials Chemistry* **2010**, *20*, 4781-4783.

[153] a) V. Sridhar, J.-H. Jeon and I.-K. Oh, *Carbon* **2010**, *48*, 2953-2957; b) Z. Wang, J. Liu, W. Wang, H. Chen, Z. Liu, Q. Yu, H. Zeng and L. Sun, *Chemical Communications* **2013**, *49*, 10835-10837; c) Z. Luo, Y. Lu, L. A. Somers and A. T. C. Johnson, *Journal of the American Chemical Society* **2009**, *131*, 898-899.

[154] S.-H. Bae, K. Karthikeyan, Y.-S. Lee and I.-K. Oh, *Carbon* **2013**, *64*, 527-536.

[155] V. Sridhar, H.-J. Kim, J.-H. Jung, C. Lee, S. Park and I.-K. Oh, *ACS Nano* **2012**, *6*, 10562-10570.

[156] a) A. R. Harutyunyan, B. K. Pradhan, J. Chang, G. Chen and P. C. Eklund, *The Journal of Physical Chemistry B* **2002**, *106*, 8671-8675; b) E. Vazquez, V. Georgakilas and M. Prato, *Chemical Communications* **2002**, 2308-2309; c) K. Chajara, C.-H. Andersson, J. Lu, E. Widenkvist and H. Grennberg, *New Journal of Chemistry* **2010**, *34*, 2275-2280.

[157] a) H. Qiu, Y. Maeda, T. Akasaka and J. Yang, *Separation and Purification Technology* **2012**, *96*, 182-186; b) H. Qiu, Y. Maeda and T. Akasaka, *Journal of the American Chemical Society* **2009**, *131*, 16529-16533.

[158] P. F. Lovell, *AIChE Journal* **1981**, *27*, 316-316.

[159] M. Endo, Y. A. Kim, M. Ezaka, K. Osada, T. Yanagisawa, T. Hayashi, M. Terrones and M. S. Dresselhaus, *Nano Letters* **2003**, *3*, 723-726.

[160] a) G. G. Wildgoose, C. E. Banks and R. G. Compton, *Small* **2006**, *2*, 182-193; b) A. Villa, D. Wang, N. Dimitratos, D. Su, V. Trevisan and L. Prati, *Catalysis Today* **2010**, *150*, 8-15.

[161] a) X. Chen, G. Wu, J. Chen, X. Chen, Z. Xie and X. Wang, *Journal of the American Chemical Society* **2011**, *133*, 3693-3695; b) G. M. Scheuermann, L. Rumi, P. Steurer, W. Bannwarth and R. Mülhaupt, *Journal of the American Chemical Society* **2009**, *131*, 8262-8270.

[162] a) D.-T. Phan and G.-S. Chung, *Sensors and Actuators B: Chemical* **2014**, *199*, 354-360; b) P. A. Pandey, N. R. Wilson and J. A. Covington, *Sensors and Actuators B: Chemical* **2013**, *183*, 478-487; c) A. R. Siamaki, A. E. R. S. Khder, V. Abdelsayed, M. S. El-Shall and B. F. Gupton, *Journal of Catalysis* **2011**, *279*, 1-11; d) G. Wu, X. Wang, N. Guan and L. Li, *Applied Catalysis B: Environmental* **2013**, *136–137*, 177-185; e) S. Moussa, A. R. Siamaki, B. F. Gupton and M. S. El-Shall, *ACS Catalysis* **2012**, *2*, 145-154.

[163] a) Y. Wang, J. Yao, H. Li, D. Su and M. Antonietti, *Journal of the American Chemical Society* **2011**, *133*, 2362-2365; b) L. Shao, X. Huang, D. Teschner and W. Zhang, *ACS Catalysis* **2014**, *4*, 2369-2373; c) A. M. Fuente, G. Pulgar, F. González, C. Pesquera and C. Blanco, *Applied Catalysis A: General* **2001**, *208*, 35-46.

[164] a) J. Wang, Y.-L. Qin, X. Liu and X.-B. Zhang, *Journal of Materials Chemistry* **2012**, *22*, 12468-12470; b) P. Xi, F. Chen, G. Xie, C. Ma, H. Liu, C. Shao, J. Wang, Z. Xu, X. Xu and Z. Zeng, *Nanoscale* **2012**, *4*, 5597-5601; c) N. Cao, L. Yang, C. Du, J. Su, W. Luo and G. Cheng, *Journal of Materials Chemistry A* **2014**, *2*, 14344-14347; d) Y. Yang, Z.-H. Lu, Y. Hu, Z. Zhang, W. Shi, X. Chen and T. Wang, *RSC Advances* **2014**, *4*, 13749-13752.

[165] a) E. G. Rodrigues, S. A. C. Carabineiro, J. J. Delgado, X. Chen, M. F. R. Pereira and J. J. M. Órfão, *Journal of Catalysis* **2012**, *285*, 83-91; b) S. Carrettin, P. McMorn, P. Johnston, K. Griffin, C. J. Kiely and G. J. Hutchings, *Physical Chemistry Chemical Physics* **2003**, *5*, 1329-1336; c) K. P. Peterson and R. C. Larock, *The Journal of Organic Chemistry* **1998**, *63*, 3185-3189; d) E. G. Rodrigues, S. A. C. Carabineiro, X. Chen, J. J. Delgado, J. L. Figueiredo, M. F. R. Pereira and J. J. M. Órfão, *Catalysis Letters* **2011**, *141*, 420-431.

[166] Y. Li, X. Fan, J. Qi, J. Ji, S. Wang, G. Zhang and F. Zhang, *Nano Research* **2010**, *3*, 429-437.

[167] a) C. Wang, S. Guo, X. Pan, W. Chen and X. Bao, *Journal of Materials Chemistry* **2008**, *18*, 5782-5786; b) J. Qu, H. Chen and S. Dong, *Electroanalysis* **2008**, *20*, 2410-2415; c) K. Pyrzyńska and M. Bystrzejewski, *Colloids and Surfaces A: Physicochemical and Engineering Aspects* **2010**, *362*, 102-109; d) V. Georgakilas, D. Gournis, V. Tzitzios, L. Pasquato, D. M. Guldi and M. Prato, *Journal of Materials Chemistry* **2007**, *17*, 2679-2694.

[168] a) P. Meric, K. M. K. Yu and S. C. Tsang, *Langmuir* **2004**, *20*, 8537-8545; b) H. Ohde, C. M. Wai, H. Kim, J. Kim and M. Ohde, *Journal of the American Chemical Society* **2002**, *124*, 4540-4541; c) P. Meric, K. M. K. Yu and S. C. Tsang, *Catalysis Letters* **2004**, *95*, 39-43.

[169] a) H. Tsunoyama, H. Sakurai and T. Tsukuda, *Chemical Physics Letters* **2006**, *429*, 528-532; b) S. Kanaoka, N. Yagi, Y. Fukuyama, S. Aoshima, H. Tsunoyama, T. Tsukuda and H. Sakurai, *Journal of the American Chemical Society* **2007**, *129*, 12060-12061; c) H. Tsunoyama, H. Sakurai, Y. Negishi and T. Tsukuda, *Journal of the American Chemical Society* **2005**, *127*, 9374-9375.

[170] a) T. Iwasawa, M. Tokunaga, Y. Obora and Y. Tsuji, *Journal of the American Chemical Society* **2004**, *126*, 6554-6555; b) T. Nishimura, T. Onoue, K. Ohe and S. Uemura, *The Journal of Organic Chemistry* **1999**, *64*, 6750-6755; c) D. J. Gorin, B. D. Sherry and F. D. Toste, *Chemical Reviews* **2008**, *108*, 3351-3378.

[171] a) E. Martono and J. M. Vohs, *Journal of Catalysis* **2012**, *291*, 79-86; b) F. de Clippel, M. Dusselier, R. Van Rompaey, P. Vanelderen, J. Dijkmans, E. Makshina, L. Giebeler, S. Oswald, G. V.

Baron, J. F. M. Denayer, P. P. Pescarmona, P. A. Jacobs and B. F. Sels, *Journal of the American Chemical Society* **2012**, *134*, 10089-10101; c) G. Prieto, J. Zečević, H. Friedrich, K. P. de Jong and P. E. de Jongh, *Nat Mater* **2013**, *12*, 34-39.

[172] a) X. Xu, Y. Li, Y. Gong, P. Zhang, H. Li and Y. Wang, *Journal of the American Chemical Society* **2012**, *134*, 16987-16990; b) V. B. Parambhath, R. Nagar and S. Ramaprabhu, *Langmuir* **2012**, *28*, 7826-7833; c) Z. Wei, Y. Gong, T. Xiong, P. Zhang, H. Li and Y. Wang, *Catalysis Science & Technology* **2015**, *5*, 397-404; d) B. P. Vinayan, R. Nagar and S. Ramaprabhu, *Journal of Materials Chemistry A* **2013**, *1*, 11192-11199; e) Z. Li, J. Liu, Z. Huang, Y. Yang, C. Xia and F. Li, *ACS Catalysis* **2013**, *3*, 839-845; f) P. Zhang, Y. Gong, H. Li, Z. Chen and Y. Wang, *Nature Communications* **2013**, *4*, 1593.

[173] M. A. Patel, F. Luo, M. R. Khoshi, E. Rabie, Q. Zhang, C. R. Flach, R. Mendelsohn, E. Garfunkel, M. Szostak and H. He, *ACS Nano* **2016**, *10*, 2305-2315.

[174] T. Harada, S. Ikeda, F. Hashimoto, T. Sakata, K. Ikeue, T. Torimoto and M. Matsumura, *Langmuir* **2010**, *26*, 17720-17725.

[175] a) E. Gelder, S. D. Jackson and C. M. Lok, *Catalysis Letters* **2002**, *84*, 205-208; b) A. Corma and P. Serna, *Science* **2006**, *313*, 332-334; c) R. V. Jagadeesh, G. Wienhofer, F. A. Westerhaus, A.-E. Surkus, M.-M. Pohl, H. Junge, K. Junge and M. Beller, *Chemical Communications* **2011**, *47*, 10972-10974; d) J. Zhang, Y. Wang, H. Ji, Y. Wei, N. Wu, B. Zuo and Q. Wang, *Journal of Catalysis* **2005**, *229*, 114-118; e) F. Ragaini and S. Cenini, *Journal of Molecular Catalysis A: Chemical* **1996**, *105*, 145-148.

[176] a) S. Kim, E. Kim and B. M. Kim, *Chemistry – An Asian Journal* **2011**, *6*, 1921-1925; b) W. Lin, H. Cheng, J. Ming, Y. Yu and F. Zhao, *Journal of Catalysis* **2012**, *291*, 149-154; c) A. K. Patra, A. Dutta and A. Bhaumik, *Catalysis Communications* **2010**, *11*, 651-655.

[177] a) X. Li, H. Wang, J. T. Robinson, H. Sanchez, G. Diankov and H. Dai, *Journal of the American Chemical Society* **2009**, *131*, 15939-15944; b) H. Zhou, L. Shi and Q. Sun, *Chinese Journal of Catalysis* **2012**, *33*, 1463-1469; c) J. W. Larsen, M. Freund, K. Y. Kim, M. Sidovar and J. L. Stuart, *Carbon* **2000**, *38*, 655-661; d) H. H. Byung, H. S. Dae and Y. C. Sung, *Tetrahedron Letters* **1985**, *26*, 6233-6234.

[178] a) J. Luo, H. Yu, H. Wang, H. Wang and F. Peng, *Chemical Engineering Journal* **2014**, *240*, 434-442; b) D. R. Dreyer, H.-P. Jia and C. W. Bielawski, *Angewandte Chemie* **2010**, *122*, 6965-6968; c) Y. Kuang, N. M. Islam, Y. Nabae, T. Hayakawa and M.-a. Kakimoto, *Angewandte Chemie International Edition* **2010**, *49*, 436-440; d) J. Vijaya Sundar and V. Subramanian, *Organic Letters* **2013**, *15*, 5920-5923; e) Y. Meng, D. Voiry, A. Goswami, X. Zou, X. Huang, M. Chhowalla, Z. Liu and T. Asefa, *Journal of the American Chemical Society* **2014**, *136*, 13554-13557.

[179] a) H. Watanabe, S. Asano, S.-i. Fujita, H. Yoshida and M. Arai, *ACS Catalysis* **2015**, *5*, 2886-2894; b) K. Chizari, I. Janowska, M. Houllé, I. Florea, O. Ersen, T. Romero, P. Bernhardt, M. J. Ledoux and C. Pham-Huu, *Applied Catalysis A: General* **2010**, *380*, 72-80; c) A. Dhakshinamoorthy, A. Primo, P. Concepcion, M. Alvaro and H. Garcia, *Chemistry – A European Journal* **2013**, *19*, 7547-7554; d) J. Long, X. Xie, J. Xu, Q. Gu, L. Chen and X. Wang, *ACS Catalysis* **2012**, *2*, 622-631; e) Y. Ding, L. Zhang, K.-H. Wu, Z. Feng, W. Shi, Q. Gao, B. Zhang and D. S. Su, *Journal of Colloid and Interface Science* **2016**, *480*, 175-183.

[180] Y. Jiang, L. Yang, T. Sun, J. Zhao, Z. Lyu, O. Zhuo, X. Wang, Q. Wu, J. Ma and Z. Hu, *ACS Catalysis* **2015**, *5*, 6707-6712.

[181] K. Gong, F. Du, Z. Xia, M. Durstock and L. Dai, *Science* **2009**, *323*, 760-764.

[182] a) D. Guo, R. Shibuya, C. Akiba, S. Saji, T. Kondo and J. Nakamura, *Science* **2016**, *351*, 361-365; b) H. B. Yang, J. Miao, S.-F. Hung, J. Chen, H. B. Tao, X. Wang, L. Zhang, R. Chen, J. Gao, H. M. Chen, L. Dai and B. Liu, *Science Advances* **2016**, *2*; c) L. Qu, Y. Liu, J.-B. Baek and L. Dai, *ACS Nano* **2010**, *4*, 1321-1326; d) R. Liu, D. Wu, X. Feng and K. Müllen, *Angewandte Chemie* **2010**, *122*, 2619-2623; e) L. Lai, J. R. Potts, D. Zhan, L. Wang, C. K. Poh, C. Tang, H. Gong, Z. Shen, J. Lin and R. S.

Ruoff, *Energy & Environmental Science* **2012**, *5*, 7936-7942; f) Z. Lin, G. Waller, Y. Liu, M. Liu and C.-P. Wong, *Advanced Energy Materials* **2012**, *2*, 884-888; g) Y. Tang, B. L. Allen, D. R. Kauffman and A. Star, *Journal of the American Chemical Society* **2009**, *131*, 13200-13201.

[183] a) Z.-W. Liu, F. Peng, H.-J. Wang, H. Yu, W.-X. Zheng and J. Yang, *Angewandte Chemie* **2011**, *123*, 3315-3319; b) C. Zhang, N. Mahmood, H. Yin, F. Liu and Y. Hou, *Advanced Materials* **2013**, *25*, 4932-4937; c) T. Y. Ma, J. Ran, S. Dai, M. Jaroniec and S. Z. Qiao, *Angewandte Chemie International Edition* **2015**, *54*, 4646-4650; d) D.-S. Yang, D. Bhattacharjya, S. Inamdar, J. Park and J.-S. Yu, *Journal of the American Chemical Society* **2012**, *134*, 16127-16130.

[184] a) Z. Yang, Z. Yao, G. Li, G. Fang, H. Nie, Z. Liu, X. Zhou, X. a. Chen and S. Huang, *ACS Nano* **2012**, *6*, 205-211; b) Z. Ma, S. Dou, A. Shen, L. Tao, L. Dai and S. Wang, *Angewandte Chemie International Edition* **2015**, *54*, 1888-1892; c) J.-e. Park, Y. J. Jang, Y. J. Kim, M.-s. Song, S. Yoon, D. H. Kim and S.-J. Kim, *Physical Chemistry Chemical Physics* **2014**, *16*, 103-109.

[185] a) L. Yang, S. Jiang, Y. Zhao, L. Zhu, S. Chen, X. Wang, Q. Wu, J. Ma, Y. Ma and Z. Hu, *Angewandte Chemie* **2011**, *123*, 7270-7273; b) Z.-H. Sheng, H.-L. Gao, W.-J. Bao, F.-B. Wang and X.-H. Xia, *Journal of Materials Chemistry* **2012**, *22*, 390-395; c) G. Jo and S. Shanmugam, *Electrochemistry Communications* **2012**, *25*, 101-104.

[186] a) C. H. Choi, S. H. Park and S. I. Woo, *ACS Nano* **2012**, *6*, 7084-7091; b) J. Liang, Y. Jiao, M. Jaroniec and S. Z. Qiao, *Angewandte Chemie International Edition* **2012**, *51*, 11496-11500; c) Y. Zheng, Y. Jiao, L. Ge, M. Jaroniec and S. Z. Qiao, *Angewandte Chemie* **2013**, *125*, 3192-3198; d) S. Wang , E. Iyyamperumal , A. Roy, Y. Xue, D. Yu and L. Dai, *Angewandte Chemie International Edition* **2011**, *50*, 11756-11760.

[187] a) Y. Zhao, L. Yang, S. Chen, X. Wang, Y. Ma, Q. Wu, Y. Jiang, W. Qian and Z. Hu, *Journal of the American Chemical Society* **2013**, *135*, 1201-1204; b) L. Yang, S. Jiang, Y. Zhao, L. Zhu, S. Chen, X. Wang, Q. Wu, J. Ma, Y. Ma and Z. Hu, *Angewandte Chemie International Edition* **2011**, *50*, 7132-7135.

[188] C. E. Banks, T. J. Davies, G. G. Wildgoose and R. G. Compton, *Chemical Communications* **2005**, 829-841.

[189] A. Shen, Y. Zou, Q. Wang, R. A. W. Dryfe, X. Huang, S. Dou, L. Dai and S. Wang, *Angewandte Chemie International Edition* **2014**, *53*, 10804-10808.

[190] R. Hage and A. Lienke, *Angewandte Chemie International Edition* **2006**, *45*, 206-222.

[191] S. R. Jennings, D. J. Dollhopf and W. P. Inskeep, *Applied Geochemistry* **2000**, *15*, 235-243.

[192] a) K. Kosaka, H. Yamada, K. Shishida, S. Echigo, R. A. Minear, H. Tsuno and S. Matsui, *Water Research* **2001**, *35*, 3587-3594; b) C. B. Chidambara Raj and H. Li Quen, *Chemical Engineering Science* **2005**, *60*, 5305-5311; c) Z. Qiang, J.-H. Chang and C.-P. Huang, *Water Research* **2002**, *36*, 85-94.

[193] a) G. Ondrey, *Chemical Engineering* **2005**, *112*; b) G. Goor in *Hydrogen Peroxide: Manufacture and Industrial Use for Production of Organic Chemicals*, *Vol. 9* (Ed. G. Strukul), Springer Netherlands, **1992**, pp. 13-43.

[194] a) G. Pfleiderer and H. J. Riedl in *Production of hydrogen peroxide*, *Vol.* US patents 2158525, **1940**; b) D. Hâncu, J. Green and E. J. Beckman, *Industrial & Engineering Chemistry Research* **2002**, *41*, 4466-4474.

[195] a) L. W. Gosser in *Catalytic process for making H2 O2 from hydrogen and oxygen*, *Vol.* US patents 4681751, **1987**; b) J. K. Edwards, B. Solsona, E. N. N, A. F. Carley, A. A. Herzing, C. J. Kiely and G. J. Hutchings, *Science* **2009**, *323*, 1037-1041; c) R. Burch and P. R. Ellis, *Applied Catalysis B: Environmental* **2003**, *42*, 203-211.

[196] a) I. Yamanaka, T. Onizawa, S. Takenaka and K. Otsuka, *Angewandte Chemie International Edition* **2003**, *42*, 3653-3655; b) S. Fukuzumi, Y. Yamada and K. D. Karlin, *Electrochimica Acta* **2012**, *82*, 493-511.

[197] D. Clement, *Journal of the American Institute for Conservation* **1983**, *23*, 47-62.

[198] a) L. E. DeLong and G. P. Meisner, *Solid State Communications* **1985**, *53*, 119-123; b) P. Wang, Y. Wang, L. Wang, X. Zhang, X. Yu, J. Zhu, S. Wang, J. Qin, K. Leinenweber, H. Chen, D. He and Y. Zhao, **2016**, *6*, 21787.

[199] O. Tegus, E. Bruck, K. H. J. Buschow and F. R. de Boer, *Nature* **2002**, *415*, 150-152.

[200] X. He, R. Wang, M. C. Stan, E. Paillard, J. Wang, H. Frielinghaus and J. Li, *Advanced Materials Interfaces* **2017**, *4*, 1601047-n/a.

[201] S. T. Oyama, *Journal of Catalysis* **2003**, *216*, 343-352.

[202] a) J. W. Wang, X. H. Liu, S. X. Mao and J. Y. Huang, *Nano Letters* **2012**, *12*, 5897-5902; b) H. Zhu, Z. Jia, Y. Chen, N. Weadock, J. Wan, O. Vaaland, X. Han, T. Li and L. Hu, *Nano Letters* **2013**, *13*, 3093-3100; c) X. Han, Y. Liu, Z. Jia, Y.-C. Chen, J. Wan, N. Weadock, K. J. Gaskell, T. Li and L. Hu, *Nano Letters* **2014**, *14*, 139-147; d) Y. Xu, Y. Zhu, Y. Liu and C. Wang, *Advanced Energy Materials* **2013**, *3*, 128-133; e) Y. Liu, Y. Xu, Y. Zhu, J. N. Culver, C. A. Lundgren, K. Xu and C. Wang, *ACS Nano* **2013**, *7*, 3627-3634; f) J. Liu, Y. Wen, P. A. van Aken, J. Maier and Y. Yu, *Nano Letters* **2014**, *14*, 6387-6392; g) Z. Li, J. Ding and D. Mitlin, *Accounts of Chemical Research* **2015**, *48*, 1657-1665; h) Y. Liu, N. Zhang, L. Jiao, Z. Tao and J. Chen, *Advanced Functional Materials* **2015**, *25*, 214-220.

[203] a) L. Wu, X. Hu, J. Qian, F. Pei, F. Wu, R. Mao, X. Ai, H. Yang and Y. Cao, *Energy & Environmental Science* **2014**, *7*, 323-328; b) Y. Zhu, X. Han, Y. Xu, Y. Liu, S. Zheng, K. Xu, L. Hu and C. Wang, *ACS Nano* **2013**, *7*, 6378-6386; c) H. Hou, M. Jing, Y. Yang, Y. Zhang, Y. Zhu, W. Song, X. Yang and X. Ji, *Journal of Materials Chemistry A* **2015**, *3*, 2971-2977; d) X. Zhou, Z. Dai, J. Bao and Y.-G. Guo, *Journal of Materials Chemistry A* **2013**, *1*, 13727-13731; e) L. Baggetto, E. Allcorn, R. R. Unocic, A. Manthiram and G. M. Veith, *Journal of Materials Chemistry A* **2013**, *1*, 11163-11169; f) J. Liu, L. Yu, C. Wu, Y. Wen, K. Yin, F.-K. Chiang, R. Hu, J. Liu, L. Sun, L. Gu, J. Maier, Y. Yu and M. Zhu, *Nano Letters* **2017**, *17*, 2034-2042.

[204] P. R. Abel, Y.-M. Lin, T. de Souza, C.-Y. Chou, A. Gupta, J. B. Goodenough, G. S. Hwang, A. Heller and C. B. Mullins, *The Journal of Physical Chemistry C* **2013**, *117*, 18885-18890.

[205] a) Y. Kim, Y. Park, A. Choi, N.-S. Choi, J. Kim, J. Lee, J. H. Ryu, S. M. Oh and K. T. Lee, *Advanced Materials* **2013**, *25*, 3045-3049; b) W.-J. Li, S.-L. Chou, J.-Z. Wang, H.-K. Liu and S.-X. Dou, *Nano Letters* **2013**, *13*, 5480-5484; c) J. Qian, X. Wu, Y. Cao, X. Ai and H. Yang, *Angewandte Chemie International Edition* **2013**, *52*, 4633-4636; d) J. Song, Z. Yu, M. L. Gordin, S. Hu, R. Yi, D. Tang, T. Walter, M. Regula, D. Choi, X. Li, A. Manivannan and D. Wang, *Nano Letters* **2014**, *14*, 6329-6335.

[206] a) I. A. Courtney, W. R. McKinnon and J. R. Dahn, *Journal of The Electrochemical Society* **1999**, *146*, 59-68; b) H. Li, L. Shi, W. Lu, X. Huang and L. Chen, *Journal of The Electrochemical Society* **2001**, *148*, A915-A922; c) H. Li, X. Huang, L. Chen, G. Zhou, Z. Zhang, D. Yu, Y. Jun Mo and N. Pei, *Solid State Ionics* **2000**, *135*, 181-191; d) J. Wang, F. Fan, Y. Liu, K. L. Jungjohann, S. W. Lee, S. X. Mao, X. Liu and T. Zhu, *Journal of The Electrochemical Society* **2014**, *161*, F3019-F3024.

[207] J. Mao, X. Fan, C. Luo and C. Wang, *ACS Applied Materials & Interfaces* **2016**, *8*, 7147-7155.

[208] a) C. Stinner, Z. Tang, M. Haouas, T. Weber and R. Prins, *Journal of Catalysis* **2002**, *208*, 456-466; b) J. A. Rodriguez, J.-Y. Kim, J. C. Hanson, S. J. Sawhill and M. E. Bussell, *The Journal of Physical Chemistry B* **2003**, *107*, 6276-6285; c) V. M. L. Whiffen, K. J. Smith and S. K. Straus, *Applied Catalysis A: General* **2012**, *419–420*, 111-125; d) R. Wang and K. J. Smith, *Applied Catalysis A: General* **2009**, *361*, 18-25; e) R. Prins and M. E. Bussell, *Catalysis Letters* **2012**, *142*, 1413-1436.

[209] a) K. A. Kovnir, Y. V. Kolen'ko, S. Ray, J. Li, T. Watanabe, M. Itoh, M. Yoshimura and A. V. Shevelkov, *Journal of Solid State Chemistry* **2006**, *179*, 3756-3762; b) Y. Xie, H. Su, B. Li and Y. Qian, *Materials Research Bulletin* **2000**, *35*, 675-680; c) V. Tallapally, R. J. A. Esteves, L. Nahar and I. U. Arachchige, *Chemistry of Materials* **2016**, *28*, 5406-5414.

[210] a) W. Li, S.-L. Chou, J.-Z. Wang, J. H. Kim, H.-K. Liu and S.-X. Dou, *Advanced Materials* **2014**, *26*, 4037-4042; b) X. Fan, J. Mao, Y. Zhu, C. Luo, L. Suo, T. Gao, F. Han, S.-C. Liou and C. Wang, *Advanced Energy Materials* **2015**, *5*, 1500174-n/a.

[211] Y. Kim, Y. Kim, A. Choi, S. Woo, D. Mok, N.-S. Choi, Y. S. Jung, J. H. Ryu, S. M. Oh and K. T. Lee, *Advanced Materials* **2014**, *26*, 4139-4144.

[212] J. Qian, Y. Xiong, Y. Cao, X. Ai and H. Yang, *Nano Letters* **2014**, *14*, 1865-1869.

[213] Z. Wang, L. Zhou and X. W. Lou, *Advanced Materials* **2012**, *24*, 1903-1911.

Chapter 2: Synergy of Oxygen and Piranha Solution for Eco-Friendly Production of Highly Conductive Graphene Dispersions

2.1. Introduction

Graphene has inspired great enthusiasm for over a decade. Due to its excellent electronic, thermal and mechanical properties along with its exceptionally large surface area and light weight, graphene holds great potential for a wide range of applications.[1] Fundamental studies and high-frequency electronics require pristine graphene.[2] "Bulk" applications such as batteries,[3] super-capacitors,[4] catalysts,[5] flexible macro-electronics,[6] and mechanically reinforced conductive coatings,[7] require large quantities of high-conductive, solution-processable graphene manufactured at low cost. Mass production of conductive and solution processable graphene sheets, such as reduced graphene oxide (r-GO) and graphene nanoplatelets, has been recently achieved.[8] The majority of r-GO sheets have been fabricated *via* rather complex series of chemical processing steps. In brief, graphite particles are first oxidized to graphite oxide (GO) *via* Staudenmaier,[9] Hofmann,[10] Hummers,[11] or Tour's methods,[12] all of which utilize metal containing oxidants, such as $KMnO_4$ and/or $KClO_3$. Trace residues of these oxidants and metal ions used or generated in these approaches can participate in further undesired reactions and can be detrimental to a wide range of applications.[7a, 13] However, purification of GO remains difficult due, among other things, to its tendency to gel. Even though these metal ions are water soluble, the gelation tendency of GO traps them making the GO products highly flammable. [13b] Therefore, extensive cleaning and purification steps are required making industrial scale

production expensive and time-consuming.[12, 14] Thermal exfoliation and deoxygenation of graphite oxide followed by solution dispersion is commonly used to produce large quantities of r-GO.[15] It has been believed that H_2O, CO and CO_2 gases were the only substances released during thermal exfoliation. However, a recent study demonstrated that a wide variety of complex organic molecules can also be released during processing, including alkanes, substituted polycyclic aromatic hydrocarbons, and heterocyclic molecules. The released molecules pose a potential hazard to our environment if not handled properly. Furthermore, the complex organic molecules released from the thermal treatment of GO is highly dependent on the GO fabrication methods and related thermal exfoliation parameters during r-GO fabrication. How to avoid the formation of these complex wastes is a great challenge for graphene industry.[16] The other commonly used approach to generate r-GO is to first exfoliate and disperse the graphene oxide sheets in solutions and then reduce the GO to a level that restores the conductivity of graphene. Even though environmentally friendly reduction protocols are being developed,[17] hydrazine, a hazardous material, is still widely used as the reducing agent. Most importantly, these processes irreparably destroy the ideal honeycomb structure of graphene, leaving only a fraction of the properties of intrinsic graphene to be recovered.[18] Finally, except for those which are sulfonyl-functionalized[19] or reduced in basic solutions,[8a, 20] highly reduced GO sheets cannot be directly dispersed into water which is the most useful and sustainable solvent. These sheets have been dispersed either in some organic solvents with high boiling points, such as N-methyl-pyrrolidone (NMP), or in aqueous solutions with the help of surfactants for stabilization.[20a] Unfortunately, both the organic solvents and the surfactants are difficult to completely remove from a graphene sheet surface without a high

temperature annealing process. Residual solvent and surfactant species inevitably increase contact resistance between individual sheets in graphene films, reducing the overall electrical conductivity of graphene films produced using these chemistries.

Several research groups, including our own have reported that defect-free graphene nanoplatelets can be directly produced from graphite particles and dispersed in NMP and other solvents, or aqueous solutions with the help of surfactants for stabilization.[8c, e, 21] Although the issue of releasing toxic gases was resolved, most of the production requires lengthy sonication and the yield is too low for practical industrial applications. Recently, a more scalable method to produce large-size pristine few-layer graphene was achieved via intercalation of metal containing compounds, followed by an interlayer exfoliation reaction.[8b, 22] These approaches are environmentally friendly and can be used for mass production of large and high quality graphene dispersion in NMP or pyridine, but unfortunately not in aqueous solutions due to the lack of oxygen containing groups on the basal plane of graphene. Therefore the issues associated with high boiling point solvents and trace quantities of metal ions remains.[13b, 23] Il Kwon Oh et al. explored eco-friendly approach to directly produce graphene nanosheets from graphite particles without involving toxic and/or metallic compounds. However, the yield is too low (5%) for practical large scale production. [24]

We recently developed a fast, scalable oxidation approach without involving metallic compounds to directly and controllably produce highly-conductive graphene sheets that can be dispersed in both aqueous and organic solvents without the aid of surfactants.[25] In that work, $KMnO_4$ (as is used in Hummers and Tour's methods) was intentionally excluded while nitronium aromatic oxidation combined with microwave heating (fast and local

heating) were exploited. The unique process leads to a controllable oxidation of randomly positioned carbon atoms across entire graphene sheets, so that a low density of oxygen containing groups were shown to be sufficient for exfoliation and dispersion into aqueous solutions. The dispersed graphene sheets, which we refer to as microwave-enabled low oxygen graphene (ME-LOGr), are highly conductive and do not require further reduction. Unfortunately, the use of nitronium ions results in the release of NO_2, a potentially toxic gas.

The current work aims to develop a more eco-friendly approach which retains the merits of the nitronium oxidation approach, without releasing toxic gases or generating potentially toxic polycyclic aromatic hydrocarbons. This new approach replaces the mixture of H_2SO_4 and HNO_3 and exploits carbon oxidation chemistry by utilizing a piranha solution, a mixture of H_2SO_4 and H_2O_2. Piranha solutions have been widely used in the semiconductor industry and research laboratories to clean silicon, glass, and gold, and they have been used for oxidative cutting of carbon nanotubes (CNTs).[26] The reaction appears to generate only H_2O, O_2, and CO_2, without releasing toxic gases. However, the direct use of piranha solution to oxidize graphite in fabricating large graphene sheets is less efficient than the H_2SO_4/HNO_3 solution. This may be due to the rapid over-oxidation of the surface layers, in part related to the limited ability of the piranha constituents to access the inner graphene layers. This chemistry results in an uncontrolled cutting of graphene sheets at the surface and carbon loss *via* gasification. To solve these problems and to achieve controllable oxidization of each graphene layer, we first prepare a reversible H_2SO_4-graphite intercalation compound (GIC) with the help of $(NH_4)_2S_2O_8$ *via* a simple room temperature process.[27] This is followed by a short period of oxygen purging and

microwave irradiation in a piranha solution **(Scheme 1)**. The synergy of the intercalated oxygen and piranha solution enables controlled oxidation of graphite particles *via* microwave heating and thus leads to rapid (60 seconds) and direct generation of highly conductive low oxygen containing graphene sheets. The intrinsic molecular oxidation mechanism leads to eco-friendly fabrication of highly conductive graphene sheets without generating toxic byproducts, as demonstrated by GC-MS. To differentiate these films to the ME-LOGr we generated previously by nitronium microwave oxidation, we refer to these graphene sheets as eco-friendly, microwave-enabled low-oxygen graphene (Eco-ME-LOGr). The Eco-ME-LOGr sheets are similar to the ME-LOGr, in that they can be dispersed in various solvents, including in aqueous solutions, without needing surfactants for stabilization. The sheets are also highly conductive without requiring a post-reduction step. The conductivity of the as-fabricated Eco-ME-LOGr film is 2.3×10^4 S m^{-1}, the highest value reported for graphene films prepared from solution processable graphene sheets *via* a simple vacuum filtration. After 2-hours of low temperature annealing (300°C), the conductivity reaches 7.4×10^4 S m^{-1}. The electrical performance of the Eco-ME-LOGr films significantly outperformed the ME-LOGr films fabricated *via* nitronium microwave oxidation (6.6×10^3 S m^{-1} for as-prepared films and 1.9×10^4 S m^{-1} after 2-hour annealing at 300°C).[25a]

2.2. Results and Discussion

In a typical experiment, a reversible H_2SO_4-GIC (instead of H_2SO_4-HNO_3 GIC) is first formed by exposing graphite particles to a mixture of sulfuric acid and $(NH_4)_2S_2O_8$, following the recipes suggested by Tour's group.[27] The H_2SO_4-GIC was purged with O_2 for 5 minutes and then subjected to 60 seconds of microwave irradiation (CEM Discover,

300 watts for smaller scale, and Synthwave from Milestone, 900W for larger scale production, **Figure 2.1.**) in a piranha solution. The reaction results in a finely dispersed suspension that is much easier to clean than the paste obtained from Hummer's method.[11] The dispersion was cleaned with water via vacuum filtration to remove residual H_2SO_4, $(NH_4)_2S_2O_8$, and any residual by-products.
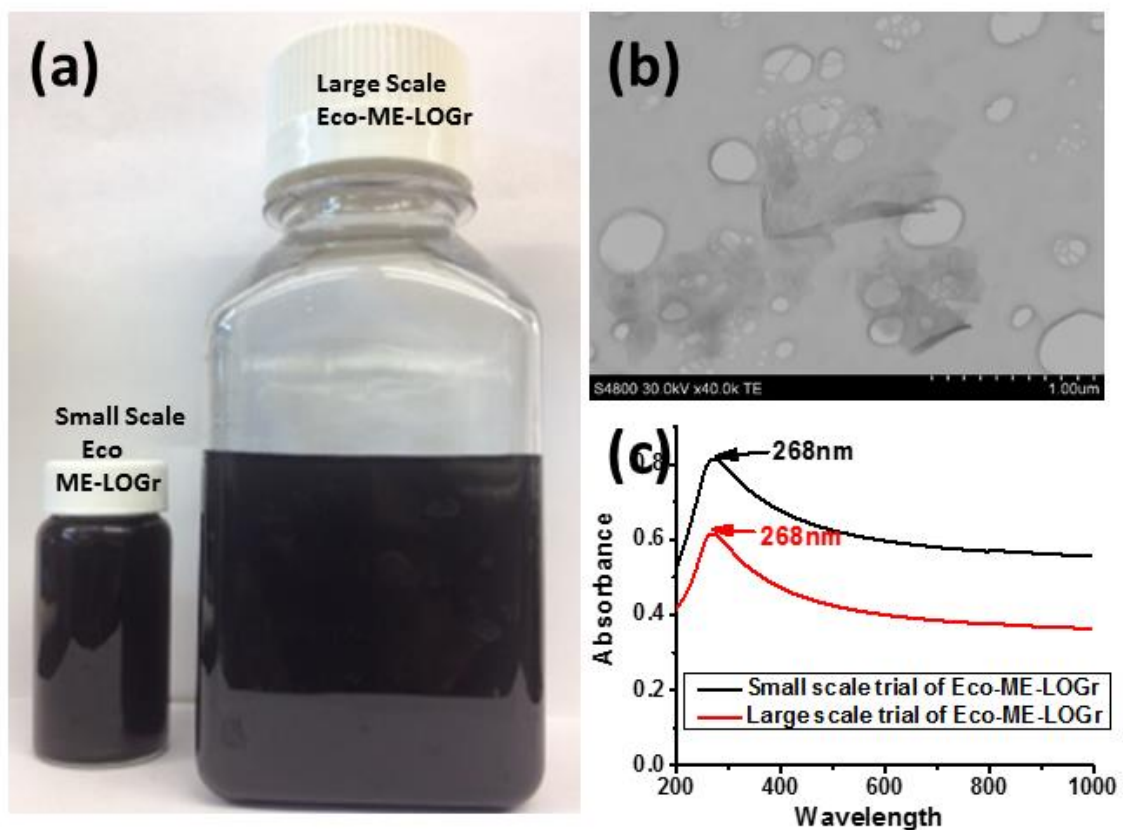
Figure 2.1. (a) Digital photographs of the stable Eco-ME-LOGr dispersions in water from small and larger scale production. (b) A representative STEM image of the graphene sheets from larger scale production achieved via Synthwave from Milestone and (c) UV-Vis-NIR spectra of the Eco-ME-LOGr in water from small and larger scale production.

With the help of bath sonication (30 min), the cleaned filtration cake can be re-dispersed into water to form a colloidal solution without using surfactants or stabilizers. The similar lateral sizes of the graphene sheets, and the overlapping of the two UV-Vis-NIR spectra indicate that similar quality of graphene sheets were obtained, demonstrating that this Eco-

Friendly approach can be easily scaled up for mass production. The lateral size and thickness of the dispersed Eco-ME-LOGr sheets were characterized by a scanning transmission electron microscope (STEM), a scanning electron microscope (SEM), and an atomic force microscope (AFM). The thickness of the Eco-ME-LOGr sheets was found to be 0.7-3 nm, between one and a few layers. The sheets have an average lateral size of one to two micrometers with some as large as tens of micrometers across (**Figure 2.2.**), similar to the ME-LOGr sheets reported earlier.[25a]
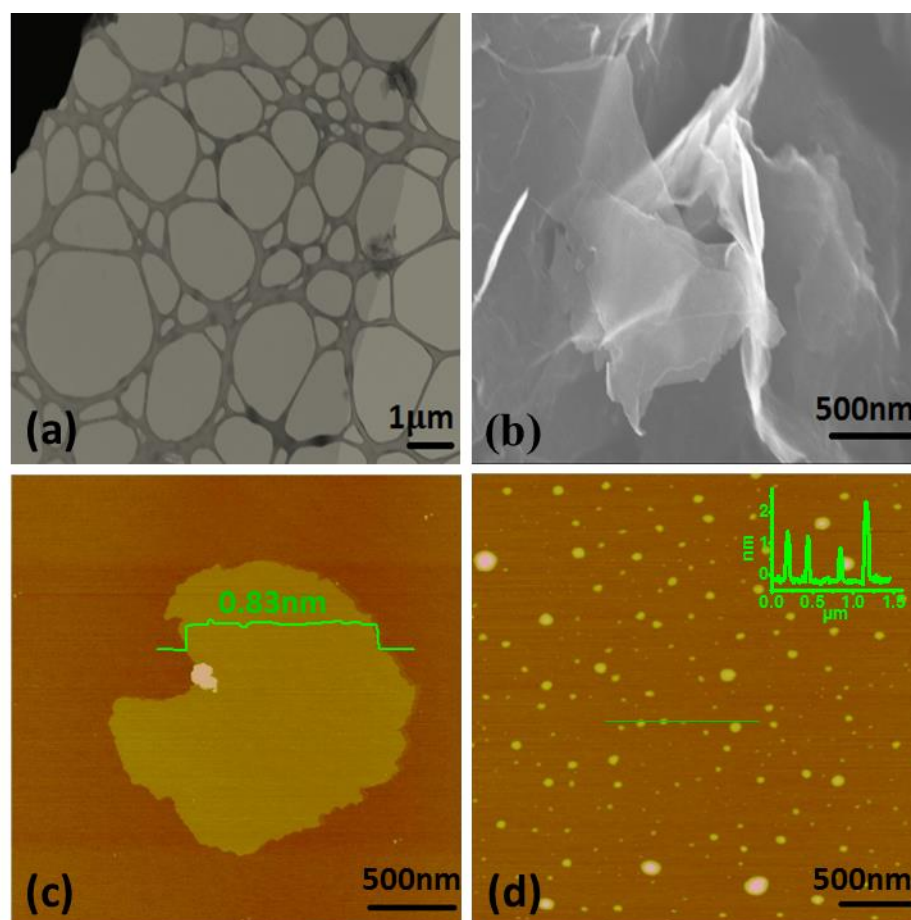
Figure 2.2. A representative STEM, SEM and AFM images of the Eco-ME-LOGr fabricated via 5 min O_2 purging of freshly prepared GIC, followed by 60 seconds microwave irradiation in piranha solution (a-c). Panel d shows an AFM picture of Eco-ME-LOGr sheets fabricated via microwave irradiation of graphite particles in piranha solution.

The color of the Eco-ME-LOGr suspensions is grayish-black. The UV-Vis-near infrared (NIR) spectrum of the Eco-ME-LOGr solution displayed a plasmon band absorption maximum at a much longer wavelength than GO (268 nm vs. 230 nm) and much stronger absorption in the visible and NIR region (**Figure 2.3.a**). All of these characteristics are quite different from the typical brown GO solutions (**Figure 2.3.a, inset**),[8a, 28] yet similar to the previously reported r-GO and ME-LOGr suspensions. These features qualitatively suggest that the as-prepared Eco-ME-LOGr is also similar to the ME-LOGr sheets, containing a large amount of intact graphene domains without requiring a post-reduction procedure.[8a, c, 29]
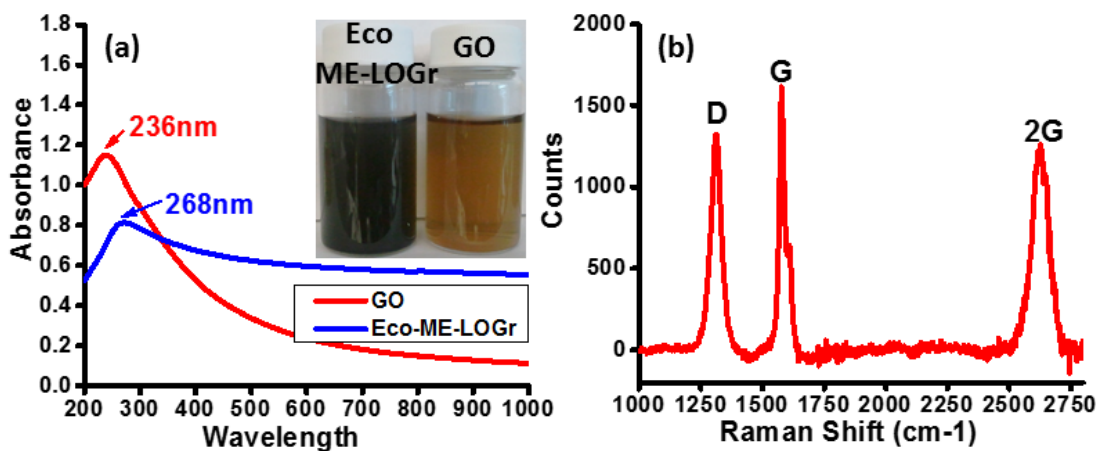
Figure 2.3. (a) Uv-Vis-Near Infrared spectroscopy of the Eco-ME-LOGr and graphene oxide dispersion in water and their digital pictures (Inset). (b) Raman spectroscopy of the Eco-ME-LOGr films on alumina anodic membrane.

Raman spectroscopy was utilized to estimate the size of the intact graphene domains. The typical G band, defect D band and 2D band features are shown in the Raman spectrum of the Eco-ME-LOGr film prepared on an anodic filter membrane *via* vacuum filtration (**Figure 2.3.b**). The intensity ratio of D to G band (I_D/I_G) is 0.75, which is much lower than those of GO and r-GO,[17a, 28] indicating the high quality of the as-produced graphene sheets

by this simple method. Furthermore, the Eco-ME-LOGr sheets also show a strong 2D band, suggesting that these sheets contain little adsorbent-induced surface contamination.[14, 25a]

In addition to water (a common solvent for graphene oxide), the Eco-ME-LOGr sheets can also be dispersed in polar organic solvents such as N-methyl pyrrolidone (NMP) (290 mg/L) and N,N-dimethyl formamide (DMF) (200 mg/L), well known solvents to disperse intrinsic graphene sheets and graphene nanoplatelets. Interestingly, even in a nonpolar solvent such as chloroform, in which neither GO, r-GO, nor graphene platelets can be dispersed, the Eco-ME-LOGr can be dispersed with a concentration of 190 mg/L, ten times higher than that of the ME-LOGr sheets (**Figure 2.4.** and **table 2.1.**).[25a]
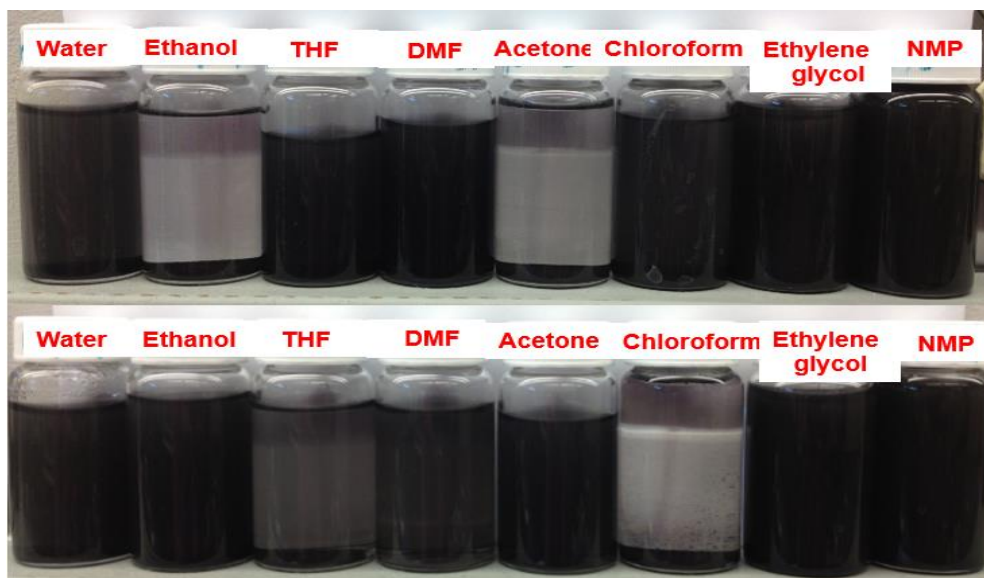
Figure 2.4. Digital pictures of graphene dispersion in different solvents. The dispersions on the top are fabricated via the Eco-friendly approach and the bottom ones were fabricated via nitronium oxidation.

It has been reported that the ability of graphene to be dispersed in various solvents is determined primarily by the surface functionalities of the graphene and Hansen parameters of the solvents. Good dispersibility can be reached when all three Hansen solubility parameters (dispersive, polar, and hydrogen-bonding) of a solvent match well

with those of the graphene.[8c, 30] The high dispersibility in aqueous and organic (both polar and nonpolar) solvents without requiring surfactants or stabilizers implies that the molecular structure (oxygen containing groups, their relative ratio and distribution on the surface) of the Eco-ME-LOGr sheets is quite different from previously reported GO, r-GO, graphene nanoplatelets.[31] On the other hand, ME-LOGr can be nicely dispersed in ethanol and acetone, in which the Eco-ME-LOGr is barely dispersed, indicating differences exist in their surface functionalities.[25a]

Table 2.1. Concentration and production yield of the Eco-ME-LOGr in various solvents.

Solvent	Concentration (mg/ml)	Total weight in the solution	Initial weight(mg)	% yield
Ethylene glycol	0.40	16.1	20	80.6
NMP	0.29	11.4	20	57.2
Water	0.22	10.3	20	51.4
DMF	0.20	8.0	20	40.1
Chloroform	0.19	7.6	20	37.8
THF	0.071	2.8	20	14.2
Acetone	0.026	1.0	20	5.3

The functional groups attached to the Eco-ME-LOGr sheets were studied with X-ray photoelectron spectroscopy (XPS). The C 1s core-level XPS spectrum of Eco-ME-LOGr shows a main peak from oxygen-free carbon and a shoulder resulting from carbon bound to various oxygen species (**Figure 2.5.a.**). The oxygen-free carbon makes up ~76% of the spectrum, similar to that observed for reduced GO sheets[31] and the ME-LOGr sheets

reported previously.[25a] However, the O1s spectrum of Eco-ME-LOGr is different from that of ME-LOGr (**Figure 2.5.b** and **2.5.c**). The main peak in each spectrum was deconvoluted to three or four peaks and their assignment is based on the literature.[32] The peak at 533 eV corresponds to oxygen present as C-O in epoxides, anhydrides, and carboxylic groups (due to the very close overlap in binding energies of these functional groups, it is difficult to distinguish them from each other).
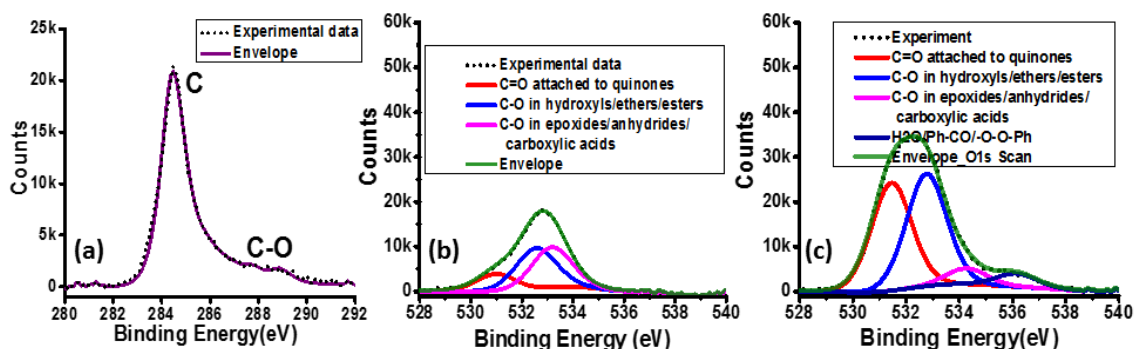
Figure 2.5. XPS spectra of Eco-ME-LOGr films and ME-LOGr films on Au substrates. Panel a and b is C1s and O2p signal from the Eco-ME-LOGr films. The O2p signal, panel c from ME-LOGr film was displayed here for comparison.

The peaks at 532 and 531 eV were assigned to oxygen in hydroxyls and ethers along with carbonyl groups in esters and anhydrides, and oxygen in carbonyl groups attached to aromatic structures (quinone groups), respectively. From **Table 2.2.**, it is apparent that the Eco-ME-LOGr contains much more C-O component in epoxide, anhydrides, and carboxylic groups, while carbonyl groups existed more in the ME-LOGr.

Table 2.2. Different oxygen containing groups in Eco-ME-LOGr and ME-LOGr**.**

Functional groups	Binding energy(eV)	% in Eco-MELOGr	% in MELOGr
C-O in epoxide, anhydrides and carboxylic acids	533	41	6.4

C-O in hydroxyls and ethers, C-O with carbonyl groups in esters and anhydrides	532	42	45.1
C-O in carbonyl groups attached to aromatic structures (quinones)	531	18	43.3
Water	536	0	5.2

The conductivity of the Eco-ME-LOGr sheets was also studied. It has been reported that the conductivity of graphene films formed from graphene dispersions exhibit percolation behavior.[33] The percolation threshold and the conductivity after percolation of graphene films are determined by the conductivity of the individual graphene sheets (itself a function of extent of functionalization as well as structure) and by their electrical connectivity (number of contacts and the contact resistance between individual sheets in the films). Films of different thicknesses from the Eco-ME-LOGr aqueous suspension were prepared by vacuum filtration, a common technique to make relatively uniform films from solution phase graphene sheets.[31b, 34] Under a filtration-induced directional flow, graphene films are formed by stacking and interlocking of the individual sheet together.[31b] After drying in vacuum at room temperature, the average thickness for each film was estimated from the areal density of the films measured with Rutherford Backscattering Spectroscopy.[25a] The sheet resistance of the films was measured with a four-probe approach. As shown in **Figure 2.6. (a)**, the sheet resistance of the Eco-ME-LOGr film decreases with increasing film thickness. The electronic percolation of the Eco-ME-LOGr films is reached at a thickness of ~88 nm, which has a sheet resistance of 0.5 kΩ/square, corresponding to a DC conductivity of 2.3×10^4 S/m. This conductivity is significantly higher than all the chemically reduced GO films reported (see **Table 2.3.**). It should be

noted that the r-GO films listed here were obtained from stable r-GO aqueous suspensions without surfactants, so that their low conductivities are not due to surfactant or solvent effects.[8a, 20] The high quality of the Eco-ME-LOGr (the existence of larger intact graphene domains and fewer defects indicated by the low I_D/I_G ratio and strong 2D band in its Raman spectrum) likely contributes to the observed high conductivity. This conductivity is also significantly higher than the graphene sheets directly exfoliated in NMP and other organic solvents, as well as in aqueous solutions in the presence of surfactants/stabilizers, even though they were known to have lower defect densities.[8c, 21b] The clean surface of Eco-ME-LOGr conveys better electronic communication between individual sheets when they were assembled into a film. Overall, the combination of the high conductivity of individual sheets and low inter-sheet contact resistance leads to the high conductivity of the Eco-ME-LOGr films.

Table 2.3. Electrical conductivity of graphene films prepared via vacuum filtration of different solution phase graphene sheets.

Fabrication techniques	Conductivity(S/m)
Eco-ME-LOGr	22,600
ME-LOGr [42]	6600
Reduced graphene oxide via hydrazine at basic conditions [17,55]	7200
Reduced graphene oxide via hydrazine in the presence of Pyrene derivatives [61]	200
Flash reduced GO [63]	1000
Reduced K-modified reduced GO [36]	690
Sulfonyl modified Reduced Graphene oxide in aqueous [34]	17
Electrochemical reduction of graphene oxide[62]	3500

Reduced GO in variety of organic solvent mixures [35]	1700
Solvothermal reduction of graphene oxide in NMP [14]	374
Graphene nanoplatelets in NMP [19]	5
Graphene nanoplatelets dispersed in aqueous solution via sonication with pyrene derivatives [37]	1900-2150
Graphene nanoplatelets dispersed in aqueous solution via sonication with sodium dodecyl benzene sulfate [38]	35

Thermal annealing has been used to enhance the conductivity of graphene films by evaporating residual solvent/surfactant molecules, and/or thermal deoxygenation of the oxygen containing groups. Upon annealing the Eco-ME-LOGr film at 300°C in Ar for 2 hours, the conductivity was further increased to 7.44×10^4 S m^{-1}, which is significantly higher than similar r-GO films (**table 2.4.**). Although GO films can be directly converted to conductive films via thermal annealing, the electrical conductivity of thermally treated GO films was found to be much lower than comparably annealed r-GO films.[34] Recently, the evolution of carbon bonds in GO films upon thermal annealing has been carefully studied by molecular dynamic simulations and *in situ* spectroscopic techniques (XPS and infrared spectroscopy) as a function of the initial oxygen density in GO films and annealing temperatures.[31a, 35] It was revealed that significant atomic rearrangement has taken place and the GO sheets were substantially disordered after thermal annealing, with the highest initial oxygen content resulting in the most severe distortion. In contrast, thermal annealing improved the ordering of the graphene sheets due to the initial low oxygen concentration of the chemically reduced GO films. It also gave rise to additional deoxygenation of the sheets. The improved ordering and additional deoxygenation in the chemically reduced GO films have been ascribed to the observed higher conductivity than those directly annealed GO films.[20a, 34] It is noteworthy that the conductivity of the annealed Eco-ME-LOGr film

at 300°C is six times higher than the r-GO films annealed at 220°C and two times higher than the r-GO annealed at 500 °C.[34] This result soundly demonstrates that even though the oxygen content is similar to that in r-GO, the high quality (less defective structure) of Eco-ME-LOGr makes it much easier to recover the pristine electronic properties of graphene.

It should also be noted that the conductivity of the Eco-ME-LOGr films outperformed our ME-LOGr films fabricated *via* nitronium microwave oxidation as indicated by: a thinner percolation threshold (88 nm vs. 200 nm), lower sheet resistance at percolation threshold (0.5 vs. 0.76 kΩ/square), which corresponds to the much higher DC conductivity (2.26× 10^4 S/m vs. 6.6× 10^3 S/m) for as-prepared films. After 2-hour annealing at 300°C, the conductivity of the Eco-ME-LOGr films and the ME-LOGr films increased to 7.44× 10^4 S/m vs. 1.92× 10^4 S/m, respectively.[25a]

Table 2.4. Electrical conductivity of graphene films after low temperature thermal annealing.

Graphene dispersion technique	Annealing temperature	Conductivity(S/m)
Eco-ME-LOGr	300 °C for 2hrs with Ar	74,400
ME-LOGr[42]	300 °C for 2hrs with Ar	19,200
Reduced graphene oxide via hydrazine at basic conditions [17,55]	220 °C for 2hrs with Ar	11,800
	500 °C for 2hrs with Ar	35,100
Reduced GO in variety of organic solvent mixures[35]	150 °C for 12hrs	16,000
Solvothermal reduction of graphene oxide in NMP[14]	250 °C for 2hrs	1380
Graphene nanoplatelets in NMP[19]	300 °C for 2hrs with Ar	5000
	250 °C for 2hrs with Ar/H$_2$	6500

We emphasize that not only are the Eco-ME-LOGr films significantly more conductive but also that the chemistry to fabricate these high quality graphene sheets is eco-friendly without releasing toxic gases and generating toxic byproducts. First, we found that the gas released during the reaction is colorless, which is expected as no nitronium ions are involved in the piranha/O_2 oxidation approach. To our surprise, the filtrate was also colorless, which is significantly different from the yellow/brown filtrates obtained from nitronium oxidation (**Figure 2.6.(c), inset**). Gas chromatography-mass spectroscopy (GC-MS) was used to carefully study the composition of the released gas phase and the byproducts in the filtrates collected during cleaning of the microwave oxidized products. The gas phase collected during the microwave oxidation was directly injected to GC-MS. The results show that the majority of the components are O_2 and a small amount of CO_2; no toxic SO_2 and CO were detected. Note that the 28m/z peak is assigned to N_2, not to CO as the GC-MS does not exhibit a strong carbon peak at 12m/z which is characteristic for the CO spectrum.(**Figure 2.6.(b)**).
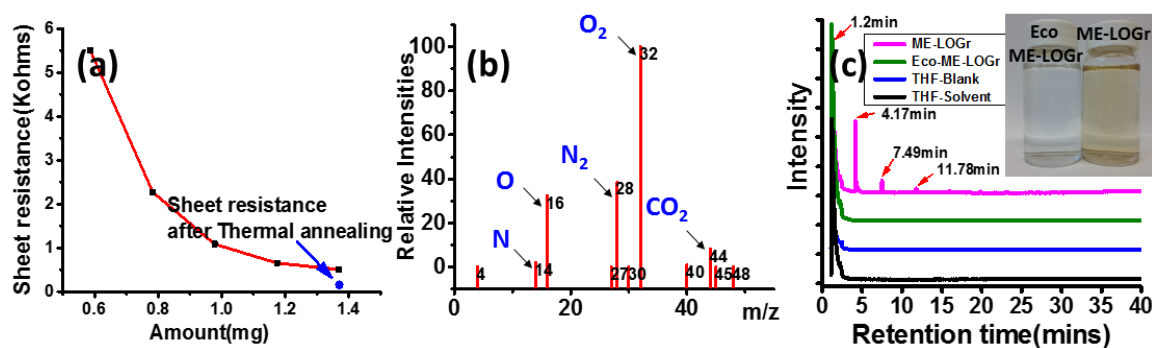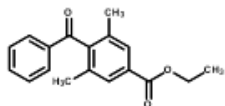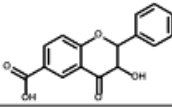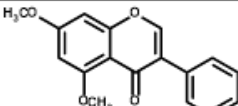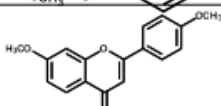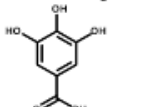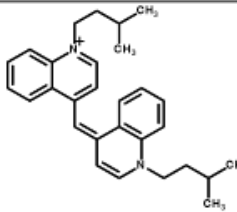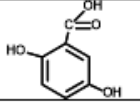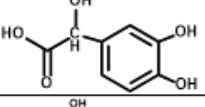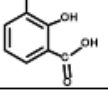
Figure 2.6. Electronic percolation of the Eco-ME-LOGr films prepared by vacuum filtration (a). MS spectrum of the exhausted gas collected during microwave irradiation via the Eco-friendly approach (b). GC spectra of the filtrates collected during cleaning of the microwaved products (c). The curves from top to bottom are for the filtrates from nitronium oxidation, the Eco-friendly approach, and a control experiment via the eco-friendly

74

approach without adding graphite particles during microwave irradiation, and pure THF solvent. Inset: Digital Pictures of the two filtrates.

To study the components in the cleaning filtrates, we first mixed the filtrate with a low boiling point polar organic solvent, such as tetrahydrofuran (THF) before injection. For comparison, the filtrate from nitronium oxidation and a blank solution (obtained by microwave irradiation of the same amount of $(NH_4)_2S_2O_8$ and piranha solution but without graphite particles) were also studied. In **Figure 2.6.(c)**, the chromatogram of the filtrate from nitronium oxidation shows several peaks at retention times of 1.5 min, 4.17min, 7.49min and 11.78 min. The mass spectrum (MS) for each of the peaks was collected and the molecule structures associated with the peaks were identified based on the score (max score is 1.00) of the MS compared to spectra in the mass bank database. The peak at 1.5 min is mainly from THF and the peak at 4.17 min is most likely from flavanol derivatives, while the peaks at 7.49 min and 11.78 min were due to relatively high molecular weight compounds like cyanine or 1,1'-dianthrimide. Detailed molecular structures and their scores are given in **Table 2.5.** In marked contrast, the GC of the filtrate of the piranha oxidation approach is similar to that of the blank solution. Only a peak from the solvent itself (THF) was observed, demonstrating this new piranha/O_2 oxidation approach is indeed eco-friendly without releasing any detectable toxic gases and generating any potentially toxic aromatic byproducts.

Table 2.5. Detailed molecular structures and their score compared to the mass spectra in the mass bank database.

Name	Molecular weight	Mass Bank Score	Structure
Ethyl 4 benzoyl 3,5 dimethyl benzoate	282.126	0.79	
6-Carboxy Flavanol	282.053	0.77	
5,7 dimethyl isoflavone	282.089	0.71	
4',7 dimethoxy isoflavone	282.089	0.66	
Gallic acid	170.02	0.65	
Cyanine	411.280	0.82	
Gentisic acid	156.027	0.82	
3,4 di hydroxy mandelic acid	184.15	0.81	
2,3 dihydroxy benzoic acid	154.12	0.80	

In general, an efficient approach to controllably fabricate graphene sheets from graphite requires the following conditions: (1) enabling the oxidant molecules to access internal surfaces of graphite particles (Due to the strong interaction and close distance between the sheets, only the edges of graphite particles and the exposed graphene surface are readily accessible to oxidants; the rest of the graphene is simply physically blocked

from interacting with the oxidant molecules); [36] (2) ensuring that the reactions proceed in a manner such that oxygen containing groups (or other solubilizing groups) can be evenly (or at least randomly) placed across the graphene to have strong interactions with solvent molecules for dispersion; and (3) generating oxygenated groups in a controlled manner such that the process does not cut the graphene sheets into very small pieces. In addition, the oxidation of each layer of graphene includes several steps: First, oxidation is initiated to create oxygen containing groups, such as -OH and/or epoxy groups, on the basal plane and edges of graphene sheets. Further oxidation includes two simultaneous and competing processes: (i) continuing initiation of oxidation in the intrinsic graphene domains resulting in generation of more -OH and/or epoxy groups; and/or (ii) further oxidation of the already oxidized carbon atoms, ultimately leading to gasification of the carbon atoms (mostly CO or CO_2) and generation of small carbon residual species (which are separated during filtration), resulting in vacancies and holes throughout the graphene basal planes. This process is referred to defect consumption or etching. [26a, 37] Consumption of the defects and generation of vacancies and holes in graphene sheets lead to rapid cutting of the CNTs into short pipes and cutting graphene sheets to small pieces. [26] The relative reaction rates of these processes determine the overall speed of the graphene fabrication and also the lateral sizes and oxidation level of the fabricated graphene sheets.

The molecular mechanism leading to all those different results compared to the nitronium oxidation approach need further study. We hypothesize that it is due to their different intercalation capabilities, initial oxidation mechanisms and the following oxidization pathways (**scheme 2.1.**). The mechanism for nitronium oxidation approach is discussed in detail in our previous reports.[25a] There is no detailed study of the piranha

oxidation mechanism even though it has been used to oxidize and cut carbon nanotubes (CNTs).[26b, 38] [39] It has been proposed that the most likely route by which piranha oxidation occurs is *via* the generation of atomic oxygen, which directly attacks a carbon in a graphene sheet to form a <u>carbonyl</u> group.[40] With the formation of carbonyl groups, the bonds of neighboring carbon atoms get disrupted. With further oxidation, the formed carbonyl group can be converted into CO_2, and simultaneously a new carbonyl group is created on a neighboring carbon atom. Compared to oxidation by nitronium ions, oxidation by piranha solution only generates water, CO_2 and O_2 as byproducts. If H_2SO_4/H_2O_2 can be used to oxidize graphite and fabricate graphene sheets, the issue of releasing toxic gases and aromatics in nitronium involved oxidation approaches will be solved naturally.
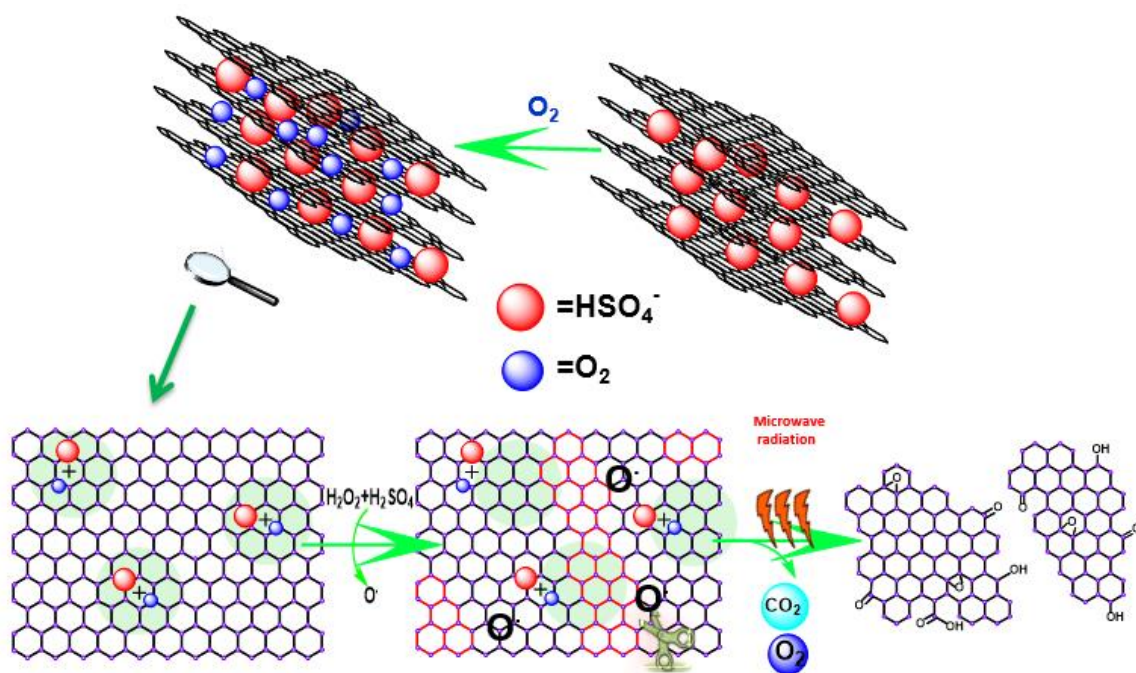
Scheme 2.1. Schematic drawing showing the process and oxidation mechanism of the proposed eco-friendly approach to directly produce highly conductive, low oxygen containing graphene sheets. A reversible H_2SO_4-GIC is formed by exposing graphite particles to a mixture of sulfuric acid and $(NH_4)_2S_2O_8$. The enlarged distance between the individual graphene sheets and the positive charges formed on their surfaces allow the purged molecular oxygen intercalating into the gallery of the graphene sheets in the GIC. Upon microwave irradiation in a piranha solution, the atomic oxygen generated from

piranha and molecular oxygen intercalated inside the GIC synergistically oxidize the graphene sheets both inside and outside of the GIC particles without releasing toxic gases and generating aromatic small molecules as byproducts. This process rapidly generates enough epoxy and other oxygen containing groups, which facilitate exfoliation of highly conductive graphene sheets into water and other solvents without requirement of post-reduction and surfactants for stabilization.

However, our results demonstrated that directly replacing HNO_3/H_2SO_4 with piranha solution to efficiently fabricate conductive graphene in aqueous solution was not successful. The concentration of the dispersed graphene nanosheets is low (0.1 mg/ml). A majority of the graphite particles are precipitated out. This suggests that only small amounts of graphene sheets, which are located on the surface of the graphite particles were oxidized. This result indicates that the atomic oxygen from piranha solution is different from nitronium ions and has limited capability to reach and oxidize the internal sites of the graphite particles. Furthermore, most of the dispersed sheets are smaller than 200 nm, suggesting the oxidized sheets were quickly cut to small pieces (**Figure 2.2. (d)**). It was reported that at room temperature H_2SO_4/H_2O_2 is not able to initiate oxidation of the graphene sidewall of carbon nanotubes, while it has much faster speed to etch away the defects thus, cutting the tubes into small pipes compared to nitronium ions. [26] Even though the capability of H_2SO_4/H_2O_2 to initiate oxidation is increased with the microwave heating (high reaction temperature is achieved), it is very possible that the etching speed increased more dramatically. As a result, the oxidized graphene sheets were quickly cut to small pieces.

To let the oxygen radicals access the inner parts of graphite particles, we thought to take advantage of the enlarged distance between graphene sheets in a graphite intercalation compound (GIC). It was reported that exposing graphite powders to a mixture of $(NH_4)_2S_2O_8$ and H_2SO_4 at room-temperature leads to formation of a reversible sulfuric

acid-based GIC.[27] During GIC formation, positive charges were generated in the graphene sheets, which were balanced with intercalated HSO_4^- ions. Both HSO_4^- ions and H_2SO_4 molecules were intercalated in the interlayer galleries of the GIC. To our surprise, the efficiency of oxidation was just marginally improved, indicated by slightly increased graphene concentration (0.17 mg/ml), while the size of the sheets is still very small (< 200 nm) (**Figure 2.7. (a)**). It was reported that the H_2SO_4-GIC formed from $(NH_4)_2S_2O_8$ is reversible since there were no C-O bonds formed. With water washing, the intercalated HSO_4^- and H_2SO_4 could be quickly de-intercalated.[27] Since the H_2O_2 solution contains 70% of water (by wt), possibly large amount of HSO_4^{2-} and H_2SO_4 were already de-intercalated before the O· radicals reach the inner graphite particles.
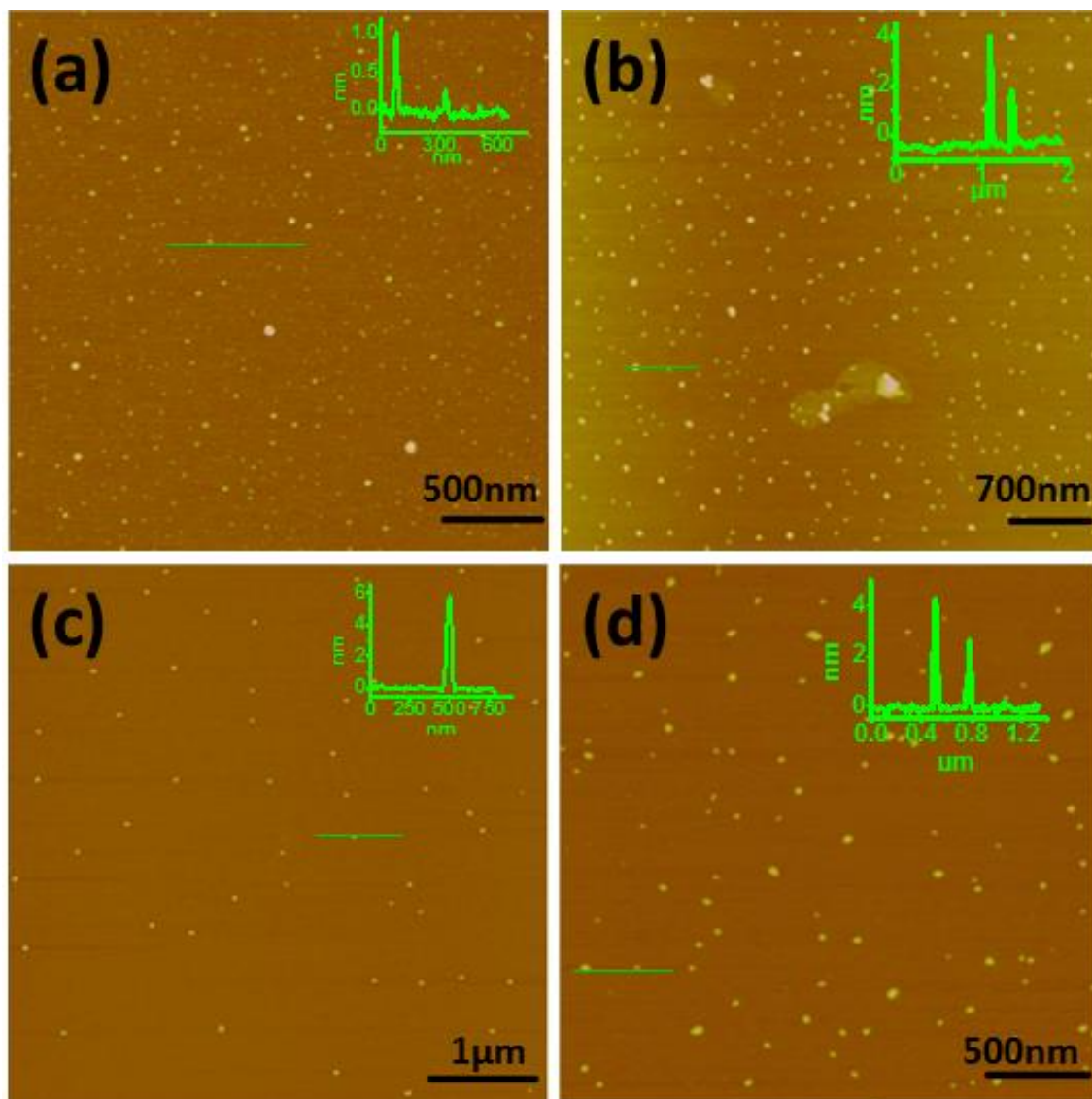
Figure 2.7. AFM images of graphene sheets prepared from fresh GIC without O_2 purging (a); GIC purged with 20 minutes O_2 (b); GIC with 5 minutes O_2 purging, but longer microwave irradiation (75 second, instead of 60 seconds) (c); GIC with 5 minutes O_2 purging with traditional heating instead of microwave heating (d).

To keep the enlarged distance in the GIC for O· radicals internalization, we purged O_2 to the freshly prepared GIC before putting them into piranha solution. We hypothesize the distance between graphene sheets in the GIC is large enough for O_2 intercalation. Further, due to the high electronegativity of O_2, a strong attractive interaction between O_2 and the positive charges on the graphene sheets exists, which would facilitate O_2 intercalation and prevent its de-intercalation when the GIC is exposed to an aqueous environment. To study

81

if purging O_2 would help to stabilize the GIC against de-intercalation, we compared the weight of the GICs with and without O_2 purging after water cleaning. The weight of the GIC with O_2 purging remained larger extents compared to the one without experiencing O_2 purging supporting our assumption (**Table 2.6.**). Therefore, it is very likely that the larger distances between graphene sheets in the GIC are largely remained compared to those without O_2 purging. Accordingly, oxidation of both internal and external graphene sheets in a graphite particle is expected upon addition of piranha solution and followed by microwave irradiation.

Table 2.6. Weights of Graphite and GICs with/ and without purging with 5 min of O_2 after washing with water.

Reaction mixtures	Initial weight (mg)	Weight after washing (mg)
Fresh GIC	40.1	40.2
Fresh GIC purged with O_2	40	41.6

Furthermore, it was reported that trace amounts of C-O bonds were detected after keeping the reversible GIC in its parent $(NH_4)_2S_2O_8$-H_2SO_4 solution at ambient conditions for seven days.[27] Molecular level understanding of the chemical reaction of reversible GIC with oxygen in highly acidic solution has not been extensively studied. We hypothesize that O_2 in air may intercalate and absorb around the positive charges, an electron/oxygen transfer reaction between the absorbed molecular oxygen and the positively charged graphene may occur, gradually generating a few epoxy groups, similar scenario as the nitronium ion intercalated GIC.[25a] Considering higher concentration of O_2 may be intercalated into the galleries of GIC with pure O_2 purging, and the rapidly increased temperature *via* microwave heating, multiple oxygen containing groups can be

efficiently generated not only along the edges, but also across the basal plane of graphene sheets *via* oxygen transfer reactions.[41] The synergy of intercalated oxygen and piranha may lead to increased speed in generating oxygen-containing groups relatively to the cutting speed. Therefore, higher graphene production yield and less carbon loss are expected. Indeed, not only the concentration of graphene sheets is increased, very importantly the lateral sizes of the graphene sheets are also increased dramatically (**Figure 2.2**).

A control experiment was performed by directly microwave heating the O_2 purged GIC without adding piranha solution. The results demonstrated that relatively larger graphene sheets were obtained compared to those obtained *via* piranha oxidation of GIC without O_2 purging. However, the obtained graphene sheets are much thicker while having smoother edges compared to the ones obtained in the presence of piranha solution. We should also mention that purging O_2 directly to a mixture of H_2SO_4/graphite particles did not produce large graphene sheets presumably due to the small distance between graphene sheets in graphite particles for O_2 intercalation. Furthermore, since there are no positive charges on graphene sheets in pristine graphite particles, there is no driving force for O_2 to internalize without forming a GIC in the first place. On the other hand, however, purging O_2 for longer times with piranha solution and/or increasing the microwave irradiation time caused a significant decrease in the lateral sizes of the graphene sheets, or even more carbon loss, possibly due to over-oxidation induced cutting and etching (**Figure 2.8.**).[26a]
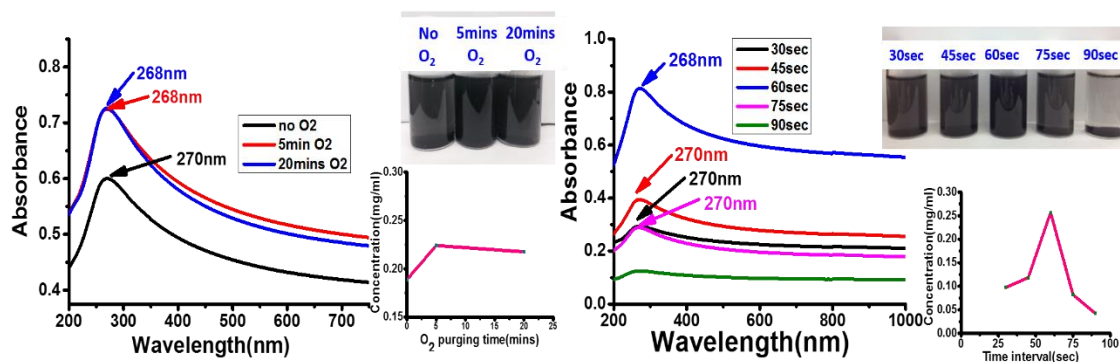
Figure 2.8. UV-Vis spectra and digital pictures of the dispersed graphene solution to show the yield of the products depends on the O_2 purging time with the same microwave power (300 W)(a) and the effect of microwave irradiation time with the same microwave power (300 W) (b). With 60 second of irradiation, the concentration of the dispersed graphene sheets reached the maximum.

In addition, the size and yield of the graphene sheets also depend on the ratio of H_2O_2/H_2SO_4 and the microwave power. Increasing the ratio of H_2O_2/H_2SO_4 and decreasing the microwave power results in deficient oxidation. Most of the graphite particles precipitate out (**Figure 2.9.**).
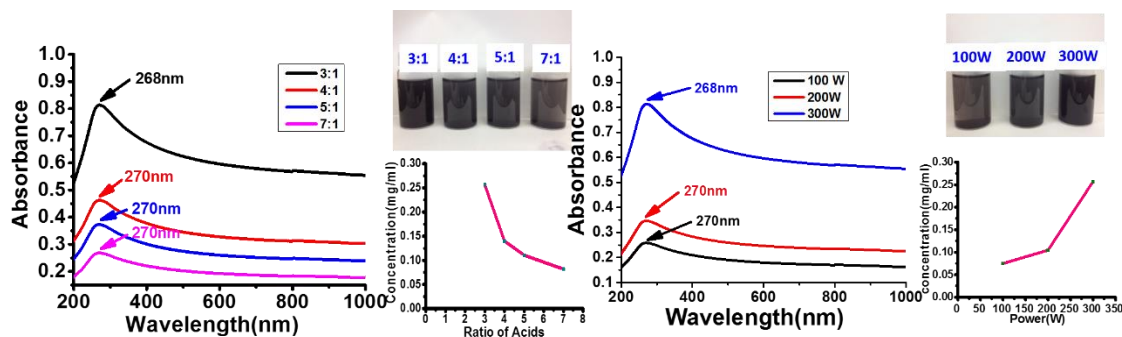
Figure 2.9. UV-Vis spectra and digital pictures of the dispersed graphene solution to show the yield of the products depends on the ratio of H_2SO_4 to H_2O_2 of the piranha solutions, with 3:1 ratio giving the highest production yield (Microwave irradiation time 60 seconds and microwave power of 300 W)(a). UV-Vis spectra and digital pictures of the dispersed graphene solution to show the yield of the products depends on the microwave power (b).

Finally, due to the different molecular oxidation mechanisms and their different kinetics in the initiation and the following oxidation pathways, we found the role of microwave heating in these two approaches also slightly changed. In nitronium oxidation

84

approach, microwave heating enables direct production of highly conductive graphene sheets without the requirement of post reduction process, while traditional heating results in nonconductive graphene oxide nanosheets. On the contrary, both traditional heating and microwave heating lead to highly conductive graphene sheets via the piranha/O_2 oxidation chemistry. The graphene sheets produced via microwave heating are much larger (several µm's) than the ones from traditional heating (< 200 nm) (**Figure 2.7. (d)**).

2.3. Conclusion

In summary, by formation of reversible GIC, the distance between graphene sheets is increased simultaneously with the generation of positive charges on the graphene sheets, which provides enough space and imparts a strong attractive driving force for O_2 intercalation. The interaction between the positive charges and O_2 also helps stabilizing the intercalated O_2 and HSO_4^- ions against de-intercalation upon introduction of the piranha solution. The existence of the intercalated O_2 not only maintains the distance for piranha to access and oxidize the inner parts of graphite particles, but also acts as a mild oxidant to generate more oxygen containing groups on the graphene sheets which facilitate graphene sheets dispersion into aqueous solutions. The synergy of the piranha generated oxygen radicals, the intercalated O_2 and microwave heating enables rapid (60 seconds), direct and controllable fabrication of highly conductive graphene sheets of different lateral sizes without requiring post reduction procedure. The intrinsic oxidation mechanism of this new approach determines that no small aromatic toxic molecules are generated thus, without the release of toxic gas. Finally, the unique microwave heating not only dramatically speeds up the fabrication process but also facilities larger graphene sheets production compared to those utilizing traditional heating. Collectively, this approach has the following

advantages for mass production of high quality graphene dispersions: (1) eco-friendly, no toxic agents are involved, no toxic gas and potentially toxic aromatic byproducts are released and generated; (2) Rapid and low energy consuming fabrication process (3) direct production of graphene sheets of different lateral sizes without the requirement for a post-reduction process. All these sheets as fabricated have a lower level of oxygen-containing groups, which ensures substantial reservation of the outstanding electrical and optical properties without the need for a high temperature annealing process;[31a] (4) high-concentration dispersions both in aqueous and organic solvents (without requiring polymeric or surfactant stabilizers) allows a "clean" graphene surface to be obtained; (5) reduced waste from purification steps; (6) since only $(NH_4)_2S_2O_8$, O_2, H_2SO_4 and H_2O_2 are used for the production, the byproducts are essentially $(NH_4)_2SO_4$, and diluted H_2SO_4, which can be reused to produce more $(NH_4)_2SO_4$ as soil fertilizers. All these advantages ensure mass production of high quality graphene dispersions with low environmental footprints and at a much lower-cost.

2.4. Experimental Method

2.4.1. Material synthesis

The Synthetic Graphite powder (size ≤20μm) and ammonium persulfate (reagent grade 98%) were obtained from Sigma Aldrich. The concentration of sulfuric acid used is 98% and is obtained from Pharmaco Aaper. The H_2O_2 is a laboratory grade solution with a concentration of wt 35% obtained from BDH. All the chemicals were used as received. The extra dry grade O_2 is used for O_2 purging. The small-scale graphene synthesis was conducted *via* CEM discover microwave vessel whereas the large scale synthesis is

conducted *via* Synthwave from Milestone. Dispersion of the microwaved graphite powers to graphene sheets into various solvents was performed *via* 5210 bath sonicator.

Eco-friendly approach for fabrication of graphene sheets

Graphite intercalation compound with SO_4^{2-} is achieved by following the recipe process described by Tour et al. [27] In brief, 1000mg of ammonium persulfate $[(NH_4)_2S_2O_8]$ was dissolved in 10ml H_2SO_4. The obtained mixture solution was stirred for 5-10 mins and then 200mg of Graphite powder was added. The obtained mixture was stirred for 24hrs, which led to the formation of Graphite Intercalation Compound (reversible SO_4^{2-}-GIC). To the GIC-SO_4 solution, oxygen is purged for 5mins at a rate of 79-84 ml/min. 1ml of the O_2 purged GIC-SO_4 solution is taken and mixed with 9ml of Piranha solution (H_2SO_4: H_2O_2 = 3:1), which is microwaved at 300W for 60sec. The reaction is initially quenched with 200ml deionized water. The obtained slurry was washed *via* vacuum filtration through a polycarbonate membrane with a pore size of 0.8µm with 200ml water each for four times. The final product is dispersed in 40ml deionized water by sonication in a bath sonicator for 30mins. The solution is allowed to settle for 3-5days and the supernatant solution obtained contains large graphene sheets. The filtrate was collected and then extracted with THF to study the byproducts *via* gas chromatography-mass spectrometry (GC-MS)

To demonstrate that this approach can be scaled up for mass production, 10ml of graphite intercalated solution, which is purged with O_2 for 5mins, is taken and to it add 90ml of Piranha solution (H_2SO_4: H_2O_2- 3:1) and microwave at 900W for 60sec with synthwave from Milestone. The quenching and cleaning of the product is similar to the small scale fabrication. The microwave enabled nitronium oxidation approach of graphene synthesis is conducted according to the procedure described in our previous work.[25a]

However the starting material is the graphite intercalated compound. The traditional heating of the piranha trial is conducted by heating 1ml of O_2 purged GIC with 9ml of Piranha solution at 100°C for 7hrs and then quenching the reaction mixture with 200ml deionized water and washing it with 200ml water each for four times.

2.4.2. Material characterization

Surface Morphology: The surface morphology of our as fabricated product is characterized by an Atomic force Microscopy using a Nanoscope IIIa multimode SPM (Digital instruments) operated in "Tapping mode" and Scanning Electron Microscopy (SEM) and scanning Transmission Electron Microscopy (STEM) using a Hitachi S-4800 Field Emission Scanning Electron Microscope (FE-SEM, Hitachi Co.Ltd.). The functional groups information was acquired using a thermo scientific Kα system with a monochromatic Al Kα X-ray source (hv=1486.7ev) in XPS. The quality of the graphene sheets were analyzed using a Raman spectra with a Kaiser Optical Systems Raman Microprobe.

Optical and Electronic properties: The optical properties of the graphene dispersions were measured by the UV-VIS NIR spectroscopy from Cary-5000 Ultra violet-Visible-Near Infrared Spectroscopy operated in double beam with 200-1000nm wavelength range. As for the electronic properties assessment, the sheet resistance is measured by a manual four-point resistivity probe from Lucas Laboratories, model 302. The conductivity of the films is calculated from the sheet resistance and thickness by the formula:

$$\text{Conductivity} = \frac{1}{Sheet\ resistance \times thickness}$$

Rutherford back scattering (RBS) was performed to calculate the thickness of the film to obtain the conductivity of the as prepared graphene film, using a 2 MeV He2+ ion beam produced in a tandem accelerator with an ion current of 2–3 nA. Spectra were collected in the back scattering geometry and simulations were performed using the SIMNRA program.

Gas Chromatography-Mass Spectrometry (GC-MS). The gas evolved and the filtrate during the reaction process is carefully collected and analyzed using an Agilent HP6890 system, which was equipped with a HP-5-MS capillary column.

2.5. References

[1] a) K. S. Novoselov, V. I. Fal'ko, L. Colombo, P. R. Gellert, M. G. Schwab and K. Kim, *Nature* **2012**, *490*, 192-200; b) F. Bonaccorso, A. Lombardo, T. Hasan, Z. Sun, L. Colombo and A. Ferrari, *Materials Today* **2013**, *15*, 564-589.

[2] Y. Q. Wu, Y. M. Lin, A. A. Bol, K. A. Jenkins, F. N. Xia, D. B. Farmer, Y. Zhu and P. Avouris, *Nature* **2011**, *472*, 74-78.

[3] a) K. Han, J. M. Shen, C. M. Hayner, H. Q. Ye, M. C. Kung and H. H. Kung, *Journal of Power Sources* **2014**, *251*, 331-337; b) L. L. Jiang and Z. J. Fan, *Nanoscale* **2014**, *6*, 1922-1945; c) H. Kim, H. D. Lim, J. Kim and K. Kang, *Journal of Materials Chemistry A* **2014**, *2*, 33-47; d) A. H. Li, J. Q. Liu and S. Y. Feng, *Science of Advanced Materials* **2014**, *6*, 209-234; e) N. Mahmood, C. Z. Zhang, H. Yin and Y. L. Hou, *Journal of Materials Chemistry A* **2014**, *2*, 15-32.

[4] Z. J. Jiang, Z. Q. Jiang and W. H. Chen, *Journal of Power Sources* **2014**, *251*, 55-65.

[5] a) Y. Zhu, S. Murali, M. D. Stoller, K. J. Ganesh, W. Cai, P. J. Ferreira, A. Pirkle, R. M. Wallace, K. A. Cychosz, M. Thommes, D. Su, E. A. Stach and R. S. Ruoff, *Science* **2011**, *332*, 1537-1541; b) Z. Jin, W. Lu, K. J. O'Neill, P. A. Parilla, L. J. Simpson, C. Kittrell and J. M. Tour, *Chemistry of Materials* **2011**, *23*, 923-925.

[6] a) G. Eda and M. Chhowalla, *Advanced Materials* **2010**, *22*, 2392-2415; b) P. H. Wobkenberg, G. Eda, D. S. Leem, J. C. de Mello, D. D. C. Bradley, M. Chhowalla and T. D. Anthopoulos, *Advanced Materials* **2011**, *23*, 1558-1562.

[7] a) S. Dubin, S. Gilje, K. Wang, V. C. Tung, K. Cha, A. S. Hall, J. Farrar, R. Varshneya, Y. Yang and R. B. Kaner, *ACS Nano* **2010**, *4*, 3845-3852; b) S. Stankovich, D. A. Dikin, G. H. B. Dommett, K. M. Kohlhaas, E. J. Zimney, E. A. Stach, R. D. Piner, S. T. Nguyen and R. S. Ruoff, *Nature* **2006**, *442*, 282-286; c) T. Ramanathan, A. A. Abdala, S. Stankovich, D. A. Dikin, M. Herrera-Alonso, R. D. Piner, D. H. Adamson, H. C. Schniepp, X. Chen, R. S. Ruoff, S. T. Nguyen, I. A. Aksay, R. K. Prud'homme and L. C. Brinson, *Nature Nanotechnology* **2008**, *3*, 327-331.

[8] a) D. Li, M. B. Muller, S. Gilje, R. B. Kaner and G. G. Wallace, *Nature Nanotechnology* **2008**, *3*, 101-105; b) X. Geng, Y. G. Guo, D. Li, C. Zhu, X. Wei, M. N. Chen, S. Gao, S. Qiu, Y. Gong, L. Wu, M. Long, M. Sun, G. Pan and L. Liu, *Science Reports* **2013**, *3*, 1134; c) Y. Hernandez, V. Nicolosi, M. Lotya, F. M. Blighe, Z. Y. Sun, S. De, I. T. McGovern, B. Holland, M. Byrne, Y. K. Gun'Ko, J. J. Boland, P. Niraj, G. Duesberg, S. Krishnamurthy, S. Goodhue, J. Hutchison, V. Scardaci, A. C. Ferrari and J. N. Coleman, *Nature Nanotech.* **2008**, *3*, 563 - 568; d) D. Yang, A. Velamakanni, G. Bozoklu, S. Park, M. Stoller, R. D. Piner, S. Stankovich, I. Jung, D. A. Field, C. A. Ventrice and R. S. Ruoff, *Carbon* **2009**, *47*, 145-152; e) K. R. Paton, E. Varrla, C. Backes, R. J. Smith, U. Khan, A. O'Neill, C. Boland, M. Lotya, O. M. Istrate, P. King, T. Higgins, S. Barwich, P. May, P. Puczkarski, I. Ahmed, M. Moebius, H. Pettersson, E. Long, J. Coelho, S. E. O'Brien, E. K. McGuire, B. M. Sanchez, G. S. Duesberg, N. McEvoy, T. J. Pennycook, C. Downing, A. Crossley, V. Nicolosi and J. N. Coleman, *Nat Mater* **2014**, *13*, 624-630.

[9] L. Staudenmaier, *Berichte Der Deutschen Chemischen Gesellschaft* **1898**, *31*, 1481-1487.

[10] U. Hofmann and E. Konig, *Z. Anorg. Allg. Chem.* **1937**, *234*, 311.

[11] W. S. Hummers and R. E. Offeman, *J. Am. Chem. Soc.* **1958**, *80*, 1339-1339

[12] D. C. Marcano, D. V. Kosynkin, J. M. Berlin, A. Sinitskii, Z. Z. Sun, A. Slesarev, L. B. Alemany, W. Lu and J. M. Tour, *ACS Nano* **2010**, *4*, 4806-4814.

[13] a) S. J. You, S. M. Luzan, T. Szabo and A. V. Talyzin, *Carbon* **2013**, *52*, 171-180; b) F. Kim, J. Y. Luo, R. Cruz-Silva, L. J. Cote, K. Sohn and J. X. Huang, *Advanced Functional Materials* **2010**, *20*, 2867-2873.

[14] I. K. Moon, J. Lee, R. S. Ruoff and H. Lee, *Nat Commun* **2010**, *1*, 73.

[15] a) H. C. Schniepp, J. L. Li, M. J. McAllister, H. Sai, M. Herrera-Alonso, D. H. Adamson, R. K. Prud'homme, R. Car, D. A. Saville and I. A. Aksay, *Journal of Physical Chemistry B* **2006**, *110*, 8535-8539; b) M. J. McAllister, J. L. Li, D. H. Adamson, H. C. Schniepp, A. A. Abdala, J. Liu, M. Herrera-Alonso, D. L. Milius, R. Car, R. K. Prud'homme and I. A. Aksay, *Chemistry of Materials* **2007**, *19*, 4396-4404.

[16] Z. Sofer, P. Simek and M. Pumera, *Physical Chemistry Chemical Physics* **2013**, *15*, 9257-9264.

[17] a) I. K. Moon, J. Lee, R. S. Ruoff and H. Lee, *Nature Communications* **2010**, *1*; b) C. Z. Zhu, S. J. Guo, Y. X. Fang and S. J. Dong, *ACS Nano* **2010**, *4*, 2429-2437; c) H.-L. Guo, X.-F. Wang, Q.-Y. Qian, F.-B. Wang and X.-H. Xia, *ACS Nano* **2009**, *3*, 2653-2659; d) J. Chen, B. Yao, C. Li and G. Shi, *Carbon* **2013**, *64*, 225-229; e) N. Liu, F. Luo, H. Wu, Y. Liu, C. Zhang and J. Chen, *Advanced Functional Materials* **2008**, *18*, 1518-1525.

[18] A. K. Geim, *Science* **2009**, *324*, 1530-1534.

[19] Y. C. Si and E. T. Samulski, *Nano Letters* **2008**, *8*, 1679-1682.

[20] a) S. Park, J. H. An, I. W. Jung, R. D. Piner, S. J. An, X. S. Li, A. Velamakanni and R. S. Ruoff, *Nano Letters* **2009**, *9*, 1593-1597; b) S. Park, J. H. An, R. D. Piner, I. Jung, D. X. Yang, A. Velamakanni, S. T. Nguyen and R. S. Ruoff, *Chemistry of Materials* **2008**, *20*, 6592-6594.

[21] a) M. Zhang, R. R. Parajuli, D. Mastrogiovanni, B. Dai, P. Lo, W. Cheung, R. Brukh, P. L. Chiu, T. Zhou, Z. F. Liu, E. Garfunkel and H. X. He, *Small* **2010**, *6*, 1100-1107; b) M. Lotya, Y. Hernandez, P. J. King, R. J. Smith, V. Nicolosi, L. S. Karlsson, F. M. Blighe, S. De, Z. Wang, I. T. McGovern, G. S. Duesberg and J. N. Coleman, *J. Am. Chem. Soc.* **2009**, *131*, 3611-3620

[22] K. H. Park, B. H. Kim, S. H. Song, J. Kwon, B. S. Kong, K. Kang and S. Jeon, *Nano Letters* **2012**, *12*, 2871-2876.

[23] a) A. C. Jachak, M. Creighton, Y. Qiu, A. B. Kane and R. H. Hurt, *Mrs Bulletin* **2012**, *37*, 1307-1313; b) V. C. Sanchez, A. Jachak, R. H. Hurt and A. B. Kane, *Chemical Research in Toxicology* **2012**, *25*, 15-34.

[24] V. Sridhar, J.-H. Jeon and I.-K. Oh, *Carbon* **2010**, *48*, 2953-2957.

[25] a) P. L. Chiu, D. Mastrogiovanni, D. Wei, C. Louis, M. Jeong, G. Yu, P. Saad, C. R. Flach, R. Mendelsohn, E. Garfunkel and H. X. He, *J. Am. Chem. Soc.* **2012**, *134*, 5850-5856; b) M. A. Patel, H. Yang, P. L. Chiu, D. Mastrogiovanni, C. R. Flach, K. Savaram, L. Gomez, A. Hemnarine, R. Mendelsohn, E. Garfunkel, H. Jiang and H. X. He, *Acs Nano* **2013**, *7*, 8147-8157.

[26] a) K. J. Ziegler, Z. N. Gu, H. Q. Peng, E. L. Flor, R. H. Hauge and R. E. Smalley, *J. Am. Chem. Soc.* **2005**, *127*, 1541; b) J. Liu, A. G. Rinzler, H. J. Dai, J. H. Hafner, R. K. Bradley, P. J. Boul, A. Lu, T. Iverson, K. Shelimov, C. B. Huffman, F. Rodriguez-Macias, Y. S. Shon, T. R. Lee, D. T. Colbert and R. E. Smalley, *Science* **1998**, *280*, 1253-1256.

[27] A. M. Dimiev, S. M. Bachilo, R. Saito and J. M. Tour, *Acs Nano* **2012**, *6*, 7842-7849.

[28] V. T. Tung, M. J. Allen, Y. Yang and R. B. Kaner, *Nature Nanotech.* **2009**, *4*, 25-29.

[29] H. A. Becerril, J. Mao, Z. F. Liu, R. M. Stoltenberg, Z. Bao and Y. S. Chen, *ACS Nano* **2008**, *2*, 463–470.

[30] Y. Hernandez, M. Lotya, D. Rickard, S. D. Bergin and J. N. Coleman, *Langmuir* **2010**, *26*, 3208-3213.

[31] a) A. Bagri, C. Mattevi, M. Acik, Y. J. Chabal, M. Chhowalla and V. B. Shenoy, *Nature Chemistry* **2010**, *2*, 581-587; b) G. Eda, G. Fanchini and M. Chhowalla, *Nature Nanotech.* **2008**, *3*, 270-274.

[32] B. Frank, A. Rinaldi, R. Blume, R. Schlogl and D. S. Su, *Chemistry of Materials* **2010**, *22*, 4462-4470.

[33] G. E. Pike and C. H. Seager, *Phys. Rev. B* **1974**, *10*, 1421-1434.

[34] H. Chen, M. B. Muller, K. J. Gilmore, G. G. Wallace and D. Li, *Advanced Materials* **2008**, *20*, 3557-3561.

[35] A. Bagri, R. Grantab, N. V. Medhekar and V. B. Shenoy, *Journal of Physical Chemistry C* **2010**, *114*, 12053-12061.

[36] A. M. Dimiev and J. M. Tour, *Acs Nano* **2014**, *8*, 3060-3068.

[37] T. H. Han, Y. K. Huang, A. T. L. Tan, V. P. Dravid and J. X. Huang, *Journal of the American Chemical Society* **2011**, *133*, 15264-15267.

[38] H. M. (Skip) Kingston and S. J. Haswell in *Microwave-Enhanced Chemistry: Fundamentals, Sample Preparation, and Applications*, *Vol.* American chemical society, Washington DC, **1997**.

[39] J. Zhang, H. L. Zou, Q. Qing, Y. L. Yang, Q. W. Li, Z. F. Liu, X. Y. Guo and Z. L. Du, *Journal of Physical Chemistry B* **2003**, *107*, 3712-3718.

[40] Wikipedia, **2014**.

[41] a) J. F. de Queiroz, J. W. D. Carneiro, A. A. Sabino, R. Sparrapan, M. N. Eberlin and P. M. Esteves, *Journal of Organic Chemistry* **2006**, *71*, 6192-6203; b) P. M. Esteves, J. W. D. Carneiro, S. P. Cardoso, A. G. H. Barbosa, K. K. Laali, G. Rasul, G. K. S. Prakash and G. A. Olah, *Journal of the American Chemical Society* **2003**, *125*, 4836-4849.

Chapter 3- Dry Microwave Chemistry for Scalable Fabrication of Pristine Holey Graphene Rich in Zigzag Edges and their Catalytic Activity

3.1. Introduction

Holey graphene, referred to graphene with nanoholes in their basal planes, recently attracted increasing research interests from both fundamental and practical application points of view [1]. Different from porous graphene, in which the porous structures are formed by creating physical spaces between intact graphene sheets, holey graphene is synthesized by etching through the graphene sheets to form holes in their basal planes. For practical applications, graphene is usually used as bulk 3D materials with graphene sheets randomly assembled together [2]. The existence of nanoholes in bulk 3D materials assembled from holey graphene not only increase accessible surface area, but also provides desired "short-cuts" for efficient mass transport across graphene planes and ultimate access to inner surfaces, which is very different from the intrinsic perfect graphene sheets without holes[3]. Most importantly, generating nanoholes naturally transforms a large number of in-plane atoms into edge atoms. It has been theoretically predicted and experimentally demonstrated that the edges of graphene sheets have different electronic states and chemical functionalities from their basal planes, which render them unique molecule and ionic absorption capability, dramatically increased quantum capacitance and electrochemical double layer capacitances. Recent years have witnessed wide applications

93

of holey graphene in gas storage/separation, oil absorption, photonic devices, catalysis, sensing, electrochemical energy generation and storage.

Furthermore, if these edge atoms are arranged to form zigzag edges, nonbonding π-electrons emerge on these edge atoms and couple with itinerant π-carriers [4]. It was reported that these electrons are localized along exterior zigzag edges and strongly spin-polarized, which have been referred to as π-electronic spin-polarized states, or Fujita states [4]. The existence of Fujita states has been the foundation to explain experimentally observed exotic electronic and magnetic properties of graphene, especially the ones rich with edges, such as graphene nanosheets and nanoribbons [5]. The exceptional magnetic and electronic features of Fujita states in graphene resemble those in traditional s-d metal magnets, not only raising new fundamental excitations in condensed matter physics, but also providing promising applications in electronics and spintronic [6]. Since traditional s-d transition metals have been the workhorse in developing various industrially important chemical catalysts, it is reasonable to assume that the unique features of holey graphene combined with a large amount of Fujita zigzag states and nanoholes in a macroscopic 3D structure can be used to develop metal free catalysts with similar or even better performance, while in the same time, avoiding sustainability and environmental issues associated with transition metals [2a, 7].

A plethora of works have been reported to explore graphene materials to develop heterogeneous metal-free catalysts [2]. Most of the catalytic studies utilize graphene oxide (GO) and reduced graphene oxide (rGO) possibly due to their wide accessibility. GO/rGO with holey structures was also explored for catalytic applications [3]. Quite a few works have mentioned catalytic role of the zigzag edges [3a, 7-8]. However, the catalysts not only

contain edge defects, but also other defects, such as 5-8-member rings and various residual oxygen functional groups, which negatively influence their chemical and thermal stability for long term practical applications. Furthermore, these groups could also possibly involve in catalytic reactions [9]. The co-existence of multi-type defects complicates fundamental understanding the role of π-electronic spin-polarized states in chemical catalysis [10]. There is no clear picture yet if experimentally observed catalytic performance is due to defects on the basal planes, or π-electronic spin-polarized states in the GO/rGO materials, or a synergy of all these components. It is also not clear how the electronic and chemical structures of basal planes contributed to the observed catalytic efficiency. No study has been reported so far, to use pristine holey graphene materials with unique combination of Fujita zigzag states, holey structures, high electronic/thermal conductivity and high chemical/thermal stability for the development of metal free catalysts. The lack of access to pristine holey graphene nanomaterials with only edge defects (meaning high conductivity and crystalline structure of graphene largely remained) as a *true* material possibly drags behind the chemical catalytic studies.

Due to the wide range of applications, various approaches have been developed for production of holey graphene sheets. Bottom-up approaches based on chemical vapor deposition (CVD) methods, and top-down approaches such as photo, electron or plasma etching of graphene utilize various templates, which provide good control over sizes, shapes, and positions of holes. These strategies start with high quality graphene and generate holes on the basal planes of graphene while leaving other parts of basal planes intact. This type of holey graphene is referred as pristine holey graphene to differentiate from those holey graphene materials with large amount of defects (i.e. oxygen containing

95

groups, 5-8 member rings, sp3 carbons) on the basal planes. However, all these methods are designed for electronic and spintronic device applications, some of them even need a solid substrate to support graphene sheets during the hole drilling process, so suffering from high cost and difficulties in scaling up to produce large quantity of materials for bulk applications.

On the other hand, bulk chemical etching approaches, such as KOH etching, H_3PO_4 activation, HNO_3 oxidation, hot steam etching, enzymatic oxidation, and oxidative etching with or without catalytic nanoparticles, have advantages for large scale and cost effective synthesis. Most of these chemical etching based-approaches require graphene oxide (GO) or reduced graphene oxide (rGO) as a starting material, which contains various defects on their basal planes. During the hole generating process, some of these defects are partially gasified or etched away. While some of them may evolve to other defective forms such as 5-8 member rings, carbonyl, ether, and lactose groups, which are difficult to be removed even after high temperature annealing. Further, fabrication of GO and/or rGO starting materials usually takes hours to days, and the possibility of metal contamination exist during their synthesis, depending on oxidation methods applied. Therefore, fundamental molecular basis in fabricating holey graphene materials determined that the existence of various defects on their basal planes, which not only decreased their electrical and thermal conductivity, but also negatively influence the chemical and thermal stability of holey graphene materials for their long-term practical applications. There are no scalable approaches reported to date which is capable for mass production of highly conductive and chemically stable pristine holey graphene materials without involving metallic containing compounds and at low cost for practical bulk applications. Furthermore, none of the

scalable approaches could generate pristine holey graphene materials with controlled geometric structures, such as zigzag or armchair, of their hole edges.

This work reports a novel, rapid, eco-friendly mass production approach to fundamentally solve the problems mentioned above, so that selective and controllable generation of nanoholes can be achieved while leaving other parts of graphene basal plane largely intact. Furthermore, the hole edges can be controlled to be rich in zigzag geometry, which is the preferred edge structure for catalytic and spintronic applications. To differentiate our product to others, we refer our product as pristine graphene nanoplatelets. Note that we call them nanoplatelets not graphene because they normally have a thickness of more than one layer. The method has following advantages for both fundamental and practical applications: (1) The holey graphene structures are rich in holes ranging from nanometer to micrometers. Most importantly, their basal planes are nearly free of other defects. (2) There are no metal containing compounds involved in the production. (3) Large quantity of these materials can be quickly and inexpensively generated using abundant graphite instead of graphene/graphene derivatives as starting materials. All these features ensure the reservation of outstanding electron and thermal transport properties and chemical inertness of basal plane of graphene, providing not only clean "edge" samples for fundamental chemical catalytic studies, but also *real* materials for future practical industry applications. For first time, the catalytic role of π-electronic spin-polarized states was unambiguously illustrated in hydrogen atom transfer reactions. These reactions were chosen due to its wide application in organic synthesis, while usually precious metal or transition metal based catalysts are required. Using reduction of nitrobenzene as an example, we found that the holey graphene materials not only exhibits high conversion and

selectivity to aniline, but also are much more chemically stable for recyclability compared to those defective GO based catalysts.

3.2. Results and discussion

The new approach has two key features which secure the fabrication of pristine holey graphene materials with hole edges rich in zigzag geometry. The first key feature is the use of partially oxidized graphite (POG), instead of GO or rGO as starting materials. The POG contains various defects uniformly distributed across each graphene sheets on entire graphite flakes. It was reported that the formation of those kind of hard-to-remove defects and oxygen containing species can be avoided if GO has lower initial oxygen content. This is because isolated oxygen containing groups can be easily removed at lower temperature and recover to pristine graphene when an annealing process was performed in an inert environment, such as Ar[11].

To fabricate this kind of POG, we first prepared oxygen-purged stable GIC solution as described in our previous work [12]. The as-made solution was heated up in oil bath for 1 hour to partially oxidize the GIC, which we named as partially oxidized graphite (POG). It is worthy to mention that we choose this oxidation chemistry instead of widely used KMnO$_4$ oxidation chemistry, for GO production [13]. This is because, the rate of diffusion of oxidizing agent (KMnO$_4$) into graphite interlayer galleries is lower than the rate of chemical reaction itself [14]. As soon as the oxidizing agent diffuses between graphene layers, it quickly reacts with nearby carbon atoms. As a result, over oxidation at some parts was observed, thereby making it hard to achieve controlled oxidation. Here, the unique oxidation chemistry, where initial intercalation, increases the interlayer space between

graphene sheets, to allow access to the oxidant and hence leads to POG with a large amount of point defects. A prominent D band (breathing modes of the sp^2 carbon in the ring activated by defects can be either on the basal plane or edges) with an I_D/I_G of 0.42 was recorded *via* Raman spectra, with XPS revealing a C/O ratio of 2.31, indicating partial oxidation of GIC, as shown in Figure 3.1.
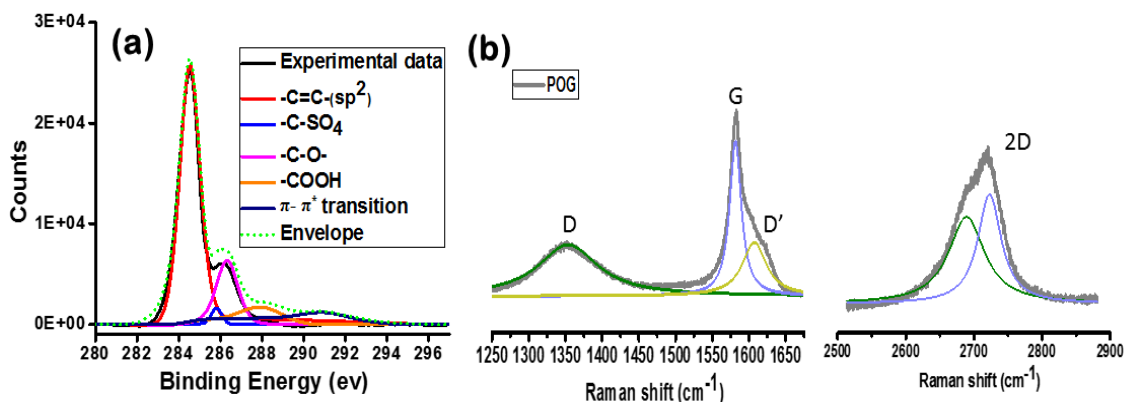
Figure 3.1. The C deconvolution spectra from XPS and Raman spectra of POG.

The second feature of this approach is to make full use of the key advantages of microwave heating in air instead of traditional convection heating. For carbon materials with only slight oxidation as observed in POG, strong microwave absorption and rapid transformation of absorbed MW energy into heat with high efficiency are expected. The heat generated can achieve very fast temperature rise. It was reported that the rise rate can be as high as 200°C/s, which can induce rapid degassing, building up inner gas pressure inside POGs, and pushing the graphene sheets apart (exfoliation).

Furthermore, for partially oxidized carbon materials, in the absence of solvent, mechanism of microwave heating is mainly wireless (contactless) joule heating. In this heating mechanism, electromagnetic waves of microwave irradiation does not directly heat

conducting materials, rather, induces motion of electrons, which causes heating by electrical resistance. Therefore, the current induced during microwave irradiation is not converted to heat in perfect graphene domains due to their ballistic conduction behavior. On the other hand, presence of oxygen containing groups and other topological defects will scatter electrons and provide electrical resistance, hence allowing selective heating. This region-selective heating can induce different chemical reactions depending on microwave power, time, and chemical nature of the carbon materials subjected to microwave irradiation, which includes: (1) direct carbon combustion selectively at defective regions to generate vacancies or nanoholes (direct holey graphene fabrication); and (2) deoxygenation and reconstruction of defective sp^3 carbon bonds into desired sp^2 configuration, resulting in, increased quality of carbon nanomaterials. Note that Joule heating mechanism has been applied to reduce GO to graphene without any reducing agents or solvents (fix defect). Possibly the power and time used were lower than those used to directly knock out the atoms at defect sites for direct perforation as stated above, especially if the irradiation is performed in an inert environment. We found that even in an oxidative environment, such as air, some of the defects can be fixed instead of direct perforation to generate holes.

Seitsonen et al., predicted that the graphene nanoribbons in an oxygen-rich environment is preferentially formed along the armchair direction at thermodynamic equilibrium [15]. The activation energy for oxygen desorption at armchair edges was estimated to be 435 kJ mol$^-$^{1}, which is larger than for zigzag edges (416 kJ mol^{-1}), indicating higher stability of the former case [16]. It was reported that the traditional heating induced carbon combustion or oxidation induced etching lead to nanographene with rich armchair edges [17]. This

phenomenon was explained by the thermodynamically unstable zigzag edges, which react preferentially with oxygen and get converted to stable armchair edges.

By carefully controlling microwave power and time, it is possible to control the geometries of hole edges to be zigzag dominated in this work. As the generated holes may be a mixture of armchair and zigzag geometries, further microwave treatment can be processed to adjust the ratio of these two kinds of edges. As in the fundamental studies by Dresselhaus et al. in wired joule heating of graphene nanoribbons, electronic flow is mainly along the zigzag edges due to their electronic states. Similarly, this concept also suits in the process of wireless joule heating induced by microwave irradiation. The region-selective heating confines at large resistance spots which are located at the junctions of different edge intersections. If energy dissipated is high enough at these junctions, the atomic structure will be rearranged into zigzag edges. Therefore, with careful control of microwave energy, the armchair carbon atoms will be preferentially evaporated, leaving zigzag edge as the prevailing kind of edge.
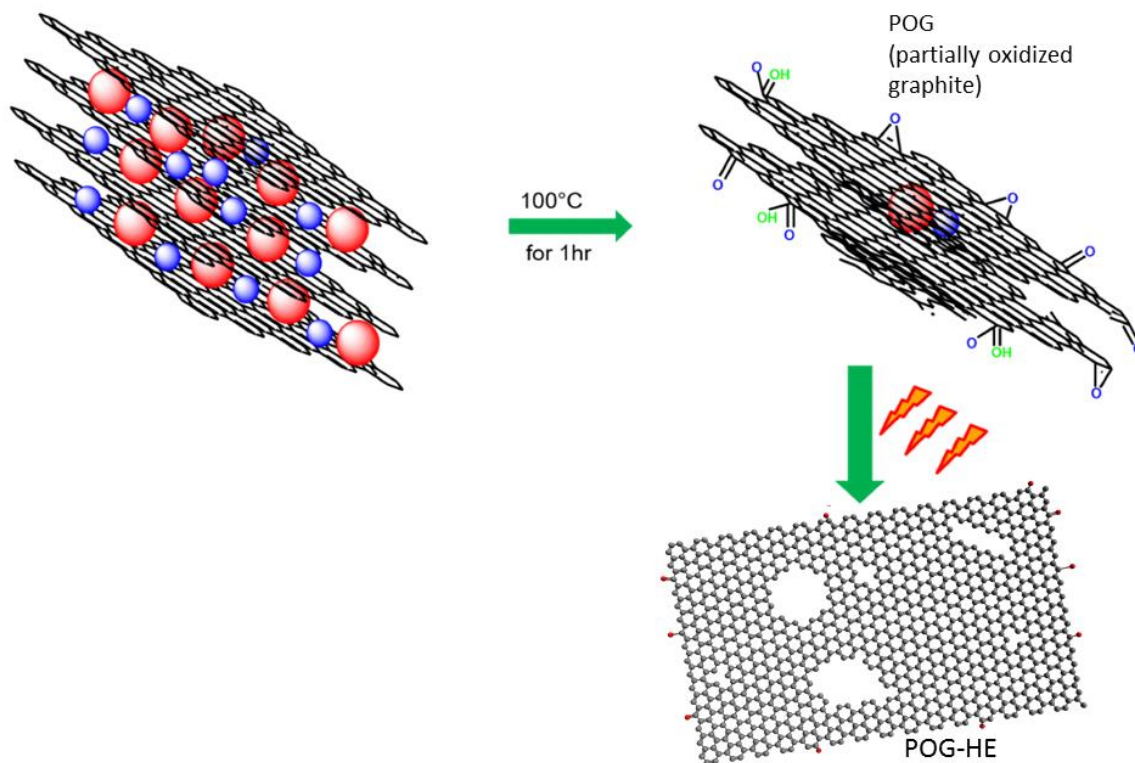
Scheme 3. 1. The schematic of holey graphene synthesized from POG.

The working principle of this novel approach was summarized in **Scheme 1.** Upon the exposure of POG to microwave irradiation, functional groups with the associated carbon atoms are selectively gasified, which leads to rapid expansion of GIC, with simultaneous generation of vacancies or nanometer holes on basal planes, **Figure 3.2**. Alternatively, pulse microwave irradiation may be used to remedy the defects during expansion for first pulse, followed by generation of holes on basal planes of the exfoliated graphene sheets for second pulse. With increased microwave irradiation pulses, the holes will be enlarged, with generation of some baby holes at the same time.

102
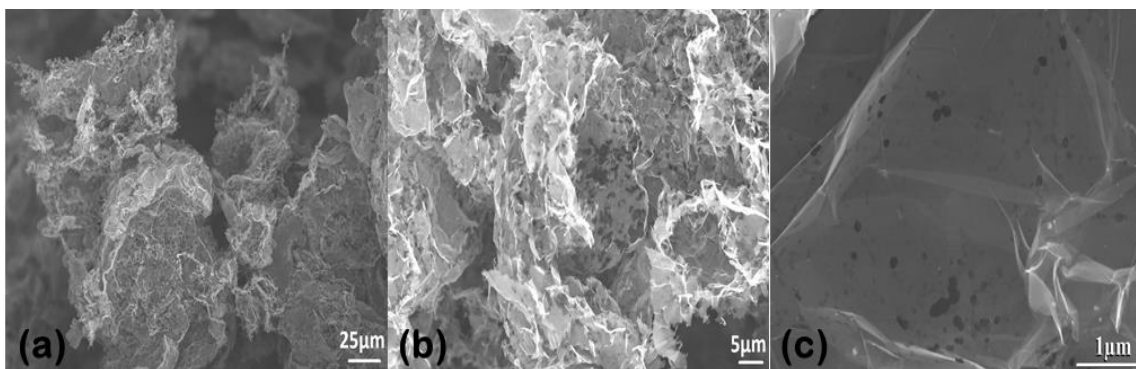
Figure 3. 2. The SEM image of POG microwave irradiated at 300W for 10sec(a-c).

Indeed, by controlling microwave irradiation power, time, and irradiation pattern, the graphene structure can be fine-tuned. Microwave irradiation of dried POG for 5 seconds at 200 W leads to quick expansion of POG (POG-exp) without generation of holes on the basal plane (**Figure 3.3. (a, b)**). The POG-exp has a "worm-like" morphology, similar to expanded graphite (EG) obtained by microwave treatment of GICs and microwave exfoliated graphite oxide (MEGO) from GO. The surface area of the as-prepared POG-exp powder was measured by methylene blue technique, and it has a surface area of 346 m^2/g, 4-7 times higher than the typical values (50-77 m^2/g) obtained from the EG [18] and is lower than MEGO (463 m^2/g) [19]. By extending microwave irradiation to another 5 seconds, the POG-exp was further expanded and holes of 300-500 nm holes can be found in most of the basal planes (POG-H, **Figure 3.3. (c, d)**, whereas holes with etched edges (POG-HE) were observed upon further prolonging the microwave irradiation, **Figure 3.3. (e, f)**, with a surface area of 744m^2/g.
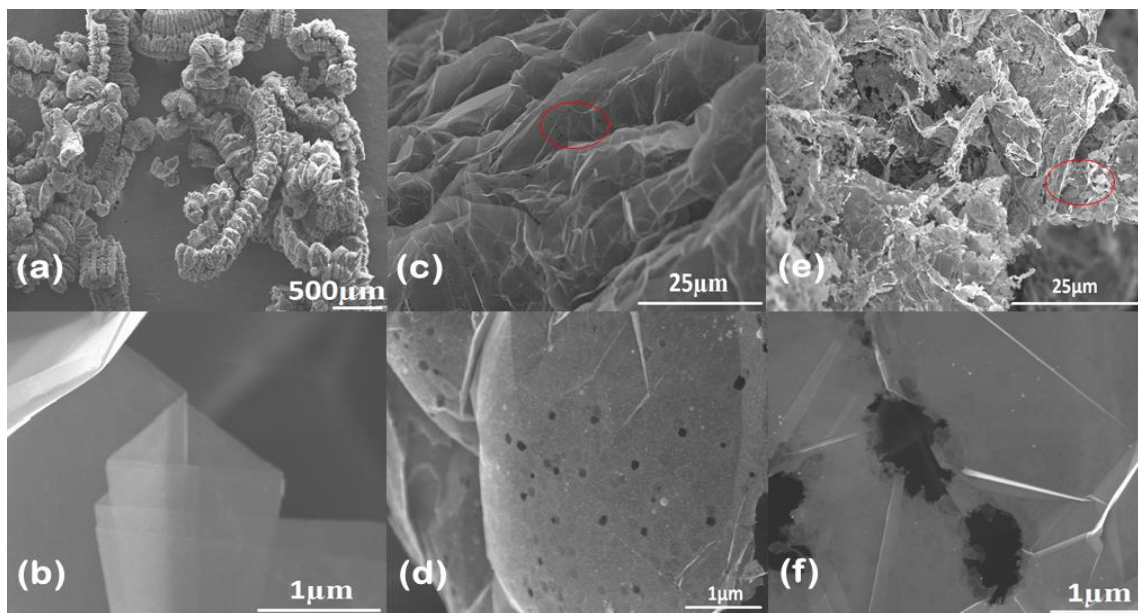
Figure 3. 3. SEM image of POG sample upon pulse microwave irradiation, POG-exp (a, b), POG-H (c, d) where holes of <500nm are observed, POG -HE (e, f) where edges with enlarged holes of >500nm were observed.

To further understand the structure of products on an atomic level, low-voltage aberration-corrected high-resolution transmission electron microscopy (HRTEM) was applied. **Figure 3.4.**, shows HRTEM images for POG (a), POG-exp (b), and POG-HE (c), (d). The outer part of bulk POG flake shows a step-terrace structure with high step-density and tiny area of each terrace, where large numbers of graphene sheets are stacked, as shown in **Figure 3.4. (a)**. The periphery part of each graphene sheet appears like a fjord having wavy and round-shaped coastline. Considering the strong chemical activity of the edge part, an erosion of oxidation process from the edge by O_2 approaching from outside of bulk POG flake is responsible for convoluted periphery structure of graphene sheets with most part of graphene consisting of edge-free basal planes. Indeed, HRTEM image for POG-exp, **Figure 3.4. (b)** exhibits a larger area of terrace part and population of edges is apparently decreased, where the number of layers for stacked graphene sheets is also decreased compared to that of POG due to partial exfoliation during expansion process. From sharp

FFT spots shown in the inset, stacking of edges in POG-exp is similar to that of POG, which is a typical ABAB stacking. This is further supported by the doublet of Lorentzian peak fit of 2D band in Raman spectra [20], **Figure 3.5. (b)**. The HRTEM imaging also revealed that the edges exist at just periphery part of graphene sheets, and actual population of edges is low in both POG and POG-exp. These edges were referred to as "open edges", with the direction of edges random. On other hand, a remarkable change occurs in POG-HE, as seen in **Figure 3.4. (c)**. Holes with diameter of about ~5 nm appear inside graphene sheets, with edges along its circumference. Moreover, holes do not deeply penetrate into lower layers of stacked graphene sheets but they occupy only single or few layers of graphene sheet (**Figure 3.4. (d)**). In contrast to POG and POG-exp, POG-HE contains many holes with edges inside basal plane of graphene sheets in addition to periphery, where edges are referred to as "closed edge". The presence of individual holes on each graphene sheets strongly suggests an etching (erosion) of graphene sheets by oxidant species not approaching from outside of stacked sheet but being present between layers by the intercalation process. Interestingly, the peripheral of holes in POG-HE do appear like a polygon, where mainly zig-zag edges are observed with the defect free basal plane.
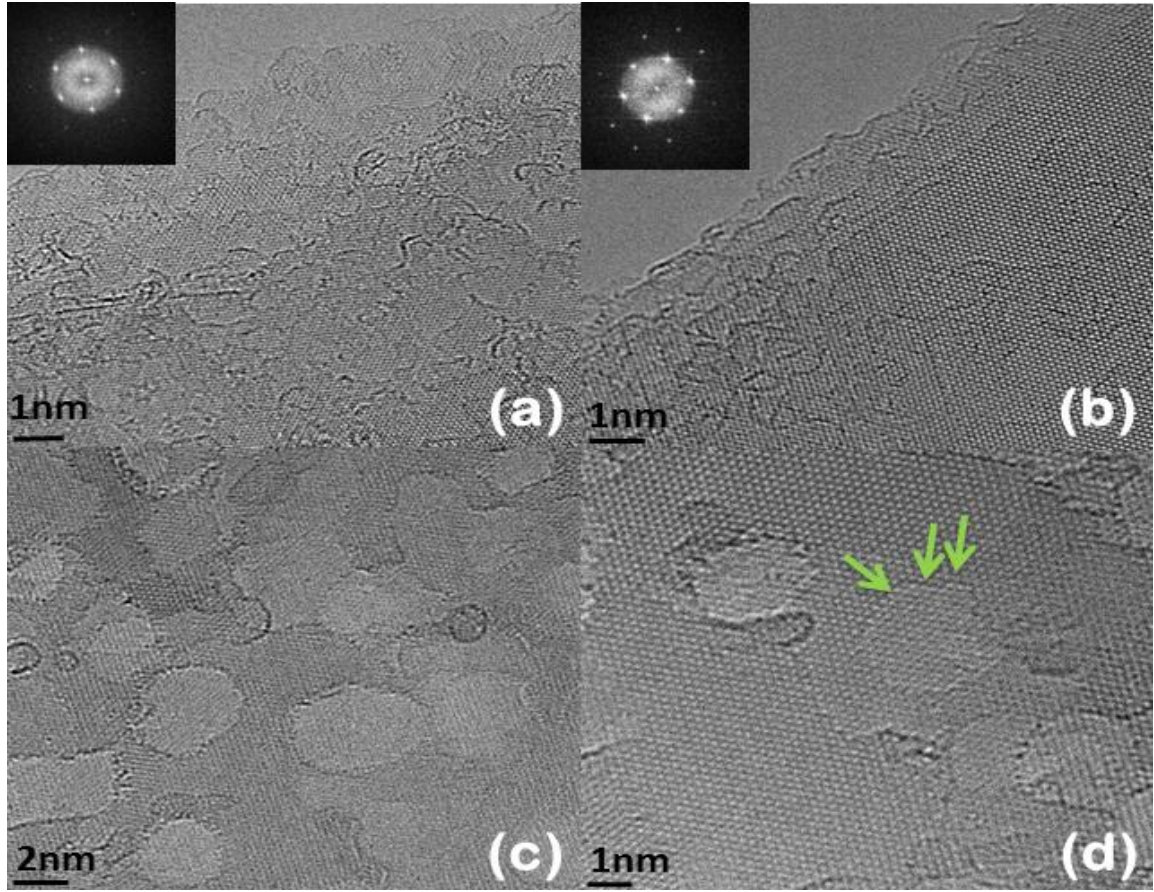
Figure 3. 4. HRTEM images for POG (a), POG-exp (c), and POG-HE (c), (d). Inset shows the FFT of corresponding image. Clear spots show that the samples have nicely stacked graphene structures. Green arrows indicate the zigzag edges. Considering the angular relations of the edges, other parts of holes also mainly consists of zigzag edges.

The POG-HE reports an I_D/I_G of 0.28 which is higher than holey graphene synthesized *via* air oxidized rGO[21], enzymatic oxidation of GO[22], activation of rGO with CO_2[23]. D and D' bands appear due to the presence of defects and edges of graphene. The D band is observed in the case of armchair and other defects but not with zigzag edges due to their property of momentum conservation, while D' band can be attributed only to the presence of zigzag edges [24] [25].
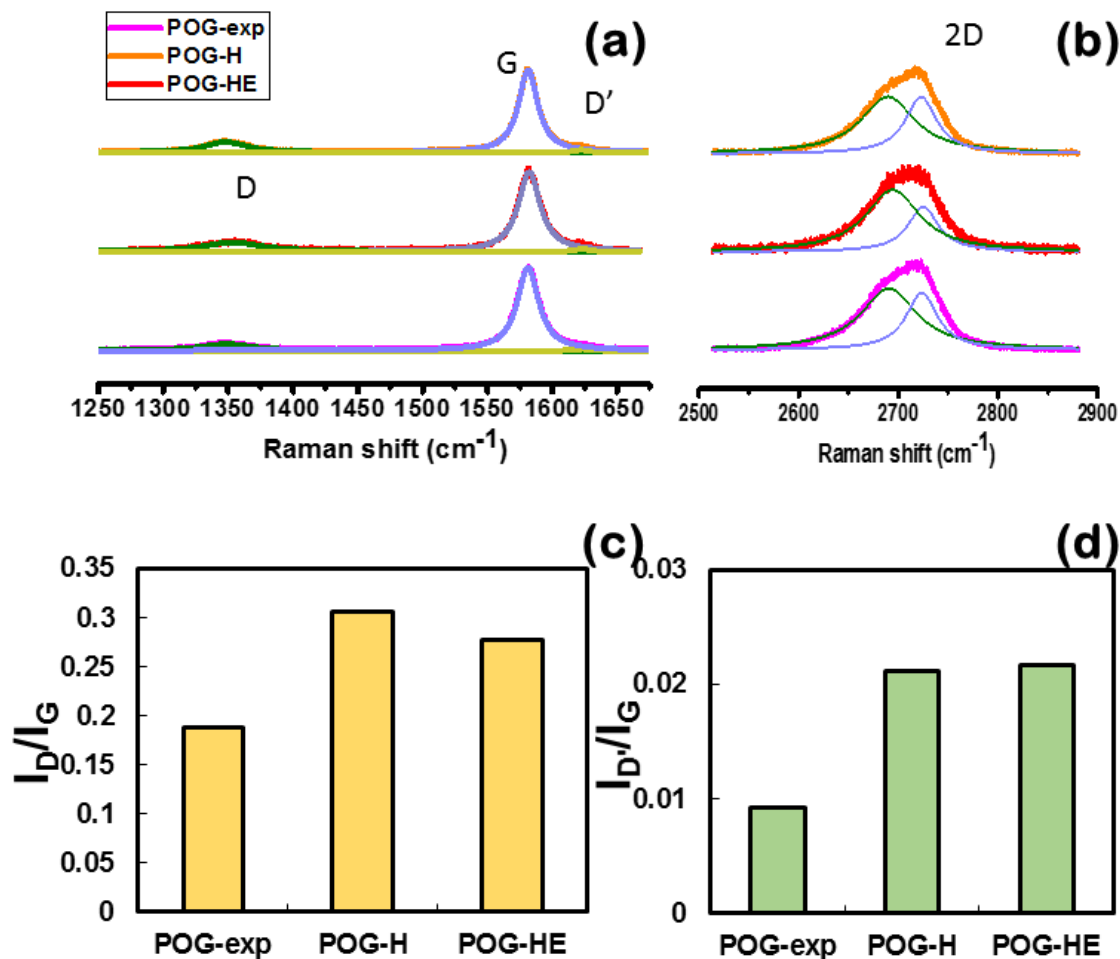
Figure 3. 5. The Raman spectra exhibiting characteristic D, G and D' bands for POG series. The large intensities of D and D' bands for POG do not represent average of whole part of POG flake but the outer part which is locally damaged at extremely high degree due to oxidant approaching from surrounding solvent during heating as discussed by HRTEM analysis. Hence, we compare Raman spectra after microwave irradiation of POG. The D and D' bands increases as holes and edges are introduced into POG-exp, as shown in **Figure 3.5. (c), (d)**. In typical graphene derivative materials, D' band is not significant due to less population of zigzag edges because of its thermodynamically unstable nature. Nevertheless, the presence of D' / G bands in POG-H and POG-HE indicates larger

contribution of zigzag edges having edge-state with chemical activity. The summary of intensities of D, G and D' are listed in **table 3.1.**

Table 3.1. The ratio of I_D/I_G of the POG series in comparison with graphite flakes.

	I_D/I_G	$I_D/I_{D'}$	$I_{D'}/I_G$
Graphite flakes	0.089	0	0
POG	2.37	1.71	1.39
POH-exp	0.19	20.42	0.0092
POG-H	0.31	14.49	0.021
POG-HE	0.28	12.86	0.022

The high quality of graphene is further demonstrated by C deconvolution spectra from XPS studies. A characteristic C peak at 284.5 eV and a weak O peak at 532 eV was observed in all survey scan (**Figure 3.6. (a)**), whereas an additional S peak at 167eV was observed in case of POG, **Figure 3.6. (b)**. This S peak can be attributed to the presence of sulfate moieties in POG, supported by TGA analysis. TGA analysis recorded a total weight loss of 15%, when ramped at 2°C/min from 40-900°C. The initial weight loss was observed at 100°C, with total 13% weight loss till it reached 500°C. This phenomenon can be attributed to loss of O_2 functionalities on intercalated graphite, similar to GO [26], whereas weight loss at high temperatures >270^0 C can be attributed to loss of organo-sulfates [27] , **Figure 3.6. (c)**. Remaining 2% can be assigned to the loss of other oxygen functional groups.
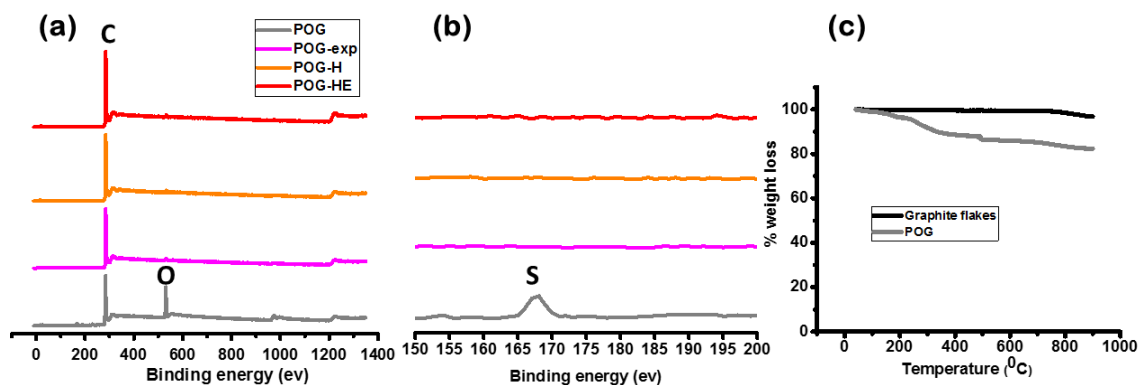
Figure 3. 6. XPS survey scan of POG series (a) with S peak observed in POG (b). The TGA of POG in comparison with graphite flakes (c).

The deconvolution of C peak exhibits a strong sharp peak at 284ev along with 291ev, where former is attributed to C=C in graphene lattice and latter is attributed to π- π^* peak transition, indicating preservation of delocalized π conjugation [28]. The low C/O ratio was recorded for POG (2.3214.66), which increased when subjected to microwave irradiation in the order: POG-H (13.51) < POG-exp (14.66) <POG-HE (21.41).
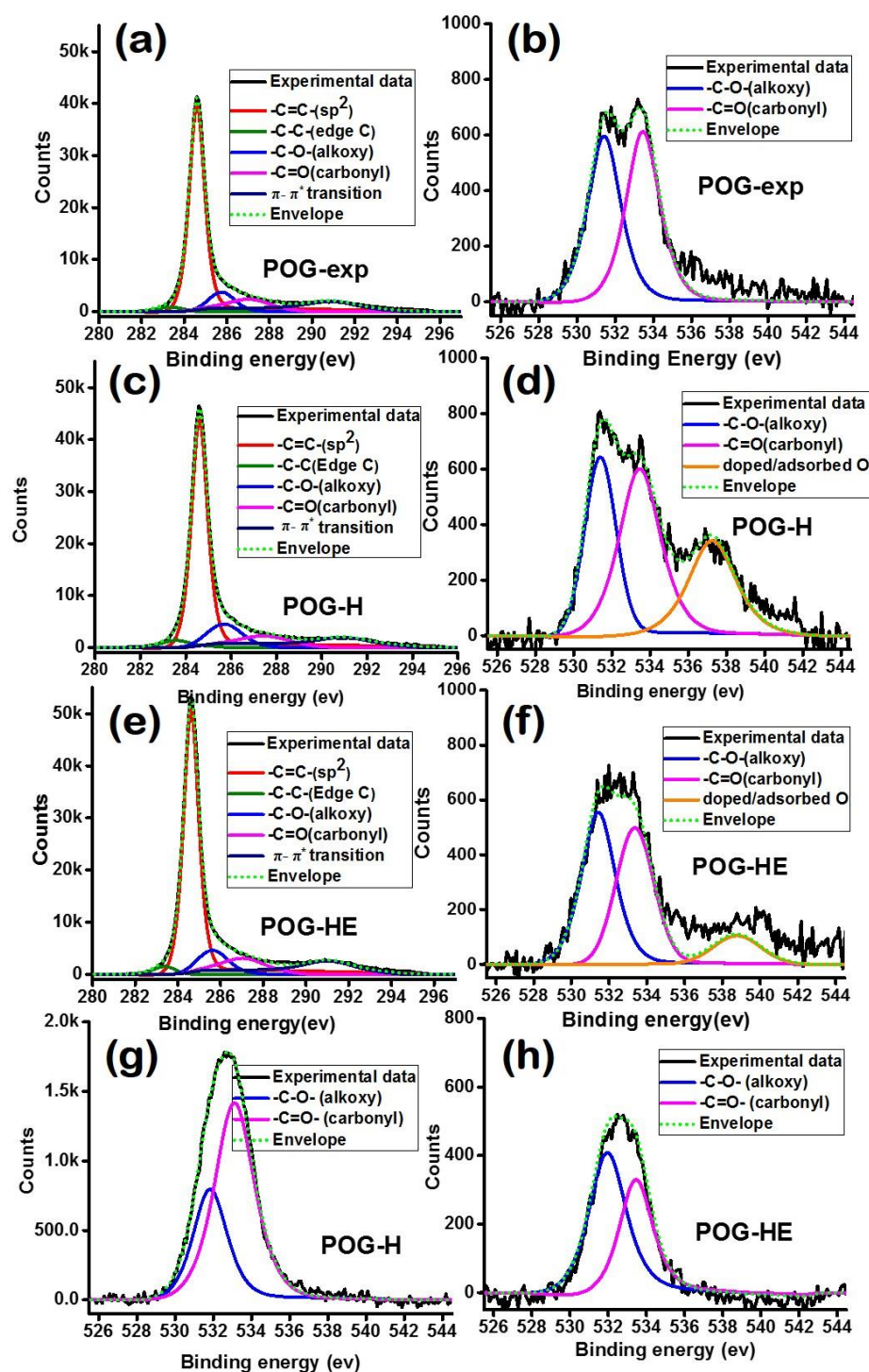
Figure 3. 7. XPS deconvolution of C and O peak in POG-exp (a,b), POG-H (c,d), POG-HE (e,f). The O deconvolution spectra of POG-H (g) and POG-HE (h) in Ar.

The microwave irradiation of POG initially leads to the removal of existing defects (POG-exp), which upon prolonged microwave might lead to generation of new defects and gasification of existing defects (POG-H). This upon further microwave irradiation leads to the removal of defects with hole generation (POG-HE). The presence of peaks at 286 eV and 287eV are contributed to C-O[21, 29] (532ev for O) and C=O[30] [31] (533ev for O) functionalized carbons, which may locate along the edges, thereby proving high quality of basal plane. Below is a **table 3.2.**, summarizing the XPS quantification of C and O peaks. The XPS of O spectra exhibited an additional deconvolution peak at higher binding energies (537-539eV), which disappeared when the spectra were collected in Ar environment in case of POG-H (Figure **3.7. (d, g)**) and POG-HE (Figure **3.7. (f, h)**). This can be explained by the fact that zigzag edges, which are highly reactive gets stabilized by adsorbing O_2 in air.

Table 3.2. The XPS quantification of deconvoluted C and O peaks of POG samples.

Catalyst	C-H/ C-C (283 ev)	C=C (284ev)	C-O (286e V)	-C-OH/ (287ev)	Π-Π transition(291e v)	C-O (531. 4ev)	C=O (533 ev)	C/O ratio	% C	% O
POG	10.03	46.84	15.43	7.32	5.47	8.32	6.6	2.32	69.87	30.13
POG-exp	11.2	60.74	8.69	8.56	8.1	1.67	1.03	14.66	93.62	6.38
POG-H	11.3	59.85	8.83	8.88	8.21	1	1.93	13.51	93.11	6.89
POG-HE	10.57	62.87	9.34	7.97	7.21	1.07	0.8	21.41	95.54	4.46

The EPR analysis was used to further confirm the presence of edges. A single lorentzian EPR signal with g-factor g=2.0046±0.0003 and linewidth $\Delta H_{pp} \approx 1.50$ mT was recorded for POG, as shown in **Figure 3.8. (a), curve 1**. This signal relates mainly with dangling σ-bonds in interior defective species of partially oxidized graphite or with small amount of edge spins localized on the periphery of graphitic crystallites during oxidation. The broadening of this EPR signal through magnetic or dipole-dipole interaction of such paramagnetic species S=1/2 with other paramagnetic species of the same origin (or with molecular oxygen from the ambient) is not essential, although it is the reason of observed linewidth of narrow EPR signal.

Consequently, EPR spectra of POG-H and POG-HE consist of two lines: the broad signal of prevalent double integrated intensity and the narrow signal with insignificant intensity (**Figure 3.8. (a), curve 2 and Figure 3.8. (b)**). An abnormally broad EPR line width was observed in both the cases with ΔH_{pp} exceeding 50-60 mT in POG-H and $\Delta H_{pp} \approx 70$ mT for POG-HE, whereas in the latter case, its center is located in between 3rd and 4th narrow hyperfine structure lines of Mn^{2+}: MgO standard (**Figure 3.8. b**). The g-factors of 3rd and 4th lines of Mn^{2+} standard equal g_3=2.0314±0.0003 and g_4=1.9812±0.0003. The corresponding *g*-factor of broad EPR line of sample POG-HE equals 2.0020±0.0006. The presence of such abnormally broad EPR line permits us to conclude that it is caused from edge-localized π- electronic spin states (S=1/2) both on periphery of graphene flakes and interior perimeters of holes in graphene. The narrow EPR signal is probably from some point-like defects with dangling σ- bonds inside graphene flakes. The concentration of paramagnetic species S=1/2 responsible for broad EPR signal in POG-H and POG-HE samples is at least several times more than that one in precursor

sample of partially oxidized graphite (POG) and exceeds $\sim 5 \times 10^{20}$ g^{-1}. Such concentration of paramagnetic species corresponds to ~10000 ppm or in other words ~1 species per 100 carbon atoms. Indeed, π- electronic edge spins may present there in such high concentration and at the same time, be the only paramagnetic agents coupled by strong magnetic interaction mediated by itinerant π- electrons of holey graphene. Evacuation in capillary tube down to the secondary vacuum condition, in POG-H or POG-HE sample does not lead to essential narrowing of broad EPR line. The corresponding change in EPR linewidth does not exceed 5-8 mT. It means that the main mechanism of EPR line super-broadening is a magnetic interaction between carbon-inherited paramagnetic species located in holey graphene flakes with holes and edges. At the same time such paramagnetic species with excessive local π- electronic charge probably provide abnormally high ability of interior and exterior edges to catalyze the chemical reactions.
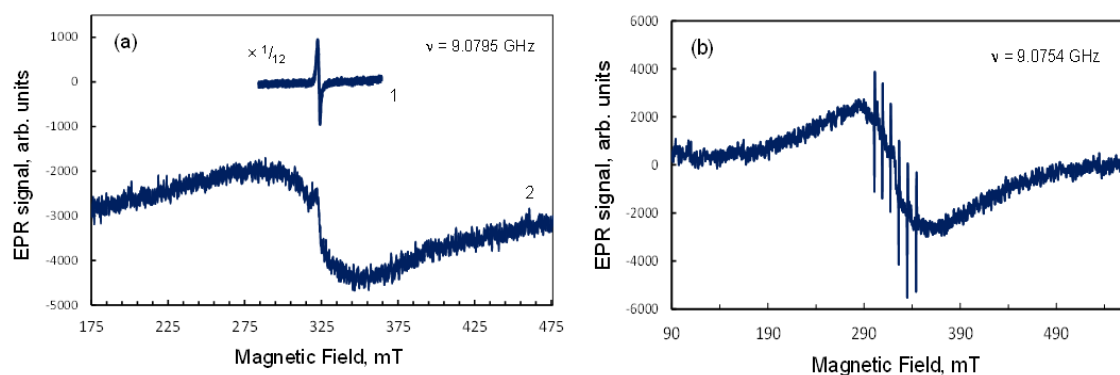
Figure 3. 8. Room temperature EPR spectra of samples of POG series. (a) for partially oxidized graphite original (curve 1) and partially oxidized graphite with holes (curve 2); (b) for partially oxidized graphite with holes and edges recorded together with EPR spectrum of Mn^{2+}: MgO standard consisting of six sharp lines. The sextet line arises from the hyperfine splitting of Mn^{2+} ions. Microwave power – 2 mW. Magnetic field modulation amplitude – 2 mT for both broad EPR lines of samples with holes and holes/edges and 0.3 mT for upper single narrow line.

Catalytic activity: The selective hydrogenation of nitrobenzene, a toxic chemical can generate aniline, which is an important intermediate in the synthesis of agrochemicals, urethanes, pharmaceuticals, dyes etc [32]. Hence selective reduction of nitrobenzene has attracted considerable attentiveness. High selectivity was achieved with noble metals such as Au, Pd, Pt and Ru [33] and transition metals such as Fe, Ni and Cu [34]. However, their use has been limited due to scarcity and cost of noble metals, agglomeration of the metals and metal oxides, which leads to deactivation of catalyst eventually leading to lower conversions. High temperatures and high catalyst loadings were required to achieve considerable conversions.

Hence alternatives to overcome these shortcomings have been explored. Recent reports indicate that carbon can serve as a metal free catalyst for nitroarenes reduction [35], with hydrazine hydrate as the reducing agent. The catalytic activity of these materials is attributed to the following parameters in each case (1) The carbon not only serves as an adsorbent, but also as an electrical conductor, (2) The heteroatom-doped graphene induces electronic and morphological changes on the graphene and leads to have a different electronic state from the bulk[36] and in the case of (3) rGO, defects and edges on the graphene leads to different electronic state from the bulk[37] .

For the first time we report the catalytic activity of the holey edge graphene with a hydride donor, isopropanol in the presence of a promoter, KOH. 5wt% of POG-HE recorded 100% conversion with 38% selectivity towards aniline in 1atm Ar (entry 1a) with azobenzene and azoxy benzene as byproducts. Increasing the pressure in reactor to 4atm with same wt% of catalyst, lead to increased selectivity of 92±2 % of aniline. However,

changing the reaction condition to H_2 at 4atm, lead to decreased nitrobenzene conversion

of 25% (entry 1c), indicating its negative effect.

Table 3. 3. 5wt% of the catalyst, nitrobenzene (0.3mmol), isopropanol (2ml, 26mmol), KOH (1mmol), at 100°C for 24hrs. The samples were analyzed with GC-MS after the reaction.

Catalyst used	Atm condtn	% Conversion	% Selectivity			% Yield
			Aniline	Azobenzene	Azoxy Benzene	
[1]POG-HE	[a]Ar_1atm	100	38.18	49.62	12.20	≈99%
	[b]Ar_4atm	100	94.41	5.59	0	≈99%
	[c]H_2_4atm	25.19	100	0	0	≈25%
[2]ba-GO	Ar_4atm	88.60	70.22	29.78	0	86.11
[3]rMHGO	Ar_4atm	65.03	46.99	53.01	0	63.86
[4]rMGO	Ar_4atm	61.05	16.76	83.24	0	59.20
[5]Graphite flakes	Ar_4atm	28.67	73.69	26.31	0	25.43
[6]No catalyst	Ar_4atm	13.95	8.14	91.86	0	11.58

[7]POG-HE reusability	Ar_4atm	100	85.08	12.78	2.14	≈99%
	Ar_4atm1[st] reuse	100	82.38	12.64	4.98	≈99%
	Ar_4atm2[nd] reuse	100	86.62	6.65	6.73	≈99%
	Ar_4atm3[rd] reuse	100	85.42	6.62	6.50	≈99%

The reaction was conducted with other carbon based catalyst at 4atm Ar, where 88.6% conversion was achieved with 70.22% selectivity in ba-GO, where the spins in conjugation with COOH groups are the active sites for oxidative coupling of primary amines. The holey graphene oxide synthesized via microwave is reduced by thermal annealing (rMHGO) and tested for its catalytic activity for the reduction of nitrobenzene. A conversion of 65.03% with 46.99% selectivity was recorded, which decreased to 61.05% conversion in its thermally reduced non holey graphene oxide (rMGO). The original graphite was also tested for its intrinsic catalytic activity in nitrobenzene reduction, where 28% conversion was observed, which decreased to 13% in the absence of catalyst. Nevertheless, GO based carbons decomposed during the reaction and exhibited brown colored filtrate during catalyst recovery, **Figure 3.9.,** which indicates their instability, whereas the POG-HE exhibited similar conversion and selectivity even after 4 recycles

(entry 7). The above results suggest the reusability and catalyst stability for reduction of nitrobenzene.
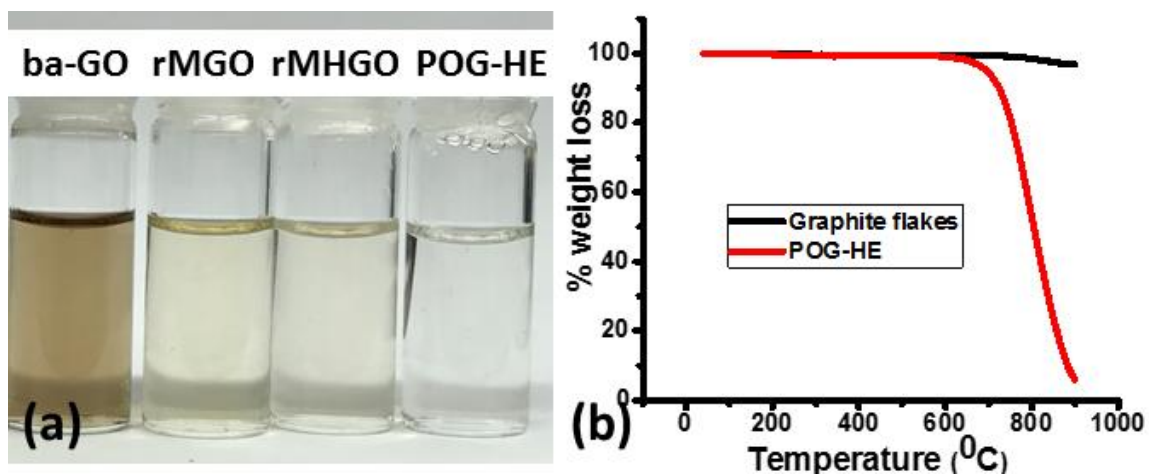
Figure 3. 9. Digital image of the filtrates collected during washing of catalyst (a). The thermal stability of POG-HE at different temperatures in N_2.

Most of the carbon based catalyst exhibits small amounts of metal impurity accrued either during synthesis process or might be present in parent material itself. Hence to eliminate reason of doubt whether the catalytic activity is due to presence of trace amount of metal, AAS of the acid treated catalyst was performed, which did not exhibit any trace amount of metals in the range of 0.8 to 50ppb. However, Fe was detected in the parent graphite, with 20ppb of Fe as the detection limit in AAS. Hence, 20ppb of standard Fe is used in nitrobenzene reduction. A conversion of 15% was observed which is similar to the result without catalyst, indicating the catalytic activity is indeed from POG-HE.

The nitrobenzene undergoes reduction in either direct or condensation pathway as shown in **scheme 3.2**. To determine the reaction pathway with POG-HE, nitrosobenzene and phenyl hydroxylamine were used as reactant. The intermediate azobenzene was observed as final product over time in both the cases. This indicates that phenyl hydroxylamine

undergoes oxidation to form nitrosobenzene, which couples with phenyl hydroxylamine to form azobenzene rather than undergo direct reduction to aniline. To further confirm the pathway, Azobenzene was used as reactant and to our delight, we found 100% conversion with ≈99% selectivity to aniline. These above results point out the fact that the reduction of nitrobenzene occurs *via* condensation pathway.
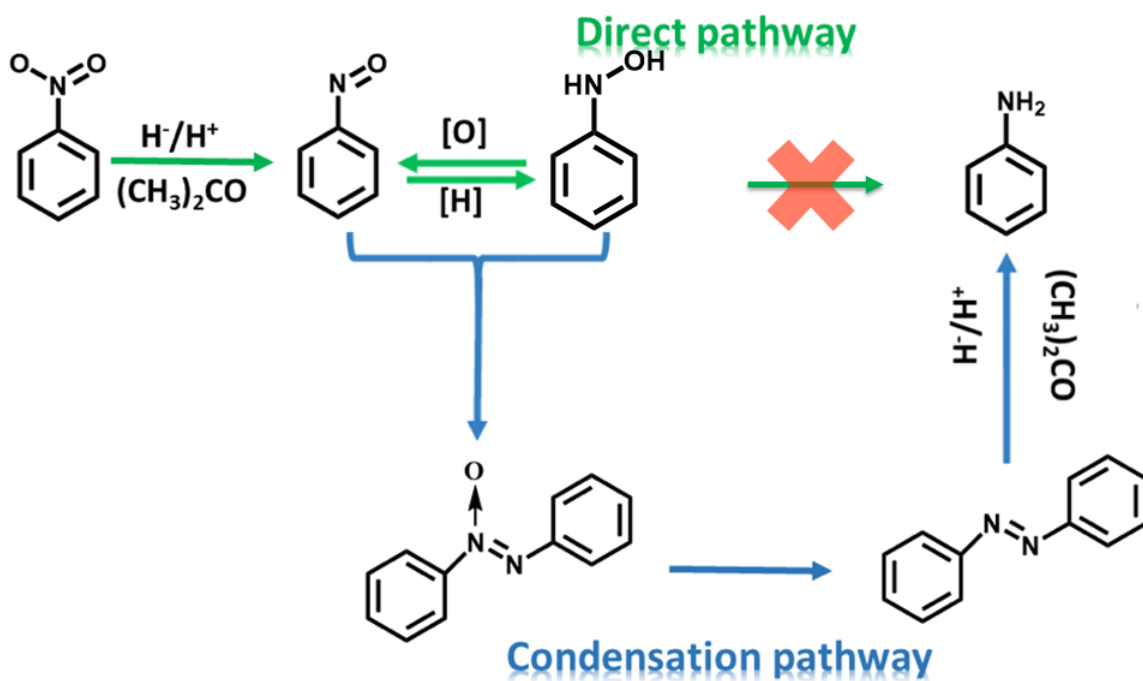
Scheme 3.2. The reaction pathway of nitrobenzene reduction.

As per our knowledge, for the first time, Shi et al demonstrated the use of carbon catalyst for nitrobenzene reduction via hydrogen atom transfer. The mechanism of reduction was reported to be similar to that of metal via MPV (Meerwein–Ponndorf–Verley) pathway. Several theoretical predictions indicated the activation of nitrobenzene at zigzag edge, hence in this present scenario, we report that it might hold true for our catalyst with edges. The alkoxy group as ethers and the carbonyl groups at edges are involved in transfer of proton and hydride to the activated nitrobenzene molecule, and promote its reduction [38].

Hence we propose that the zigzag edges to be catalytically active centers to activate the nitrobenzene and promote its reduction. However, no direct evidence can be provided at this time and this mechanism needs further study.

3.3. Conclusion

In summary, we developed a novel **dry (solvent free)** microwave enabled approach, which we referred as "**Microwave Enabled Rapid Simultaneous Expansion and Hole generation approach" to ecofriendly** and rapidly produce holey graphene. This novel approach has similar merits as the wet microwave chemistry approach[26]: (1)Direct production of highly conductive graphene without requirement of post-reduction, (2) eco-friendly, no heavy metal waste and toxic by-products, (3) fast (less than 1 minute) and low energy consuming. Compared to the wet microwave chemistry approach, **additional advantages** of dry microwave chemistry were brought in: (I) the issues, such as safety and corrosion to equipment and devices, and the requirement of large amount of water to clean and purify the products, which are associated with the usage of strong acids and oxidants are naturally avoided, further minimized environmental impact as well as eliminating the cost of waste/toxic material collection and treatment. (II) efficient absorption by the only reactant. (III) The required microwave time is short (5s), which make it easy for continuous large scale production. These holey graphene sheets can be used as sustainable metal free catalysts due to the capability of large scale production. It is also relevant for fundamental studies due to the existence of nanoholes and associated large amount of edges. Most importantly, they can be made free of metal ion contamination. They can be also made nearly defect free on its basal plane or with intentional introduction of metal ions or defects. These unique features of graphene give us excellent opportunity to systematically

investigate the *intrinsic* and *purposely modified* electronic, magnetic structures and properties at both atomic levels of singe sheets and bulk level as a true material for the reduction of nitrobenzene.

3.4. Experimental Section

3.4.1 Material synthesis

POG: Graphite intercalation compound with SO_4^{-2} is achieved by following the recipe process described by Tours group[39]. In brief, 1000mg of Ammonium persulfate (reagent grade 98%, Sigma Aldrich) was dissolved in 10ml H_2SO_4 (98% Pharmaco Aaper). The solution mixture was stirred for 5-10mins to dissolve the salt and form a uniform suspension. To this solution mixture, 200mg of Graphite flakes was added (size >500µm). The reaction mixture was stirred for 6hrs to form the reversible Graphite intercalation compound. Graphite intercalation compound is purged with O_2 at the rate of 90-120ml/min for a period of 1hr as discussed in our previous work[12] and then heated at 100^0C for 1hr. This sample is quenched in 200ml water and then washed via vacuum filtration through a polycarbonate membrane with a pore size of 0.8 µm with 200ml water each for four times. The product was dried in the high vacuum.

POG-exp: For the expansion of the POG, approximately 50 – 60 mg of the as prepared vacuum dried POG was taken into a 50ml Round bottom flask, which was subjected to microwave irradiation at 300W for 5sec in CEM microwave. The obtained product was collected as such without any post treatment.

POG-H: For the generation of only holes on the POG sample, approximately 50 – 60 mg of the as prepared vacuum dried POG was taken into a 50ml Round bottom flask, which

was subjected to microwave irradiation at 200w for 5sec each for two times (total 10sec) in CEM microwave . The obtained product was collected as such without any post treatment.

POG-HE: For the generation of holes and edges on the POG sample, approximately 50 – 60 mg of the as prepared vacuum dried POG was taken into a 50ml Round bottom flask, which was subjected to microwave irradiation at 200w for 5sec each for three times (total 15sec) in CEM microwave vessel. The obtained product was collected as such without any post treatment and characterized.

rMHGO and rMHGO: The MGO and MHGO were synthesized accordingly as mentioned in our previous paper. In brief, 20mg of synthetic Graphite ($\leq$20μm) is added to a Round bottomed flask, to which 8ml of H_2SO_4 is added and the reaction mixture is cooled in an ice bath for 5mins. To this, add 2ml of HNO_3, and cool for another 5mins. To this reaction mixture, add $KMnO_4$ and swirl for 30sec in the ice bath and this solution is subjected to microwave irradiation at 300W for 30sec in the case of MGO and for 40sec in the case of MHGO. The as obtained reaction mixtures are quenched in 200ml of H_2O_2 (10%) solution and filtered with 0.2μm polycarbonate filter. The product is further washed with 200ml of dil. HCl (5%) and then finally washed with 1000ml of water (200ml each washing for 5 times). The as obtained product is dried in vacuum for three days.

These samples are placed in a quartz tube and then placed in a furnace. The N_2 gas is allowed to flow through the tube at the rate 60ml/min for 1hr to replace the air in the tube. Then the sample is reduced at 500^0C for 2hrs. The as annealed samples are referred to as rMHGO (MHGO annealed) and rMHGO (MGO annealed). The samples are washed with HCl to remove any impurities and then dried overnight at 80^0C for overnight.

3.4.2. Material characterization

SEM: The Surface morphology of the as synthesized catalyst is characterized via Scanning Electron Microscopy (SEM) using a HITACHI S-4800 Field emission Scanning Electron Microscope (FE-SEM, Hitachi Co.Ltd). The SEM sample is prepared by placing the powder on the carbon tape which is fixed to the stud and the sample is analyzed by applying a voltage range of 2-5KV,

TEM: High resolution transmission electron microscopy was used to investigate the structure of obtained materials using a HRTEM, JEOL JEM-2100F equipped with CEOS Cs correctors, 80 kV.

Raman spectroscopy: The Raman spectroscopy was collected by depositing the dispersed samples on anodisc membrane and the spectra collected with the instrument Witech alpha 300 Raman spectroscopy. A laser power of 12W with an integration time of 20sec and the excitation laser wavelength of 532nm was used to collect the spectra. The spectra was collected on a sample size of 20µm W*H with 4 images per line (total 16 spectra).

XPS: X-ray photoelectron spectroscopy (XPS) is used to detect the functional state of the carbon and oxygen in the holey graphene. The gold substrate is used for the analysis on which the slurry of the catalyst were dropped (thickness of approximately 30-50nm). The XPS spectra was acquired using a Thermo scientific K-Alpha system with a monochromatic Al Kα x-ray source (hν = 1486.7ev). For data analysis, smart background subtraction was performed and the spectra were fit with the Gaussian/Lorentzian peaks using a minimum deviation curve fitting method (Advantage software package). The Integrated peak areas along with Scofield sensitivity factor were used to determine the functional composition.

TGA analysis: $\approx$3-5mg of the sample is heated in the Discover TGA instrument in the N_2 environment with a flow rate of 20ml/min. The samples are initially stabilized at 40^0C and then heated at 2^0C till 900^0C.

Surface area determination: Methylene blue adsorption method is used to determine the surface area of the as synthesized holey expanded graphite. Each mg of the adsorbed methylene blue on the sample represents $2.54m^2$ of surface area. A standard methylene blue solution with a concentration of 2mg/ml in water is prepared and then added to the holey expanded graphite. For each mg of holey expanded graphite, 750ul of the standard methylene blue solution is added and the reaction mixture is stirred for 24hrs. The mixture was then centrifuged at 6000rpm for 10mins to separate the unabsorbed methylene blue molecules. The concentration of the methylene blue in the supernatant separated was determined by the UV-Vis spectroscopy at a wavelength of 664nm. The surface area is calculated based on the standard calibration graph of the methylene blue and the interpolation of the methylene blue supernatant after the experiment.

EPR measurements: EPR measurements at room temperature were carried out using a JEOL JES-TE200 X-band (Δ ~9 GHz) EPR spectrometer at microwave power P_{MW} ranging from 1 mW to 6 mW. Spectra were recorded in the wide magnetic field range from ~70 to 570 mT. Each spectrum was registered during several (up to 9) coherent acquisitions. For EPR study the loose packed sample (~3 mg) was sealed in 1 mm internal diameter (i.d.) ~45 mm long quartz capillary tube at ambient conditions (air pressure 1 bar). Processing of EPR spectra was done using JEOL-JES-TE200 and Microsoft Excel software. The doubly integrated intensity $DI \sim I_{pp} \times (\Delta H_{pp})^2$ of each corresponding EPR signal was analyzed for evaluation the intensity of EPR line. Here I_{pp} and ΔH_{pp} are peak intensity and

peak-to-peak line width of the EPR signal recorded in the conventional form of 1st derivative of EPR absorption spectrum.

3.4.3. Catalytic activity

The nitrobenzene reduction was carried out in a pressure reactor of 30ml capacity. The POG-HE catalyst (5wt%) was added to the pressure reactor, to which 1mmol of KOH is added along with 2ml of propanol as solvent. To this reaction mixture, nitro derivatives were added and then, the reactor is pressurized with 4 atm Ar, unless specified and heated at 100^{0}C for 24hrs in an oil bath. The reactor is cooled down to room temperature and then the pressure is released before opening the reactor, to which toluene is added as an internal standard with ethanol as a solvent to clean the catalyst. The sample conversion and yield were calculated by sample analysis using GC-MS and HPLC.

3.5. References

[1] a) S. D. Lacey, E. D. Walsh, E. Hitz, J. Q. Dai, J. W. Connell, L. B. Hu and Y. Lin, *Nano Energy* **2017**, *31*, 386-392; b) X. G. Han, Z. Yang, B. Zhao, S. Z. Zhu, L. H. Zhou, J. Q. Dai, J. W. Kim, B. Y. Liu, J. W. Connell, T. Li, B. Yang, Y. Lin and L. B. Hu, *Acs Nano* **2017**, *11*, 3189-3197; c) J. T. Xu, Y. Lin, J. W. Connell and L. M. Dai, *Small* **2015**, *11*, 6179-6185; d) T. H. Han, Y. K. Huang, A. T. L. Tan, V. P. Dravid and J. X. Huang, *Journal of the American Chemical Society* **2011**, *133*, 15264-15267.

[2] a) S. Navalon, A. Dhakshinamoorthy, M. Alvaro and H. Garcia, *Chemical Reviews* **2014**, *114*, 6179-6212; b) C. K. Chua and M. Pumera, *Chem. Eur. J.* **2015**, *21*, 12550-12562; c) H. W. Hu, J. H. Xin, H. Hu, X. W. Wang and Y. Y. Kong, *Applied Catalysis a-General* **2015**, *492*, 1-9; d) P. Tang, G. Hu, M. Z. Li and D. Ma, *Acs Catalysis* **2016**, *6*, 6948-6958; e) D. S. Su, G. D. Wen, S. C. Wu, F. Peng and R. Schlogl, *Angewandte Chemie-International Edition* **2017**, *56*, 936-964; f) C. Ampelli, S. Perathoner and G. Centi, *Chinese Journal of Catalysis* **2014**, *35*, 783-791.

[3] a) C. L. Su, M. Acik, K. Takai, J. Lu, S. J. Hao, Y. Zheng, P. P. Wu, Q. L. Bao, T. Enoki, Y. J. Chabal and K. P. Loh, *Nature Communications* **2012**, *3*; b) M. Patel, W. Feng, K. Savaram, M. R. Khoshi, R. Huang, J. Sun, E. Rabie, C. Flach, R. Mendelsohn, E. Garfunkel and H. He, *Small* **2015**, *11*, 3358-3368.

[4] a) K. Nakada, K. Fujita, G. Dresselhaus and M. S. Dresselhaus, *Phys. Rev. B* **1996**, *54*, 17954; b) M. Fujita, K. Wakabayashi, K. Nakada and K. Kusakabe, *J. Phys. Soc. Jpn.* **1996**, *65*, 01920.

[5] a) D. W. Boukhvalov, V. Y. Osipov, A. I. Shames, K. Takai, T. Hayashi and T. Enoki, *Carbon* **2016**, *107*, 810 - 810 ; b) A. M. Panich, A. I. Shames, M. I. Tsindlekht, V. Y. Osipov, M. Patel, K. Savaram and H. He, *Journal of Physical Chemistry C* **2016**, *120*, 3042-3053; c) K. A. Ritter and J. W. Lyding, *Nature Materials* **2009**, *8*, 235-242; d) V. L. J. Joly, M. Kiguchi, S. J. Hao, K. Takai, T. Enoki, R. Sumii, K. Amemiya, H. Muramatsu, T. Hayashi, Y. A. Kim, M. Endo, J. Campos-Delgado, F. Lopez-Urias, A. Botello-Mendez, H. Terrones, M. Terrones and M. S. Dresselhaus, *Physical Review B* **2010**, *81*.

[6] P. Ruffieux, S. Y. Wang, B. Yang, C. Sanchez-Sanchez, J. Liu, T. Dienel, L. Talirz, P. Shinde, C. A. Pignedoli, D. Passerone, T. Dumslaff, X. L. Feng, K. Mullen and R. Fasel, *Nature* **2016**, *531*, 489-+.

[7] D. Su, G. Wen, S. Wu, F. Peng and R. Schloegl, *Angewandte Chemie International Edition* **2016**, n/a-n/a.

[8] H. Hu, J. H. Xin, H. Hu, X. Wang and Y. Kong, *Applied Catalysis a-General* **2015**, *492*, 1-9.

[9] C. Gomez-Navarro, J. C. Meyer, R. S. Sundaram, A. Chuvilin, S. Kurasch, M. Burghard, K. Kern and U. Kaiser, *Nano Letters* **2010**, *10*, 1144-1148.

[10] a) Y. Jia, L. Zhang, A. Du, G. Gao, J. Chen, X. Yan, C. L. Brown and X. Yao, *Advanced Materials* **2016**, *28*, 9532-9538; b) Y. F. Jiang, L. J. Yang, T. Sun, J. Zhao, Z. Y. Lyu, O. Zhuo, X. Z. Wang, Q. Wu, J. Ma and Z. Hu, *ACS Catalysis* **2015**, *5*, 6707-6712.

[11] A. Bagri, C. Mattevi, M. Acik, Y. J. Chabal, M. Chhowalla and V. B. Shenoy, *Nature Chemistry* **2010**, *2*, 581-587.

[12] K. Savaram, M. Kalyanikar, M. Patel, R. Brukh, C. R. Flach, R. Huang, M. R. Khoshi, R. Mendelsohn, A. Wang, E. Garfunkel and H. He, *Green Chemistry* **2015**, *17*, 869-881.

[13] W. S. Hummers and R. E. Offeman, *J. Am. Chem. Soc.* **1958**, *80*, 1339-1339

[14] A. M. Dimiev and J. M. Tour, *Acs Nano* **2014**, *8*, 3060-3068.

[15] A. P. Seitsonen, A. M. Saitta, T. Wassmann, M. Lazzeri and F. Mauri, *Physical Review B* **2010**, *82*.

[16] a) K. Sendt and B. S. Haynes, *Proceedings of the Combustion Institute* **2005**, *30*, 2141-2149; b) K. Sendt and B. S. Haynes, *Combustion and Flame* **2005**, *143*, 629-643.

[17] J. Takashiro, Y. Kudo, S. J. Hao, K. Takai, D. N. Futaba, T. Enoki and M. Kiguchi, *Physical Chemistry Chemical Physics* **2014**, *16*, 21363-21371.

[18] a) B. Tryba, A. W. Morawski and M. Inagaki, *Carbon* **2005**, *43*, 2417-2419; b) E. H. L. Falcao, R. G. Blair, J. J. Mack, L. M. Viculis, C.-W. Kwon, M. Bendikov, R. B. Kaner, B. S. Dunn and F. Wudl, *Carbon* **2007**, *45*, 1367-1369.

[19] Y. Zhu, S. Murali, M. D. Stoller, A. Velamakanni, R. D. Piner and R. S. Ruoff, *Carbon* **2010**, *48*, 2118-2122.

[20] a) C. Faugeras, A. Nerrière, M. Potemski, A. Mahmood, E. Dujardin, C. Berger and W. A. d. Heer, *Applied Physics Letters* **2008**, *92*, 011914; b) A. C. Ferrari, J. C. Meyer, V. Scardaci, C. Casiraghi, M. Lazzeri, F. Mauri, S. Piscanec, D. Jiang, K. S. Novoselov, S. Roth and A. K. Geim, *Physical Review Letters* **2006**, *97*, 187401.

[21] X. Han, M. R. Funk, F. Shen, Y.-C. Chen, Y. Li, C. J. Campbell, J. Dai, X. Yang, J.-W. Kim, Y. Liao, J. W. Connell, V. Barone, Z. Chen, Y. Lin and L. Hu, *ACS Nano* **2014**, *8*, 8255-8265.

[22] G. P. Kotchey, B. L. Allen, H. Vedala, N. Yanamala, A. A. Kapralov, Y. Y. Tyurina, J. Klein-Seetharaman, V. E. Kagan and A. Star, *ACS Nano* **2011**, *5*, 2098-2108.

[23] W. Peng, S. Liu, H. Sun, Y. Yao, L. Zhi and S. Wang, *Journal of Materials Chemistry A* **2013**, *1*, 5854-5859.

[24] M. A. Pimenta, G. Dresselhaus, M. S. Dresselhaus, L. G. Cancado, A. Jorioa and R. Saito, *Phys. Chem. Chem. Phys.* **2007**, *9*, 1276–1291.

[25] A. Eckmann, A. Felten, A. Mishchenko, L. Britnell, R. Krupke, K. S. Novoselov and C. Casiraghi, *Nano Letters* **2012**, *12*, 3925-3930.

[26] A. Dimiev, D. V. Kosynkin, L. B. Alemany, P. Chaguine and J. M. Tour, *Journal of the American Chemical Society* **2012**, *134*, 2815-2822.

[27] a) S. Eigler, *Chemical Communications* **2015**, *51*, 3162-3165; b) S. Eigler, C. Dotzer, F. Hof, W. Bauer and A. Hirsch, *Chemistry – A European Journal* **2013**, *19*, 9490-9496.

[28] W. Gao, L. B. Alemany, L. Ci and P. M. Ajayan, *Nat Chem* **2009**, *1*, 403-408.

[29] Y. Lin, X. Han, C. J. Campbell, J.-W. Kim, B. Zhao, W. Luo, J. Dai, L. Hu and J. W. Connell, *Advanced Functional Materials* **2015**, *25*, 2920-2927.

[30] C. Su, M. Acik, K. Takai, J. Lu, S.-j. Hao, Y. Zheng, P. Wu, Q. Bao, T. Enoki, Y. J. Chabal and K. Ping Loh, *Nature Communications* **2012**, *3*, 1298.

[31] D. Yang, A. Velamakanni, G. Bozoklu, S. Park, M. Stoller, R. D. Piner, S. Stankovich, I. Jung, D. A. Field, C. A. Ventrice and R. S. Ruoff, *Carbon* **2009**, *47*, 145-152.

[32] a) T. E. Nickson, *The Journal of Organic Chemistry* **1986**, *51*, 3903-3904; b) B. Coq and F. Figueras, *Journal of Molecular Catalysis A: Chemical* **2001**, *173*, 117-134; c) R. S. Downing, P. J. Kunkeler and H. van Bekkum, *Catalysis Today* **1997**, *37*, 121-136.

[33] a) E. Gelder, S. D. Jackson and C. M. Lok, *Catalysis Letters* **2002**, *84*, 205-208; b) A. Corma and P. Serna, *Science* **2006**, *313*, 332-334; c) R. V. Jagadeesh, G. Wienhofer, F. A. Westerhaus, A.-E. Surkus, M.-M. Pohl, H. Junge, K. Junge and M. Beller, *Chemical Communications* **2011**, *47*, 10972-10974; d) J. Zhang, Y. Wang, H. Ji, Y. Wei, N. Wu, B. Zuo and Q. Wang, *Journal of Catalysis* **2005**, *229*, 114-118; e) F. Ragaini and S. Cenini, *Journal of Molecular Catalysis A: Chemical* **1996**, *105*, 145-148.

[34] a) S. Kim, E. Kim and B. M. Kim, *Chemistry – An Asian Journal* **2011**, *6*, 1921-1925; b) W. Lin, H. Cheng, J. Ming, Y. Yu and F. Zhao, *Journal of Catalysis* **2012**, *291*, 149-154; c) A. K. Patra, A. Dutta and A. Bhaumik, *Catalysis Communications* **2010**, *11*, 651-655.

[35] a) X. Li, H. Wang, J. T. Robinson, H. Sanchez, G. Diankov and H. Dai, *Journal of the American Chemical Society* **2009**, *131*, 15939-15944; b) H. Zhou, L. Shi and Q. Sun, *Chinese Journal of Catalysis* **2012**, *33*, 1463-1469; c) J. W. Larsen, M. Freund, K. Y. Kim, M. Sidovar and J. L. Stuart, *Carbon* **2000**, *38*, 655-661; d) H. H. Byung, H. S. Dae and Y. C. Sung, *Tetrahedron Letters* **1985**, *26*, 6233-6234.

[36] P. Tang, G. Hu, Y. Gao, W. Li, S. Yao, Z. Liu and D. Ma, *Sci. Rep.* **2014**, *4*.

[37] Y. Gao, D. Ma, C. Wang, J. Guan and X. Bao, *Chemical Communications* **2011**, *47*, 2432-2434.
[38] T. Taniguchi, S. Kurihara, H. Tateishi, K. Hatakeyama, M. Koinuma, H. Yokoi, M. Hara, H. Ishikawa and Y. Matsumoto, *Carbon* **2015**, *84*, 560-566.
[39] A. M. Dimiev, S. M. Bachilo, R. Saito and J. M. Tour, *ACS Nano* **2012**, *6*, 7842-7849.

Chapter 4- Microwave Assisted Carbon Combustion for Fabrication of Pristine Holey Graphene Nanoplatelets and their Application in Electrochemical Catalysis for Oxygen Reduction Reaction

4.1. Introduction

In the prior chapter, we reported a novel scalable approach to fabricate pristine holey graphene nanoplatelets, from microwave irradiation of partially oxidized graphite. In this work, we report a similar approach to fabricate pristine holey graphene nanoplatelets material directly from O_2 intercalated GIC (graphite intercalation compound) with short microwave irradiation. This not only shortened the fabrication time (as the intercalated GIC is directly used), but also changed the intrinsic holey graphene generation basic chemistry. It was inspired by earlier reports that, with the aid of high temperatures, both single layer ($< 400°C$) and multiple layer graphene ($600°C$) can be oxidized by molecular oxygen to form holes in their basal planes [1]. The mentioned oxidation chemistry also works for graphite [2]. However, only several top layers of graphene in graphite can be drilled through, due to the difficulty of the oxidant (molecular O_2 here) to access the inner graphene layers. Since we already demonstrated the intercalation of molecular O_2 into GICs in our previous work, we hypothesize that the intercalated O_2 molecules can act as an internal oxidant. With high local temperature achieved by dry microwave irradiation, generation of holes due to efficient oxidation in both internal and external graphene sheets in a graphitic particle is expected. In the same time, the quickly generated gases build up high internal pressure to push the graphene sheets apart. As a result, pristine holey graphene

nanoplatelets are also produced, which are referred as IGO series to differentiate the POG series of products. To our delight, we found that as synthesized IGO-HE nanoplatelets are of pristine quality, which is proved by the low I_D/I_G of 0.040 (Raman spectra) and high C/O ratio of 33.26 (XPS). The high conductivity of 35,195 S/m was reported in IGO-HE, in comparison to holey edge graphene synthesized from gasification of point defects in our previous work (POG-HE 17,514 S/m). Equally important, EPR studies demonstrated that the IGO series of holey graphene nanoplatelets product are also rich in zigzag edges.

A theoretical study demonstrated that the zigzag edge states in graphene nanoribbons chemically behave like a partial radical, capable to activate a wide range of molecules, including molecular oxygen.[3] Due to the existence of rich zigzag edges combined with high conductivity of holey graphene nanoplatelets, it is reasonable to assume that they should be an excellent electrochemical catalyst for ORR (oxygen reduction reactions). Dai and Wang et al. studied the electrochemical catalytic behavior of O_2 reduction, by depositing an air saturated electrolyte solution droplet (~15 µm) on the edge and on the basal plane of a piece of highly oriented pyrolytic graphite (HOPG). Since the basal plane of HOPG is almost defect free, direct evidence for catalytic roles of edge carbon atoms in ORR was correlated [4]. It was also reported that the defects in the highly ordered pyrolytic graphite (HOPG) exhibited an electron rate transfer constant 7 times higher than the defect-free HOPG, indicative of varying electron structure between the basal plane and the edge plane[5]. However in general, due to limited edges in HOPG or graphite, their practical applications as an efficient electrochemical catalysts is limited. Hence, so far no study has been reported on electrochemical catalytic activities of pristine holey graphene materials, which are both fundamentally and practically important.

ORR can occur either via a direct four-electron reduction pathway or a two-step, two-electron pathway and often these two pathways co-existed. The current platinum-based electro-catalysts for oxygen reduction reaction (ORR) are expensive and are susceptible to methanol crossover and carbon monoxide (CO) poisoning effects. Henceforth intensive research efforts were explored to develop new carbon-based materials as efficient, stable, low-cost, and sustainable metal-free catalysts as an alternative to Pt for ORR, including the work reported by our group[6]. The majority of carbon-based catalysts were developed by doping heteroatoms (non-carbon atoms) into graphene matrices to fine tune their physicochemical and electronic properties. The reactivity can be attributed to the electron transfer induced by the heteroatom doping between the electron donating/accepting heteroatom and the adjacent carbon. For instance, the carbon next to electron donating N or electron withdrawing B[7] can act as the active center. The electro-neutrality break induced by heteroatom occurs due to the disruption of π-π conjugation, indicating that the generated defects or edges can also act as the catalytic active sites.

While direct four-electron reduction pathway is preferred for fuel cell applications. The two-electron pathway is ideal for electrochemical generation of H_2O_2, a green oxidant, an environmentally benign chemical currently being used in diverse technological areas, ranging from industrial bleaching of paper and wastewater treatment, to oxidation of hazardous chemicals and bioremediation.[8] The only degradation product of its use is water, which also makes it one of the cleanest, most versatile chemical oxidants available for many large-scale syntheses *via* chemical oxidation processes.[9] The annual world production of hydrogen peroxide is approximately 2.2 million metric tons, synthesized by anthraquinone oxidation (AO) process[10]. The AO process is a multistep method that

requires significant energy input and generates waste. It requires noble metal based catalysts such as Pd and Au[11], stabilizers to delay or prevent decomposition of hydrogen peroxide [11a, 12], special equipment to transport, storage, and handling of bulk H_2O_2, thereby escalating expenses [11e, 13].

Continuous on-site electrochemical production of H_2O_2 via oxygen reduction reaction (ORR) provide an attractive alternative to replace AO-based H_2O_2 production technology[9], minimizing the above mentioned limitations. While there are tremendous efforts to develop graphene based electrochemical catalysts to improve 4-electron pathway for fuel cell applications, efforts to for $2e^-$ peroxide production are scant, especially in basic conditions.[14] Furthermore, direct generation of peroxide in acid media is desired for its application as Fenton's reagent, whereas in alkaline media, it is best suited for pulp bleaching. On-site electrochemical production of H_2O_2 for industrial applications requires a production method with high reaction rates, high efficiency, and low costs. Graphite chips coated with carbon black, graphite and a fluorocarbon binder to facilitate O_2 transfer at atmospheric pressure[15], are the commonly used electrodes for this process. Carbon fiber has been proposed to increase porous structures without losing selectivity of H_2O_2 production due to the high content of graphite component in carbon fiber. However, the catalytic active sites are still limited for high efficiency production. The number of catalytic active sites in our holey graphene materials are expected to be significantly increased by the largely expanded edges on the basal plane of graphene.[16] Furthermore, the existence of holes will also greatly facilitate mass transport.[16-17] All these features ensure efficient electrochemical H_2O_2 production. To our delight, we found that that in basic conditions the holey graphene nanoplatelets activate ORR mainly *via* a $2e^-$ pathway. A faradaic efficiency

of H_2O_2 production reached as high as 97%. This, combined with rapid and energy saving approach to be able to fabricate the material in a large scale, suggests that the holey graphene nanoplatelets material is promising material for metal free sustainable catalysts for electrochemical H_2O_2 production at low cost.

4.2. Results and Discussion

The present invention realizes the exploitation of microwave irradiation technique for synthesis of high quality holey edge graphene, not by creating point defects on basal plane but by realizing oxidation of graphite intercalated with O_2 as the oxidant. The IGO exhibits an I_D/I_G of 0.035, lower than POG (2.37), with C/O ratio of 5. The stabilized intercalated GIC was synthesized according to our previous work[18] and is referred to as IGO. The microwave heating mechanism is via joule heating, with the working principle summarized in **Scheme 4.1.** Upon the exposure of IGO to pulse microwave irradiation, rapid expansion of GIC, was observed with the first pulse. Further microwave irradiation, generates high local temperature, which in the presence of O_2, leads to the combustion of carbon atoms, generating holes.
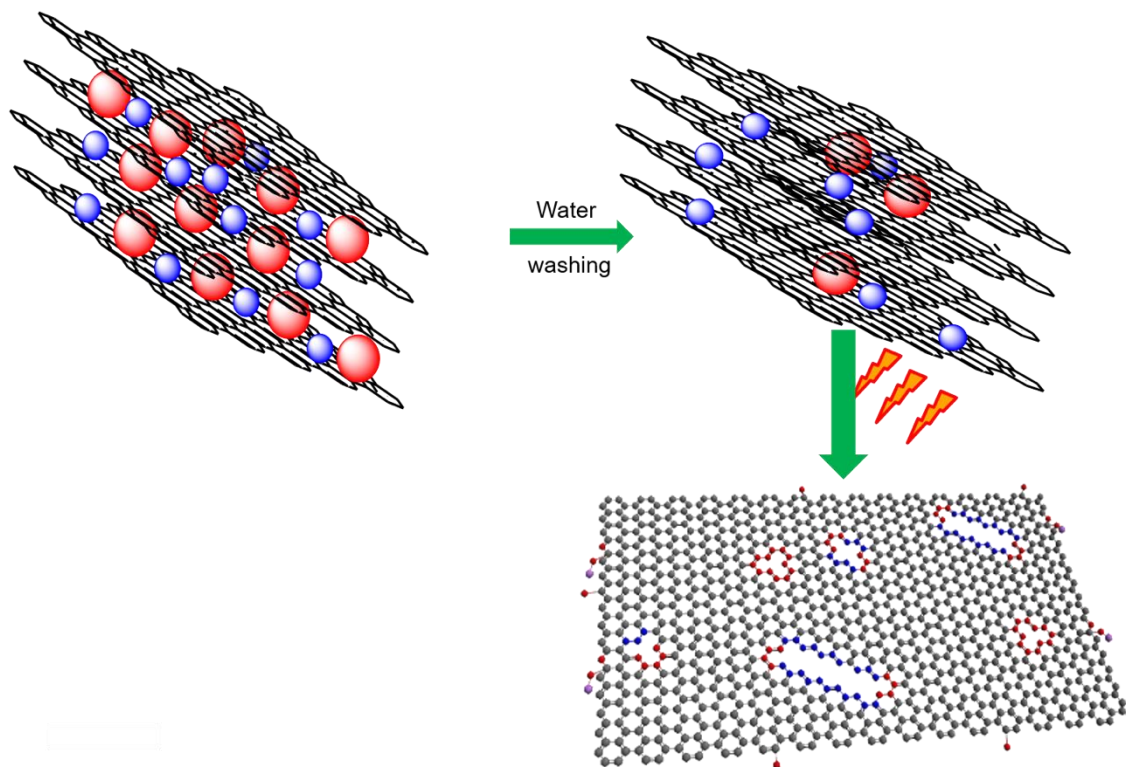
Scheme 4. 3. The schematic of holey graphene synthesized from IGO.

Indeed, the microwave irradiation of IGO for a duration of 5sec leads to expansion of intercalated graphite (IGO-exp), as shown in **Figure 4.1. (a, b)**, which upon further microwave irradiation generated holes (IGO-H), **Figure 4.1. (c, d),** whereas holes with etched edges were observed upon further prolonging the microwave irradiation (IGO-HE), **Figure 4.1. (e, f)**. The surface area of IGO-HE is 651m^2/g, which is slightly lower than the POG-HE (744m^2/g) and higher than the typical values (50-77 m^2/g) obtained from EG (expanded graphite) [19] and MEGO (microwave exfoliated graphite oxide) (463 m^2/g)[20].
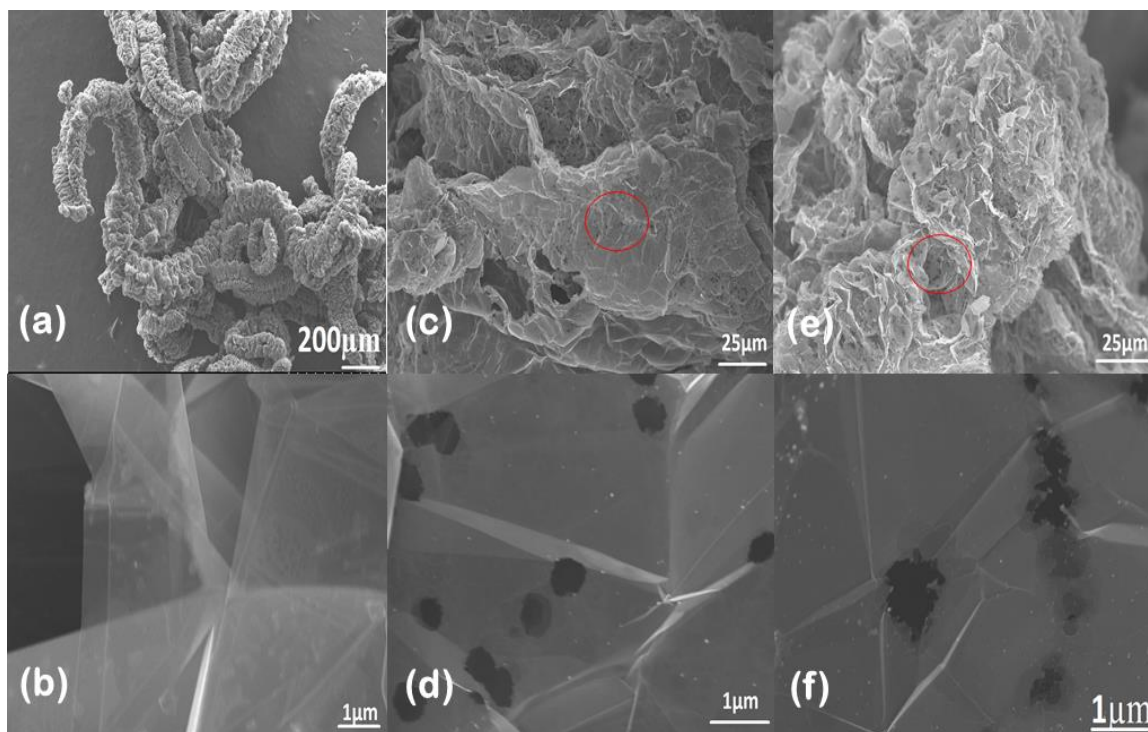
Figure 4.1. SEM image of IGO sample upon pulse microwave irradiation, expansion of IGO (a, b), IGO-H (c, d) where holes of <500nm were observed, and IGO-HE (e, f) where edges with enlarged holes of >500nm were observed.

The synergy of air and trapped O_2 in the oxidation of the intercalated graphite @ temperature was studied *via* TGA analysis. The high temperature heating of the intercalated samples was conducted to measure the amount of O_2 that is entrapped in the intercalated graphite. A total of 20% weight loss was observed at the end of 900°C, with an initial weight loss at 40°C after stabilization. This is followed by a 1% decrease for every 10-15°C till 200°C, contributing to the removal of the trapped O_2. There was a 1% weight loss for every 30-50°C from 200-380°C, which indicates the presence of organo-sulfates[21] in the intercalated graphite. Then, there was only a 2% weight loss until it reached the final temperature of 900°C. The major weight loss reported is due to the presence of trapped O_2 and the sulfate moieties, **Figure 4.2. (a).** The SEM images of the TGA treated samples, when analyzed indicate the expansion of IGO, with no holes or edges observed **Figure 4.2. (c)**, whereas holes were rarely observed in POG. This provides insight into the importance of

microwave heating, where high local temperatures in combination with the oxidants, i.e. O_2, and air lead to hole generation on the expanded graphite[1].
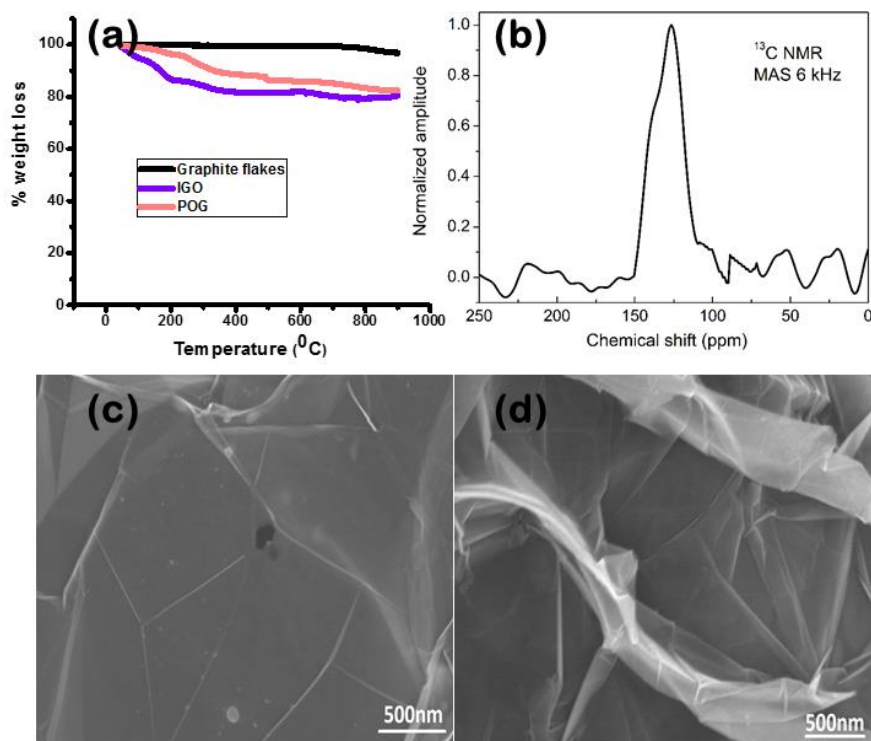
Figure 4.2. The TGA curves of IGO and POG compared with the graphite flakes (a),SEM analysis of the IGO (c) and POG (d) after TGA in N_2 at 40-900° C. Typical ^{13}C MAS NMR spectrum of IGO-HE (MAS rate 6 kHz) (b).

The high degree of crystallinity of these edged holey graphene was studied by Raman spectra, which indicated the presence of a D band (breathing modes of the sp^2 carbon in the ring activated by defects can be either on the basal plane or edges) and a prominent G band (bond stretching of sp^2 carbons in the ring) in all of the IGO series. The lowest I_D/I_G (0.040) was reported for IGO-HE when compared to POG-HE (0.28), indicating its high quality[22]. A doublet in the 2D region was observed by a Lorentzian fit, as shown in **Figure**

4.3. (c), indicating that the as synthesized IGO-HE consist of few layers.
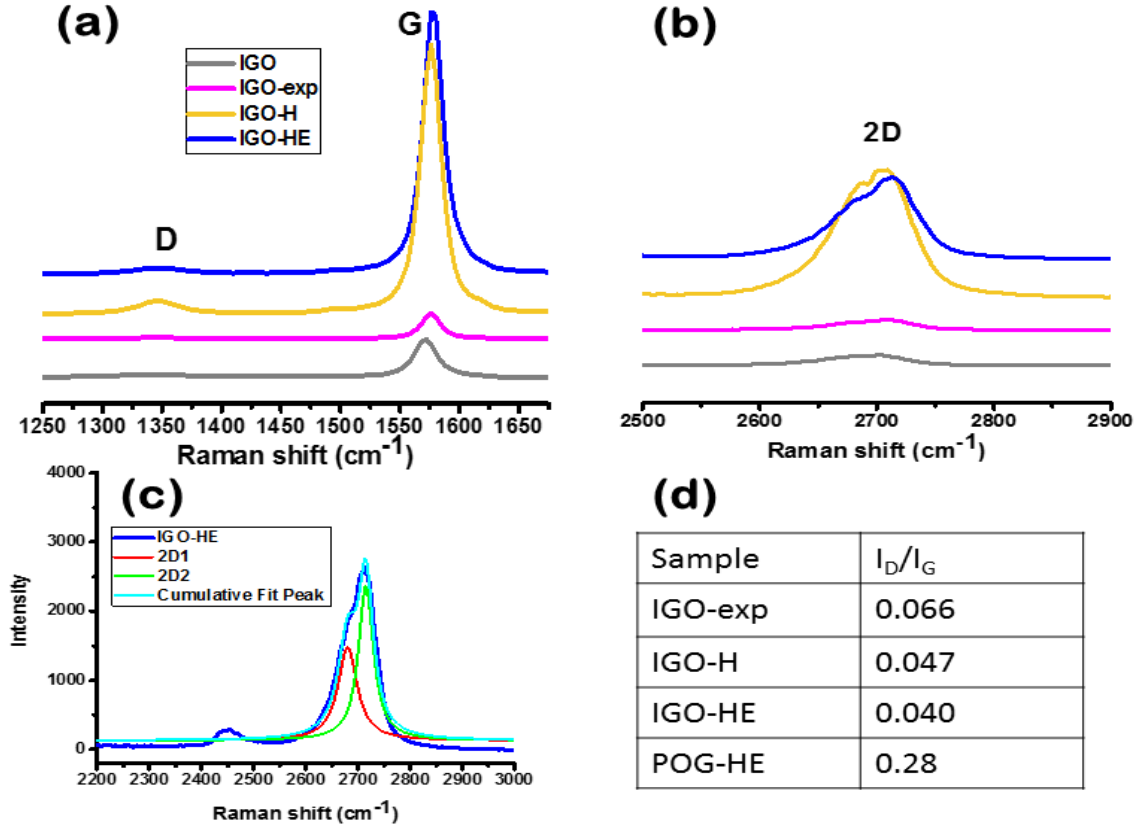
Figure 4.3. Raman data showing a characteristic D and G band (a), and 2D band (b), the deconvolution of 2D band (c), I_D/I_G values of IGO series, with increased microwave irradiation.

The deconvolution of C spectra exhibits a sharp peak at binding energies of 284ev, assigned to sp^2 carbon in C=C, and 291ev, assigned to π-π^* transition peak, indicating the preservation of delocalized π conjugation[23] and supporting high crystalline graphitic domains as recorded from Raman spectra. The increased microwave irradiation time exhibits an increased C=C peak in the order: IGO-exp (64.9%) < IGO-H (65.88%) < IGO-HE (74.47%), which is supported by the decreased I_D/I_G. The microwave irradiation of IGO initially generates defects (IGO-exp) which upon prolonged microwave irradiation, leads to the gasification of existing defects, accompanied with the generation of new

defects (POG-H). Further microwave irradiation leads to the removal of defects with enlarged hole generation (POG-HE). A single peak at 128ppm in the ^{13}C SSNMR, a characteristic of graphitic sp^2 carbon[24], was observed in the IGO-HE as shown in Figure **4.2.(b)**. The superior crystalline structure of the IGO-HE was further supported by a high conductivity of 35,195 S/m compared to POG-HE (17,514 S/m) when calculated according to four-point probe method.

The presence of peaks at 286ev and 287ev are attributed to C-O [25] (532ev for O) and C=O (533ev for O). An additional O deconvolution peak is observed at high binding energies in IGO-HE, which disappears in the presence of Ar etching, as seen in **Figure 4.4. (g,h)** , indicative of active edges that gets saturated with atmospheric O$_2$.
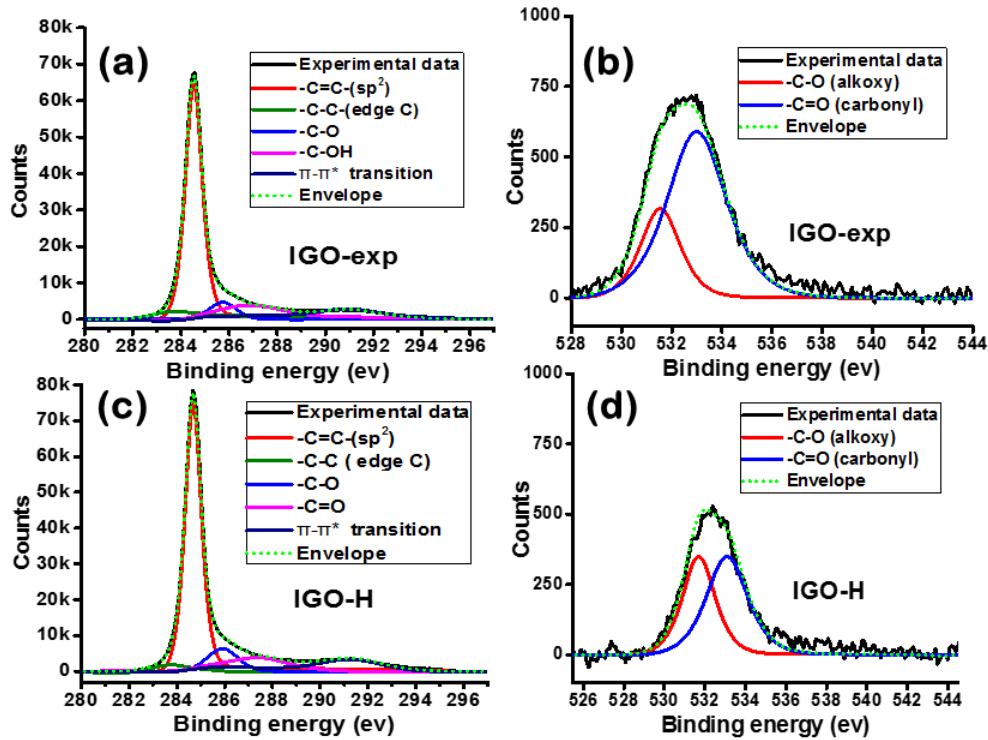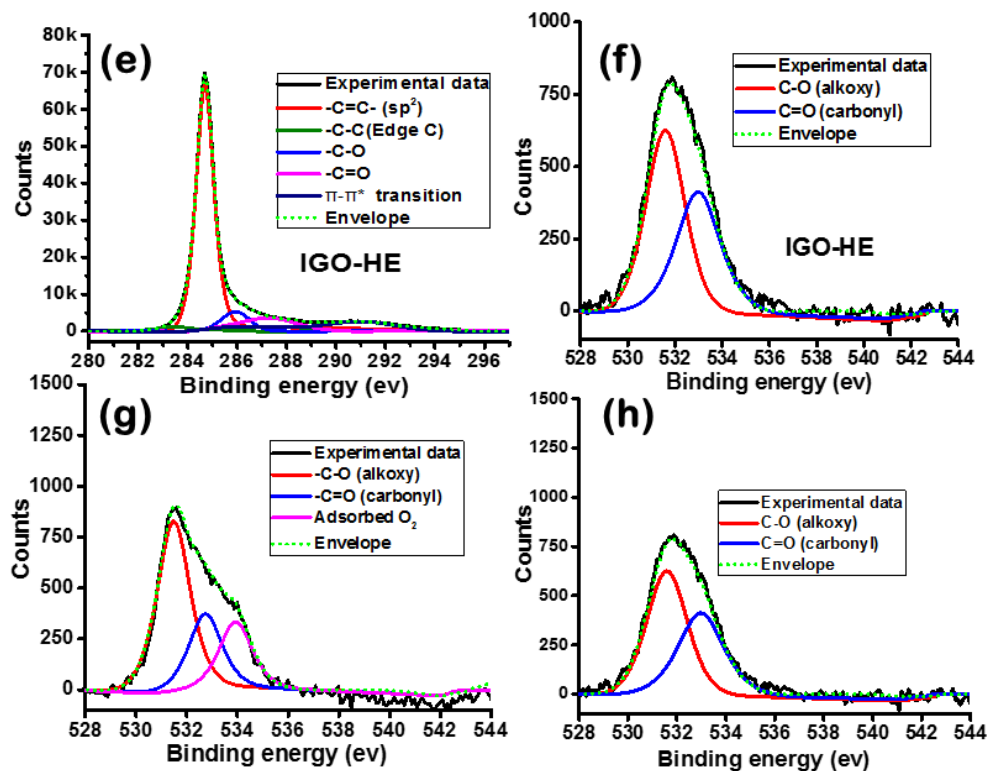
Figure 4.4. The XPS deconvolution data of C and O peaks in IGO-exp (a, b), IGO-H (c, d), and IGO-HE (e, f). XPS of O deconvolution before (g) and after Ar etching (h), indicative of reactive edges.

The quantification of various C and O functionalities with varying microwave irradiation time is listed below in **table 4.1.**

Table 4. 1. The quantification of % C and %O in IGO at different microwave irradiation time.

Cataly st	C-H/C-C (283e v)	C=C (284e v)	C-O (286e V)	-C=O - (287e v)	Π-Π transition(291 ev)	C/O rati o	% C	% O
IGO-exp	6.57	64.93	11.3	8.61	8.59	32.05	96.97	3.03
IGO-H	6.57	65.88	8.58	9.92	9.06	56.96	98.27	1.73

IGO-HE	5.59	74.48	8.04	10.99	0.89		33.26	97.08	2.92

	C-O(531.4ev)	C=O (533ev)
IGO-exp	27.11	72.88
IGO-H	44.91	55.09
IGO-HE	58.35	41.65

The presence of edges in holey graphene was confirmed by the broad EPR signals, as observed in **Figure 4.5. (a, b)**. The red traces clearly demonstrate that oxygen evacuation causes narrowing of the broad components. Thus, line widths ΔH_{pp} decrease by ~ 3 mT and 7 mT for IGO-H and IGO-HE respectively. Opening of sealed capillary tubes back to ambient air, broaden the lines back to initial line width values.
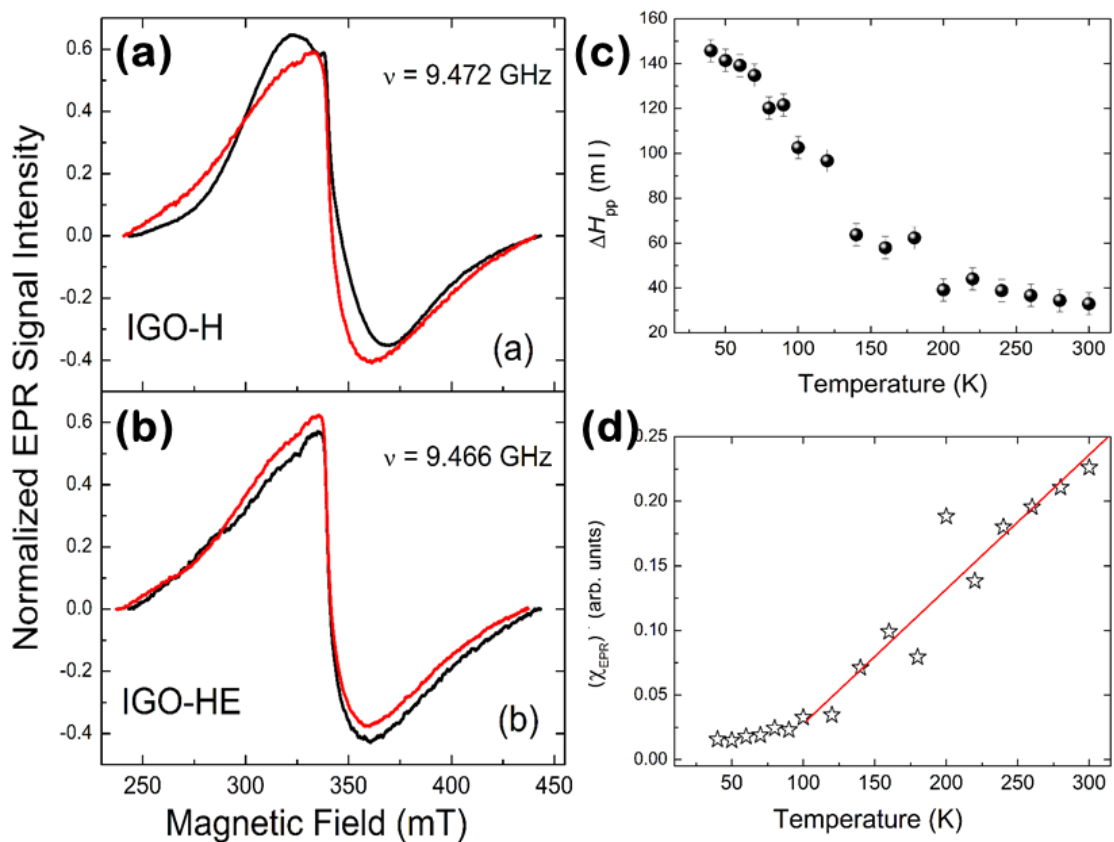
Figure 4.5. The RT EPR spectra of IGO-H (c, n = 9.472 GHz) and IGO-HE (d, n = 9.466 GHz) samples. Black traces – samples open to air, red traces – samples evacuated to 10^{-4} mbar. The temperature dependence of broad line width ΔH_{pp} for air containing IGO-H sample (c) with temperature dependence of inverse integral intensity (proportional to χ_{EPR}^{-1}) of the EPR signal for air containing IGO-H sample (d). Above $T = 120$ K χ_{EPR}^{-1} obeys the Curie-Weiss law with $\theta \sim 75$ K whereas below 120 K θ changes to $\sim$ -10 K.

On decreasing the temperature, EPR for both air containing samples show similar patterns:

(i) the broad components continuously broaden and remain unobservable below $T \sim 40$ K;

(ii) the narrow component remains practically unchanged and very weak in intensity

(**Figure 4.5. (c, d)**). The data infers that the interactions of edge spins with triplet molecular

oxygen may be responsible for the EPR line narrowing upon air evacuation. Moreover,

adsorption of oxygen molecules on graphene in the vicinity of edge spins explains

progressive line broadening on cooling of air-containing IGO-HE and IGO-H. In addition,

complicated behavior of the EPR susceptibility on cooling may indicate direct involvement of oxygen in the interactions between edge spins, which is responsible for the broad EPR signals.

The as synthesized catalyst was tested for oxygen reduction due to its (1) superior conductivity (high quality defect-free basal plane), (2) presence of edges which act as catalytic centers for the activation of molecular O_2 and (3) presence of holes on the basal planes which enhance the mass transport. The CV of IGO-HE exhibited a cathodic reduction peak in O_2 saturated solution, which is absent when saturated with N_2, indicating the electrochemically active nature of edge graphene for reduction of oxygen in basic media (**Figure 4.6.**). This catalytic activity can be explained by DFT calculations, where Dai and coworkers stated that the edge carbon can exhibit high charge densities when compared to basal plane[26], i.e. edge carbon can induce an electron transfer leading to acquisition of positive charges on edge carbon, which renders negative charge on the neighboring carbon[27]. The IGO-HE exhibits a lower onset potential (vs. RHE) when compared to carbon black and the bare electrode, **Figure 4.6. (b)**.
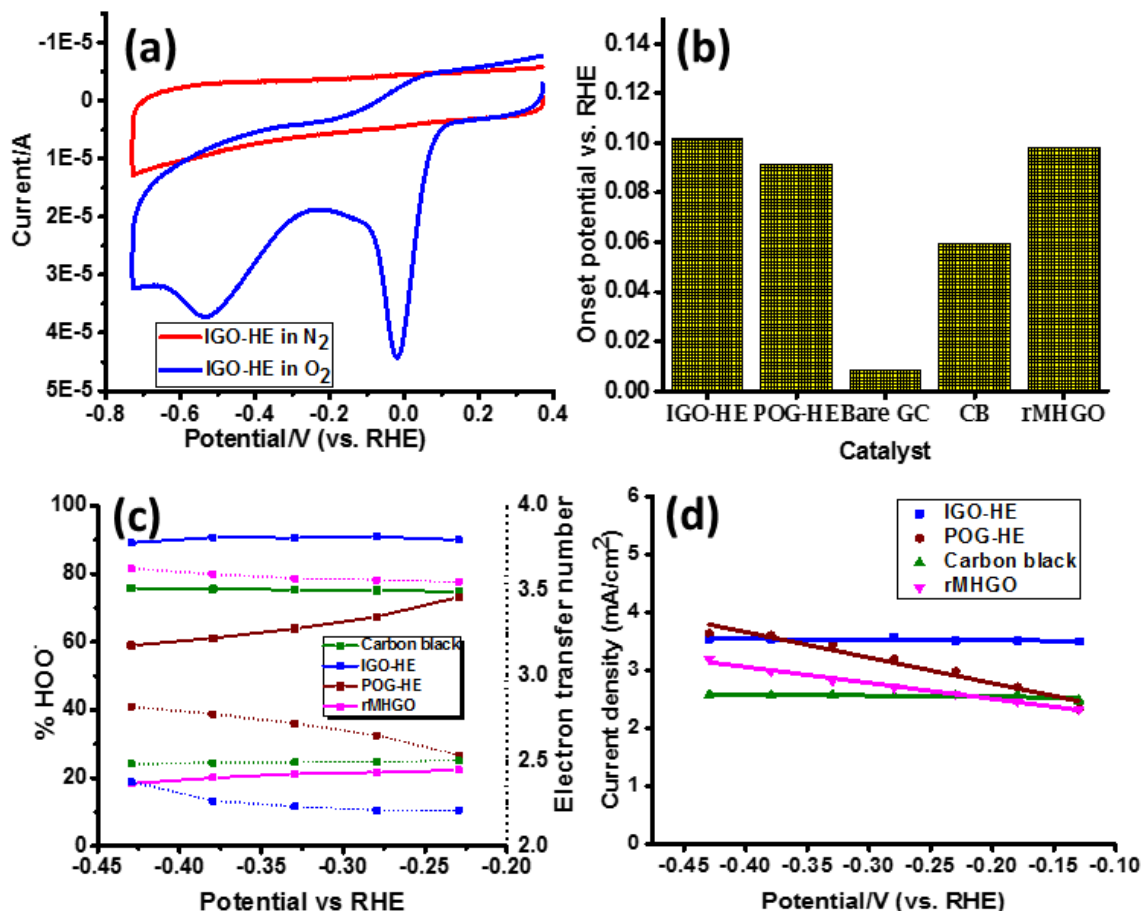
Figure 4.6. The CV of IGO-HE in 0.5 M KOH (a), and onset potential in comparison (b) with other catalyst, the electron transfer number (c) with peroxide yield (d) of various catalysts in 0.5M H_2SO_4 (c).

The ORR exhibits 2 peaks, indicating that the oxygen reduction occurred *via* $2e^-$ pathway, i.e. initial peroxide generation followed by its reduction to water. The difference in potential between two steps is around 0.37-0.40 in IGO-HE, indicating that the two processes occur far away from one another and can be separated to produce peroxide in alkaline media, facilitating its application in bleaching industry. The % peroxide and electron transfer number were calculated by recording the LSV using a Rotating Ring Disk electrode (RRDE). The % HO_2^- and electron transfer number (n) was measured according to the equation below:

$$\% \ HO_2^- = \frac{200 \times \frac{Ir}{N}}{I_d \times \frac{Ir}{N}} \qquad (1)$$

$$n = \frac{4 \times I_d}{I_d + \frac{Ir}{N}} \qquad (2)$$

I_d and I_r are the disk and ring currents, whereas N is referred to as the current collection efficiency of Pt ring electrode. N was determined using the redox reaction of $K_3Fe(CN)_6$ and was calculated to be 0.424. The LSV of IGO-HE exhibited the lowest % HO_2^- generation, which was quantified as 90-95% with an electron transfer number of 2.21 to 2.12 at -0.5V vs Ag/AgCl. This reported % HO_2^- generation is much higher than carbon black 77.96% (2.44 is the electron transfer number), a common electrode used for onsite peroxide production [28].

The current density at 2000rpm was found to be higher in the case of IGO-HE as compared to the traditional carbon black and somewhat higher than that of rMHGO and POG-HE. The Koutecky-Levich (K-L) equation is used to analyze kinetic parameters such as effective diffusion coefficient of O_2 (D_0) and electron transfer rate constant. The Koutecky-Levich equation is as follows:

$$1/J = 1/J_L + 1/J_K = 1/B\omega^{0.5} + 1/J_K$$

where J_K is the kinetic limiting current density, J_L is the diffusion limiting current density, B is the Levich constant and ω is the angular rotation rate of the disc electrode (rad/s). The Levich constant is given by the equation, $B = 0.62nFC_0(D_0)^{2/3}v^{-1/6}$ and $J_K = nFkC_0$, where n is the number of electrons transferred in oxygen reduction reaction (mol^{-1}), F is the Faraday constant (F=96485 C mol^{-1}), C_0 is the oxygen concentration (mol cm^{-3}), D_0 is the effective diffusion coefficient of O_2 (cm^2s^{-1}), v is the kinematic viscosity of electrolyte

$(cm^2 s^{-1})$ and k is the electron transfer rate constant. The K-L plots (J^{-1} vs $\omega^{-1/2}$) for IGO-HE, POG-HE, carbon black and rMHGO at a potential of -0.5V are compared in **Figure 4.7(a)**.
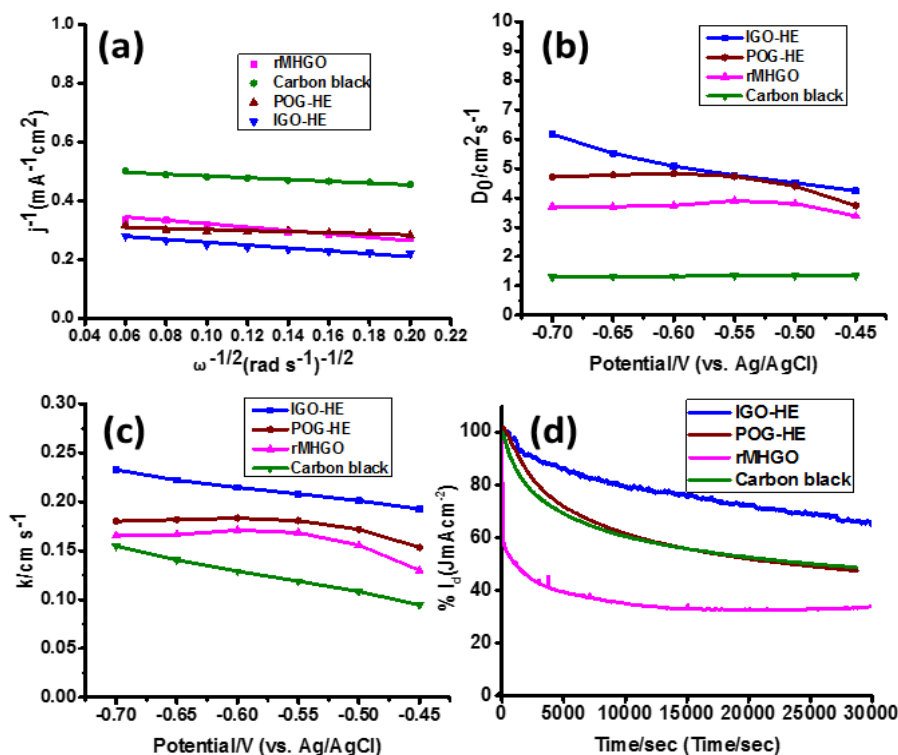
Figure 4.7. The K-L plots (a), effective diffusion coefficient, D_0 (b), electron transfer constant (c), and stability of the catalyst over time (d) of IGO-HE in comparison with other catalysts.

The slope and intercept of K-L plot affords Levich constant (B) and J_K, which are used to calculate D_0 and k. The IGO-HE has a superior O_2 diffusion coefficient of 5.51, indicating smoother and faster diffusion of O_2 due to the presence of holes, and an electron transfer rate constant of 0.21, indicating higher catalytic activity of the edges, in comparison to other catalyst. The effective diffusion coefficient and rate constant of various electrode catalysts are compared and elucidated in **table 4.2.**

Table 4.2. The effective diffusion coefficient, electron transfer rate constant, and tafel slope of the catalysts.

Sample	Effective diffusion coefficient , D_0	Electron transfer rate constant	Tafel slopes	
			a	b
IGO-HE	5.51	0.21	60.47	118.11
POG-HE	4.40	0.17	61.63	125.09
Carbon black	1.34	0.11	70.73	130
ErHGO	3.81	0.17	62.52	120.58

The kinetics of O_2 adsorption can be explained *via* Tafel plots. The typical ORR of IGO-HE exhibits two slopes, one at 60.47mV corresponding to surface reaction rate on the catalyst, the representative of overall ORR speed of the reaction. An additional slope at 118.11mV in higher over potential region was also recorded, which denotes the dependence of ORR rate on O_2 diffusion (a higher diffusion coefficient), as seen in **Figure 4.8. (a)**. The reported values are similar to that of Pt/C (60mV, 120mV). The IGO-HE also exhibits tolerance to methanol poisoning, as seen in **Figure 4.8. (b),** similar to carbon based catalyst reported in the literature.
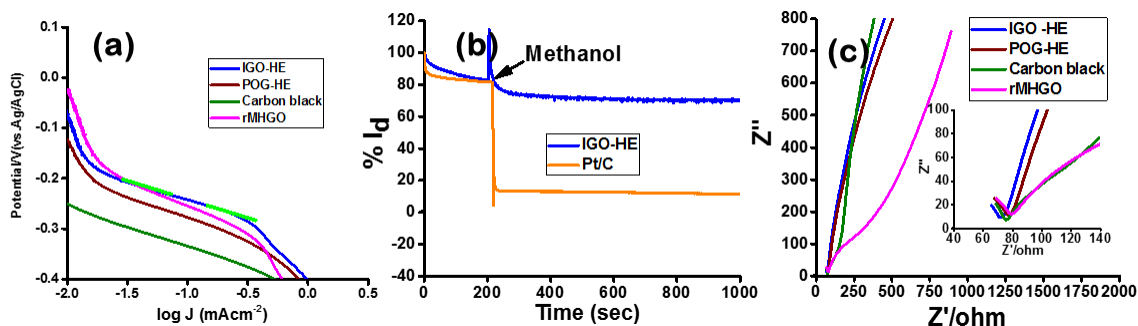
Figure 4.8. The Tafel slope (a), the methanol poisoning in comparison to Pt/C (b), the electron impedance spectra (c) of IGO-HE.

Nyquist plots from electron impedance spectra (EIS) were collected to gain insight into the reaction at the electrode surface. IGO-HE and POG-HE have diminished surface resistance at the active electrode surface in higher frequency region and the slope of the tail is more vertical to real axis, indicating superior conductivity of the catalyst, **Figure 4.8. (c)**.

For practical applications, stability and durability of the catalyst are of significant importance. The chrono-amperometry response of current over time was recorded for IGO-HE, which exhibited a current decrease to 65.83% by the end of 8hrs, a value much higher than carbon black (47.28%) and POG-HE (48.45%), indicating the stability of catalyst towards in situ peroxide generated. A faradaic efficiency of 97% was recorded for IGO-HE after 7hrs (from 94% at the beginning), while in the case of carbon black and rMHGO, it gradually increased to 85% in former case and 80% in latter case. The increased peroxide production over time indicates modification of catalyst to generate more active centers for peroxide production and hence decreased stability over time. The intrinsic stability of IGO-HE exhibited superior performance in various electrolyte solutions, as, elucidated in **Figure 4.9**.
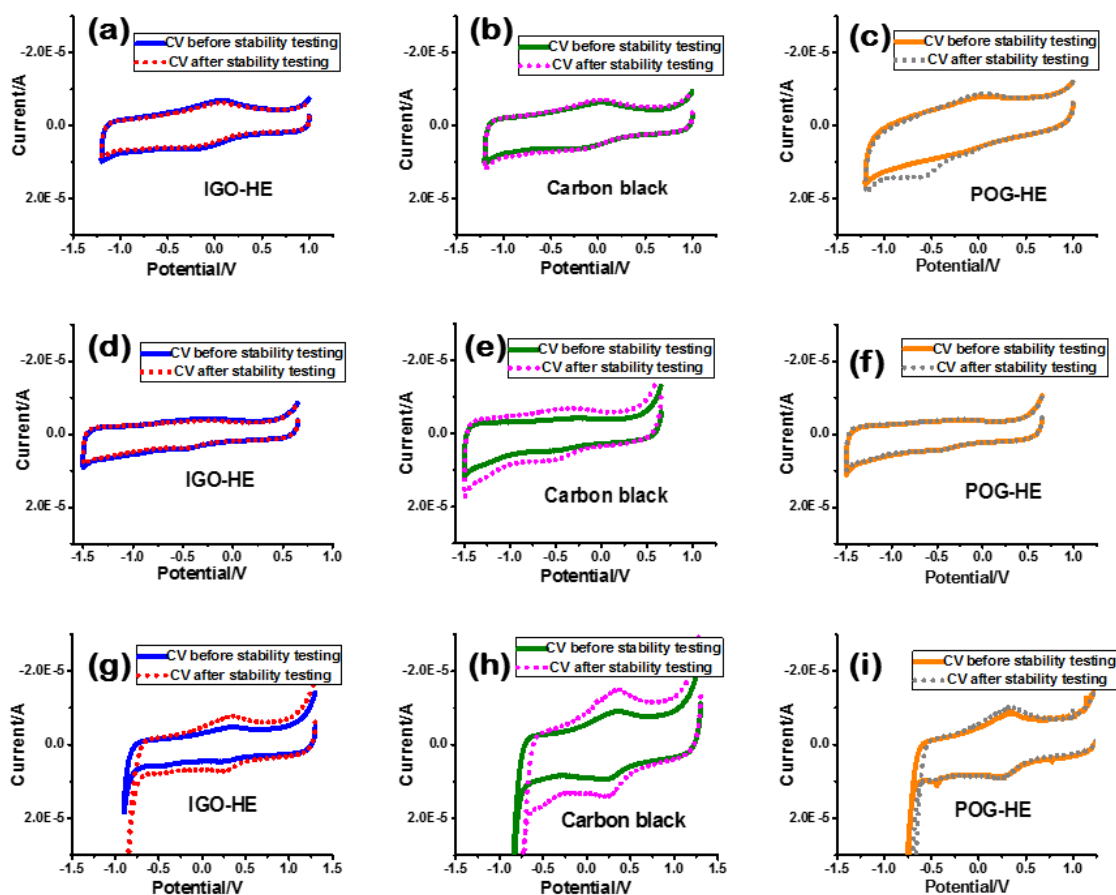
Figure 4.9. The intrinsic stability of catalysts in various electrolyte solutions, (a-c) buffer, (d-f) 0.1M KOH, (g-i) 0.5M H_2SO_4.

The sweep step function in electrochemistry helps us to understand the stability of the compound when it is oxidized at higher potential and then the CV recorded. The compound which is resistant to oxidation remain similar without any change in the CV before and after the testing whereas the one's which are not resistant show reduction peaks, which can be reversible or irreversible.

In buffer solution i.e. pH 7, ten CV's were recorded in the potential range of -1.25V to +1.2V. The electrode is swept to a potential from 0 to +1.2V and then it is kept at that particular potential for 2hrs. Subsequently, it is swept to 0V, then to -1.25V and again to 0V. After this step, ten more CV's were recorded from -1.25V to +1.2V. The overlay of

the CV's before and after stability testing, indicates that the IGO-HE exhibits higher stability, when compared to carbon black which has reversible intrinsic oxidation and reduction peaks. However, POG-HE exhibits a reduction peak after undergoing the stability testing, represented in **Figure 4.9. (a-c)**.

In basic solution, i.e., 0.1M KOH, ten CV's were recorded in the potential range of -1.5V to +0.5V. Then the electrode is swept to a potential from 0V to +0.5V and then it is kept at that particular potential for 2hrs. Subsequently, it is swept to 0V, then to -1.5V and again to 0V. After this step, ten more CV's were recorded from -1.5V to +0.5V. The overlay of the CV's before and after stability testing, indicates that the IGO-HE and POG-HE exhibits superior stability compared to carbon black which exhibits reversible intrinsic oxidation and reduction peaks after stability testing, represented in **Figure 4.9. (d-f)**.

In the case of acidic solution, i.e., 0.5M H_2SO_4, ten CV's was recorded in the potential range of -0.9V to +1.5V. Then the electrode is swept to a potential from -0.9V to +1.5V and then it is kept at that particular potential for 2hrs. Subsequently, it is swept to 0V, then to -0.9V and again to 0V. After this step, ten more CV's were recorded from -0.9V to +1.5V. The IGO-HE and carbon black exhibits reversible intrinsic oxidation and reduction peaks after stability testing, whereas no change is observed in POG sample, as represented in **Figure 4.9. (g-i)**. The above data gives us information about the superior stability of IGO-HE when compared to carbon black and POG-HE in various electrolyte solutions with different pH.

4.3. Conclusion

The present invention offers advantages for the large-scale synthesis of holey structures, which are as follows: [1] The use of microwave irradiation makes the approach rapid and low-energy consuming. [2] Dry oxidation chemistry eliminates the need for post treatment to obtain the product. [3] Cheap raw materials are used, since intercalated graphite flakes were utilized. [4] The use of H_2SO_4, ammonium persulfate and O_2 for the intercalation process marks the approach to be environmentally friendly. [5] The holey graphene/graphite synthesis does not require cleaning of the product after microwave irradiation. [6] The as fabricated holey graphene does not have high oxygen containing functional groups, which leads to superior conducting properties. These benefits allow for the practice of the above-mentioned technique for large-scale synthesis of holey graphene/graphite structures with superior conductivity of 35,195S/m, allowing its application as electro catalyst for reduction of O_2. The as synthesized holey structures can be used for the onsite peroxide production, which is an important bleaching agent in paper and textile industry.

4.4. Experimental section

4.4.1. Material synthesis

IGO-HE synthesis: Graphite intercalation compound with SO_4^{-2} is achieved by following the recipe process described by Tour's group. In brief, 1000mg of ammonium persulfate (reagent grade 98%, Sigma Aldrich) was dissolved in 10ml H_2SO_4 (98% Pharmaco Aaper). The solution mixture was stirred for 5-10mins to dissolve the salt and form a uniform suspension. To this solution mixture, 200mg of graphite flakes were added (size >500μm).

The reaction mixture was stirred for 6hrs to form the reversible graphite intercalation compound. The graphite intercalation compound is purged with O_2 at the rate of 90-120ml/min for a period of 1hr and then the sample is quenched in 200ml of water and then washed via vacuum filtration through a polycarbonate membrane with a pore size of 0.8 µm using 200ml water each for four times. The product was dried in the oven at 80°C overnight.

Approximately 50mg of the above sample, referred to as Intercalated Graphite with O_2 (IGO), was microwaved at different powers, pursuing pulse radiation of 5sec each. The obtained product is a dry oxidation chemistry approach and hence does not need further cleaning of the sample. The product is collected and characterized.

For the expansion of the IGO, approximately 50mg of the sample was microwaved at 200W for 5sec in a CEM microwave vessel. The obtained product was collected as such without any post treatment (IGO-exp). For the generation of only holes on the IGO sample, approximately 50mg of the sample is taken and microwaved twice at 300W for 5sec each (total 10sec) in a CEM microwave vessel. The obtained product was collected as such without any post treatment (IGO-H). For the generation of holes and edges on the IGO sample, approximately 50mg of the sample is taken and microwaved at 300W for 5sec each for three times (total 15sec) in CEM microwave vessel. The obtained product was collected as such without any post treatment (IGO-HE).

POG-HE synthesis: Graphite intercalation compound with SO_4^{-2} is achieved by following the recipe process described by Tour's group. In brief, 1000mg of ammonium persulfate (reagent grade 98%, Sigma Aldrich) was dissolved in 10ml H_2SO_4 (98% Pharmaco Aaper). The solution mixture was stirred for 5-10mins to dissolve the salt and form a uniform

suspension. To this solution mixture, 200mg of graphite flakes were added (size >500µm). The reaction mixture was stirred for 6hrs to form the reversible graphite intercalation compound. The graphite intercalation compound is purged with O_2 at the rate of 90-120ml/min for a period of 1hr and then heated at 80^0C for 1hr. This sample is quenched in 200ml of water and then washed via vacuum filtration through a polycarbonate membrane with a pore size of 0.8 µm using 200ml of water each for four times. The product was dried in the oven at 80^0C overnight.

Approximately 50mg of the above sample, referred to as Partially Oxidized Graphite (POG), was microwaved three times at 200W for 5sec each (total 15sec) in a CEM microwave vessel. The obtained product was collected as such without any post treatment and characterized.

rMHGO (reduced Microwave holey GO): In a 50ml round bottomed flask, 20mg of graphite powder (Sigma Aldrich, ≤20µm lateral size) was added and mixed with 8ml of concentrated sulfuric acid (98%, ACS grade). The mixture was cooled in an ice bath for 5mins and then to this mixture, 2ml of concentrated nitric acid (70% ACS grade) is added and further cooled for another 5mins. To this reaction mixture, 100mg of potassium permanganate (ACS grade) is added and mixed for about 1min until it is properly dispersed and then subjected to microwave irradiation at 300W for 40sec. The as obtained product is quenched with 200ml of ice containing 5ml of 35% H_2O_2 and then filtered through 0.2µm polycarbonate filter paper. This is followed by washing with 4% HCl solution and then with 1000ml of deionized water in 200ml aliquots. The as obtained product is dried in a vacuum at room temperature for 3 days. The vacuum dried product is placed in a glass boat into the CVD tube and then N_2 is allowed to flow into the tube for 1hr at 50ml/min.

The resulting setup is heated at 500^0C for 2hrs in N_2 and then the sample is allowed to cool down. The resulting product is cleaned with dil. HCl to remove any contamination and then dried in the oven at 60^0C overnight.

4.4.2. Material characterization

SEM: The surface morphology of the as synthesized catalyst is characterized via Scanning Electron Microscopy (SEM) using a HITACHI S-4800 Field Emission Scanning Electron Microscope (FE-SEM, Hitachi Co. Ltd). The SEM sample is prepared by placing the powder on carbon tape, which is affixed to the stud, and the sample is analyzed by applying a voltage range of 2-5KV.

Raman spectroscopy: The Raman spectroscopy was collected by depositing the dispersed samples on an Anodisc membrane and the spectra were collected with a Witech alpha 300 Raman spectroscopy instrument. A laser power of 12W with an integration time of 20sec and an excitation laser wavelength of 532nm was used to collect the spectra. The spectra was collected on a sample size of 20µm W*H with 4 images per line (total 16 spectra).

XPS: X-ray photoelectron spectroscopy (XPS) is used to detect the functional state of carbon and oxygen in the holey graphene. A gold substrate is used for the analysis on which a slurry of the catalyst was dropped (thickness of approximately 30-50nm). The XPS spectra was acquired using a Thermo scientific K-Alpha system with a monochromatic Al Kα x-ray source (hν = 1486.7ev). For data analysis, smart background subtraction was performed and the spectra were fit with the Gaussian/Lorentzian peaks using a minimum deviation curve fitting method (Advantage software package). The integrated peak areas

along with the Scofield sensitivity factor were used to determine the functional composition.

Electronic properties: The IGO-HE and POG-HE samples were sonicated in an ethanol water solution (3:2 vol ratio) and these solutions were used to make the films. The films were fabricated by vacuum filtering the above solutions through an anodic filter membrane with a 0.2µm pore size. The films were vacuum dried to remove the residual solvent before making sheet resistance measurements. The sheet resistance is measured using a four probe resistivity probe from Lucas laboratories, model 302. The IGO-HE film recorded a sheet resistance of 115.5Ω whereas 230.85Ω was recorded for POG-HE. The films were assembled by using the same concentration of 1.03mg/ml. The graphene films were then transferred onto Si surfaces after etching the alumina anodic membrane using 4M NaOH. Then, the sample is washed with water thoroughly until the pH of the washed solution becomes neutral and the film is transferred onto a silica substrate, which are vacuum dried. The film thickness for these graphene films was measured with Rutherford Backscattering spectroscopy (RBS) using a 2MeV He^{+2} ion beam produced in a tandem accelerator with an ionic current of 2-3nA. Spectra were collected in a back scattering geometry and simulations were performed using the SIMNRA program. The thickness of the film was found to be 246nm for IGO-HE and 247nm for POG-HE. The conductivity of the films was calculated from the sheet resistance and thickness using the following formula

$$\text{Conductivity} = \frac{1}{sheet\ resistance \times thickness}$$

This formula can be used to measure films thickness not more than half of the probe spacing (the distance between two probes of the four-point probe instrument). The error in this case is less than 1%.

4.4.3. Electrochemical measurements

A typical three electrode cell is used to perform the electrochemical oxygen reduction reaction. A rotating ring disc electrode (RRDE) is used as a working electrode onto which the catalytic materials were coated. Ag/AgCl is used as a reference electrode and gold (acidic media)/Pt wire (basic media) is used as the counter electrode. The CV (Cyclic Voltammetry) and LSV (Linear Sweep Voltammetry) of the as prepared samples were analyzed by using a computer-controlled potentiostat (CHI 760C CH Instrument, USA). The working electrodes were prepared by dispersing 4.6mg of the as prepared catalyst in 980μl of NMP and 20μl of 10wt% nafion aqueous solution by sonication and drop casting 15μl of the above dispersed solution onto the RRDE. The electrode is dried under vacuum and then the dried electrode is immersed into either 0.1M KOH/0.5M KOH/0.5M H$_2$SO$_4$ solutions which are saturated with N$_2$ gas for 1hour and the cyclic voltammetry is recorded 5 times at a scan rate of 100mV/s. The potential was swept from 0.2 to 1.2 V vs. Ag/AgCl in basic media, and 0.4 to -0.6V vs. Ag/AgCl in acidic media. The CVs were overlapped one over another to check if the electrode has been stabilized and then 2 more CVs were recorded at a scan rate of 10mv/s in N$_2$ saturated electrolyte. Then, the electrolyte is saturated with O$_2$ for 30mins and then 2 more CVs were recorded at a scan rate of 10mV/s. This step is repeated one more time and overlapped to see that there is no change in the onset and peak potentials. Then, the linear sweep voltammetry is recorded at different rotations per min (400-2000 rpm) with continuous O$_2$ purging. The % peroxide generated

(eq.1) and the electron transfer number (eq.2) is calculated from the LSVs. The stability and durability tests are recorded using the RRDE electrode by stabilizing the electrode through recording CVs prior to the testing.

4.5. References

[1] L. Liu, S. Ryu, M. R. Tomasik, E. Stolyarova, N. Jung, M. S. Hybertsen, M. L. Steigerwald, L. E. Brus and G. W. Flynn, *Nano Letters* **2008**, *8*, 1965-1970.

[2] H. Chang and A. J. Bard, *Journal of the American Chemical Society* **1990**, *112*, 4598-4599.

[3] D. Jiang, B. G. Sumpter and S. Dai, *J. Chem. Phys.* **2007**, *126*, 134701.

[4] A. L. Shen, Y. Q. Zou, Q. Wang, R. A. W. Dryfe, X. B. Huang, S. Dou, L. M. Dai and S. Y. Wang, *Angewandte Chemie-International Edition* **2014**, *53*, 10804-10808.

[5] C. E. Banks, T. J. Davies, G. G. Wildgoose and R. G. Compton, *Chemical Communications* **2005**, 829-841.

[6] a) M. Patel, W. Feng, K. Savaram, M. R. Khoshi, R. Huang, J. Sun, E. Rabie, C. Flach, R. Mendelsohn, E. Garfunkel and H. He, *Small* **2015**, *11*, 3358-3368; b) M. Patel, W. Feng, K. Savaram, M. R. Khoshi, R. Huang, J. Sun, E. Rabie, C. Flach, R. Mendelsohn, E. Garfunkel and H. He, *Small (Weinheim an der Bergstrasse, Germany)* **2015**, *11*, 3357-3357; c) M. Patel, F. Luo, M. R. Khoshi, E. Rabie, Q. Zhang, C. R. Flach, R. Mendelsohn, E. Garfunkel, M. Szostak and H. He, *ACS Nano* **2016**, *10*, 2305-2315; d) M. Patel, K. Savaram, Keating, Kristina and H. He, *Journal of Natural Products Research Updates* **2015**, *1*, 18-28.

[7] a) Y. Zhao, L. Yang, S. Chen, X. Wang, Y. Ma, Q. Wu, Y. Jiang, W. Qian and Z. Hu, *Journal of the American Chemical Society* **2013**, *135*, 1201-1204; b) L. Yang, S. Jiang, Y. Zhao, L. Zhu, S. Chen, X. Wang, Q. Wu, J. Ma, Y. Ma and Z. Hu, *Angewandte Chemie International Edition* **2011**, *50*, 7132-7135.

[8] Y. B. Mo and D. A. Scherson, *Journal of the Electrochemical Society* **2003**, *150*, E39-E46.

[9] J. M. Campos-Martin, G. Blanco-Brieva and J. L. G. Fierro, *Angewandte Chemie-International Edition* **2006**, *45*, 6962-6984.

[10] R. Hage and A. Lienke, *Angewandte Chemie-International Edition* **2006**, *45*, 206-222.

[11] a) R. Burch and P. R. Ellis, *Applied Catalysis B-Environmental* **2003**, *42*, 203-211; b) V. R. Choudhary, A. G. Gaikwad and S. D. Sansare, *Catalysis Letters* **2002**, *83*, 235-239; c) V. R. Choudhary, S. D. Sansare and A. G. Gaikwad, *Catalysis Letters* **2002**, *84*, 81-87; d) A. G. Gaikwad, S. D. Sansare and V. R. Choudhary, *Journal of Molecular Catalysis a-Chemical* **2002**, *181*, 143-149; e) D. P. Dissanayake and J. H. Lunsford, *Journal of Catalysis* **2003**, *214*, 113-120; f) J. H. Lunsford, *Journal of Catalysis* **2003**, *216*, 455-460.

[12] a) Q. Liu and J. H. Lunsford, *Applied Catalysis a-General* **2006**, *314*, 94-100; b) Q. S. Liu and J. H. Lunsford, *Journal of Catalysis* **2006**, *239*, 237-243.

[13] D. P. Dissanayake and J. H. Lunsford, *Journal of Catalysis* **2002**, *206*, 173-176.

[14] C. H. Choi, H. C. Kwon, S. Yook, H. Shin, H. Kim and M. Choi, *The Journal of Physical Chemistry C* **2014**, *118*, 30063-30070.

[15] P. C. Foller and R. T. Bombard, *Journal of Applied Electrochemistry* **1995**, *25*, 613-627.

[16] D. Yu, L. Wei, W. Jiang, H. Wang, B. Sun, Q. Zhang, K. Goh, R. Si and Y. Chen, *Nanoscale* **2013**, *5*, 3457-3464.

[17] a) Z. J. Jiang, Z. Q. Jiang and W. H. Chen, *Journal of Power Sources* **2014**, *251*, 55-65; b) M. A. Patel, W. C. Feng, K. Savaram, M. R. Khoshi, R. M. Huang, J. Sun, E. Rabie, C. R. Flach, R. Mendelsohn, E. Garfunkel and H. X. He, *Small* **2015**, *11*, 3357.

[18] K. Savaram, M. Kalyanikar, M. Patel, R. Brukh, C. R. Flach, R. Huang, M. R. Khoshi, R. Mendelsohn, A. Wang, E. Garfunkel and H. He, *Green Chemistry* **2015**, *17*, 869-881.

[19] a) B. Tryba, A. W. Morawski and M. Inagaki, *Carbon* **2005**, *43*, 2417-2419; b) E. H. L. Falcao, R. G. Blair, J. J. Mack, L. M. Viculis, C.-W. Kwon, M. Bendikov, R. B. Kaner, B. S. Dunn and F. Wudl, *Carbon* **2007**, *45*, 1367-1369.

[20] Y. Zhu, S. Murali, M. D. Stoller, A. Velamakanni, R. D. Piner and R. S. Ruoff, *Carbon* **2010**, *48*, 2118-2122.

[21] A. M. Dimiev, G. Ceriotti, A. Metzger, N. D. Kim and J. M. Tour, *ACS Nano* **2016**, *10*, 274-279.

[22] D. Voiry, J. Yang, J. Kupferberg, R. Fullon, C. Lee, H. Y. Jeong, H. S. Shin and M. Chhowalla, *Science* **2016**.

[23] W. Gao, L. B. Alemany, L. Ci and P. M. Ajayan, *Nat Chem* **2009**, *1*, 403-408.

[24] A. M. Panich, *Critical Reviews in Solid State and Materials Sciences* **2012**, *37*, 276-303.

[25] a) Y. Lin, X. Han, C. J. Campbell, J.-W. Kim, B. Zhao, W. Luo, J. Dai, L. Hu and J. W. Connell, *Advanced Functional Materials* **2015**, *25*, 2920-2927; b) X. Han, M. R. Funk, F. Shen, Y.-C. Chen, Y. Li, C. J. Campbell, J. Dai, X. Yang, J.-W. Kim, Y. Liao, J. W. Connell, V. Barone, Z. Chen, Y. Lin and L. Hu, *ACS Nano* **2014**, *8*, 8255-8265.

[26] L. Tao, Q. Wang, S. Dou, Z. Ma, J. Huo, S. Wang and L. Dai, *Chemical Communications* **2016**, *52*, 2764-2767.

[27] G. Zhong, H. Wang, H. Yu and F. Peng, *Electrochemistry Communications* **2014**, *40*, 5-8.

[28] N. Li, J. An, L. Zhou, T. Li, J. Li, C. Feng and X. Wang, *Journal of Power Sources* **2016**, *306*, 495-502.

Chapter 5- Microwave Enabled Swift One Step Fabrication of Pd Nanoparticles Embedded into Sandwich like P-doped Carbon and its Catalytic Application

5.1. Introduction

Selective oxidation of alcohols is one of the most fundamental and industrially utilized organic reactions, often catalyzed by noble metals such as Au[1], Pd[2], Pt[2a, 3] etc. However, their cost, particle aggregation, surface alteration by product adsorption, limits the use of these metal nanoparticles for large scale applications. Stabilizers such as surfactants [4], polymers[5], ligands[6] etc., are used to prevent particle aggregation, but resulted in the interference of catalytic activity. Co-doping a noble metal with another noble metal [7] or with a cheap transition metal [8] can reduce the amount of active material required for catalysis, consequently reducing the cost of overall process with improved conversions and selectivity. Nevertheless, the problem regarding aggregation, as well as surface alteration still exist in these bimetallic catalysts.

A porous carbon[9] core shell could prevent particle aggregation and surface alteration of metal in comparison to impermeable graphene layer which needs additional activation [10] to expose the active metal for their catalytic activity. However, regeneration of the catalyst is inevitable due to surface modifications, thereby rendering a decrease in overall efficiency of the catalyst. A Heterogeneous catalyst consists of an active phase (metal/metal oxide) finely dispersed on high surface area supports, thereby reducing metal loading, ensure recyclability, easy catalyst recovery and prevent particle aggregation.

The overall reactivity in a heterogeneous catalyst depends on suitable supports [11] which can aid in altering of acid base properties, redox properties, metal leaching and prevent particle aggregation. Carbon supports have gained immense interest due to their sustainability and their synthesis from biomass molecules. However, the metal leaching was observed due to its poor interaction with carbon support. It was reported that the heteroatoms such as Oxygen (O) [12], Nitrogen (N) [12d, e, 13], Phosphorous (P) [14] doped into carbon supports can act as catalysts themselves due to altered electronic and chemical properties, compared to their non-doped catalyst. However, the amount of catalyst required is extremely large (100-200wt %), making it unrealistic for practical purposes. Doped carbon matrix can be used as a substitute to carbon supports, which promote better interaction with metal, and hence enhancing their catalytic efficiency.

Owing to the wide application of noble metals in catalysis, metal nanoparticles loaded onto carbon support was widely studied. In the case of Pd metal, the uniform dispersion of the metal on the N doped carbon matrix was broadly explored. As reported in literature, presence of N improves the interaction of reactant with active center[15], and N doped carbon can act as a bulky heterogeneous ligand[15f]. P which has the same valence as N, has aroused emergent research interest due to their similar electron rich nature [16] in metal free carbo-catalysis. The activation energy was greatly reduced upon use of P(49.6 kJ/mol)[14] instead of N doped carbon (56.1 kJ/mol)[13d] as catalyst for alcohol oxidation. Some of the factors which can be considered for superior performance of P over N includes; lower electronegativity of P, which leads to opposite polarity in C-P bond, making P to be the active center[17], rather than C, which was reported in the case of N doped carbon catalyst [13c, 18]. Theoretical and experimental results[14, 17a] reported the observation of structural

distortion upon doping of large diameter P into carbon matrix, hence reducing steric hindrance effect observed in case of N doped carbon catalyst[13c, d]. Additionally, vacant 3d orbitals in P may exhibit distinct effects in comparison to N.

Current studies have been focused on N doped carbon support and their influence on loaded metal nanoparticles. For the first time, we report the influence of phosphorous doped carbon support on Pd and its catalytic activity in the oxidation of alcohols. Most of the metal loaded onto heteroatom doped carbon support were synthesized via co-precipitation[19], impregnation[20], etc., under inert conditions. The initial step involves doping of carbon with heteroatom, followed by immobilization of metal nanoparticles. The synthesis consists of long reaction times and inert environmental conditions, thus increasing, the complexity of fabrication process. In this work, a simple one step microwave approach was utilized, with phytic acid, a biomass molecule, which acts as both carbon and phosphorous source. The reaction is carried out under atmospheric conditions, subjected to microwave irradiation for 50sec. Carbon not only acted as a carbon source, but also reduced [21] the metal salt (Pd in this case) along with external reducing agent, ethylene glycol. A Mesoporous structure with nanoparticles was observed via SEM, and it is embedded in between a phosphorous doped graphene-like carbon matrix. Hence additional protection to metal particles against surface oxidation was provided and thereby preventing necessity for reactivation of the catalyst. Different wt% loadings of Pd incorporated into phosphorous doped graphene like carbon (Pd-PGc) were synthesized, with 80% of Pd as Pd^0 in 3% Pd-PGc. 3% Pd-PGc synthesized exhibited a higher conversion of 85% with TOF of $23000h^{-1}$ higher than Pd@NGc $(14600h^{-1})$[15f] and Pd@Gc $(2940h^{-1})$[9] indicating enhanced performance of the catalyst.

5.2. Results and Discussion

The Pd nanoparticles, which are embedded into porous doped carbon and sandwiched in between the phosphorous doped graphene like carbon in a facile one step approach was synthesized *via* microwave chemistry. In this work, phytic acid a biomass and anti-nutrient molecule which acts as both carbon and phosphorous source was used. Different wt% loadings of Pd into PGc was synthesized and labelled according to the weight of Pd, as quantified via EDS (1%, 3%, 5%, 7% Pd-PGc). SEM of 3% Pd-PGc revealed Pd nanoparticles to be embedded inside porous matrix and are covered with a blanket of phosphorous doped graphene like carbon sheet as shown in **Figure5.1.(b).**
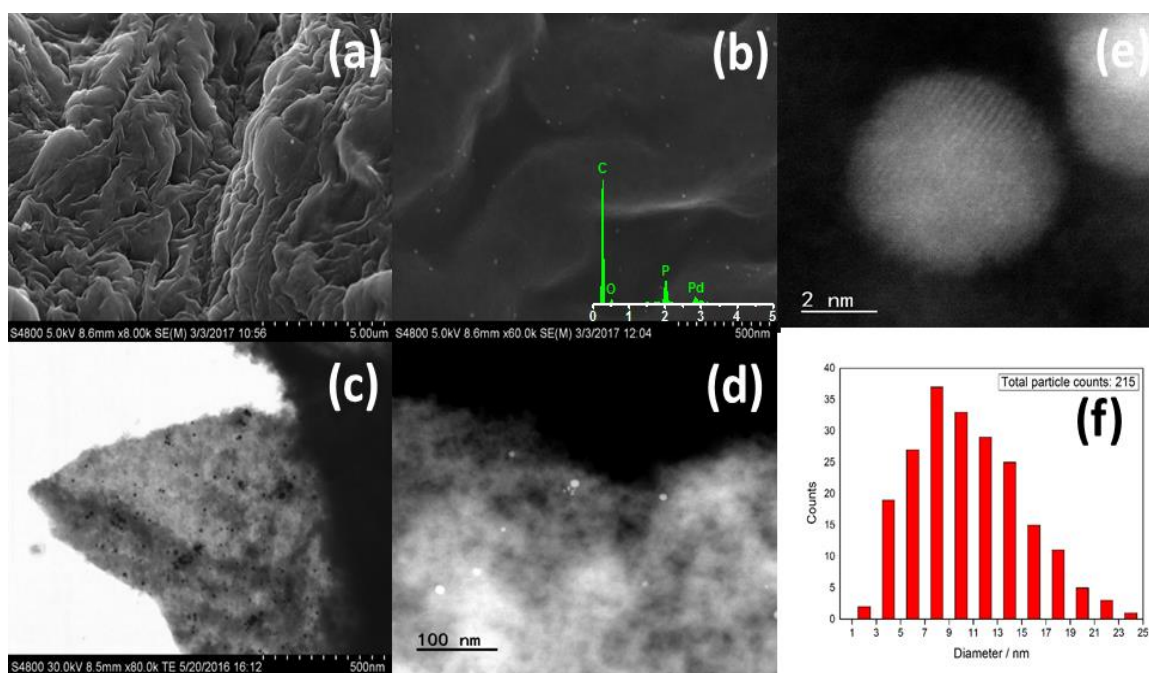
Figure 5.1. The SEM of 3% Pd-PGc, wrinkled morphology (a), Pd nanoparticles embedded in PGc blanket (b). STEM imaging of 3% Pd-PGc, showing 10nm Pd nanoparticles (c) distributed uniformly and HRTEM image of Pd nanoparticles with crystal lattice of Pd^0 (d,e) and histogram of the particle size distribution in 3% Pd-PGc(f).

The wrinkled morphology can be attributed to the doping of phosphorous into carbon matrix, as reported previously by our group [14]. HRTEM revealed Pd nanoparticles with a

size distribution of 10nm and with crystal lattice spacing of 2.340A$^{\circ}$ and 2.442A$^{\circ}$, characteristic of Pd^0, supported by typical 2Θ at 40° by XRD. The intensity of Pd^0 increases with increased Pd loading, **Figure 5.2. (a)**. The 2Θ reflection observed at 24-26° accounts for presence of graphitic domains, as reported in PGc, and is supported by the presence of G band ($\approx$1570cm^{-1}) corresponding to non-defective graphene [22][23], in Raman spectra. **Figure 5.2. (b)**.

	I$_D$/I$_G$	Crystalline size (nm)
PGc	0.71	27.2
1% Pd-PGc	0.56	34.23
3% Pd-PGc	0.61	21.38
3% Pd-IPGc	0.62	31.06
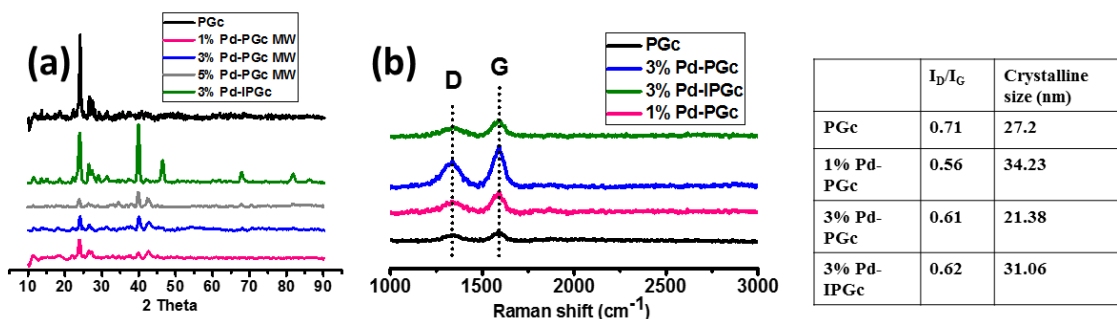
Figure 5.2. The XRD (a), and Raman spectra of 3% Pd-PGc with other catalyst, with their graphitic crystalline sizes listed in adjoining table.

The nature of porous carbon and its influence on surface area of Pd-PGc was studied via Brunauer–Emmett–Teller (BET) and BJH adsorption-desorption isotherms. PGc exhibits a surface area of 704.01m^2/g, whereas the presence of Pd in Pd-PGc increased its surface area by 50-60%, **Figure 5.3. (a)**. According to IUPAC classification [24], BJH adsorption-desorption plot exhibits a typical type IV isotherm [25], suggesting mesoporous nature with multilayer adsorption followed by capillary condensation. The H1 hysteresis, further demonstrates presence of agglomerates or compacts of spherical particles arranged in a fairly uniform way. There was no influence of Pd nanoparticles on pore diameter in PGc

matrix, as summarized in table. The pore diameter of <10nm, indicates the confinement of the Pd nanoparticles (10nm) in the narrow pore size.
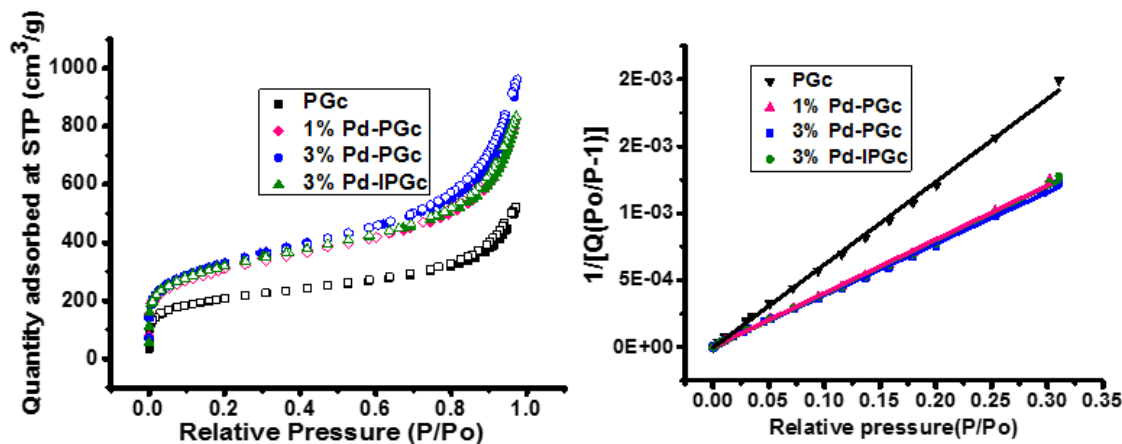
Catalyst	Surface area (m2/g)	Avg pore diameter (adj/Des) nm	R^2	Slope	Intercept
PGc	704.01	8.13/6.97	0.99795	0.00619	2.54722e-6
1% Pd-PGc	1084.00	7.88/6.45	0.99855	0.00401	2.64131e-6
3% Pd-PGc	1133.16	8.21/6.83	0.99906	0.00384	5.38863e-6
3% Pd-IPGc	1088.92	7.90/6.45	0.9985	0.00401	3.46957e-7

Figure 5.3. The BET isotherm with summary of surface areas of PGc and Pd-PGc, along with their pore size distribution.

The surface chemical functionalities, was recorded via XPS. Deconvolution of Pd in 3% Pd-PGc resulted in 80% as Pd^0 and remaining 20% was assigned to Pd^{+2}, with a total of 0.2% of Pd in the material, **Figure 5.4. (a)**. The C/O ratio was 7.34, where 67% of carbon is present as sp^2 suggesting graphitic domains. Deconvolution of phosphorous spectra revealed presence of an additional peak in the case of Pd-PGc, which accounted for Pd-P-O with a binding energy of 133.7ev. This suggests formation of metal phosphate ligands like structure in Pd-PGc, **Figure 5.4.(b)**. The characteristic peaks of C-P bond at 132.6ev

and P-O bond at 135ev was recorded, which are observed in PGc, **Figure 5.4., table 5.3**.

The FTIR spectra revealed that the as synthesized Pd-PGc exhibits similar peaks as PGc, however there were blue shifts observed at 1200cm^{-1} in the case of 3% Pd-PGc, indicating formation of Pd/C-P-O bonds, **Figure 5.4.(e)**.
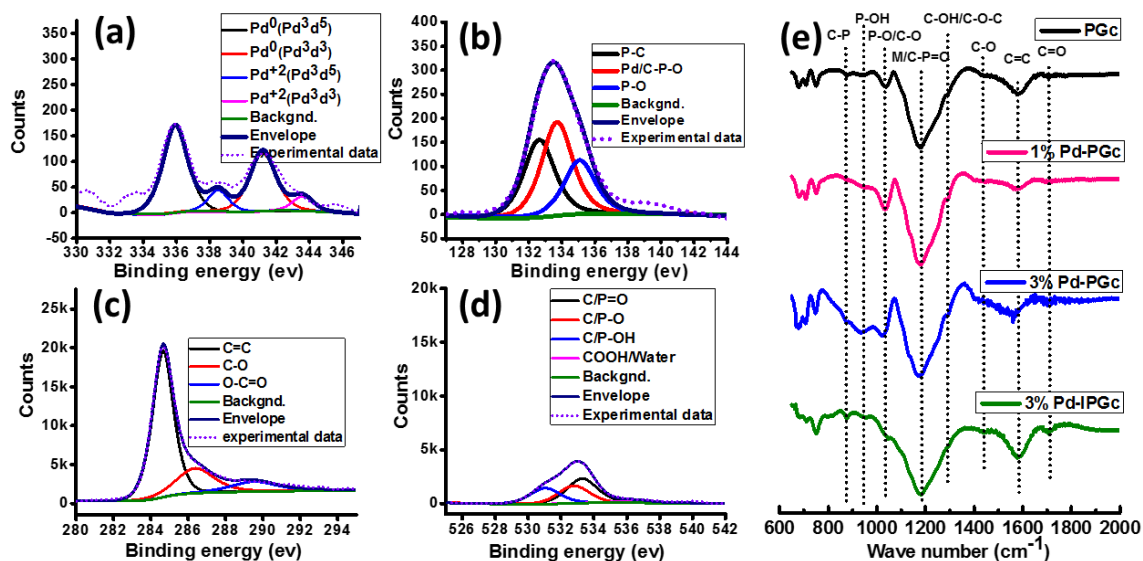
Figure 5.4. The XPS deconvolution spectra of Pd (a), P (b), C (c), O (d) in 3% Pd-PGc, and FTIR spectra of Pd-PGc in comparison with PGc (e).

Following this approach, different non-noble metals such as Co, Ni, Fe etc. were loaded into PGc matrix via one step microwave approach. The wrinkled morphology was observed via SEM with nanoparticles embedded in PGc matrix, and EDX analysis indicated the presence of respective metal, **Figure 5.5.**
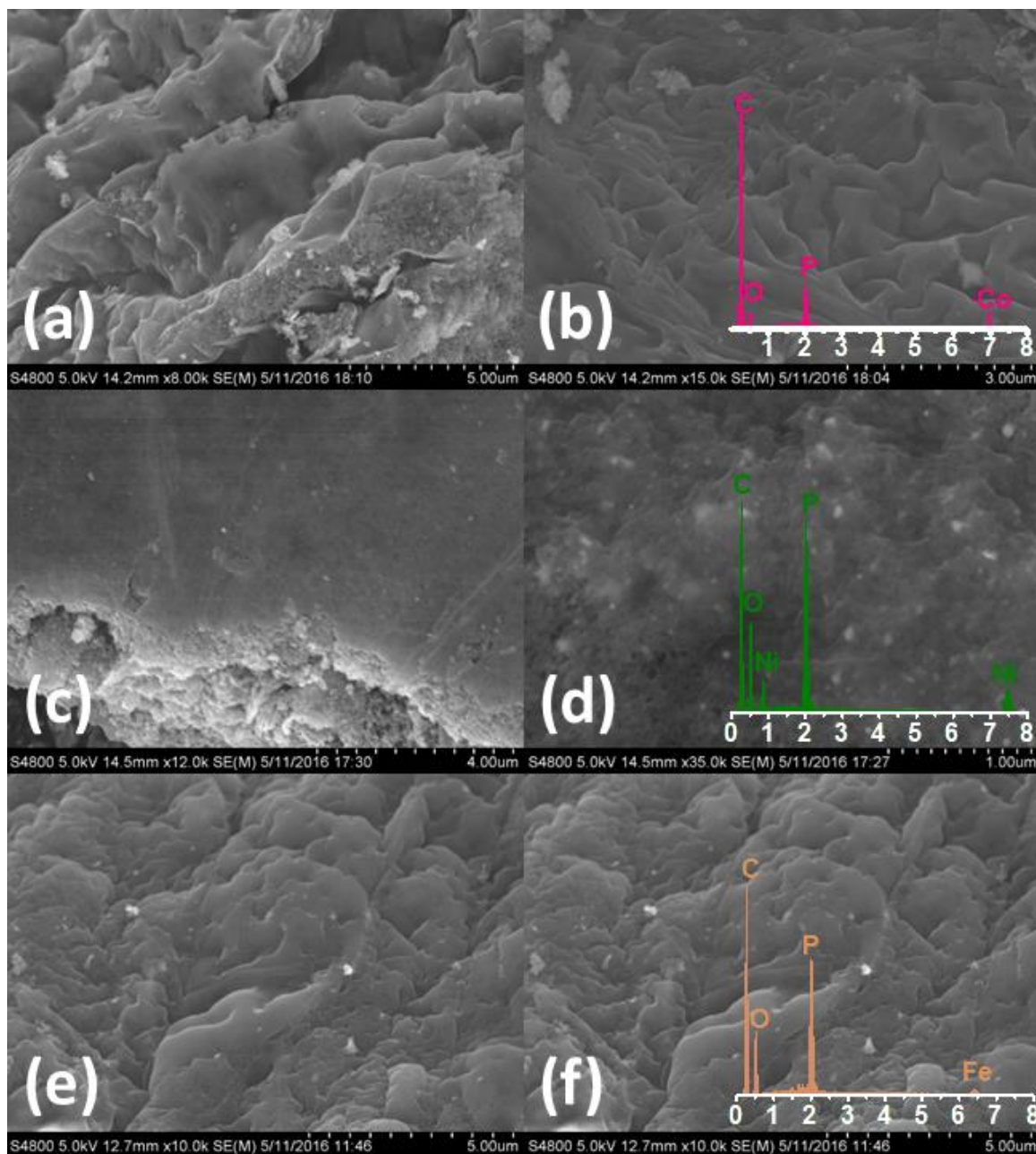
Figure 5.5. The SEM images of Co-PGC (a,b), Ni-PGC (a,b), Fe-PGC (a,b) along with their EDAX spectra indicating presence of the corresponding metal.

The Pd-PGc was tested as a catalyst for oxidation of benzyl alcohol with green oxidant, O_2 in this current study. Increase in wt % of Pd in Pd-PGc enhances conversion of alcohol up to 3% metal loading, entry 4, **table 5.1.** Further Pd increase does not exhibit enhanced results (5% and 9% Pd-PGc), hence 3wt% Pd-PGc was used as catalyst of choice. The

efficiency of 3% Pd-PGc is realized by conducting benzyl alcohol oxidation at different temperatures (entries 1, 8, 9), different wt% of catalyst in reaction mixture (entries 1-7) and different time intervals (entries 5,9-11) as listed in **table 5.2**. As the temperature is increased, time required to reach desired conversion is decreased by preserving selectivity of the catalyst. A conversion of 86% was achieved with 10wt% of catalyst, with a TOF of 23000h^{-1} , at 120°C for 4hrs. The reported turnover is 0.64 times higher than Pd@NGc[15f].

Table 5.1. The reaction was performed with different Pd weight loadings onto PGc with 5wt% of the catalyst at 80°C for 24hrs with benzyl alcohol. 10µl of nitromethane was added as an internal standard and analyzed via ^{1}H NMR.

Catalysts	Wt% of metal (expected)	% Conversion	% Selectivity				Yield of benzaldehyde	Total yield
			benzaldehyde	Benzoic acid	Toulene	Ether		
[1]0.1% Pd-PGC	0.1	4.79	97.35	2.65	0.00	0.00	2.27	2.33
[2]0.5% Pd-PGC	0.5	3.92	97.79	2.21	0.00	0.00	1.96	2.01
[3]1% Pd-PGC	1	25.96	78.78	2.43	15.80	2.99	18.95	24.05
[4]3% Pd-PGC	3	38.47	77.19	4.19	14.05	4.57	24.19	31.33
[5]5% Pd-PGC	7	29.23	77.18	2.56	16.20	4.06	19.10	24.75
[6]9% Pd-PGC	9	41.24	77.40	3.51	15.40	3.69	27.14	35..06

Table 5.2. The reaction was performed at different temperatures, different time intervals and different wt% of the catalyst with the reactant , benzyl alcohol. 10µl of nitromethane was added as an internal standard and analyzed via ^{1}H NMR.

Temperature	Reaction time	Wt% of catalyst	%Conversion	% Selectivity				Yield of benzaldehyde	Total yield
				benzaldehyde	Benzoic acid	Toulene	Ether		
[1]80°C	24hrs	5	67.67	71.91	10.89	12.53	4.66	19.99	27.79
[2]80°C	24hrs	7.5	74.19	69.36	19.88	7.55	3.22	20.21	29.15
[3]80°C	24hrs	10	74.97	68.20	19.05	10.48	2.27	20.71	30.38
[4]120°C	4hrs	2.5	59.72	68.26	4.20	22.75	4.78	16.91	24.77
[5]120°C	4hrs	5	67.14	68.87	3.85	22.50	4.79	40.58	58.92
[6]120°C	4hrs	7.5	75.58	62.45	11.79	21.75	4.00	19.93	24.77
[7]120°C	4hrs	10	69.40	70.72	7.16	18.66	3.46	21.12	31.91
[8]100°C	24hrs	5	77.49	74.55	5.51	17.18	2.76	21.04	28.22
[9]120°C	24hrs	5	95.29	61.94	20.99	13.49	3.59	34.86	56.29
[10]120°C	16hrs	5	88.88	54.82	25.39	14.58	5.21	36.22	66.07
[11]120°C	8hrs	5	84.01	57.48	21.89	15.40	5.23	35.08	61.03

To prove the catalytic performance, 3% Pd-PGc was tested for its recyclability. The selectivity and conversion remained constant even up to 8 recycles preserving their catalytic activity, **Figure 5.6. (a).** EDX of the reused catalyst did not exhibit significant change in wt% of Pd. The higher activity can be attributed to synergy of Pd with PGc, where the latter might act as a bulky ligand, along with contribution of Pd nanoparticles detainment in porous structures.
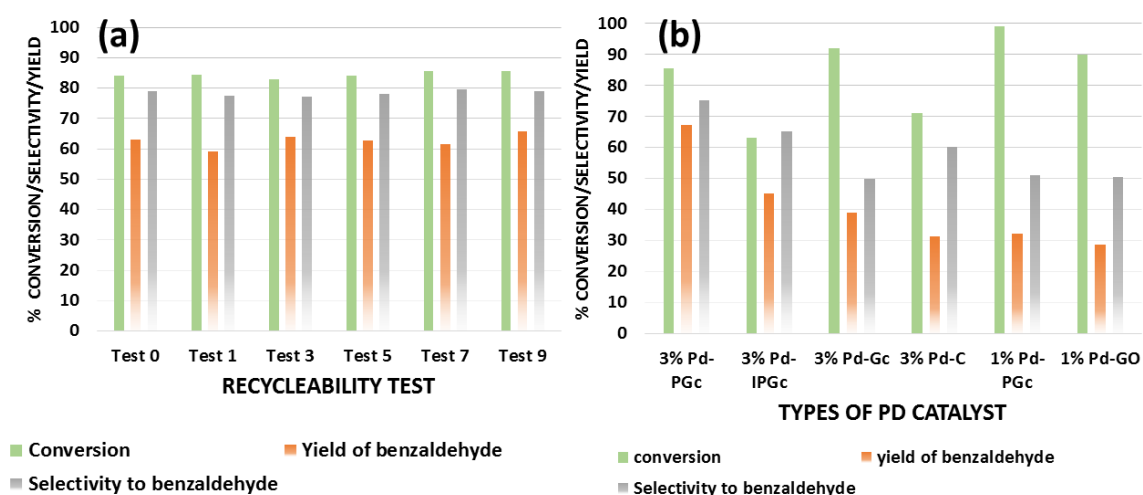
Figure 5.6. The histograms which depict conversion, yield and selectivity of Pd on different carbon supports (a) and recyclability of 3% Pd-PGc(b).

The lower Pd loading in 1% Pd-PGc reported increased conversion (99%) but selectivity is greatly decreased. This can be explained by the absence of metal phosphate peak as analyzed via XPS. The importance of phosphorus in carbon matrix is studied by using Pd loaded onto different carbon supports along with immobilization of Pd onto PGc matrix (Pd-IPGc). The 3% Pd-IPGc exhibited a decreased conversion and selectivity (63.12%, 65.30%), with further decrease upon first recycle (52.14%, 62.18%).

Table 5.3. Summarized quantification of the type of possible bonding in Pd-PGc samples.

Sample	XPS data																	
	Carbon				Oxygen					C/O ratio	Phosphorous				Palladium			
	Total	% C-C (284.56ev)	% C-O (286.27 ev)	% O-C=O (289.43ev)	Total amount	% C=O (531.04ev)	% C-O (532.76)	%C-OH (533.28 ev)	%COOH/ Water (536.52 ev)		Total	%P-C (132.66 ev)	%Pd/ C-P-O (133.71 ev)	%P-O (135.08ev)	Total	%Pd⁰ (335.93,341.19 ev)	%Pd⁺² (338.5, 343.6 ev)	
PGc	51.62	77.36	16.4	6.24	31.77	0	39.97	60.03	0	1.62	16.62	50.06	0	49.94	0	0	0	
1% Pd-PGc	82.11	80.96	12.51	6.53	12.39	59.56	21.79	18.64	0	6.63	5.31	50.09	0	49.91	0.18	33.33	66.67	
3% Pd-PGc	86.16	67.86	21.78	10.35	11.74	25.89	28.36	41.48	4.26	7.34	1.93	34.72	41.45	23.83	0.2	80	20	0
3% Pd-PGc 1ˢᵗ use	86.94	68.27	21	10.74	11.34	19.13	24.51	51.59	4.76	7.66	1.49	44.3	40.94	14.77	0.23	65.22	34.78	0
3% Pd-IPGc	75.67	68.68	20.47	10.85	19.18	43.07	40.67	7.40	8.86	3.95	4.31	7.66	0	92.34	0.85	83.53	16.47	0
3% Pd-IPGc 1ˢᵗ use	81.29	48.35	41.12	10.53	16.73	3.95	32.64	58.04	5.38	7.86	1.98	34.85	51.01	14.14	0	0	0	0
3% Pd-AC	87.17	69.94	16.07	13.98	10.42	13.41	30.96	42.56	13.08	8.37	0	0	0	0	2.4	49.17	32.5	18.33
3% Pd-AC 1ˢᵗ use	90.16	73.33	10.99	15.98	9.85	4.47	40.30	40.30	9.15		0	0	0	0	0	0	0	0

The SEM of 3% Pd-IPGc indicated the presence of Pd nanoparticles on the surface, **Figure 5.7.**, hence suggesting leaching of the metal nanoparticles into reaction mixture, thereby decreasing conversion after 1ˢᵗ recycle. However, an additional Pd-P-O peak, was observed via XPS (**table 5.3.**), proposing catalyst modification during oxidation. Similar conversions and selectivity's were reported for Pd decorated on GO[26] and porous carbon, emphasizing the structural property influence in Pd-PGc for oxidation reactions.
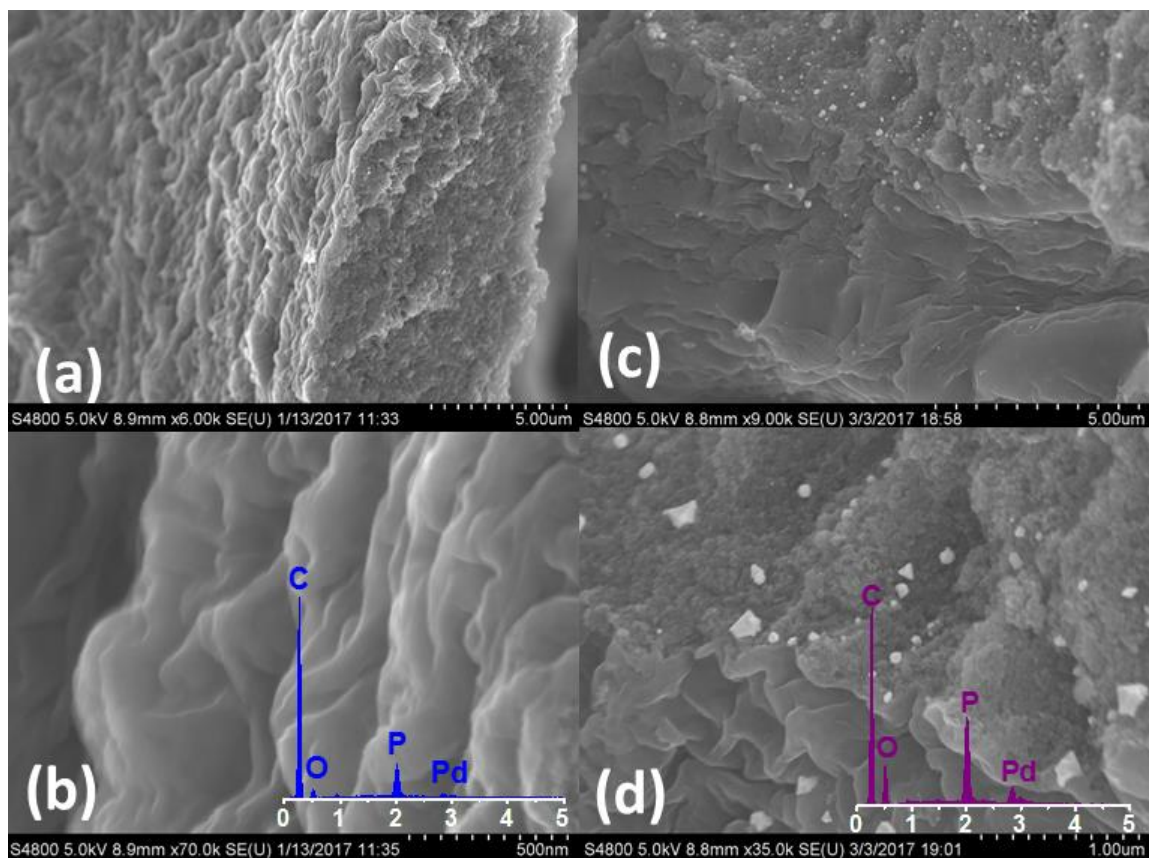
Figure 5.7. The SEM image of 1% Pd-PGc (c,d), which shows porous structures in cross sectional view and Pd-IPGc(e,f) which indicates presence of immobilized Pd on surface.

To further understand the kinetics of O_2 reduction, the electro-catalytic activation of O_2 of Pd-PGc was examined by performing ORR in 0.1M KOH. The increased Pd loading in Pd-PGc exhibits higher reduction potential with lower peroxide generation and electron transfer number (17%, 3.65e$^-$ for 3% Pd-PGc and 34%, 3.31e$^-$ for 1% Pd-PGc), whereas the reduction potential decreases in 3% Pd-IPGc (32.3% and 3.35e$^-$) **Figure 5.8.** The results suggest higher energy requirement for O_2 dissociation in the case of 3% Pd-PGc whereas its unique structure of Pd with phosphorous allows the catalyst to reduce O_2 with domination towards 4e$^-$.
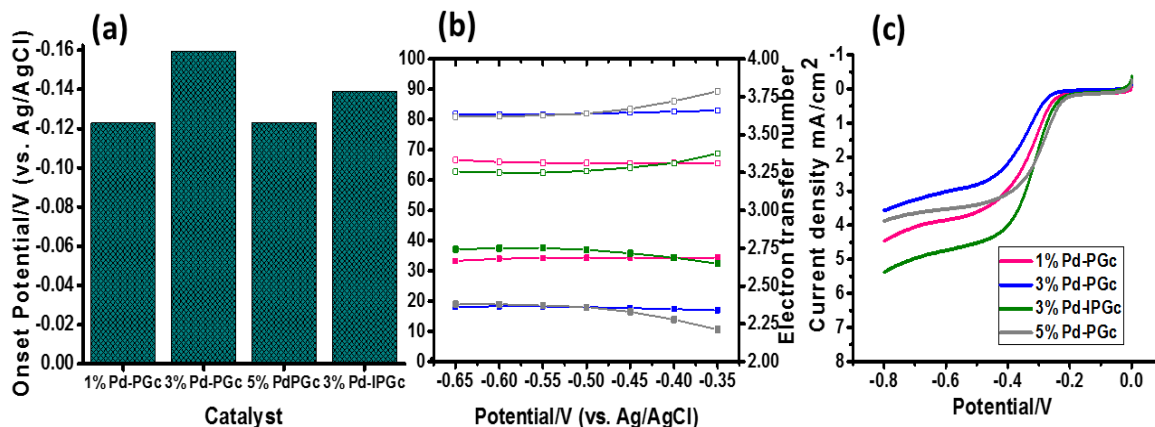
Figure 5.8. The plot of various %Pd on PGc and IPGc matrix with onset potential (a), their % peroxide and electron transfer number (b), and their current density (c) *vs.* potential (Ag/AgCl).

To understand the mechanism of alcohol oxidation, the active center and the role of oxidant, more experiments were pursued. Intrinsic effect of support in the oxidation of benzyl alcohol was not observed entry 1, **table 5.4.**, when PGc was used. It was also observed that, the reaction proceeds via 1st order kinetics with an activation energy of 22.57 ± 2 kJ/mol, which is lower than actual Pd^0 or Pd nanoparticles loaded onto various supports[27], but complies with Pd loaded carbon supports[28], indicating the synergy of metal with support, **Figure 5.9.**

Figure 5.9. The kinetics of Benzyl alcohol oxidation at different temperatures (a) and its activation energy plot (b).

Alcohol oxidation when conducted in N_2, greatly decreased conversion to 6% (entry 3,

table 5.4.) and conversion was regained to 77% (entry 4, **table 5.4.**), when the same

catalyst was reused with O_2. Addition of BHT (Butylated Hydroxyl Toluene), a known

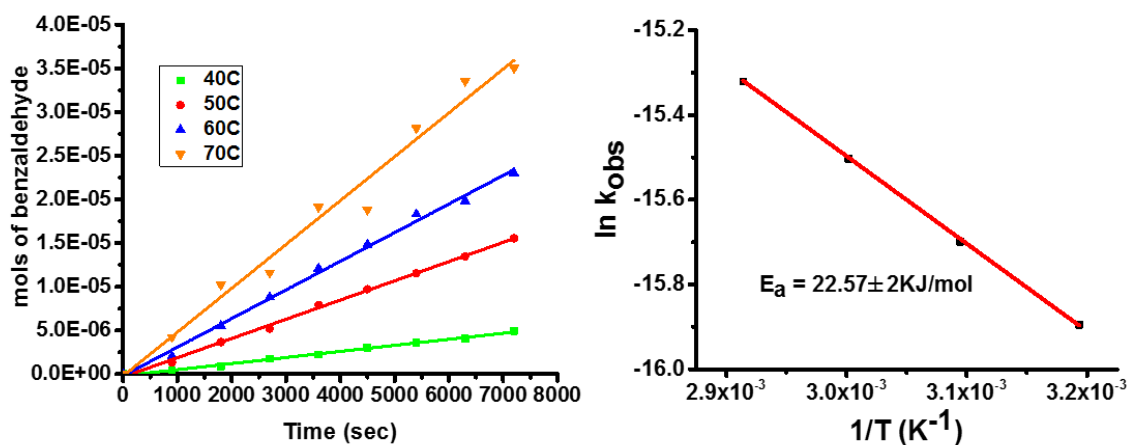radical quencher, decreased conversion to 33%, whereas no peroxide is detected when

analyzed via HPLC. These results suggest that O_2 is the primary oxidant with reactive O_2

$(^1\Delta_g)$ [29] as the species.

Table 5.4. The reaction was performed at 120^0 C for 4hrs with 10wt% catalyst, 1mmol of benzyl alcohol. 10µl of nitromethane was added as an internal standard and analyzed via ^{1}H NMR.

Catalyst	% Conversion	% Selectivity				Yield of benzaldehyde	Total yield
		benzaldehyde	Benzoic acid	Toulene	Ether		
[1]PGC	6.94	100	0	0	0	2.86	2.86
[2]No catalyst_120C_4hrs	3.97	39.03	60.97	0.00	0.00	0.77	1.97
[3]3% Pd-PGC_120C_4hrs_N₂	6.81	65.23	0.00	34.77	0.00	4.62	7.08
[4]3% Pd-PGC_120C_4hrs_N₂_O₂	77.04	72.15	5.24	22.61	0.00	44.48	61.65
[5]3% Pd-PGC_120C_4hrs_BHT	29.55	14.18	0.00	85.82	0.00	5.24	36.93
[6]3% Pd-PGC_120C_4hrs_no BHT	73.67	64.32	8.05	22.69	4.94	40.65	63.19
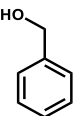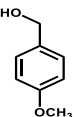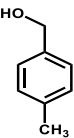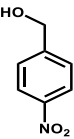
The following mechanism was proposed, based on the above results, **scheme 5.1.,** where initial absorption of O_2 on the Pd occurs, leading to the formation of PdO_x species. The oxidation of alcohol can follow either alkoxy route (2) to generate benzaldehyde or carbonyloxyl route (3) to generate benzoic acid. The alkoxy intermediate can undergo disproportionation (4) to generate toluene or it can accepts another benzyl alcohol molecule and forms benzyl ether [30].
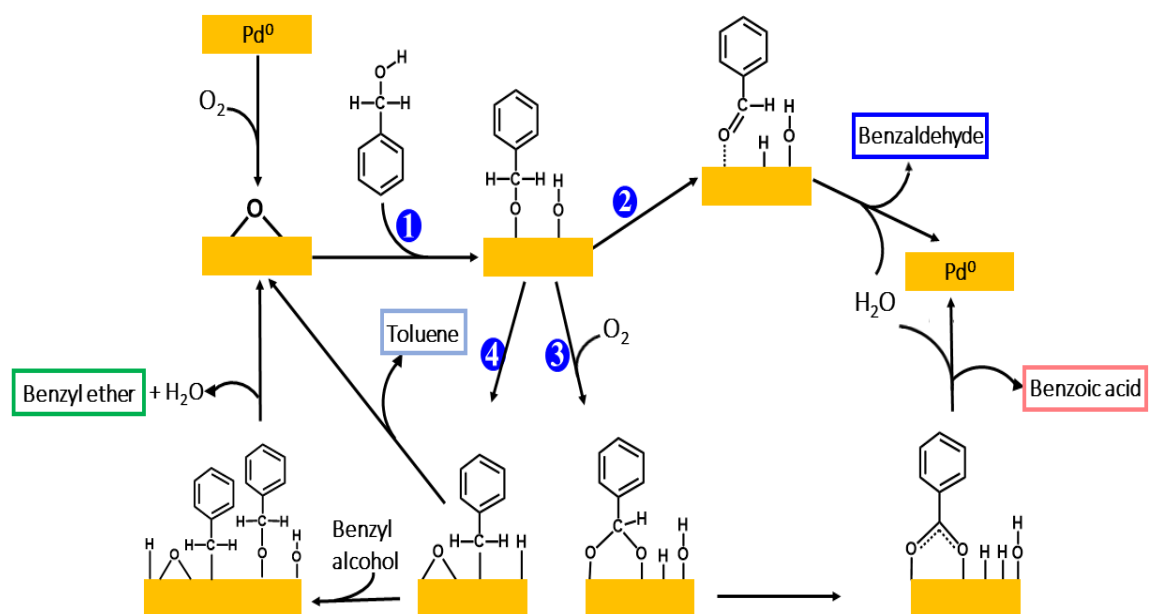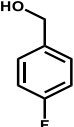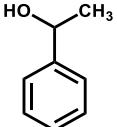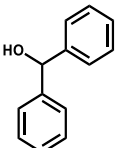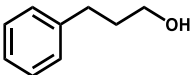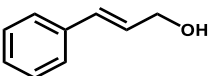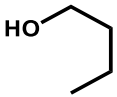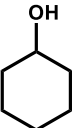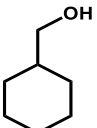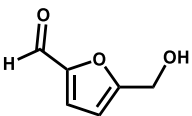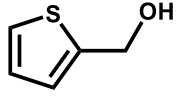
Scheme 5.1. The possible reaction mechanism of alcohol oxidation with Pd^0 in Pd-PGc.

The scope of the 3% Pd-PGc was further explored for oxidation of various primary, secondary, allylic alcohols etc., **table 5.5.** 3% Pd-PGc was able to catalyze oxidation of secondary alcohols (entries 6, 7). However, bulky secondary alcohol (entry 7), lead to low conversion due to steric hindrance which limits accessibility of reactant to pass through porous structure and come in contact with the catalytic center. Oxidation of aliphatic alcohols (entries 11,12), saturated cyclic alcohols which lack unsaturation in the aliphatic chain (entries 8,9) and aliphatic alcohols (entry 10) exhibited decreased/no conversion.

This indicates, the importance of π conjugated structure to promote π-π interaction between reactant and substrate, which facilitates the mobility of reactants through porous matrix and come in contact with the catalytic center. The as synthesized catalyst can also selectively oxidize 5-Hydroxy methyl furfural (5-HMF), which has a great potential in bio-refinery field (entry 13). Influence of substituents on benzyl alcohol oxidation was also studied, where the presence of electron withdrawing groups (entry 4) exhibits lower conversion and electron donating group's exhibit similar conversion as benzyl alcohol.

Table 5.5. The reaction was performed at 120^0 C for 4hrs with 5wt% catalyst, 1mmol of alcohol derivatives. 10µl of nitromethane was added as an internal standard and analyzed via ^{1}H NMR.

Subtrate	Subtrate structure	% Conversion from Moles	% Yield		Total Yield	% Selectivity	
			-CHO	-COOH		-CHO	-COOH
[1]Benzyl alcohol	HO	88.11	42.12	2.13	44.25	95.18	4.82
[2]4-methoxy benzyl alcohol	HO OCH₃	99	6.84	0.00	6.84	100.00	0.00
[3]4-methyl benzyl alcohol	HO CH₃	46.53	17.35	0.64	17.99	96.43	3.57
[4]4-nitro benzyl alcohol	HO NO₂	1.58	1.02	0.00	1.02	100.00	0.00

[5]4- fluoro benzyl alcohol		11.63	10.57	0.93	11.50	91.91	8.09
[6]1- phenyl ethanol		82.96	93.27	0.00	93.27	100.00	0.00
[7]Di phenyl methanol		2.76	3.01	0.00	3.01	100.00	0.00
[8]3-phenyl 1-propanol		0.45	0.33	0.00	0.33	100.00	0.00
[9]Cinnamyl alcohol		40.36	26.56	0.00	26.56	100.00	0.00
[10]Butanol		1.05	1.04	0.00	1.04	100.00	0.00
[11]Cyclohexanol		4.20	3.81	0.00	3.81	100.00	0.00
[12]Cyclohexane methanaol		0.09	0.07	0.00	0.07	100.00	0.00
[13]5-OH methyl furfuraldehyde		44.65	37.29	0.73	38.02	98.08	1.92

[14]Thiophene methanol	(structure) S / OH	8.15	4.38	0.00	4.38	100.00	0.00

5.3. Conclusion

In summary, we have reported for the first time, microwave assisted single step fabrication of Pd embedded in phosphorous doped graphene-like carbon. Pd-PGc has a high surface area of $1133m^2/g$ with mesoporous structure, confining the nanoparticles. These Pd nanoparticles were embedded in porous structure and are sandwiched between phosphorous doped graphene like carbon, providing protection against surface oxidation. The nanoparticles are in the range of 10nm, with an additional P deconvolution peak indicating formation of Pd-P-O. Different transition metals such as Co, Fe, Ni etc., in phosphorous doped graphene like carbon were fabricated. The as synthesized Pd-PGc were tested for their catalytic activity for alcohol oxidation. 3% Pd-PGc exhibited high conversion of 80-90% with a high TOF of $23000h^{-1}$, which is 0.65 times higher than Pd@NGc. The enhanced catalytic activity can be attributed to the presence of P in carbon matrix which acts as a bulky ligand attached to Pd. The as synthesized catalyst maintains conversion and selectivity up to 8 cycles, indicating reusability of catalyst.

5.4. Experimental conditions

5.4.1. Catalyst synthesis

Pd-PGc-MW: In a typical experimental procedure, various loadings of Pd-PGc are synthesized by weighing required amount of $PdCl_2$ (99.9% Pd from STREM chemicals, CAS # 7647-10-1, 0.133mg for 0.1wt% Pd-PGc, 0.666mg for 0.5wt% Pd-PGc, 1.9mg for

1% Pd-PGc, 5.3mg for 3wt% Pd-PGc, 6.7mg for 7% Pd-PGc, 12mg for 9wt% Pd-PGc into a 35ml Pyrex glass vessel (CEM, # 909036). The salt is dissolved by adding 0.5ml of acetone via bath sonicator. To this solution, 56.3ul of Ethylene Glycol is added and further sonicated. To the reaction mixture, 1ml of Phytic acid (Sigma Aldrich, 50 w/w % is added in water) is added and closed with a Teflon lined cap (CEM, # 909235). This sample is sonicated again in bath sonicator for 5mins to get a uniform suspension and then is placed in 500ml glass beaker and covered with a watch glass. This assembly is now placed in microwave (Panasonic commercial microwave 1000W) and subjected to microwave irradiation to 50sec. After microwave treatment, the microwave door is opened with fume hood door closed, to allow the reaction tube to cool down and remove gases generated during reaction. The resulting product is sonicated with ethanol via bath sonication and then filtered using a 0.8µm polycarbonate filter paper (Millipore, ATTP 04700). The product is washed with water (1000ml) and ethanol (200ml), and is dried in oven at $80^{\circ}C$ overnight.

PGc: The PGc carbon material is synthesized as described in our previous work[14]. In brief, 1ml of phytic acid is subjected to 50sec of microwave irradiation. This sample is filtered using a 0.8µm polycarbonate filter paper. The product is washed with water (1000ml) and ethanol (200ml), and is dried in oven at $80^{0}C$ overnight.

Pd-IPGc: In a glass vial, 2.8mg of $PdCl_2$ is sonicated with ethanol for 30mins. This $PdCl_2$ suspension is added dropwise to PGc solution (40mg bath sonicated in 10ml of water). The reaction mixture is stirred at 600rpm at $60^{0}C$ for 12hrs. Later, $NaBH_4$ solution ($0.2mol^{-1}$, 5 equivalents) is added dropwise while sonicating the solution for 30mins. This solution is

filtered using a 0.8µm polycarbonate filter paper, and is washed with water (1000ml) and ethanol (200ml). The as obtained product is dried in oven at 80^0C overnight.

Pd-C: The Pd-C is used as received from Sigma Aldrich (CAS# 237515). The weight loading of Pd is 3% on the activated carbon support.

5.4.2. Catalyst characterization

SEM/STEM: Surface morphology of the as synthesized catalyst is characterized via Scanning Electron Microscopy (SEM) and the distribution of Pd nanoparticles in PGc matrix is analyzed with Scanning Tunneling Electron Microscopy (STEM) using a HITACHI S-4800 Field Emission Scanning Electron Microscope (FE-SEM, Hitachi Co.Ltd). The SEM sample is prepared by placing the powder on carbon tape, which is fixed to the stud and sample analysis is executed by applying a voltage range of 2-5KV, whereas STEM sample is prepared by sonicating the sample in water (approx. 1mg in 5ml water) for 1min. The as prepared solution is drop casted onto Cu grid mesh size 400, which is dried under vacuum and then analyzed at 30KV accelerating voltage.

EDS: The weight % of metal loading (Pd, Co, Fe, Ni) onto the PGc support is analyzed via Energy Dispersive X-ray Spectroscopy (EDS). The sample is prepared by drop casting slurry of sample onto a carbon tape and allowed it to dry. An accelerating voltage of 15-20Kv is used to collect the spectra.

XRD: The crystal structure of the nanoparticles were studied using Bruker D8-Eco X-ray powder diffraction instrument (XRD) which is equipped with a Cu Kα irradiator (λ=0.154056nm). This instrument is interfaced to a computer equipped with Eva-diffraction suit software for data treatment/analysis. The samples are grounded into fine

powder in a mortar and pestle and then they are filled into X-ray holder which is placed on the stage and X-ray diffraction collected from 5-45^0 2Θ.

XPS: X-ray photoelectron spectroscopy (XPS) is used to detect functional state of the as dispersed Pd nanoparticles along with that of PGc. The Silica substrate (Silicon Prime Wafers P type, Boron dopant, thickness 500+/-25μ with a resistivity of 0.001-0.005Ωcm) is used for analysis on which the slurry of catalyst were dropped (thickness of approximately 30-50nm). XPS spectra was acquired using a Thermo scientific K-Alpha system with a monochromatic Al Kα x-ray source (hν = 1486.7ev). For data analysis, smart background subtraction was performed and the spectra were fit with Gaussian/Lorentzian peaks using a minimum deviation curve fitting method (Advantage software package). The Integrated peak areas along with Scofield sensitivity factor were used to determine the functional composition.

TEM: High resolution transmission electron microscopy was used to investigate the structure of obtained materials using a HRTEM acquired by a FEI Titan G2 60-300 with an image-forming Cs corrector at an accelerating voltage of 80 kV.

Raman spectroscopy: Raman spectroscopy was collected by depositing the dispersed samples on anodisc membrane and the spectra collected with Witech alpha 300 Raman spectroscopy instrument. A laser power of 12W with an integration time of 20sec and excitation laser wavelength of 532nm was used to collect the spectra. A total of 5 spectra were collected for each sample.

FTIR: FTIR (Fourier transform infra-red)spectra was collected by depositing thin films on ZnSe windows and were acquired with a Thermo-Nicolet 6700 spectrometer (ThermoElectron Corp., Madison, WI), using a sample shuttle and a mercury− cadmium-

telluride (MCT) detector. Four blocks of 128 scans each were co-added with 4 cm^{-1} spectral resolution and two levels of zero- filling so that data was encoded for every 1 cm^{-1}.

BET (Brunauer–Emmett–Teller) measurements: The surface area and porosity measurements of Pd-PGc were carried out at 77 °K using Micromeritics ASAP 2020. Pd-PGc sample was dried at 100 °C for overnight under vacuum, prior to measurement. The pore size was calculated using BJH adsorption-desorption analysis. After BET measurements, isotherms of the measurement were converted into BET plots and then specific surface area of catalyst was calculated using value of slope and intercept of linear best fit line using BET equation.

$$\frac{1}{Q[(P0/P) - 1]} = \frac{c-1}{Qmc}\left(\frac{P}{P0}\right) + \frac{1}{Wmc}$$

Here, Q is the adsorbed gas quantity, Qm is the monolayer quantity of adsorbed gas (N$_2$), c is the   BET constant, *P* and *P$_0$* are the equilibrium and the saturation pressure of adsorbates at the temperature of adsorption, respectively.

5.4.3. Oxidation of Primary Alcohols

Benzyl Alcohol (>- 99%) from Millipore, DL-sec-phenyl ethyl alcohol (97%), from Acros organics; Cyclohexane methanol (99%),4-nitrobenzyl alcohol(99%), Nitromethane (+98%), from Alfa aesar; 3-phenyl-1-propanol (>98%), 4-methoxy benzyl alcohol (>98%) from TCI; n-butanol (anhydrous 99.8%), 4-methyl benzyl alcohol (98%), Diphenyl methanol (99%) 2-Thiophene methanol (98%), cyclohexanol (Reagent plus, 98%), Cinnamyl alcohol (>-98%), 4-Fluorobenzyl alcohol (97%), 5-Hydroxy methyl furfuraldehyde (99%) from Sigma Aldrich. All the above chemicals were used in the catalytic reaction as received.

The aerobic oxidation of the alcohols was carried out by placing required amount of catalyst and the reactant in a 10ml Pyrex glass vessel (CEM, # 908035). The reaction vessel is sealed with PTFE lined Aluminum cap and then it is evacuated and filled with 1atm of O_2. The reactions are performed in various reaction conditions and they are listed in foot note of that particular table. The reaction is quenched by adding Nitromethane as an internal standard and then with $CDCl_3$ as deuterated solvent and ^1H NMR collected. The catalyst is separated from the reaction mixture by filtration using 0.2 µm syringe filter.

For Kinetic studies, experiments were carried at different temperatures. 20ml of water is purged with O_2 and then the catalyst is added into water solution and further purged with O_2 for another 15mins. 15µl of Benzyl alcohol is added and the reaction vessel is sealed with PTFE lined Aluminum cap. Sample is collected for every 15mins, and the amount of product consumed vs. amount of product formed over time is analyzed with HPLC (Varian Pro-star with C18 column) using water (0.44% Acetic acid) and methanol as mobile phase (50:50).

5.4.4. Electrochemical characterization

For ORR catalytic activity, CV (Cyclic Voltammetry) and LSV (Linear Sweep Voltammetry) of the as prepared samples were analyzed by using a computer controlled potentiostat (CHI 760C CH Instrument, USA). A typical three electrode cell was used with Platinum wire as the counter electrode, saturated Ag/AgCl as the reference electrode and the RRDE as the working electrode in 0.1M KOH electrolyte. The working electrodes were prepared by dispersing 4mg of as prepared catalyst in 0.9ml of deionized water and 0.1 ml of 10 wt.% nafion in aqueous ethanol solution by sonication and drop casting 15µl of above dispersed solution onto RRDE. The dried electrode is immersed into the 0.1M KOH

solution which was saturated with N_2 gas for 1hour and CVs were recorded for 5 times at a scan rate of 100 mV/s for stabilization of electrode. The potential was swept from 0.1 to -0.8 V vs. Ag/AgCl, and CVs were overlapped one over another to check if electrode is stabilized. Then 2 more CVs were recorded at a scan rate of 5 mV/s in N_2 saturated 0.1M KOH electrolyte. The electrolyte is saturated with O_2 for 30 min and 2 more CVs were recorded at a scan rate of 5 mV/s. This step was repeated one more time and overlaid to see that there is no change in onset and peak potentials. LSV measurements was carried out at 2000rpm with continuous O_2 purging. The % peroxide generated (eq.1) and electron transfer number (eq.2) were calculated from the LSVs using following equation.

$$\% \ HO_2^- \ = \ \frac{200 \times \frac{I_r}{N}}{I_d \times \frac{I_r}{N}} \tag{1}$$

$$n \ = \ \frac{4 \times I_d}{I_d + \frac{I_r}{N}} \tag{2}$$

where I_d and I_r are the ring and disk currents measured with RRDE. All the experiments were conducted at room temperature and t collection efficiency number N was determined to be 0.424 from redox reaction of $K_3Fe(CN)_6$. The current densities were calculated using surface area of the electrode, which is determined by integration of peak current from CV curves collected at different scan rates of $K_3Fe(CN)_6$ redox reaction.

5.5. References:

[1] a) G. Zhang, L. Cui, Y. Wang and L. Zhang, *Journal of the American Chemical Society* **2010**, *132*, 1474-1475; b) G. Zhang, Y. Peng, L. Cui and L. Zhang, *Angewandte Chemie International Edition* **2009**, *48*, 3112-3115; c) L. Cui, G. Zhang and L. Zhang, *Bioorganic & Medicinal Chemistry Letters* **2009**, *19*, 3884-3887; d) Y. Peng, L. Cui, G. Zhang and L. Zhang, *Journal of the American Chemical Society* **2009**, *131*, 5062-5063.

[2] a) M. Besson and P. Gallezot, *Catalysis Today* **2000**, *57*, 127-141; b) S. S. Stahl, *Science* **2005**, *309*, 1824-1826; c) P. D. Stevens, G. Li, J. Fan, M. Yen and Y. Gao, *Chemical Communications* **2005**, 4435-4437; d) K. Kaneda, M. Fujii and K. Morioka, *The Journal of Organic Chemistry* **1996**, *61*, 4502-4503.

[3] a) T. Mallat and A. Baiker, *Catalysis Today* **1994**, *19*, 247-283; b) R. A. Periana, D. J. Taube, S. Gamble, H. Taube, T. Satoh and H. Fujii, *Science* **1998**, *280*, 560-564; c) H. G. J. de Wilt, *Product R&D* **1972**, *11*, 370-373; d) H. G. J. de Wilt and H. S. van der Baan, *Product R&D* **1972**, *11*, 374-378.

[4] a) P. Meric, K. M. K. Yu and S. C. Tsang, *Langmuir* **2004**, *20*, 8537-8545; b) H. Ohde, C. M. Wai, H. Kim, J. Kim and M. Ohde, *Journal of the American Chemical Society* **2002**, *124*, 4540-4541; c) P. Meric, K. M. K. Yu and S. C. Tsang, *Catalysis Letters* **2004**, *95*, 39-43.

[5] a) H. Tsunoyama, H. Sakurai and T. Tsukuda, *Chemical Physics Letters* **2006**, *429*, 528-532; b) S. Kanaoka, N. Yagi, Y. Fukuyama, S. Aoshima, H. Tsunoyama, T. Tsukuda and H. Sakurai, *Journal of the American Chemical Society* **2007**, *129*, 12060-12061; c) H. Tsunoyama, H. Sakurai, Y. Negishi and T. Tsukuda, *Journal of the American Chemical Society* **2005**, *127*, 9374-9375.

[6] a) T. Iwasawa, M. Tokunaga, Y. Obora and Y. Tsuji, *Journal of the American Chemical Society* **2004**, *126*, 6554-6555; b) T. Nishimura, T. Onoue, K. Ohe and S. Uemura, *The Journal of Organic Chemistry* **1999**, *64*, 6750-6755; c) D. J. Gorin, B. D. Sherry and F. D. Toste, *Chemical Reviews* **2008**, *108*, 3351-3378.

[7] a) J. Pritchard, L. Kesavan, M. Piccinini, Q. He, R. Tiruvalam, N. Dimitratos, J. A. Lopez-Sanchez, A. F. Carley, J. K. Edwards, C. J. Kiely and G. J. Hutchings, *Langmuir* **2010**, *26*, 16568-16577; b) S. Xie, H. Tsunoyama, W. Kurashige, Y. Negishi and T. Tsukuda, *ACS Catalysis* **2012**, *2*, 1519-1523; c) T. A. G. Silva, E. Teixeira-Neto, N. López and L. M. Rossi, *Scientific Reports* **2014**, *4*, 5766; d) H. Wang, C. Wang, H. Yan, H. Yi and J. Lu, *Journal of Catalysis* **2015**, *324*, 59-68; e) K. Tedsree, T. Li, S. Jones, C. W. A. Chan, K. M. K. Yu, P. A. J. Bagot, E. A. Marquis, G. D. W. Smith and S. C. E. Tsang, *Nat Nano* **2011**, *6*, 302-307.

[8] a) C. Della Pina, E. Falletta and M. Rossi, *Journal of Catalysis* **2008**, *260*, 384-386; b) K. Sonogashira, *Journal of Organometallic Chemistry* **2002**, *653*, 46-49; c) S. U. Son, Y. Jang, J. Park, H. B. Na, H. M. Park, H. J. Yun, J. Lee and T. Hyeon, *Journal of the American Chemical Society* **2004**, *126*, 5026-5027.

[9] T. Harada, S. Ikeda, F. Hashimoto, T. Sakata, K. Ikeue, T. Torimoto and M. Matsumura, *Langmuir* **2010**, *26*, 17720-17725.

[10] a) V. Singh, B. R. Mehta, S. K. Sengar, P. K. Kulriya, S. A. Khan and S. M. Shivaprasad, *The Journal of Physical Chemistry C* **2015**, *119*, 14455-14460; b) X. Sun and Y. Li, *Angewandte Chemie International Edition* **2004**, *43*, 597-601; c) L. Guo, W.-J. Jiang, Y. Zhang, J.-S. Hu, Z.-D. Wei and L.-J. Wan, *ACS Catalysis* **2015**, *5*, 2903-2909; d) R. Harpeness and A. Gedanken, *Langmuir* **2004**, *20*, 3431-3434; e) D. Y. Chung, S. W. Jun, G. Yoon, S. G. Kwon, D. Y. Shin, P. Seo, J. M. Yoo, H. Shin, Y.-H. Chung, H. Kim, B. S. Mun, K.-S. Lee, N.-S. Lee, S. J. Yoo, D.-H. Lim, K. Kang, Y.-E. Sung and T. Hyeon, *Journal of the American Chemical Society* **2015**, *137*, 15478-15485.

[11] a) E. Martono and J. M. Vohs, *Journal of Catalysis* **2012**, *291*, 79-86; b) F. de Clippel, M. Dusselier, R. Van Rompaey, P. Vanelderen, J. Dijkmans, E. Makshina, L. Giebeler, S. Oswald, G. V.

Baron, J. F. M. Denayer, P. P. Pescarmona, P. A. Jacobs and B. F. Sels, *Journal of the American Chemical Society* **2012**, *134*, 10089-10101; c) G. Prieto, J. Zečević, H. Friedrich, K. P. de Jong and P. E. de Jongh, *Nat Mater* **2013**, *12*, 34-39.

[12] a) J. Luo, H. Yu, H. Wang, H. Wang and F. Peng, *Chemical Engineering Journal* **2014**, *240*, 434-442; b) D. R. Dreyer, H.-P. Jia and C. W. Bielawski, *Angewandte Chemie* **2010**, *122*, 6965-6968; c) Y. Kuang, N. M. Islam, Y. Nabae, T. Hayakawa and M.-a. Kakimoto, *Angewandte Chemie International Edition* **2010**, *49*, 436-440; d) J. Vijaya Sundar and V. Subramanian, *Organic Letters* **2013**, *15*, 5920-5923; e) Y. Meng, D. Voiry, A. Goswami, X. Zou, X. Huang, M. Chhowalla, Z. Liu and T. Asefa, *Journal of the American Chemical Society* **2014**, *136*, 13554-13557.

[13] a) H. Watanabe, S. Asano, S.-i. Fujita, H. Yoshida and M. Arai, *ACS Catalysis* **2015**, *5*, 2886-2894; b) K. Chizari, I. Janowska, M. Houllé, I. Florea, O. Ersen, T. Romero, P. Bernhardt, M. J. Ledoux and C. Pham-Huu, *Applied Catalysis A: General* **2010**, *380*, 72-80; c) A. Dhakshinamoorthy, A. Primo, P. Concepcion, M. Alvaro and H. Garcia, *Chemistry – A European Journal* **2013**, *19*, 7547-7554; d) J. Long, X. Xie, J. Xu, Q. Gu, L. Chen and X. Wang, *ACS Catalysis* **2012**, *2*, 622-631; e) Y. Ding, L. Zhang, K.-H. Wu, Z. Feng, W. Shi, Q. Gao, B. Zhang and D. S. Su, *Journal of Colloid and Interface Science* **2016**, *480*, 175-183.

[14] M. A. Patel, F. Luo, M. R. Khoshi, E. Rabie, Q. Zhang, C. R. Flach, R. Mendelsohn, E. Garfunkel, M. Szostak and H. He, *ACS Nano* **2016**, *10*, 2305-2315.

[15] a) X. Xu, Y. Li, Y. Gong, P. Zhang, H. Li and Y. Wang, *Journal of the American Chemical Society* **2012**, *134*, 16987-16990; b) V. B. Parambhath, R. Nagar and S. Ramaprabhu, *Langmuir* **2012**, *28*, 7826-7833; c) Z. Wei, Y. Gong, T. Xiong, P. Zhang, H. Li and Y. Wang, *Catalysis Science & Technology* **2015**, *5*, 397-404; d) B. P. Vinayan, R. Nagar and S. Ramaprabhu, *Journal of Materials Chemistry A* **2013**, *1*, 11192-11199; e) Z. Li, J. Liu, Z. Huang, Y. Yang, C. Xia and F. Li, *ACS Catalysis* **2013**, *3*, 839-845; f) P. Zhang, Y. Gong, H. Li, Z. Chen and Y. Wang, *Nature Communications* **2013**, *4*, 1593.

[16] a) Z.-W. Liu, F. Peng, H.-J. Wang, H. Yu, W.-X. Zheng and J. Yang, *Angewandte Chemie International Edition* **2011**, *50*, 3257-3261; b) M. Latorre-Sánchez, A. Primo and H. García, *Angewandte Chemie International Edition* **2013**, *52*, 11813-11816; c) D.-S. Yang, D. Bhattacharjya, S. Inamdar, J. Park and J.-S. Yu, *Journal of the American Chemical Society* **2012**, *134*, 16127-16130; d) R. Li, Z. Wei and X. Gou, *ACS Catalysis* **2015**, *5*, 4133-4142; e) C. H. Choi, S. H. Park and S. I. Woo, *Journal of Materials Chemistry* **2012**, *22*, 12107-12115.

[17] a) H.-m. Wang, H.-x. Wang, Y. Chen, Y.-j. Liu, J.-x. Zhao, Q.-h. Cai and X.-z. Wang, *Applied Surface Science* **2013**, *273*, 302-309; b) X. Zhang, Z. Lu, Z. Fu, Y. Tang, D. Ma and Z. Yang, *Journal of Power Sources* **2015**, *276*, 222-229.

[18] a) Y. Gao, G. Hu, J. Zhong, Z. Shi, Y. Zhu, D. S. Su, J. Wang, X. Bao and D. Ma, *Angewandte Chemie International Edition* **2013**, *52*, 2109-2113; b) W. Li, Y. Gao, W. Chen, P. Tang, W. Li, Z. Shi, D. Su, J. Wang and D. Ma, *ACS Catalysis* **2014**, *4*, 1261-1266.

[19] A. Barau, V. Budarin, A. Caragheorgheopol, R. Luque, D. J. Macquarrie, A. Prelle, V. S. Teodorescu and M. Zaharescu, *Catalysis Letters* **2008**, *124*, 204-214.

[20] a) J. M. Campelo, A. F. Lee, R. Luque, D. Luna, J. M. Marinas and A. A. Romero, *Chemistry – A European Journal* **2008**, *14*, 5988-5995; b) H. Choi, S. R. Al-Abed, S. Agarwal and D. D. Dionysiou, *Chemistry of Materials* **2008**, *20*, 3649-3655.

[21] a) C. Wang, C. Wu, S. Chen, Q. He, D. Liu, X. Zheng, Y. A. Haleem and L. Song, *RSC Advances* **2017**, *7*, 4667-4670; b) K. M. Metz, S. E. Sanders, J. P. Pender, M. R. Dix, D. T. Hinds, S. J. Quinn, A. D. Ward, P. Duffy, R. J. Cullen and P. E. Colavita, *ACS Sustainable Chemistry & Engineering* **2015**, *3*, 1610-1617; c) S. H. Yu, X. J. Cui, L. L. Li, K. Li, B. Yu, M. Antonietti and H. Cölfen, *Advanced Materials* **2004**, *16*, 1636-1640.

[22] a) A. J. Pollard, B. Brennan, H. Stec, B. J. Tyler, M. P. Seah, I. S. Gilmore and D. Roy, *Applied Physics Letters* **2014**, *105*, 253107; b) A. C. Ferrari and D. M. Basko, *Nat Nano* **2013**, *8*, 235-246.

[23] a) L. G. Cançado, K. Takai, T. Enoki, M. Endo, Y. A. Kim, H. Mizusaki, A. Jorio, L. N. Coelho, R. Magalhães-Paniago and M. A. Pimenta, *Applied Physics Letters* **2006**, *88*, 163106; b) L. G. Cançado, A. Jorio, E. H. M. Ferreira, F. Stavale, C. A. Achete, R. B. Capaz, M. V. O. Moutinho, A. Lombardo, T. S. Kulmala and A. C. Ferrari, *Nano Letters* **2011**, *11*, 3190-3196; c) D. Deng, L. Yu, X. Pan, S. Wang, X. Chen, P. Hu, L. Sun and X. Bao, *Chemical Communications* **2011**, *47*, 10016-10018.

[24] a) M. Kruk and M. Jaroniec, *Chemistry of Materials* **2001**, *13*, 3169-3183; b) K. S. W. Sing, D. H. Everett, R. A. W. Haul, L. Moscou, R. A. Pierotti, J. Rouquerol and T. Siemieniewska, *Pure and Applied Chemistry* **1985**, *57*, 603-619.

[25] a) S. Bera, A. Naskar, M. Pal and S. Jana, *RSC Advances* **2016**, *6*, 36058-36068; b) R. Tao, S. Miao, Z. Liu, Y. Xie, B. Han, G. An and K. Ding, *Green Chemistry* **2009**, *11*, 96-101; c) G. Leofanti, M. Padovan, G. Tozzola and B. Venturelli, *Catalysis Today* **1998**, *41*, 207-219.

[26] G. M. Scheuermann, L. Rumi, P. Steurer, W. Bannwarth and R. Mülhaupt, *Journal of the American Chemical Society* **2009**, *131*, 8262-8270.

[27] a) X. Yang, C. Huang, Z. Fu, H. Song, S. Liao, Y. Su, L. Du and X. Li, *Applied Catalysis B: Environmental* **2013**, *140*, 419-425; b) M. Rakap, E. E. Kalu and S. Özkar, *International Journal of Hydrogen Energy* **2011**, *36*, 1448-1455; c) D. Łomot and Z. Karpiński, *Research on Chemical Intermediates* **2015**, *41*, 9171-9179.

[28] a) S. D. Jackson and L. A. Shaw, *Applied Catalysis A: General* **1996**, *134*, 91-99; b) V. R. Choudhary, M. G. Sane and S. S. Tambe, *Industrial & Engineering Chemistry Research* **1998**, *37*, 3879-3887; c) P. Zhang, Y. Gong, H. Li, Z. Chen and Y. Wang, **2013**, *4*, 1593.

[29] H. S. Black, *Frontiers in Bioscience* **2002**, *7*, 1044-1055.

[30] a) A. Savara, C. E. Chan-Thaw, I. Rossetti, A. Villa and L. Prati, *ChemCatChem* **2014**, *6*, 3464-3473; b) A. Savara, I. Rossetti, C. E. Chan-Thaw, L. Prati and A. Villa, *ChemCatChem* **2016**, *8*, 2482-2491.

Chapter 6- A Novel One Step Microwave Assisted Fabrication of Sn_4P_3 @ Phosphorous Doped Carbon as a Superior Anode Material for Sodium Ion Battery

6.1. Introduction

Despite lithium ion batteries (LIB) demonstrating a high energy density and increased cycle life, lithium is considered a limited resource. Hence, contemporary research has marked the transition for utilization of sodium as a low cost and naturally abundant metal substituent for LIB's. However, sodium ion battery (SIB) presents its own disadvantages such as, less favorable redox potential, slower ion transport and larger volumetric expansion due to the large Na ion's radius (0.95 Å) in comparison to that of Li ion (0.6 Å). This deteriorates rate capability and Na storing reversibility in SIB's. Graphite, the most commonly used anode material in LIB's, reports a low discharge capacity (150 mAhg^{-1}) upon sodiation/desodiation in SIB's. A more practical capacity could be achieved by enlarging interlayer distance or co-intercalation of the graphite electrodes (≈300mAhg^{-1})[1]. The low capacity of carbon electrodes can be attributed to limited sodium host sites, relatively close potentials for insertion and deposition of Na, low energy capacity and poor cycling stability. Extensive efforts were pursued in order to develop an anode with a high energy density and low redox potential. Inclusion of phosphorus into the anode of SIB's could result in a high theoretical capacity of 2596 mAhg^{-1} (Na_3P)[2] and desired redox potentials (0.4V vs Na/Na$^+$), however, poor electrical conductivity was observed due to P. Alloying of Na with metals such as Pb (Na15Pb4 - 485 mAh g^{-1}), Sn[3] (Na15Sn4 - 847 mAhg^{-1}), Sb[4] (Na3Sb -660 mAh/g^{-1}), Bi (Na3Bi - 385 mAhg^{-1}), Ge[5] (NaGe – 344mAhg$^-$

[1]) also increases gravimetric capacities of SIB's. Sn is extensively used to alloy with Na ($Na_{15}Sn_4$- 847mAhg^{-1}) for its low cost, environmental friendly, high theoretical capacity, high electrical conductivity and appropriate redox potential in comparison to Sb and Ge. Nevertheless, enormous volume expansion during the formation of $Na_{15}Sn_4$ (525%) and Na_3P (420%), results in capacity decay by pulverization and hence limits practicality of their usage in SIB's. This issue can be addressed by formation of metal phosphide with a theoretical capacity as high as 1133mAhg^{-1} (for Sn_4P_3). The reversible conversion of Sn_4P_3 + 9 Na ↔ 3Na$_3$P + 4Sn prevents continuous pulverization and aggregation of Sn alloy upon sodiation/desodiation and is referred to as a self-healing mechanism[6]. Experimentally it was reported that, in Sn_4P_3, thickness of the electrode increased to ≈200% after sodiation whereas upon desodiation, it returned to ≈60% of its initial thickness. This indicates that, the self-healing mechanism is not completely reversible and hence possibility of partial pulverization cannot be eliminated. Addition of carbon into Sn_4P_3 reduced the thickness to 11% after desodiation[7], hence improving cycling stability with a discharge capacity of 718mAhg^{-1} after 100 cycles .

Henceforth extra protective barriers such as core shell structures with either carbon nanocomposites (500 mAhg^{-1} at 100 mAhg^{-1} over 150 cycles)[8] or amorphous Sn-P (465 mAhg^{-1} at 100 mAhg^{-1} over 100 cycles)[9] were explored in order to mitigate pulverization. Yu and coworkers[10] reported a yolk shell structure to further enhance the discharge capacity, to as high as 360 mAhg^{-1} (1.5C after 400 cycles). The uniqueness of this approach could be attributed to presence of in-house void space between carbon core and Sn_4P_3 yolk structure, which accommodates to the volume expansion during sodiation/desodiation. However, practicality of this approach is limited by its complicated multi step procedure,

(1) fabrication of SnO_2 hollow spheres through hydrothermal process, (2) carbonization and in situ reduction by hydrothermal carbon coating and annealing in H_2/Ar, which results in Sn@C yolk shell nanospheres, (3) low temperature phosphorization with red P, to transform Sn nanoparticles to Sn_4P_3@C nanospheres. Recently, Sn_4P_3/reduced graphene oxide (rGO) hybrids[11] with a discharge capacity of $362mAhg^{-1}$ at $1000mAg^{-1}$ after 1500cycles was reported. The rGO are interconnected to form 3D mesoporous assemblies which work to buffer volume expansion as well as enhance conductivity during sodiation/desodiation.   Even though Sn_4P_3 is fabricated by simply alloying red phosphorous with Sn, initial immobilization of $SnCl_2$ nanoparticles on rGO is realized, followed by its reduction with $NaBH_4$ and its phosphorization with red phosphorous at 200^0C for 40hr. Prolonged reaction time, however, limits the practicality of this approach.

In our current method, a single step, one pot synthesis of Sn_4P_3 protected by porous carbon shell and embedded in the PGc (phosphorous doped porous carbon) was achieved *via* microwave irradiation in as short as 100sec. Phytic acid, a biomass and anti-nutrient molecule, which absorbs microwave radiation and acts as both a phosphorous and carbon source is utilized. Ethylene glycol, added into the reaction mixture not only acts as a reducing agent, but also as a microwave absorber. The presence of heteroatoms such as N promotes better interaction and uniform dispersion nanoparticles. Phosphorous, which has same number of valence electrons as N, makes the material electron rich and should exhibit similar phenomenon. As reported in our previous work, PGc[12], the large atomic radius of phosphorous generated a wrinkled morphology. This wrinkled morphology creates additional space in Sn_4P_3 covered phosphorous doped porous carbon, to accommodate volume expansion. The present invention offers following advantages: (1) no toxic

phosphine is generated (2) energy and time efficient (3) sustainable/cheap resources (for source of phosphorous and carbon) (4) one-step approach (5) no inert environment was required. SnP@PGc, was tested for SIB's, which exhibits a capacity of ~390 mAhg^{-1} even after 1150 cycles at a charge/discharge current of 1 C, indicating the robustness of electrode for long term use.

6.2. Results and Discussion

The tin phosphides wrapped with phosphorous doped porous carbon shell and sandwiched with PGc was achieved in this present work (SnP@PGc-1). Ethylene glycol was used as an additional reducing agent apart from internal reductant, phytic acid, which is used as a carbon [13] and phosphorous source, as shown **Scheme 6.1.**
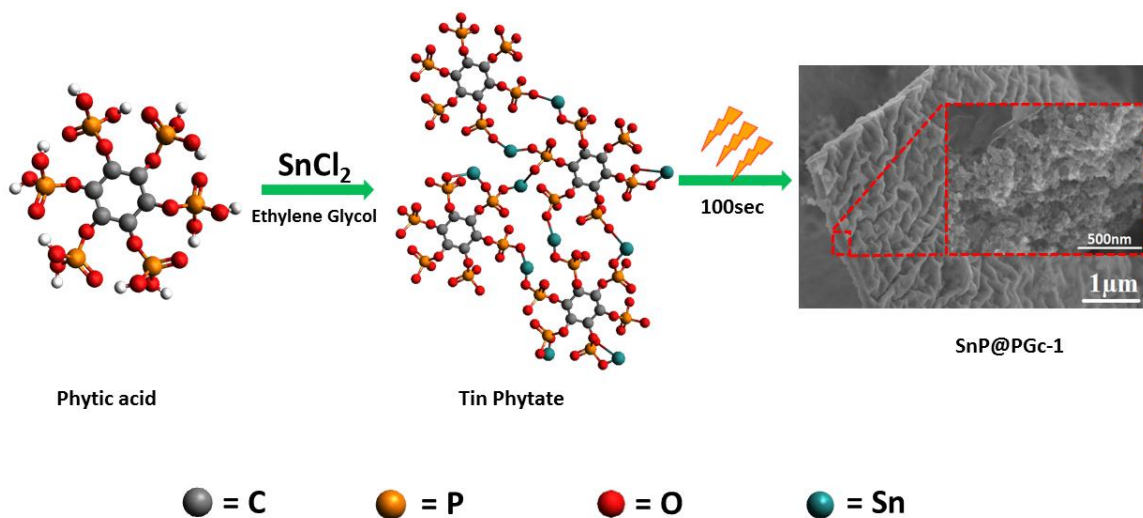
Scheme 6.1. The Graphical illustration of microwave assisted fabrication of SnP@PGc-1. The ratio of SnCl$_2$ to phytic acid used was 1.23: 1, which upon microwave irradiation for 100sec resulted in SnP@PGc-1. XRD was employed to study phase compounds of the as synthesized SnP@PGc-1. Sharp diffraction patterns at 28.8^0 and 31.5^0which account for 015 and 107 planes of rhombohedral Sn$_4$P$_3$, **Figure 6.1. (a)** were observed. This is

supported by marked d spacing's of 0.31 and 0.28nm of Sn_4P_3 crystals, by high resolution

transmission electron microscopy (HR-TEM), which are in good agreement with 015 and

107 planes of rhombohedral Sn_4P_3 **Figure 6.1. (d, e).** Low resolution TEM image indicates

the uniform distribution of Sn_4P_3 with carbon shell enclosed in PGc matrix.
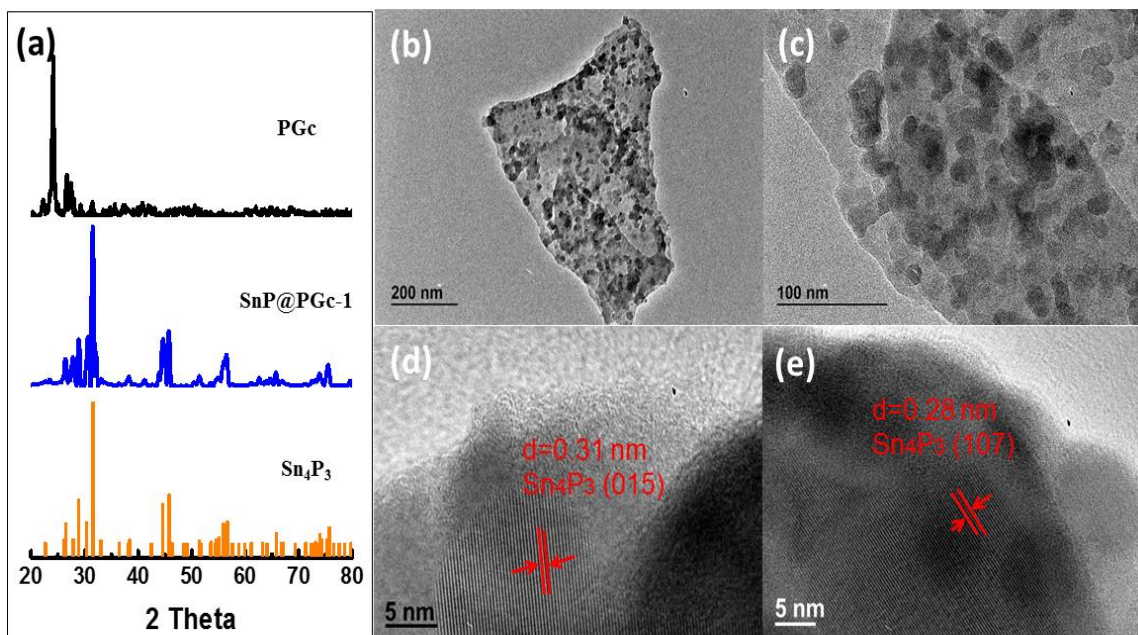

Figure 6.1. The XRD diffraction patterns of SnP@PGc corresponding to Sn_4P_3 and SnP_2O_7 diffraction patterns (a), low resolution (b, c) and high resolution (d, e) TEM imaging of SnP@PGc-1.

According to density functional theory calculations[14], incorporation of phosphorous

heteroatom with larger atomic size than carbon, induces strain. This leads to distortion of

the carbon skeleton [12], hence explaining the observed wrinkled morphology in SEM,

Figure 6.2.(b). The cross sectional view exhibited wrinkled carbon sheets sandwiching the

phosphorous doped porous carbon and Sn phosphide nanoparticles, **Figure 6.2. (a),**

whereas EDS mapping revealed uniform distribution of Sn, P, C and O in the as synthesized
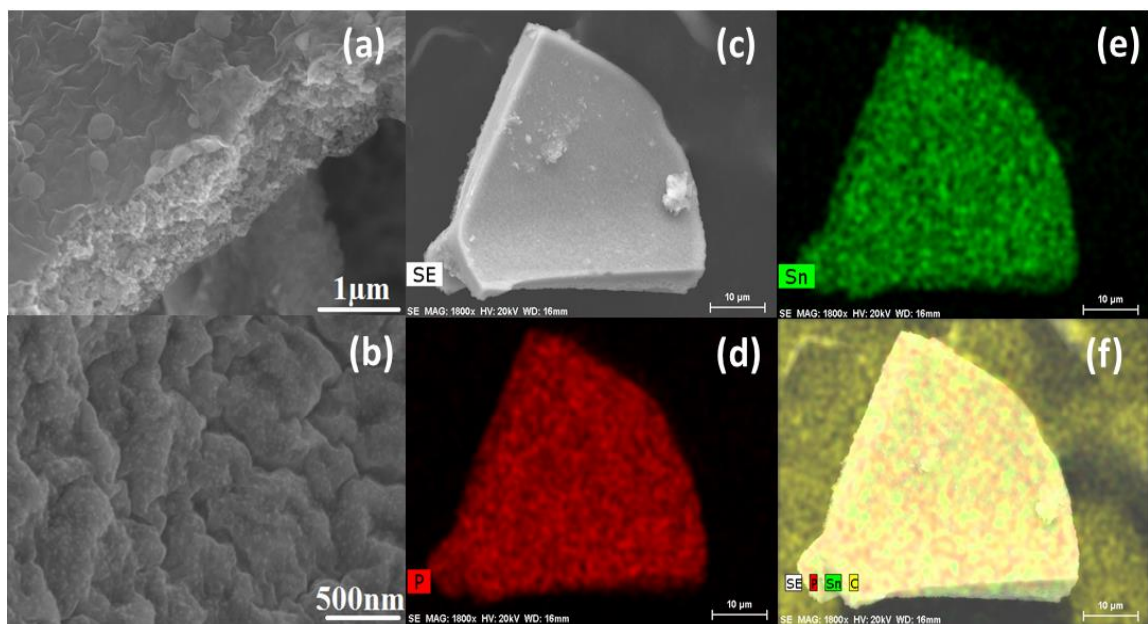
SnP@PGc-1, **Figure 6.2. (c-f)**.

Figure 6.2. The top (e, f) and cross sectional (g, h) morphology of microwave synthesized SnP@PGc-1 via SEM. EDS mapping of SnP@PGc-1, with morphology in SEM view (a), mapping view of elements Sn (b), P(c), and overlay of all the elements (d), tremendous carbon signals outside the sample are from carbon tape.

Surface chemical analysis of SnP@PGc-1 was further recorded by XPS, where survey scan indicated the presence of Sn, P, C, and O peaks. Deconvolution of Sn indicates its existence as Sn^{+4} corresponding to binding energies of 487ev and 496ev. The spin orbital splitting of Sn deconvolution peaks was 8.4ev for SnP@PGc-1, lower in comparison to tin oxides [15].The P deconvolution exhibits additional peaks at 139.6 and 140.3ev, apart from 133.9ev (Sn/C-P-O) and 134.7ev (C-P-O). Additional peak can be assigned to the presence of surface oxides corresponding to P-O (533ev) peak[16], **Figure 6.3**. C deconvolution exhibits presence of graphitic carbon domains (C=C, sp2 carbon, 284.5ev), supporting the G band of raman spectra, with a graphitic crystalline size of 20.9nm (**Figure 6.3. (e)**).
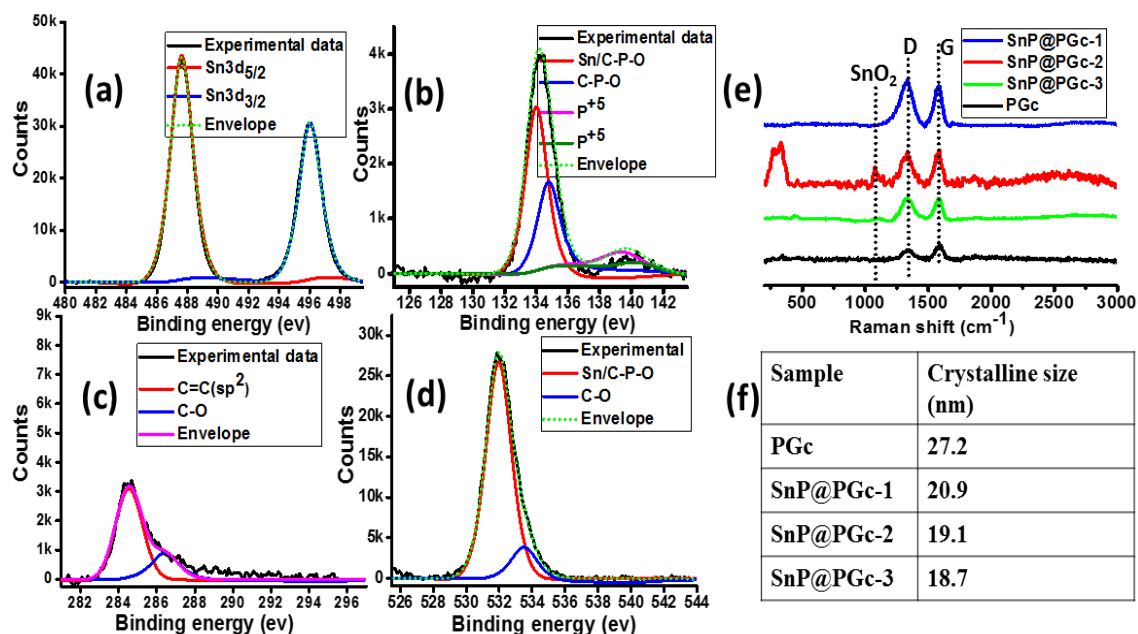
Figure 6.3. XPS deconvolution of tin (a), phosphorous (b), carbon (c), and oxygen (d). Raman spectra of SnP@PGc-1 with characteristic D and G band and their corresponding graphitic crystalline size.

The influence of PGc matrix on surface area of SnP@PGc's were analyzed by Brunauer–Emmett–Teller (BET) technique. PGc exhibits a higher surface area of $704.01 \text{m}^2/\text{g}$, whereas $17.19 \text{m}^2/\text{g}$ was recorded for SnP@PGc-1. This indicates the chelation of metal with phytic acid to form tin phosphides happened in the majority, rather than its contribution to form the PGc matrix, **Figure 6.4.**

Figure 6.4. BET surface area analysis of PGc (a), and SnP@PGc (b, c, d, e) showing hysteresis in the adsorption - desorption isotherms.
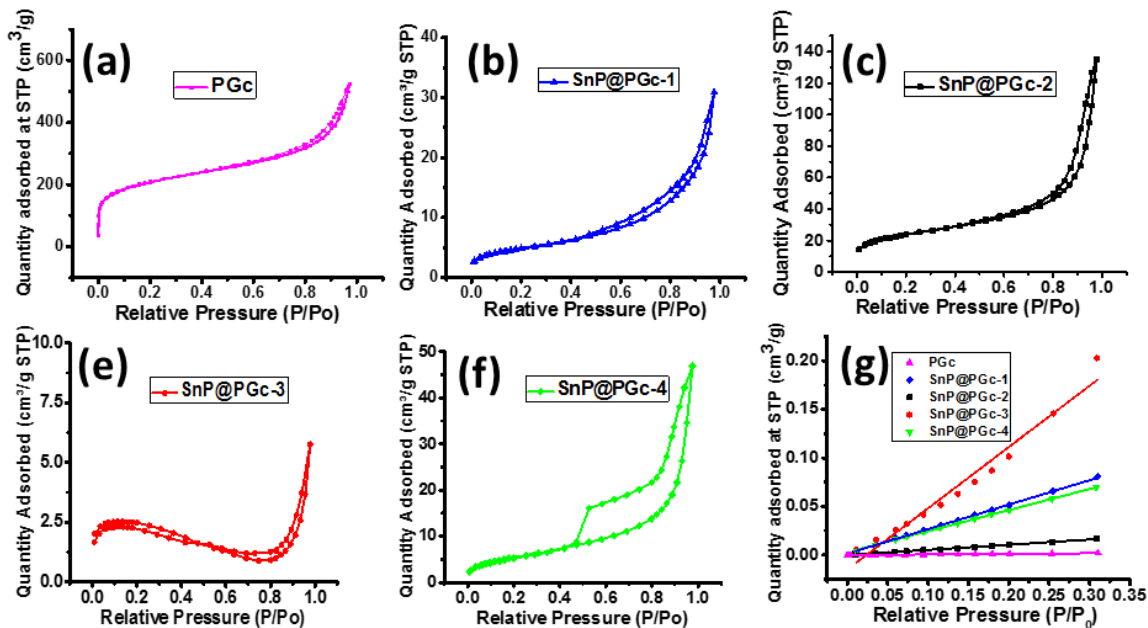
Ex situ ATR-IR was studied to monitor changes in the reaction mixture at different microwave irradiation time. A peak at $3300cm^{-1}$ accounts for presence of –OH species, attached to phosphate moieties in the parent phytic acid molecule along with its contribution from water solution (phytic acid 50% (w/v) in water). The addition of $SnCl_2$ lead to attenuation of the C-O-P peak at $1000-1160cm^{-1}$, indicating the formation of tin phytate chelate. Upon microwave irradiation, at 40sec, disappearance of OH peak, followed by cleavage of hydrogen phosphate moiety [17] ($1640cm^{-1}$) was observed. This indicates initial dehydration of reaction mixture to form gel, followed by cleavage of phosphate moiety to generate red phosphorous (visually observed). The red phosphorous then reacts with Sn to synthesize Sn_4P_3. Additional peaks at $<1000cm^{-1}$ and at $1500cm^{-1}$ indicates formation of phosphorous doped graphene like carbon structures, **Figure 6.5 (a).**
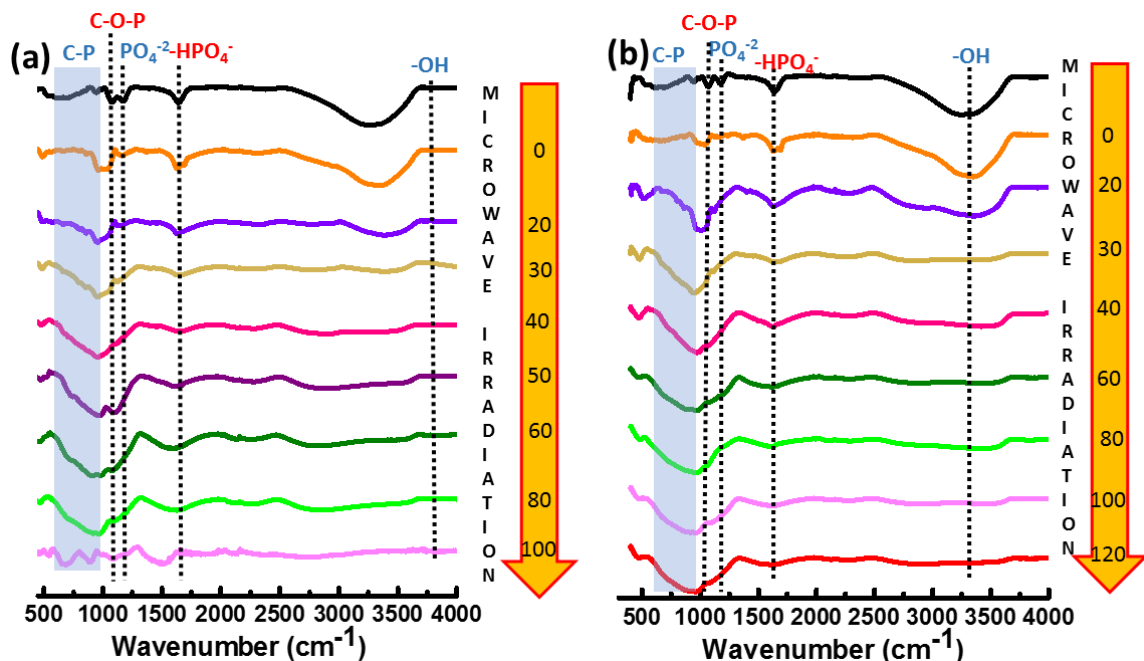
Figure 6.5. The ATR-IR at different MW irradiation times (a) which depicts the cleavage of phosphate moiety in SnP@PGc-1, whereas no cleavage of phosphate moiety was observed in case of SnP@PGc-2 and 3.

The resulting SnP@PGc samples were tested for their energy storage performance in Na ion battery. SnP@PGc-1 demonstrated an outstanding cycling performance after first cycle as shown in **Figure 6.6. (a).** The reversible capacity as high as 515 mAh/g was maintained after 750 cycles at a charge/discharge current of 0.2C with about 80% capacity retention compared to the 10th cycle. A capacity of ~390 mAh/g was maintained even after 1150 cycles at a charge/discharge current of 1 C as reported in **Figure 6.6.(b).** The enhanced rate capability was recorded with stable desodiation capacities of 650, 565, 490, 410, 320, 230 mAh/g at charge/discharge current densities of 0.2C, 0.5C, 1C, 2C, 4C, and 8C. When current density is finally returned to its initial value of 0.5 C, the capacity completely recovered, implying excellent tolerance for rapid sodium ion insertion/extraction cycles. This can be ascribed to the uniform distribution of tin phosphide nanoparticles and highly

conductive network of phosphorous doped carbon formed in situ during synthesis and thereby preventing their agglomeration.
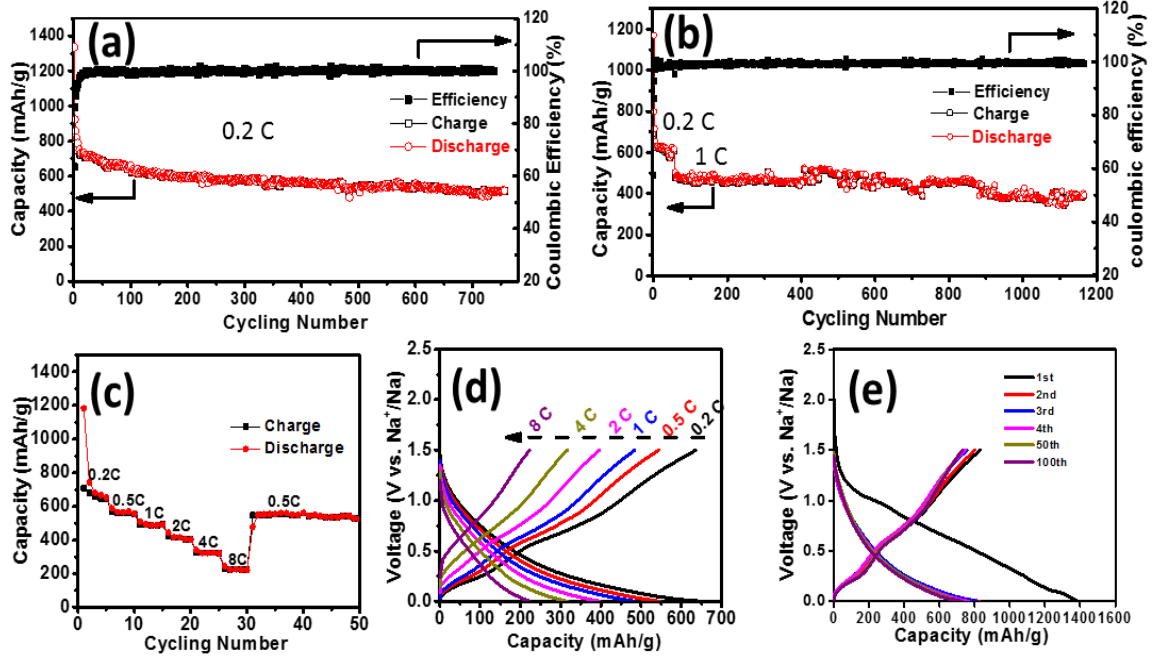

Figure 6.6. Reversible capacities at 200mAhg^{-1} for 750cycles (a), and the maintained discharge capacity even at 1150cycles after change in the current density to 1000mAhg^{-1}. Cycling performance using different charge/discharge rates (c). Sodiation/desodiation capacities and corresponding voltage profiles at different current density (d), Galvanostatic charge-discharge voltage profiles at a current density of 100 mA/g for SnP@PGc-1(e) at different cycles.

The sodiation-desodiation curves of different cycles for SnP@PGc-1 under a constant current density of 200 mA/g (0.2 C) was reported in **Figure 6.6. (d)**. The initial sodiation of the composite provides an overall capacity of 1388 mAh/g **Figure 6.6. (e)**, with extraction of 60% of inserted Na (832 mAh/g). The initial capacity loss can be attributed primarily due to consumption of Na-ions for formation of SEI layer during first discharge step, indicating the activation of electrode. In general, the sodiation curves consist of a sloping region from 1.5 V to 0 V, with two inclined plateaus at about 0.2 and 0.6 V during desodiation. These inclined plateaus should be ascribed to desodiation of Na$_x$Sn and Na$_y$P based on previous reports on Sn$_4$P$_3$ anodes for Na storage.[7-9, 18].

The TEM of cycled and washed SnP@PGc-1 indicates its structural integrity without any cracks even after 750 sodiation-desodiation cycles, revealing robust nature of the electrode and its contribution to their superior performance, **Figure 6.7.(a)**. The above result indicates that the wrinkled PGc matrix not only provides fast and efficient electron transport, but also accommodates to volume change during sodiation-desodiation reactions, which hinders pulverization of the composite.
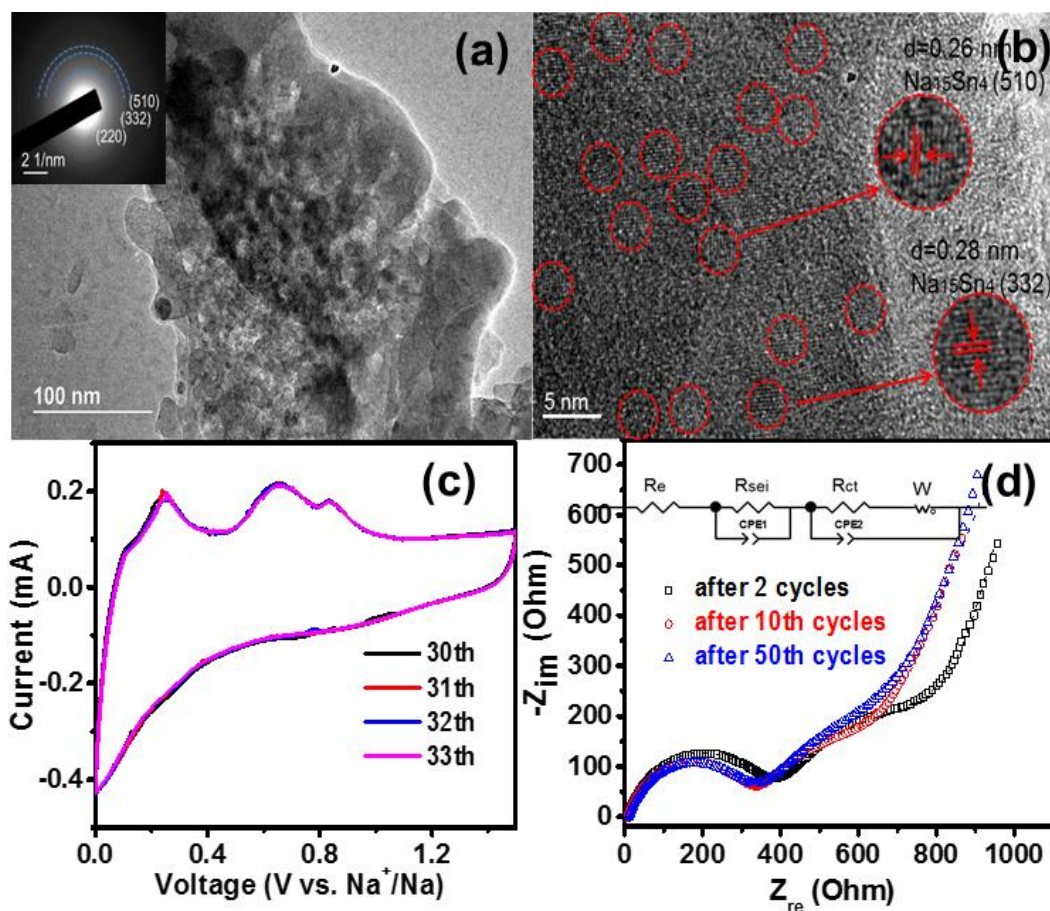
Figure 6. 7. The TEM (a) and HRTEM (b) images for SnP@PGc-1 after sodiation. Inset of Figure (a) is the selected area electron diffraction (SAED) patterns. Cyclic voltammetry of SnP@PGc-1 (c), and nyquist plot of composite cell after different cycles with inset showing equivalent circuit used for data fitting (Symbols, experimental data; dashed lines, fitting results).

The nanoparticles of $Na_{15}Sn_4$ (PDF# 65-2166) with size of about 3 nm can be clearly detected in the cycled SnP@PGc-1, *via* HRTEM, indicating the alloying of Sn_4P_3

with Na **Figure 6.7. (b)**. The HADDF-STEM image and corresponding EDS elemental mapping in **Figure 6.8.**, demonstrates robust structure of the electrode contributing to its superior performance by overlapped Sn, P and Na signal.
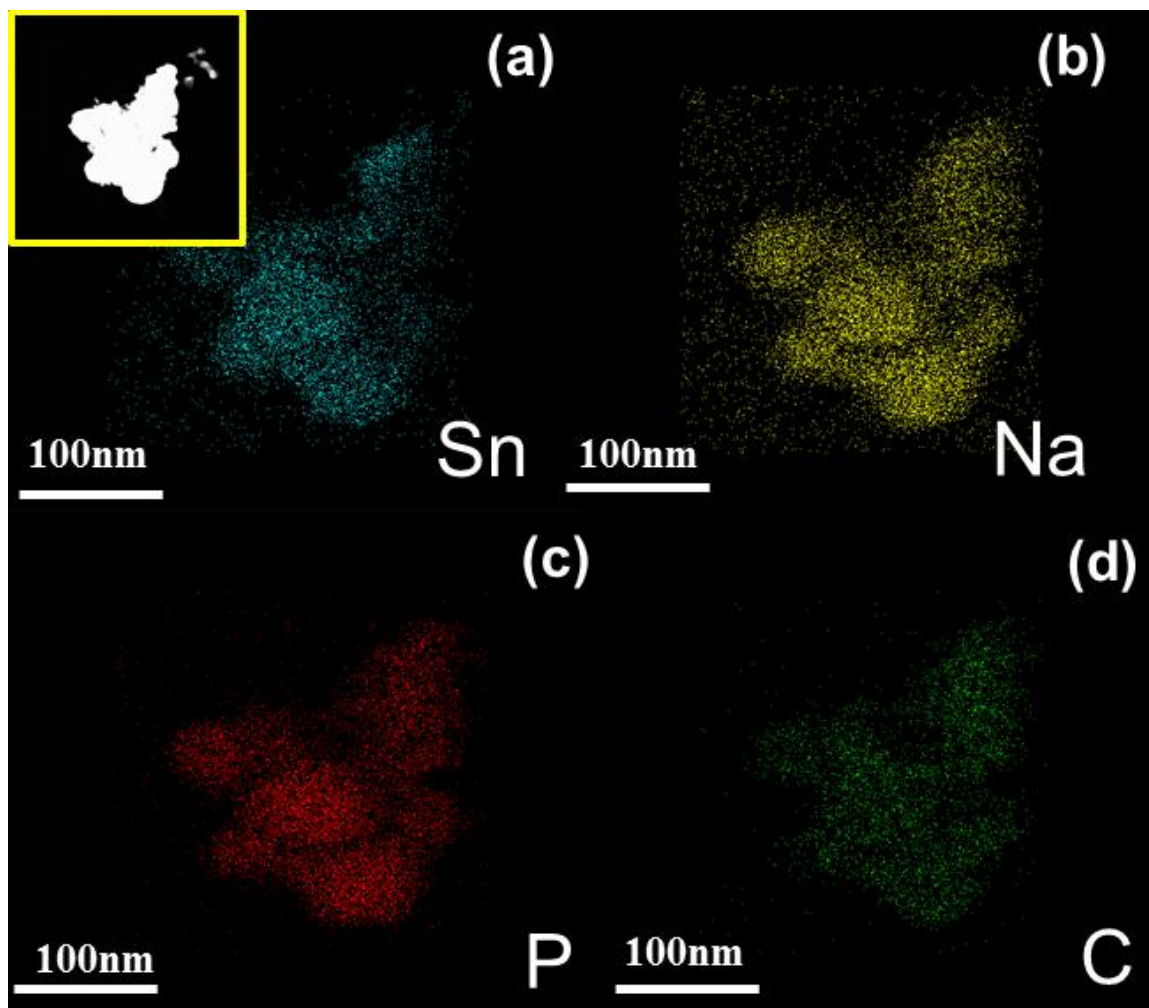
Figure 6.8. HADDF-STEM image in the inset (a) and corresponding Sn, P, Na, and C elemental mapping for SnP@PGc-1 after sodiation.

To get a detailed information in regards to the electrochemical reaction, cyclic voltammetry (CV) of SnP@PGc-1 sample was investigated at a scanning rate of 0.1 mV s^{-1} in voltage range of 0-1.5 V *vs*. Na^+/Na (**Figure 6.7.(c)**). A large reduction peak at 0.4-0.0 V is observed in cathodic scan, which is in good agreement with galvanostatic charge-discharge profiles and due to the overlap of sodiation of Sn and P species. In reversed

anodic scans, the desodiation peak at 0.27 V could be mainly attributed to the de-alloying reaction of $Na_{15}Sn_4$. Anodic peaks at 0.65 and 0.85 V could be assigned to the reversible de-alloying reaction of Na_3P together with further desodiation of Na_xSn. Thus indicative to the alloying and dealloying mechanism as reported for Sn_4P_3 [6, 8].

Electrochemical impedance spectroscopy (EIS) is used to investigate the mechanism for stable cycling performance of SnP@PGc-1 composite. **Figure 6.7. (d)** shows Nyquist plots after different sodiation-desodiation cycles. The Nyquist plot consists of two partially overlapped semicircles at high-to-medium frequency region and a straight line at low frequency region. These semicircles correspond to sodium ions passing through SEI film and charge transfer between electrolyte and active material. A straight line was observed in low frequency region, which is attributed to sodium ions diffusion inside the active materials. In the equivalent circuit, inset of **Figure 6.7. (d)**, R_e denotes the electrolyte resistance, corresponding to the intercept of high-frequency semicircle at Z_{re} axis. The R_{sei} and constant phase element (CPE1), which correspond to high-frequency semicircle, denotes the solid electrolyte interface (SEI) layer resistance and dielectric relaxation capacitance, respectively. The R_{ct} and CPE2 elements, corresponding to medium-frequency semicircle, and represent charge transfer resistance and related double-layer capacitance, and W is the Warburg impedance. The obtained R_e, R_{sei} and R_{ct} values are listed in **table 6.1.**

Table 6.1. Re, Rsei and Rct obtained by fitting experimental data in Figure 7 using equivalent circuit (inset in Figure 7) for SnP@PGc-1 anode composite after different cycles.

	2nd cycle	10th cycle	50th cycle
Re	6	6.5	9
Rsei	355	309	240
Rct	596	306	33

After cycles, all of the R_e and R_{sei} are reduced, indicating stable interface between electrolyte and active material and hence explaining extremely stable cycling performance of composite. The values of R_{ct} for the cell after 50th cycle is about 33 Ω, much smaller than reported charge transfer resistance for Sn and P composite [19]. The relatively low R_{ct} can explain better rate capability compared with the reported tin phosphide electrodes in literature.

Depending on heating technique used and time of heating[16], the size of the phosphide particles vary. The size of nanoparticles obtained via microwave irradiation vary in the range of ≈20nm (**Figure 6.2**, SnP@PGc-1), which is much smaller than traditional heating (≈100nm, SnP@ PGc-4, **Figure 6.9.**), as observed by SEM.
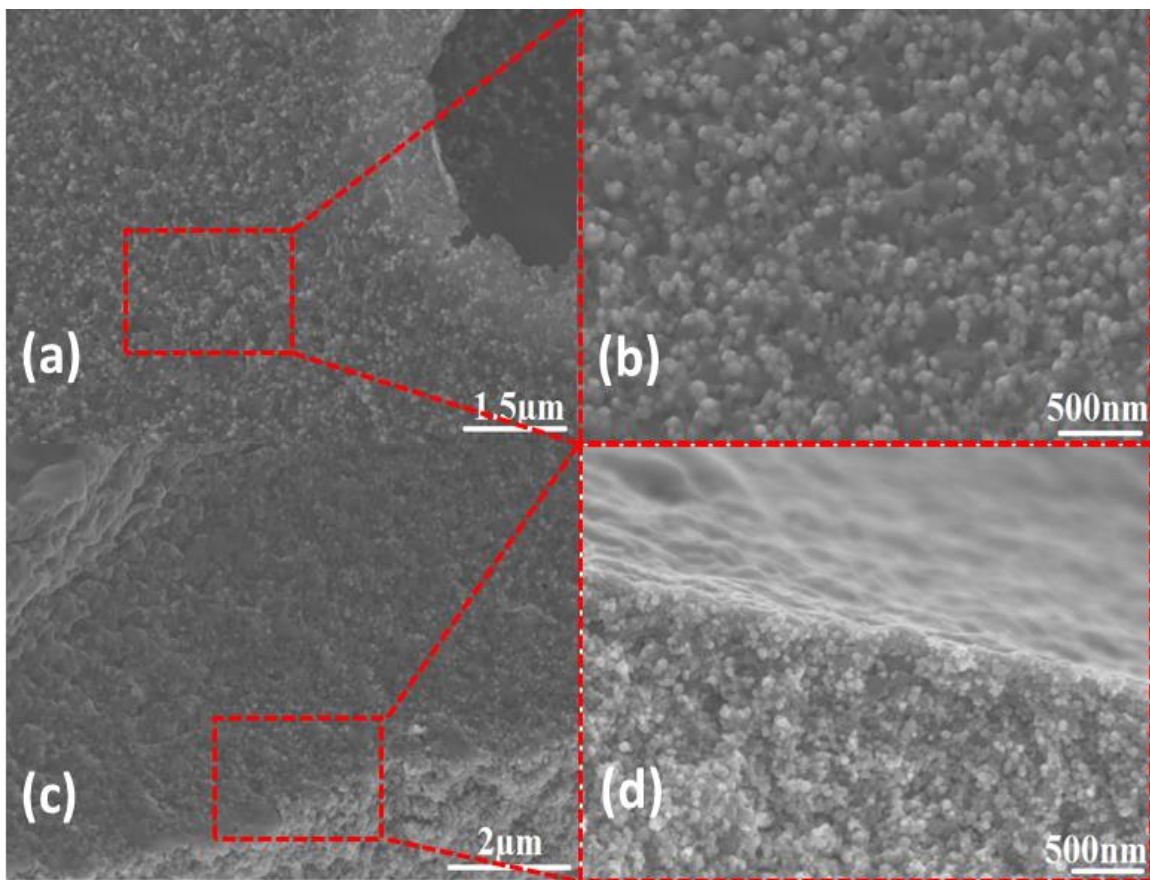
Figure 6.9. The SEM image of traditionally synthesized tin phosphides (SnP@PGc-4). SEM exhibits absence of wrinkled morphology (a) with the nanoparticles in the range of ≈100nm (b), whereas cross sectional view (c, d) indicates embedment of nanoparticles between the carbon layers.

The change in the ratio of SnCl$_2$ to phytic acid from 1.23: 1 to 1:1(SnP@PGc-2), or increased microwave irradiation of SnP@PGc-2(SnP@PGc-3) lead to the capacity of 340 and 290 mAh/g after 600 cycles at a charge/discharge current of 0.2C (**Figure 6.10.(a) and 6.10.(d)**).

Figure 6.10. The Reversible capacities at 200mAhg^{-1} for 600cycles in SnP@PGc-2 (a), and for 500cycles in SnP@PGc-2. The capacity fading was attributed to larger particle size in both SnP@PGc-2 (b, c) and SnP@PGc-3 (e, f) by TEM.

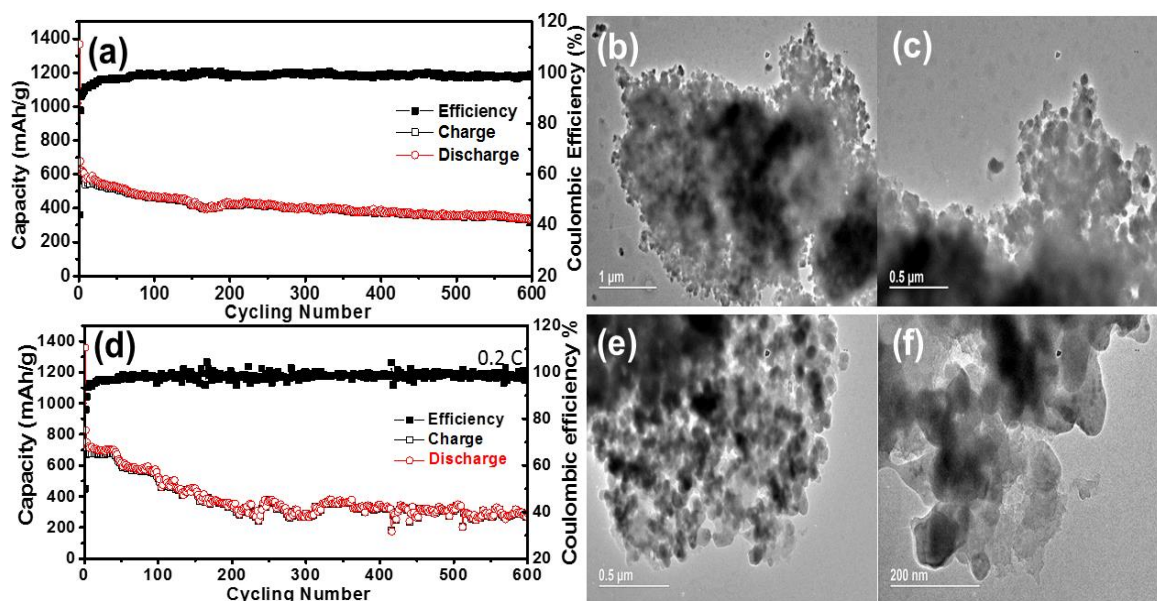The capacity decay can be attributed to larger particles sizes as observed in TEM, and relatively high impurities (additional peaks in XRD, **Figure 11(a)**) in combination with structural composition (The XPS spectra of the SnP@PGc-2 and SnP@PGc-3, recorded the Sn, P, C and O deconvolution peaks, similar to the SnP@PGc-1 with increased spin orbital splitting to 8.43ev in the former case and 8.41ev in the latter case in comparison to the SnP@PGc-1, **Figure 11**) may induce the decay of cycling capacities. The ex situ AT-IR (**Figure 6.5. (b)**) indicated the presence of a HPO$_4^-$ peak and a broad peak in the range of 600-1400cm^{-1}, even after 120sec of microwave irradiation. This indicates inefficient microwave absorption of SnP@PGc-2 & 3 mixture, to form tin phosphides.
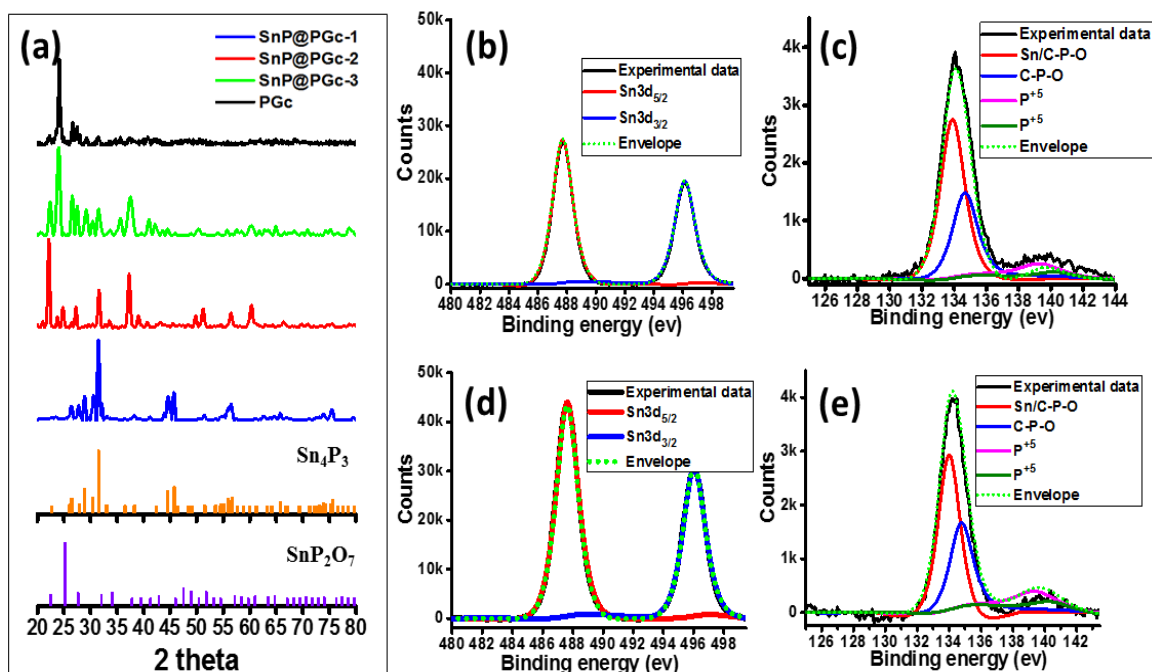
Figure 6.11. XRD spectra (a) and XPS deconvolution of tin and phosphorous of SnP@PGc-2 (b, c) and SnP@PGc-3 (c, e).

6.3. Conclusion

A single step fabrication approach of SnP@PGc composite via microwave chemistry was developed. Phosphorous doped carbon network surrounds the Sn_4P_3 nanoparticles of 20nm in diameter, forming a core shell structure. The SnP@PGc-1 composite exhibited a superior cycling stability of 515mAhg^{-1} at a current density of 200mAhg^{-1} over 750 cycles and 390mAhg^{-1} at a current density of 1000mAhg^{-1} over 1150 cycles. The outstanding cycling performance was attributed to formation of reversible Sn_4P_3 along with decelerated pulverization (volume expansion) due to presence of wrinkled PGc carbon embedding porous phosphorous doped carbon shell on tin phosphides. This approach points out importance of microwave assisted synthesis of SnP@PGc and the use of these materials in energy storage devices.

6.4. Experimental method

6.4.1. Material synthesis

SnP@PGc-1: In a typical experimental procedure, required amount of $SnCl_2$ (3.32mmol) was added into a 35ml Pyrex glass vessel (CEM, # 909036). The salt is dissolved by adding 0.5ml of acetone via bath sonicator. To this solution, 5mmol of Ethylene Glycol is added and further sonicated. 2.71mmol of Phytic acid (Sigma Aldrich, 50 w/w % in water) is added to the reactor and closed with a Teflon lined cap (CEM, # 909235). The sample is sonicated again in bath sonicator for 5mins to get a uniform suspension and then is placed in 500ml glass beaker and covered with a watch glass. The above assembly is now placed in microwave (Panasonic commercial microwave 1000W) and subjected to microwave irradiation to 100sec. After microwave treatment, reaction tube is allowed to cool down. and the resulting product is sonicated with ethanol via bath sonication and then filtered with 0.8µm polycarbonate filter paper (Millipore, ATTP 04700). The products are washed with water (1000ml) and ethanol (200ml), and is dried in oven at 80^0C overnight.

SnP@PGc-2 and SnP@PGc-3: In a typical experimental procedure, required amount of $SnCl_2$ (2.17mmol) was added into a 35ml Pyrex glass vessel (CEM, # 909036). The salt is dissolved by adding 0.5ml of acetone via bath sonicator. To this solution, 2.17mmol of Ethylene Glycol is added and further sonicated. 2.17mmol of Phytic acid (Sigma Aldrich, 50 w/w % in water) is added to the reactor and closed with a Teflon lined cap (CEM, # 909235). The sample is sonicated again in bath sonicator for 5mins to get a uniform suspension and then is placed in 500ml glass beaker and covered with a watch glass. The above assembly is now placed in microwave (Panasonic commercial microwave 1000W) and subjected to microwave irradiation to 80sec. After microwave treatment, reaction tube

is allowed to cool down and is referred to as SnP@PGc-2. In the case of SnP@PGc-3, the cooled down sample is further exposed to microwave irradiation for another 20sec and again allowed to cool down. This step is repeated for one more cycle of 20sec microwave irradiation. After cooling down, the resulting product is sonicated with ethanol via bath sonication and then filtered with 0.8µm polycarbonate filter paper (Millipore, ATTP 04700). The products are washed with water (1000ml) and ethanol (200ml), and is dried in the oven at 80^0C overnight.

SnP@PGc-4: In a typical experimental procedure, required amount of $SnCl_2$ (4.34mmol) was added into a 35ml Pyrex glass vessel (CEM, # 909036). The salt is dissolved by adding 0.5ml of acetone via bath sonicator. To this solution, 10mmol of Ethylene Glycol is added and further sonicated. 4.34 mmol of Phytic acid (Sigma Aldrich, 50 w/w % in water) is added to the reactor and closed with a Teflon lined cap (CEM, # 909235). This sample is sonicated again in bath sonicator for 5mins to get a uniform suspension and then is placed in an oil bath and heated for 2hrs at 80^0C to make a concentrated solution. The solution is placed in a quartz boat and then traditionally heated at 500^0C for 4hrs. After cooling down, the resulting product is sonicated with ethanol via bath sonication and then filtered with 0.8µm polycarbonate filter paper (Millipore, ATTP 04700). The products are washed with water (1000ml) and ethanol (200ml), and is dried in oven at 80^0C overnight.

PGc: The PGc carbon material is synthesized as described in our previous work[60]. In brief, 1ml of phytic acid is subjected to 50sec of microwave irradiation. This sample is filtered with 0.8µm polycarbonate filter paper. The product is washed with water (1000ml) and ethanol (200ml) and dried in oven at 80^0C overnight.

6.4.2. Material characterization

SEM/STEM: The surface morphology of the as synthesized catalyst is characterized via Scanning Electron Microscopy. (SEM) and the distribution of Sn_4P_3 nanoparticles in the PGc matrix is analyzed with Scanning Tunneling Electron Microscopy (STEM) using a HITACHI S-4800 Field emission Scanning Electron Microscope (FE-SEM, Hitachi Co.Ltd). The SEM sample is prepared by placing the powder on carbon tape which is fixed to the stud and sample is analyzed by applying a voltage range of 2-5KV, whereas the STEM sample is prepared by sonicating sample in water (approx. 1mg in 5ml water)for 1min. The as prepared solution is drop casted onto Cu grid mesh size 400, which is vacuum dried then analyzed at 30KV accelerating voltage.

TEM: The crystal lattice of the Sn_4P_3 nanoparticles are studied using a HRTEM, JEOL JEM-2100F equipped with CEOS Cs correctors, 200 kV on a 300 mesh Cu grid.

XRD: The crystal structure of nanoparticles was studied using Bruker D8-Eco X-ray powder diffraction (XRD) instrument which is equipped with a Cu Kα irradiator (λ=0.154056nm). This instrument is interfaced to a computer equipped with Eva-diffraction suit software for data treatment/analysis. The samples are grounded into fine powder in a mortar and pestle and then they are filled into X-ray holder which is placed on stage and the X-ray diffraction collected from 5-45^0 2Θ.

EDS: The distribution of Sn_4P_3 coated with porous carbon shell embedded in PGc matrix is analyzed via Energy Dispersive X-ray Spectroscopy (EDS) mapping. The sample is prepared by drop casting the slurry of sample onto a Cu tape and allowed it to dry. An accelerating voltage of 15-20Kv is used to collect the spectra.

Raman spectroscopy: Raman spectroscopy was collected by depositing the dispersed samples on anodisc membrane and spectra collected with the instrument Witech alpha 300 Raman spectroscopy. A laser power of 12W with an integration time of 20sec and excitation laser wavelength of 532nm was used to collect the spectra. A total of 5 spectra were collected for each sample.

XPS: X-ray photoelectron spectroscopy (XPS) is used to detect the functional state of dispersed Sn_4P_3 nanoparticles along with that of PGc. The Silica substrate (Silicon Prime Wafers P type, Boron dopant, thickness 500+/-25μ with a resistivity of 0.001-0.005Ωcm) is used for analysis on which the slurry of catalyst was dropped (thickness of approximately 30-50nm). The XPS spectra was acquired using a Thermo scientific K-Alpha system with a monochromatic Al Kα x-ray source (hν = 1486.7ev). For data analysis, smart background subtraction was performed and spectra were fit with Gaussian/Lorentzian peaks using a minimum deviation curve fitting method (Advantage software package). The Integrated peak areas along with Scofield sensitivity factor were used to determine the functional composition.

ATR-IR: The Attenuated Total Reflectance-Infra Red (ATR-IR) spectra was collected by depositing thin films on a diamond plate and were acquired with a Thermo-Nicolet 6700 spectrometer (ThermoElectron Corp., Madison, WI), using a sample shuttle and a mercury− cadmium-telluride (MCT) detector. Four blocks of 128 scans each were co-added with 4 cm^{-1} spectral resolution and two levels of zero- filling so that data was encoded every 1 cm^{-1}.

BET (Brunauer–Emmett–Teller) measurements: The surface area and porosity measurements of SnP@PGc were carried out at 77 °K using Micromeritics ASAP 2020.

SnP@PGc sample was dried at 100 °C for overnight under vacuum, prior to measurement. The pore size was calculated using BJH adsorption-desorption analysis. After BET measurements, isotherms of the measurement were converted into BET plots and then the specific surface area of catalyst was calculated using the value of slope and intercept of linear best fit line and below BET equation.

$$\frac{1}{Q[(P0/P)-1]} = \frac{c-1}{Qmc}(\frac{P}{P0}) + \frac{1}{Wmc}$$

Here, Q is the adsorbed gas quantity, Qm is the monolayer quantity of adsorbed gas (N_2), c is the   BET constant, P and P_0 are the equilibrium and the saturation pressure of adsorbates at the temperature of adsorption, respectively.

6.4.3. Battery Assembly

Electrolytes are prepared by adding $NaPF_6$ into anhydrous solvents (EC/DMC + 10%FEC). All the solvents were dried by molecular sieve (4Å, Sigma-Aldrich) to make sure the water content to be lower than 5 ppm, which is tested by Karl-Fisher titrator (Metrohm 899 Coulometer). The charge-discharge performances of the electrode materials were examined by 2032 type coin cells. The tin phosphide composite with carbon black and sodium alginate dissolved in water were mixed at a weight ratio of 70:15:15 to form a slurry, which was then pasted on the Cu foil and dried to obtain working electrodes. Pure Na foil was used as counter and reference electrode. Cyclic voltammetry (CV) testing with voltages ranging from 0 to 1.5 V under a scan rate of 0.1 mV/s was recorded using a Gamry 1000E electrochemical workstation (Gamry Instruments, USA). All the cells were assembled in a glove box with water/oxygen content lower than 2 ppm and tested at room

temperature. The galvanostatic charge/discharge test was conducted on Arbin battery test

station (BT2000, Arbin Instruments, USA).

6.5. References:

[1] a) H. Kim, J. Hong, Y.-U. Park, J. Kim, I. Hwang and K. Kang, *Advanced Functional Materials* **2015**, *25*, 534-541; b) K. Tang, L. Fu, R. J. White, L. Yu, M.-M. Titirici, M. Antonietti and J. Maier, *Advanced Energy Materials* **2012**, *2*, 873-877.

[2] a) Y. Kim, Y. Park, A. Choi, N.-S. Choi, J. Kim, J. Lee, J. H. Ryu, S. M. Oh and K. T. Lee, *Advanced Materials* **2013**, *25*, 3045-3049; b) W.-J. Li, S.-L. Chou, J.-Z. Wang, H.-K. Liu and S.-X. Dou, *Nano Letters* **2013**, *13*, 5480-5484; c) J. Qian, X. Wu, Y. Cao, X. Ai and H. Yang, *Angewandte Chemie International Edition* **2013**, *52*, 4633-4636; d) J. Song, Z. Yu, M. L. Gordin, S. Hu, R. Yi, D. Tang, T. Walter, M. Regula, D. Choi, X. Li, A. Manivannan and D. Wang, *Nano Letters* **2014**, *14*, 6329-6335.

[3] a) J. W. Wang, X. H. Liu, S. X. Mao and J. Y. Huang, *Nano Letters* **2012**, *12*, 5897-5902; b) H. Zhu, Z. Jia, Y. Chen, N. Weadock, J. Wan, O. Vaaland, X. Han, T. Li and L. Hu, *Nano Letters* **2013**, *13*, 3093-3100; c) X. Han, Y. Liu, Z. Jia, Y.-C. Chen, J. Wan, N. Weadock, K. J. Gaskell, T. Li and L. Hu, *Nano Letters* **2014**, *14*, 139-147; d) Y. Xu, Y. Zhu, Y. Liu and C. Wang, *Advanced Energy Materials* **2013**, *3*, 128-133; e) Y. Liu, Y. Xu, Y. Zhu, J. N. Culver, C. A. Lundgren, K. Xu and C. Wang, *ACS Nano* **2013**, *7*, 3627-3634; f) J. Liu, Y. Wen, P. A. van Aken, J. Maier and Y. Yu, *Nano Letters* **2014**, *14*, 6387-6392; g) Z. Li, J. Ding and D. Mitlin, *Accounts of Chemical Research* **2015**, *48*, 1657-1665; h) Y. Liu, N. Zhang, L. Jiao, Z. Tao and J. Chen, *Advanced Functional Materials* **2015**, *25*, 214-220.

[4] a) L. Wu, X. Hu, J. Qian, F. Pei, F. Wu, R. Mao, X. Ai, H. Yang and Y. Cao, *Energy & Environmental Science* **2014**, *7*, 323-328; b) Y. Zhu, X. Han, Y. Xu, Y. Liu, S. Zheng, K. Xu, L. Hu and C. Wang, *ACS Nano* **2013**, *7*, 6378-6386; c) H. Hou, M. Jing, Y. Yang, Y. Zhang, Y. Zhu, W. Song, X. Yang and X. Ji, *Journal of Materials Chemistry A* **2015**, *3*, 2971-2977; d) X. Zhou, Z. Dai, J. Bao and Y.-G. Guo, *Journal of Materials Chemistry A* **2013**, *1*, 13727-13731; e) L. Baggetto, E. Allcorn, R. R. Unocic, A. Manthiram and G. M. Veith, *Journal of Materials Chemistry A* **2013**, *1*, 11163-11169; f) J. Liu, L. Yu, C. Wu, Y. Wen, K. Yin, F.-K. Chiang, R. Hu, J. Liu, L. Sun, L. Gu, J. Maier, Y. Yu and M. Zhu, *Nano Letters* **2017**, *17*, 2034-2042.

[5] P. R. Abel, Y.-M. Lin, T. de Souza, C.-Y. Chou, A. Gupta, J. B. Goodenough, G. S. Hwang, A. Heller and C. B. Mullins, *The Journal of Physical Chemistry C* **2013**, *117*, 18885-18890.

[6] J. Mao, X. Fan, C. Luo and C. Wang, *ACS Applied Materials & Interfaces* **2016**, *8*, 7147-7155.

[7] Y. Kim, Y. Kim, A. Choi, S. Woo, D. Mok, N.-S. Choi, Y. S. Jung, J. H. Ryu, S. M. Oh and K. T. Lee, *Advanced Materials* **2014**, *26*, 4139-4144.

[8] J. Qian, Y. Xiong, Y. Cao, X. Ai and H. Yang, *Nano Letters* **2014**, *14*, 1865-1869.

[9] W. Li, S.-L. Chou, J.-Z. Wang, J. H. Kim, H.-K. Liu and S.-X. Dou, *Advanced Materials* **2014**, *26*, 4037-4042.

[10] Z. Wang, L. Zhou and X. W. Lou, *Advanced Materials* **2012**, *24*, 1903-1911.

[11] Q. Li, Z. Li, Z. Zhang, C. Li, J. Ma, C. Wang, X. Ge, S. Dong and L. Yin, *Advanced Energy Materials* **2016**, *6*, 1600376-n/a.

[12] M. A. Patel, F. Luo, M. R. Khoshi, E. Rabie, Q. Zhang, C. R. Flach, R. Mendelsohn, E. Garfunkel, M. Szostak and H. He, *ACS Nano* **2016**, *10*, 2305-2315.

[13] a) C. Wang, C. Wu, S. Chen, Q. He, D. Liu, X. Zheng, Y. A. Haleem and L. Song, *RSC Advances* **2017**, *7*, 4667-4670; b) K. M. Metz, S. E. Sanders, J. P. Pender, M. R. Dix, D. T. Hinds, S. J. Quinn, A. D. Ward, P. Duffy, R. J. Cullen and P. E. Colavita, *ACS Sustainable Chemistry & Engineering* **2015**, *3*, 1610-1617; c) S. H. Yu, X. J. Cui, L. L. Li, K. Li, B. Yu, M. Antonietti and H. Cölfen, *Advanced Materials* **2004**, *16*, 1636-1640.

[14] H.-m. Wang, H.-x. Wang, Y. Chen, Y.-j. Liu, J.-x. Zhao, Q.-h. Cai and X.-z. Wang, *Applied Surface Science* **2013**, *273*, 302-309.

[15] D. Hu, B. Han, S. Deng, Z. Feng, Y. Wang, J. Popovic, M. Nuskol, Y. Wang and I. Djerdj, *The Journal of Physical Chemistry C* **2014**, *118*, 9832-9840.

[16] V. Tallapally, R. J. A. Esteves, L. Nahar and I. U. Arachchige, *Chemistry of Materials* **2016**, *28*, 5406-5414.

[17] X. Xu, S. Tao, P. Wormald and J. T. S. Irvine, *Journal of Materials Chemistry* **2010**, *20*, 7827-7833.

[18] a) J. Liu, P. Kopold, C. Wu, P. A. van Aken, J. Maier and Y. Yu, *Energy & Environmental Science* **2015**; b) Q. Li, Z. Li, Z. Zhang, C. Li, J. Ma, C. Wang, X. Ge, S. Dong and L. Yin, *Advanced Energy Materials* **2016**, n/a-n/a.

(19) Zhu, Y.; Wen, Y.; Fan, X.; Gao, T.; Han, F.; Luo, C.; Liou, S.-C.; Wang, C. *ACS Nano* **2015**, *9*, 3254-3264.